Experimental-numerical analysis of two-phase flow within microfluidic chip porous medium models

Haohong Pi

université de BORDEAUX

THÈSE PRÉSENTÉE

POUR OBTENIR LE GRADE DE

DOCTEUR DE L'UNIVERSITÉ DE BORDEAUX

ÉCOLE DOCTORALE DE SCIENCES PHYSIQUES ET DE L'INGÉNIEUR

SPÉCIALITÉ MÉCANIQUE

Par HAOHONG PI

Analyse expérimentale-numérique de l'écoulement diphasique dans des modèles de milieu poreux sur puce microfluidique

Sous la direction de: Abdelaziz OMARI

co-directeur: Giuseppe SCIUMÈ

Soutenue le 02/July/2024

Membres du jury:

M. Stefano DAL PONT Professeur, Université Grenoble Alpes Rapporteur
Mme Irina PANFILOVA Maitre de conférences, Université de Lorraine Rapporteur
Mme Azita AHMADI SENICHAULT Professeure, ENSAM Examinateur
Mme Olga BARRERA Professeure associée, Oxford Brookes University Examinateur
M. Abdelaziz OMARI Professeur, Bordeaux INP Directeur de Thèse
M. Giuseppe SCIUMÈ Maitre de conférences, Université de Bordeaux, Co-directeur

Membres invités :

M. Henri BERTIN Directeur de recherche, CNRS invité

université de BORDEAUX

THESIS PRESENTED

TO OBTAIN THE QUALIFICATION OF

DOCTOR OF

THE UNIVERSITY OF BORDEAUX

DOCTORAL SCHOOL OF PHYSICAL SCIENCES AND ENGINEERING

SPECIALTY MECHANICS

By HAOHONG PI

Experimental-numerical analyasis of two-phase flow within microfluidic chip porous medium models

Under the supervision of: Abdelaziz OMARI

co-supervisor: Giuseppe SCIUMÈ

Defended on 02/July/2024

Jury members:

Mr. Stefano DAL PONT Professor, Université Grenoble Alpes Reviewer
Ms. Irina PANFILOVA MCF HDR, Université de Lorraine Reviewer
Ms. Azita AHMADI SENICHAULT Professor, ENSAM Examiner
Ms. Olga BARRERA Associate Professor, Oxford Brookes University Examiner
Mr. Abdelaziz OMARI Professor, Bordeaux INP Supervisor
Mr. Giuseppe SCIUMÈ MCF HDR, Université de Bordeaux, Co-supervisor

Invited members:

Mr. Henri BERTIN Research director, CNRS Invited member

Contents

I Introduction

The immiscible two-phase fluid displacement in porous media is relevant for various natural and industrial processes including Enhanced Oil Recovery (EOR) (Howe, et al., 2015) (Gong, et al., 2020) (Abolhasanzadeh, et al., 2020) (Kang, et al., 2022), CO_2 geological sequestration (Ren, et al., 2017) (Abidoye, et al., 2015), and groundwater pollutant remediation (Kao, et al., 2004) (Forey, et al., 2020). These processes often involve either drainage, where a non-wetting fluid displaces a wetting fluid, or imbibition, where a non-wetting fluid is displaced by a wetting fluid. The dynamics of fluids displacement is inherently influenced by the instability of the interface, that can lead to various flow patterns (Zhang, et al., 2011) (Wang, et al., 2013). Analyzing the patterns of these immiscible fluid displacements qualitatively and quantitatively is essential for optimizing the efficiency of these subsurface processes.

In geological CO_2 sequestration, for instance, the injection of low-viscosity supercritical CO_2 into deep saline aquifers or depleted oil and gas reservoirs often leads to unstable displacement patterns and fingering flow, significantly reducing storage efficiency due to marked fluid flow instabilities. In addition, these dynamics significantly reduce the effective saturation and storage capacity, as only a fraction of the pore space of reservoir becomes occupied by the injected gas. Moreover, remediation of Non-Aqueous Phase Liquids (NAPL) such as hydrocarbons spilled into soil and aquifers, is critical for protecting public health and the environment. Remediation methods include ex-situ techniques, which require excavating contaminated soil, and in-situ techniques like surfactant flushing and gas sparging that inject substances directly into the soil to mobilize pollutants. However, these methods often face challenges such as viscous fingering and low efficiency in heterogeneous media.

EOR is one of the most extensively studied processes within the field of petroleum engineering. The knowledge and techniques developed through EOR research, serve as the basic to address environmental challenges, such as carbon capture and storage, which aims to mitigate the impact of greenhouse gases by safely storing CO_2 underground in geological formations. Therefore, it is of high importance to deeply investigate all fluids displacement modes in porous media, as they significantly impact the efficiency and economics of targeted application.

In this work, we discuss enhanced oil recovery through extra-fluids injection as a frame to investigate the dynamics of immiscible fluids flowing through porous media. Furthermore, with the aim of developing a macroscopic model for daily engineering use, we start by characterizing such a flow at the pore scale and then by means of a scaling procedure can get a macroscale model. However, before proceeding further, let us briefly say some words about EOR.

Main steps in Oil Extraction

In EOR, the challenge of efficiently and gainfully recover the most part of the oil in place has been a major concern over the past several decades. Natural oil reservoirs are typically water-wet, and the distribution of various phases in their presence is illustrated in **Figure I-1**.

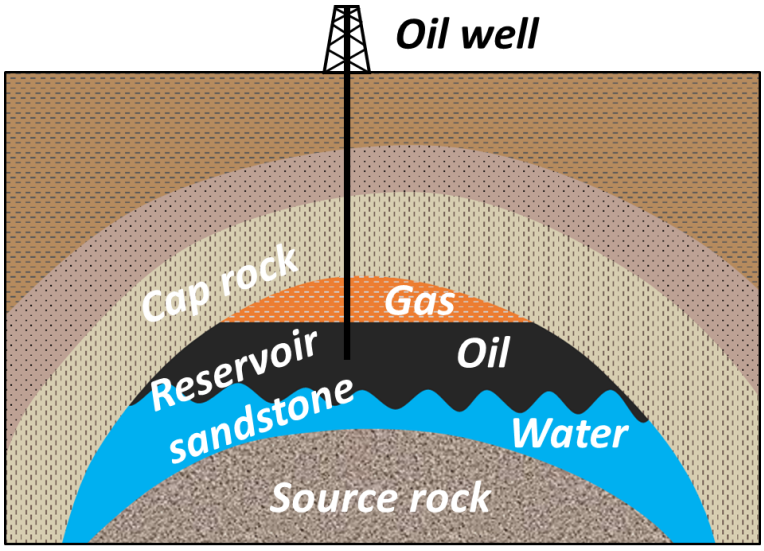

Figure I-1 *The schematic diagram of typical oil and gas reservoir*

The conventional oil recovery process generally consists of three stages: primary, secondary, and tertiary steps. In the primary step, natural oil production occurs due to the pressure differential between the reservoir and the surface, typically yielding a recovery rate of about 10% of the Original Oil in Place (OOIP). The secondary step involves methods such as water and gas injection to maintain reservoir pressure and continue oil extraction. Taking waterflooding as an example, once water breakthrough occurs, both oil and water are produced simultaneously over an extended period. Waterflooding is notably a cost-effective method to achieve the highest economic returns. As the extraction process progresses, oil production gradually decreases while water production increases, eventually leading to a high water-to-oil production ratio known as the “water cut”. At this point, the benefits of continued oil recovery become less favorable compared to the costs. To enhance production, increasing the flow rate to elevate reservoir pressure could be considered, but this method requires significant energy and incurs high expenses, often resulting in limited returns and leading to production stagnation. Recovery rates during the secondary step typically range from 20% to 45% (Allan & Sun, 2003). However and sometimes, secondary oil recovery may require the use water-soluble polymer solutions instead of water.

After waterflooding step, a significant part of the oil remains trapped within the reservoir and cannot be readily extracted. Achieving full (or almost full) recovery of the OOIP is not only economically beneficial but also important from an environmental standpoint (Saha, et al., 2019) (Nikolova & Gutierrez, 2020) (Sharma, et al., 2021). Additionally, forecasts by the International Energy Agency (IEA, 2018) have confirmed the viability of EOR to enhance oil production. Consequently, tertiary oil recovery techniques, have been developed to that end. These techniques involve various strategies beyond

traditional water and gas flooding, such as chemicals injection, thermal recovery, and gas injection, which are designed to improve the efficiency of oil extraction from depleted or underperforming reservoirs. These advanced methods aim to reduce the residual oil saturation to the lowest possible levels, thereby maximizing the extraction of available resources.

In EOR engineering applications, a variety of geological and fluid properties, such as rock porosity, permeability, fluid mobility, reservoir composition, wettability and structure, play crucial roles in influencing the effectiveness of current recovery strategies (Wang, et al., 2017) (Mogensen & Masalmeh, 2020). Fluid flow in reservoirs typically spans distances of hundreds of thousands of meters and is primarily driven by viscous forces. However, the roles of capillary and gravitational forces are also significant and should not be underestimated (Muggeridge, et al., 2014). These forces interact in complex ways to determine the relative permeability of different phases within the reservoir, which in turn influences oil well productivity. For example, viscous forces facilitate the flow of oil through the reservoir, enhancing its extraction while capillary forces act to retain oil within rock formations, particularly in smaller pore spaces where these forces are more pronounced.

However, conducting studies on such a large scale is impractical in terms of cost and operability. Therefore, research on the two-phase flow mechanisms in EOR is typically conducted through core flooding experiments using natural, synthetic or handmade cores. Core flooding experiments provide a macroscopic view of porous media characteristics at the Darcy scale, which is the standard scale for engineering studies as well as valuable information on fluids relative permeabilities in relation to their saturation, wettability, injection conditions, capillary pressure and recovery rate (Masalmeh, 2003) (Pini & Benson, 2013) (Manshad, et al., 2017). These informations are in turn important for developing mathematical models that enable numerical simulations at the reservoir scale.

Among the methods used in EOR, chemical methods are the most popular. These involve injecting fluids alternatively during the secondary or tertiary step of oil extraction. The primary objectives of chemical EOR are to lower the water/oil interfacial tension through the use of surfactants or to decrease the mobility of the injected water, often by adding polymers. This point is supported by the foundational work of Suffman and Toylar (Saffman & Taylor, 1958), which provides a theoretical basis for understanding how interfacial tension and the viscosity ratio between two phases directly affect the instability of the interface. By these ways, the sweeping of the reservoir is more efficient, leading to increased recovery rates.

In secondary oil recovery, chemical methods typically involve the direct use of solutions containing surfactants or polymers. In contrast, in tertiary oil recovery, chemical methods are applied after secondary recovery with brine, and these injections can take place at any stage from the brine's breakthrough (Humphry, et al., 2014) (Abolhasanzadeh, et al., 2020) (Guo, et al., 2022). Comparing these two cases is highly meaningful; by examining the effectiveness of these methods by optimizing

the injection optimal timing and chemicals concentration and type for maximizing economic benefits and enhancing recovery rates.

Juárez-Morejón et al. (Juárez-Morejón, et al., 2019) explored the impact of timing for polymer injection in secondary and tertiary oil recovery experiments with HPAM in water-wet and mixed-wet sandstone cores. They discovered that oil recovery rates from secondary polymer flooding consistently surpassed those from tertiary recovery by about 5% to 15%. In tertiary recovery, increased pre-flooding water volumes inversely affected oil production, attributing better outcomes to earlier polymer injections due to enhanced sweep efficiency at the pore scale. Additionally, oil recovery was notably higher from mixed-wet cores compared to water-wet cores. Further findings from polymer flooding experiments suggested that the use of polymer plugs after initial waterflooding can reduce costs and improve oil displacement, with the size and injection method of the plugs significantly affecting recovery rates. Smaller polymer plugs in low salinity water have proven sufficient for effective tertiary recovery, albeit at a slower rate (Almansour, et al., 2017) (Pal, et al., 2018). Multi-stage polymer injection techniques have further enhanced the stability of these plugs and overall recovery rates (Hu, et al., 2020).

Moreover, wettability profoundly influences fluid flow and recovery rates during oil recovery processes (Farhadi, et al., 2021) (Al-Bayati, et al., 2022). In water-wet media, capillary effects tend to trap oil more permanently, leaving bulk oil isolated at the center of pores post-waterflooding, which is beneficial for subsequent EOR operations. Conversely, in oil-wet or mixed-wet reservoirs, oil is more easily mobilized, with water phases breaking through at pore centers, expelling remaining oil along continuous flow paths. Polymer flooding augments this process by increasing water phase viscosity, reducing the mobility ratio between water and oil, and thus boosting sweep efficiency.

Nevertheless, although core experiments aim to replicate fluid flow related to EOR as accurately as possible at the Darcy scale, it is important to recognize that they typically only provide overall experimental results. Through the differences in entering and exiting fluids in a “black box” manner although sophisticated techniques are now commonly combined to get more insights. Therefore, the analysis and discussion of mechanisms and dynamics should rely on fluid-fluid and fluid-solid interactions at the pore scale. Such a pore-scale analysis is essential to deeply study how the injected fluid displaces fluids in place and how immiscible fluids flow is influenced by the topological structure of the pore network, fluid characteristics, and wettability (Meybodi, et al., 2011) (Tang, et al., 2019).

Thus, microfluidic micromodel devices and numerical simulation experiments are now extensively used in EOR labs experiments.

So in this work, we are concerned by the use of microfluidic chips that are in general easily designed to replicate desired pore structures and modified according to actual parameters such as wettability (Meybodi, et al., 2011) (Yu, et al., 2019). With the advancement of microfluidic technology, these models have been widely applied to the study of diphasic flows, and the development of imaging

technologies has further greaten their utility. The most commonly used imaging facilities (Zarikos, et al., 2018) (Jahanbakhsh, et al., 2020), encompasses high-resolution cameras, optical microscopes, 3D X-ray micro-computed tomography (CT/μCT), micro-particle tracking velocimetry(PTV), nuclear magnetic resonance (NMR), magnetic resonance imaging (MRI) and so on, that enable detailed imaging of various phases within the micromodels during experiments under controlled conditions. This imaging capability allows for detailed analysis of how changes in system's parameters may affect flow pattern, fluids distribution across the chip and the size and distribution of residual oil clusters.

Current work on microfluidic chips primarily involves injecting one phase into a chip saturated with either a wetting or non-wetting phase, with a focus on exploring the effects of Ca and M on two-phase flow displacement. This type of drainage and/or imbibition falls within the scope of secondary oil recovery. Moreover, there are few reports on the impact of capillary number and viscosity ratio during tertiary oil recovery processes, and those that exist typically provide only preliminary results on improvement of oil recovery rate.

In this study, we aim to complete the entire experimental process to explore the effects of capillary number and viscosity ratio during tertiary recovery by analyzing the mobilization mechanisms of oil clusters and their size and distribution. Our work encompasses the entire experimental process across scales, from macroscopic to microscopic, and even down to the analysis of individual cluster movement trends and sizes. This is detailed more here below.

Numerical Simulation

Numerical simulation is of great importance in understanding immiscible two-phase fluid flow within porous media, complementing and validating direct experimental observations and improving the EOR processes. Furthermore, numerical simulations make easier and more cost-effective experimentation under conditions that are difficult to achieve in the lab, making them a principal approach for studying two-phase flow displacement and mechanisms. These researchs operate at two primary scales: the pore scale and the continuum scale (Chen, et al., 2022).

In the continuum scale models, porous media are considered as homogeneous, and the fluid-fluid and fluid-solid interactions need to be explicitly considered increasing hence the complexity of the governing equations. Since these macroscopic flow models are derived based on the concept of Representative Elementary Volume (REV), they require the averaging of microscale equations by incorporating experimental features and variables (Bear & Buchlin, 1991). Continuum scale models overlook the microscale heterogeneity of porous media, and although they are widely used for large-scale transport, they have been questioned for their oversimplification of some critical parameters in the extension of Darcy's law for multiphase flow within porous media (Li, et al., 2005). On the other hand, due to advancements in imaging techniques, numerical methods, and computing technology, pore-scale models have undergone significant development in the past few decades and have been widely used to

study flow of fluids of complex rheology within porous media. In pore-scale simulations, complex flow behaviours and the real porous structure can, in principle, be directly linked, facilitating the understanding of the dynamics of immiscible two-phase flow in porous media.

In contrast to macroscopic models, explicit interactions exist between interfaces at the pore scale in two-phase flow, so interface-resolving numerical simulations are often used to model interface behaviour. These methods include Lattice Boltzmann method, level-set, front tracking, phase-field methods, and their variants (Wörner, 2012) (Raeini, et al., 2012) (Alpak, et al., 2016). To pursue consistency in multiscale models, various upscaling techniques (thermodynamic averaging, volume averaging, etc.) allow the establishment of macroscopic relationships from observed conservation equations (Bear & Buchlin, 1991) (Jackson, et al., 2009) (Lostaglio, 2019). However, once the upscaling is performed, the number of unknowns often exceeds the number of equations. Actually, the representativeness of available macroscopic models is quite limited in the sense that they do not capture fluid-fluid and fluid-solid interactions that take place at the pore scale. For this reason, the strategy in this thesis is to model in an original way two-phase flow at the microscale to derive parameters and constitutive laws for a larger-scale model. This requires more parameters and experimental results at the pore scale to support it. So, details on strategy and followed procedure are given later in chapter "Materials and Methods"

Thesis Work

In our experiments, we will focus on the tertiary EOR method, that consists in flooding a well characterized chip with viscous fluids after the common waterflooding period has ended. Naturally, experiment series enclose both drainage and imbibition that all are investigated beforehand. During these two primary steps, and depending on the value of both the capillary number and the viscosity ratio of invading fluid to that of defending one, we will primarily be interested in:

- How fluids saturation evolves in function of flow rate and injected volume of invading fluid
- The location, size and form of remaining water and oil at pore scale
- Visualise the invasion process and physical phenomena at pore scale that may happen inside such as Haines jumps during the drainage and snap-off events during imbibition, and attempting to link these phenomena with recorded pressure drops
- How fluids move and invade at a macroscale and microscale
- How variate in pore structure influence experimental results

Our findings will then be discussed and compared with available literature

After the waterflooding period, we will explore the impact of the viscosity of injected fluids on EOR characteristics. We will use glycerol/water mixtures to set the viscosity of the invading phase at a given value and observe in live the mobilization process of residual oil clusters under well defined conditions. This will include analyzing their saturation and distribution and whether a given type of oil cluster will

be mobilized or remain trapped. Finally, other statistical data on the number density and size of clusters post-waterflooding will be discussed

In this manuscript, I will present my work in five chapters:

Chapter II: This chapter reviews some typical studies on two-phase flow from macroscopic to pore scale. It discusses the parameters and models involved in two-phase flow research. After briefly discussing the contribution of traditional core flooding experiments at the Darcy scale to two-phase displacement, the focus shifts to the development and application of microfluidic models. Specific parameters such as etching depth and the accurate calculation of the Ca are explored, with the latest advancements presented. Additionally, a brief review of EOR techniques is provided, including reports on the capabilities of viscous and elastic forces in polymer flooding to enhance oil recovery and mobilize residual oil. Lastly, this chapter reviews models, and methodologies used in numerical simulations, highlighting the advantages of our modelling tool compared to others.

Chapter III: This chapter primarily details the entire experimental process, including materials, setup, followed procedures, data measurement, acquisition and processing. The focus is on the acquisition and post-processing of image information and the data analysis process.

Chapter IV: This chapter is separated into two inequal parts

The first part is allocated to “physical experiments”. It presents the properties of fluids and parameters of porous media. It analyzes and discusses the data and results obtained from drainage, waterflooding, and glycerol/water mixture injection experiments, comparing them with previously reported work to highlight our strengths and shortcomings.

Ihe the second part I will present first a validation of our modelling tool through a comparison with already published data on a viscoelastic drop outgoing from a pipe. Then I will present our first result obtained in case of imbibition and drainage and compare them to those coming from physical experiments.

Chapter V: This final chapter provides conclusions and future perspectives based on the findings and discussions presented in the preceding chapters.

II Literature Review

II.1 Multiphase Flow in Porous Media

II.1.1 General Definition of a Porous Medium

Porous media are materials characterized by the coexistence of a solid matrix and pore channels. These pore channels can be occupied by one or multiple fluids, and the morphology and physicochemical properties of pores determine the resistance experienced by fluids as they flow through the porous medium. Generally, porous media can be classified into unconsolidated and consolidated media. Unconsolidated structures are formed by the accumulation of particulate materials with non-convex solid matrices and lack of particle binding (e.g., sand). In contrast, consolidated solid matrices are composed of cemented particles, such as limestone.

II.1.1.1 Porosity

The physico-chemical properties of a porous medium are significantly influenced by the intrinsic properties of the constituent materials, the deformation behaviour of the solid skeleton, and the physical properties of the fluids within the pores. Porosity represents the ratio of pore volume V_{Pores} to the total volume of the porous medium V_{Total}.

$$\phi_{Total} = \frac{V_{Pores}}{V_{Total}} \qquad \text{Equation 0-1}$$

Pores that form interconnected percolating paths are termed “effective” pores and the effective porosity can be defined from the effective volume of pores V_{Pores}^{Eff} as follows,

$$\phi_{Eff} = \frac{V_{Pores}^{Eff}}{V_{Total}} \qquad \text{Equation 2-2}$$

Isolated and closed pores constitute the residual porosity ϕ_{Eff} and therefore is less or equal to ϕ_{Total}.

For the sake of clarity and ease of reading, we will use the effective porosity noted from now as ϕ, representing the interconnected or open pores.

II.1.1.2 Pore Size Distribution

The variability in pore size distribution provides a nuanced view of rock structures beyond simple porosity measurements. Porosity quantifies the total volume of pores within a porous medium, while pore size distribution offers detailed insights into the variability and range of these pore sizes, from micropores to macropores (Nimmo, 2004). This distribution directly influences hydraulic conductivity and capillary pressures in rock formations. Larger pores facilitate easier fluid flow but can also lead to

higher variability in permeability. Additionally, the hysteresis observed in water retention and capillary pressure curves can often be attributed to variations in pore size distribution (Lawrence & Jiang, 2017).

When discussing pore structure, it is crucial to distinguish between two main components: pore bodies and pore throats. Pore bodies are the wider sections where fluids are primarily stored, whereas pore throats are the narrower passages that connect these larger pore bodies. The ratio of pore body to pore throat sizes is a critical factor that influences fluid flow, with lower ratios indicating reduced connectivity and, consequently, lower permeability.

The distribution of pore bodies affects the storage capacity and available fluid pathways, where larger pore bodies may store more fluid but could also lead to increased bypassing if the connecting throats are restrictive. Conversely, pore throat size distribution is essential for determining how easily fluids can traverse from one pore body to another, impacting permeability and the efficiency of fluid displacement processes such as EOR. Smaller pore throats may result in higher capillary pressures, affecting oil recovery by trapping oil behind advancing fronts of water or polymer solutions.

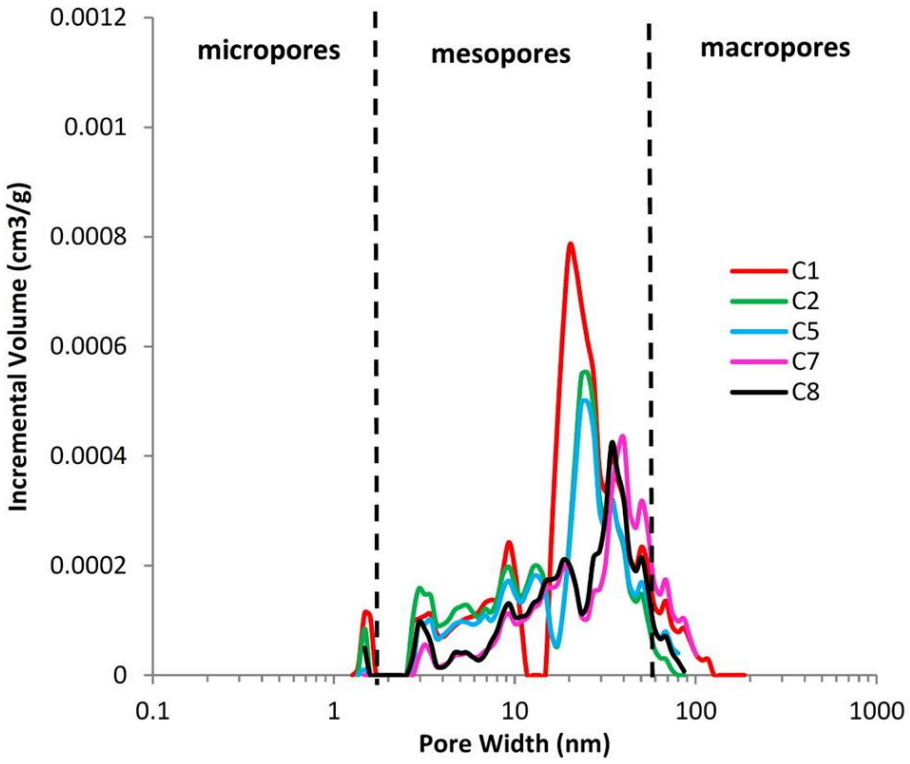

Figure II-1 *Pore size distribution from nitrogen adsorption tests with five shale formations cases (Al Hinai, et al., 2014).*

Common methods for measuring pore sizes include the Mercury Injection Capillary Pressure (MICP) method (Kale, et al., 2010), Nitrogen adsorption (N2) method (Clarkson, et al., 2013), and imaging techniques such as Scanning Electron Microscopy (SEM), Nuclear Magnetic Resonance (NMR) and X-ray Computed Tomography (CT) (Anovitz & Cole, 2015). These methods can directly or indirectly assess pore diameters, porosity, and pore size distribution. **Figure II-1** illustrates a typical shale pore

size distribution evaluated using the N2 method, highlighting the proportions of micropores, mesopores, and macropores (Al Hinai, et al., 2014).

II.1.1.3 Coordination Number

The coordination number in porous media refers to the number of connections (throats) a pore body has with other adjacent pore bodies. This metric is vital for understanding the connectivity and network complexity of the porous structure. A higher coordination number generally indicates better connectivity, which can enhance fluid flow and improve oil recovery by providing multiple pathways for the displacing fluid. In contrast, a lower coordination number might hinder flow and lead to increased residual oil saturation due to ineffective pore network utilization.

For example, in carbonate rocks (Al-Kharusi & Blunt, 2007), although some pores exhibited high connectivity, these were relatively few in number. The average coordination number was determined to be 5.0, after excluding boundary pores and pore clusters that represented less than 2% of the total (see **Figure II-2**).

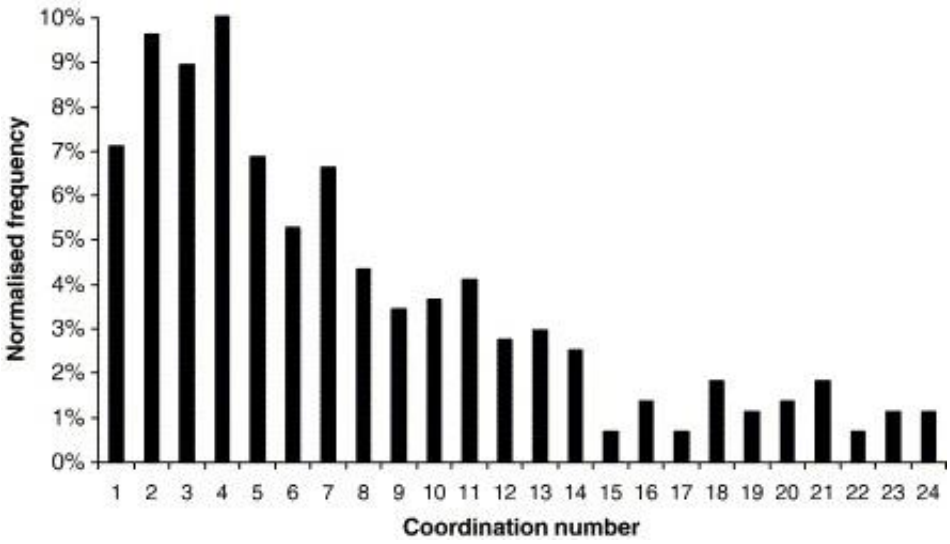

Figure II-2 Coordination number distribution for the carbonate sample.

II.1.2 Monophasic Flow in a Porous Medium

II.1.2.1 Darcy-Forchheimer Equation

The traditional viewpoints and theories concerning the flow of a fluid in a porous medium are rooted in the initial findings of sediment column filtration experiments conducted by Henry Darcy (Darcy, 1856). Darcy's experiments provided the initial insight into the linear relationship between the flow velocity of water and the hydraulic gradient in a sand filter.

Within a uniform porous medium, the commonly used expression, as refined by Morris Muskat, to represent the linear relationship between q and pressure drop is typically formulated as,

$$q = -\frac{k}{\eta L}\Delta p \qquad \text{Equation 2-3}$$

where η is the dynamic viscosity of the fluid (Pa·s), Δp (Pa) is the pressure drop across the porous medium, L is the horizontal flow distance (m), and k (m^2) is the permeability of the porous medium.

In nonisotropic porous media with incompressible flow, neglecting the gravity term, Darcy's law for volumetric flux density can be typically expressed as:

$$\mathbf{q} = -\frac{\bar{\bar{k}}}{\eta}\bar{\nabla} p \qquad \text{Equation 2-4}$$

where $\mathbf{q}$ represents the volumetric flux density (flow rate per unit area), $\bar{\bar{k}}$ is the intrinsic permeability tensor, $\bar{\nabla} p$ is the pressure gradient in the direction of flow. The Darcy's law is based on the assumption of Stokes flow, with a very low Reynolds number. Nevertheless, it has found widespread application in geophysical and engineering contexts, even when *Re* is moderately high (*Re* ≈ 1). This is particularly true for single-phase fluid flow in porous media, where effects such as inertia, friction, and variations in porosity are often negligible.

As *Re* gradually increases (1 < *Re* < 10), it has been observed that fluid flow deviates from Darcy's law (Dupuit, 1863) (Forchheimer, 1901) (Muskat, 1938) due to increased inertial effects and energy losses (Hiroyuki, et al., 2005). Consequently, modifications of the original Darcy's law have been proposed to account for these deviations (Forchheimer, 1901) (Brinkman, 1949) (Irmay, 1958) (Berkowitz, 1989). Forchheimer introduced an empirical relationship with a quadratic term, as his data indicated that Darcy's law does not hold under high flow velocities:

$$\bar{\nabla} p = a\mathbf{q} + b\mathbf{q}^2 \qquad \text{Equation 2-5}$$

where a and b are empirical parameters related to media and fluid. It is proven that the linear term represents the viscous effect and the quadratic term represents the inertial effect.

In the flow of fluids through a porous medium within a certain range of flow velocities, the observation of non-Darcy flow behaviour becomes apparent. When the pressure-drop-velocity relationship deviates from the linear trend, an extended Darcy-Forchheimer equation is employed to modify the Darcy velocity, allowing for the identification and characterization of various flow regimes encountered during the passage of fluids through the porous medium. These regimes span from linear flow to transitional states and eventually reach the inertial state (Kundu, et al., 2016) writing,

$$\Delta p = \frac{\eta L}{k} q + \frac{\rho F_d}{\sqrt{k}} q^2 \qquad \text{Equation 2-6}$$

where ρ is the fluid density (kg/m^3), F_d is Forchheimer drag coefficient. The Darcy-Forchheimer equation has been demonstrated to describe flow in porous media with sufficiently high Reynolds numbers where inertial forces play a significant role.

II.1.2.2 Flow Model in a Porous Medium

Capillary Bundle Model

In order to establish practical correlations between different flow characteristics in porous systems, we can represent these porous media with simplified models. The model representation that is widely used of a porous medium is a bundle of straight cylindrical capillaries with the same radius with fluid flow in capillaries being described by the Poiseuille equation. So,if we consider the medium as a bundle of n_t parallel capillaries, each with a radius R_p and length L, we can express the flow velocity using Poiseuille's law:

$$q = \frac{n_t \pi R_p^{\ 4}}{8\eta} \frac{\Delta p}{L} \qquad \text{Equation 2-7}$$

with,

$$A\phi = n_t \pi R_p^{\ 2} \qquad \text{Equation 2-8}$$

By combining Equation 2-8 with Darcy's law, we get,

$$R_p = \sqrt{\frac{8k}{\phi}} \qquad \text{Equation 2-9}$$

If tubes are not parallel but randomly-oriented, the pressure gradient is corrected by the tortuosity factor τ_t, and the permeability can be expressed as [Nooruddin and Hossain, 2011],

$$k = \frac{\phi R_p^{\ 2}}{8\tau_t} \qquad \text{Equation 2-10}$$

The Carman-Kozeny model

For the case of fluid flow in the porous media, the Kozeny-Carman model (1937) can provide an approximate calculation of permeability based on geometric properties of porous medium, particularly, the model relates the permeability of a porous medium to its porosity and microstructure (encompassed in the shape factor characteristic f_g of medium and tortuosity factor τ_t), the permeability (Nooruddin, 2011) is written as,

$$k = \left(\frac{1}{f_g \tau_t S_{sp}^{\ 2}}\right) \frac{\phi^3}{(1-\phi)^2} \qquad \text{Equation 2-11}$$

where the S_{sp} is the specific surface; the surface area per unit volume of the solid. The model of Kozeny and Carman was established for a column filled with spheres of diameter d_p at maximum compactness, with the $S_{sp} = 6/d_p$, so that, the permeability is given by the relation of Ergun (1952),

$$k = \frac{\phi^3 {d_p}^2}{180(1-\phi)^2} \qquad \text{Equation 2-12}$$

II.1.3 Diphasic Flow of Immiscible Fluids at Macroscale

II.1.3.1 Fractional Flow Theory

The first attempt to theoretically model diphasic fluid flow in porous media was to consider their concomitant flow ignoring the stress jump across the interface between them. This give rise to fractional flow. It describes the proportion of one fluid (often water in oil-water systems) relative to the total flow of all fluids through a porous medium. The fractional flow of a given phase is influenced by its relative permeability and viscosity compared to those of the other flowing phases. This relationship is typically depicted in fractional flow curves, which plot the fractional flow of a phase against its saturation in the porous medium. According to the fractional flow theory (Pope, 1980) (Philip Binning, 1999), the fractional flow of saturation of *w*-phase (S_w) is a function of mobility ratio M_r,

$$f_w(S_w) = \frac{M_r}{1+M_r} \qquad \text{Equation 2-13}$$

where, M_r is the ratio between the mobility (λ) of the the displacing fluid (*w*-phase) and displaced fluid (*nw*-phase); the mobility of a fluid being defined as the ratio of its permeability to viscosity in the porous medium. Therefore, the expression for M_r can be represented as,

$$M_r = \frac{\lambda_w}{\lambda_{nw}} = \frac{k_w/\eta_w}{k_{nw}/\eta_{nw}} = \frac{k_{rw}}{k_{rnw}} \cdot \frac{\eta_{nw}}{\eta_w} \qquad \text{Equation 2-14}$$

where, η_w and η_{nw} are the viscosities of *w*-phase and *nw*-phase; k_w and k_{nw} refer to *w*-phase and *nw*-phase effective permeability, respectively. Specifically, the effective permeability is the product of the absolute permeability of the fluid and its relative permeability, that is to say, $k_i = kk_{ri}$, where *i* is the different fluid phase (*w*-phase and *nw*-phase), *k* is the absolute permeability of the *i*-phase, and the k_{ri} is the relative permeability of the *i*-phase.

II.1.3.2 Darcy's Law for Two-Phase Flow

For two-phase flow, in addition, the Darcy's law must account for the interactions between two immiscible fluids, each with its own pressure, viscosity, and flow characteristics, because it occupies only part of the pore space and may also be affected by interaction with other phases. Therefore, the permeability to either fluid is expected to be lower than that for the single fluid.

The Darcy's law equation also modifies to include the relative permeability of each phase, which depends on the saturation of the fluids within the porous medium. The modified equation for each fluid phase (e.g., water and oil) becomes:

$$\mathbf{q}_w = -\frac{kk_{rw}}{\eta_w}\overline{\nabla} p_w \qquad \text{Equation 2-15}$$

$$\mathbf{q}_{nw} = -\frac{kk_{rnw}}{\eta_{nw}}\overline{\nabla} p_{nw} \qquad \text{Equation 2-16}$$

where $\overline{\nabla} p_w$ and $\overline{\nabla} p_{nw}$ are the pressure gradients for each *i*-phase.

The relative permeability is a reduction factor that quantifies the ease with which one phase flows in presence of another. It is a function of the saturation and properties of the phases. The measurement and computation methods for relative permeability vary extensively. In oil-water systems, the relative permeabilities are often given through a typical simplified function of *w*-phase saturation (S_w) as (Dahle, et al., 1990) (Young, 1984),

$$k_{rw} = S_w^3 \qquad \text{Equation 2-17}$$

$$k_{rnw} = \left(1 - S_w\right)^3 \qquad \text{Equation 2-18}$$

Figure II-3 show the classical relative permeability functions (water-wet case),

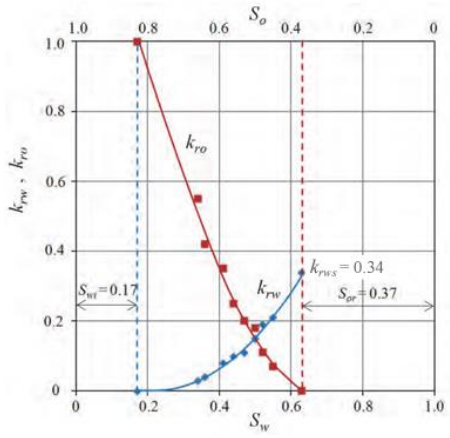

Figure II-3 *Relative permeability curves in water-wet case (Abdul Jamil NAZARI, 2016)*

Another key concept in two-phase flow is capillary pressure, which is the pressure difference between the two fluids at their interface due to surface tension and interaction with the porous medium. It is a function of the pore structure and the wetting characteristics of the fluids.

Compared to the single-phase case, the flows of several immiscible fluids are distinguished by the existence of contact zones between the different components that make up the system: the interface between the wetting phase (*w*-phase) and non-wetting phase (*nw*-phase), but also between the solid *s*-phase and the *w*-phase as well as with the *nw*-phase. The capillary pressure p_c is the pressure difference

between the *nw*-phase and the *w*-phase across their contact interface. The geometry of the interface is physically driven by the interfacial tension σ_{nw}, which is a macroscopic measure of the molecular attraction and repulsion forces between the molecules of the *w*-phase and those of the *nw*-phase and is related to capillary pressure P_c through the Laplace relationship,

$$P_c = \frac{2\sigma_{nw}}{R} \qquad \text{Equation 2-19}$$

where the R is the effective radius of the interface curvature. If the liquids are highly immiscible, the interfacial tension is high; if the liquids are weakly immiscible, the interfacial tension is low. In the water/oil system, the interfacial tension is between 15 and 35 dynes per centimetre (or mN/m) (Oss, 2007).

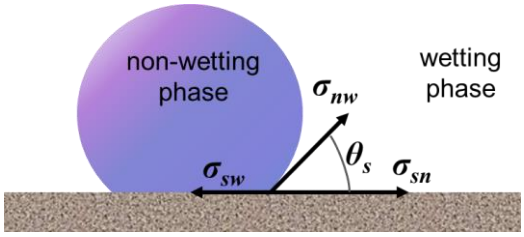

Figure II-4 *Phase wettability. The value of the angle formed between the solid surface and the interface varies as a function of the surface tensions.*

The same attraction/repulsion forces determine the degree of affinity of the fluids with the solid surfaces (wettability) and in particular the physics at the point where the interface between the two fluids and the solid matrix meets, called the triple point (**Figure II-4**). At equilibrium, the sum of the forces at this point must cancel out; this results in Young's analytical relation (Anderson, 1986), which relates the surface tension between the *s*-phase and the *nw*-phase (σ_{sn}); the surface tension between the solid and *w*-phase (σ_{sw}) and the interfacial tension between the two fluids in presence (σ_{nw}). The angle θ_s is called the static contact angle have relationship,

$$\sigma_{nw}\cos\theta_s = \sigma_{sw} - \sigma_{sn} \qquad \text{Equation 2-20}$$

If this angle is well above 90°, the *w*-phase is then qualified as wetting while the *nw*-phase will be non-wetting. It is well known that the wettability of reservoir formations is crucial for diphasic fluid displacement. Wettability refers to the inclination of reservoir rock surfaces to preferentially contact specific fluids in multiphase or diphasic fluid systems. In practical applications, wettability significantly influences various aspects of porous media performance, particularly in reservoir engineering for waterflooding and EOR techniques. For multiphase flows in porous media, the wettability of the phases is a microscopic property that has a major influence on the macroscopic parameters, as it determines the distribution of fluids inside the pores as well as the location of the interfaces, thereby dictating capillary forces.

Due to the challenge of directly measuring in-situ reservoir wettability, core plugs coming from reservoirs are utilized to indirectly determine this characteristic by several methods as the Amott test method (Amott, 1959). Wettability is related to the contact angle, following Anderson (Anderson, 1986) establishing a range of contact angle values to define wettability in porous media, as illustrated in the table below.

Table II-1 *The value of contact angle (Anderson, 1986)*

Contact angle	**Non-wetting**	**Neutral**	**Wetting agent**
Minimum	0°	60-75°	105-120°
Maximum	60-75°	105-120°	180°

II.1.3.3 Experimental Research at Macroscale in EOR

Research on immiscible two-phase flow in oil-water systems is fundamental to EOR. Considering cost-effectiveness, secondary oil recovery often employs waterflooding to produce petroleum. However, due to the pore structure and fluid properties, a significant amount of oil remains trapped in the reservoir. Moreover, while waterflooding albeit allow recovery of a significant amount of the original oil in place, the water cut level rise rapidly compromising the economics performance of the process. Therefore, some other methods have been proposed to enhance more the rate of oil recovery. Here after we give non-exhaustive list of these methods by underlying, the key ideas only although the reader may refer to standard books for more details:

a) Polymer flooding

In the context of simulating polymer flooding, two important factors that need to be considered are the resistance factor (R_r) and the residual resistance factor (R_{rr}). Polymer flooding method relies on the fact that water-soluble polymers, typically synthetic, when dissolved in water at low concentrations (0.1-1 g/L), produces a greater increase the viscosity of the solution, making their use economically attractive for EOR. Consequently, the mobility ratio of water, represented as $\lambda_w = k_w/\eta_w$, is become now $\lambda_p = k_p/\eta_p \approx M_p$, resulting in a decreased mobility ratio R_r that is a measure of the relative mobility of water λ_w compared to that of a polymer λ_p solution under the same conditions.

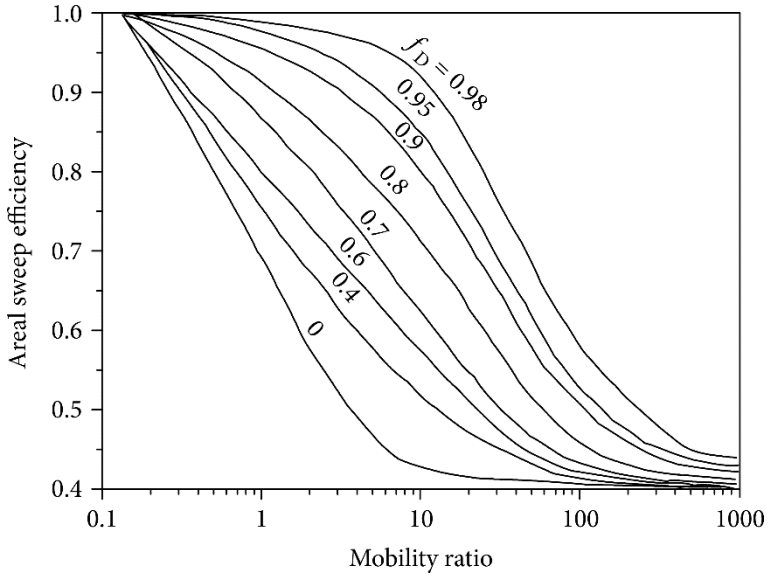

Figure II-5 *Areal sweep efficiency affected by the mobility ratio and fractional flow at displacing phase (f_D) (Caudle & Witte, 1959).*

This change enhances the sweeping efficiency of the waterflood, as depicted in **Figure II-5**, previously published by Caudle and Witte (Caudle & Witte, 1959). However, the effectiveness of enhanced recovery depends on several factors, including the salinity of the water, pH, salt composition, polymer rheology, and the geochemistry of the rock formation. These variables can significantly influence the interaction between the polymer solution and the reservoir rock, impacting the overall success of the polymer flooding process.

For instance, the R_r can be expressed as:

$$R_r = R_{rr}\eta_r \qquad \text{Equation 2-21}$$

where η_r is the relative viscosity of the polymer solution. Here, $R_{rr} = k_w/k_p$ represents the ratio of the permeability of water to that of polymer solutions, which can be highly affected when polymers adsorb onto and sorbs into the solid surface, thereby also impacting the needed quantities of polymer. The value of k_p lower than k_w normally, so $R_{rr} \geq 1$. This interaction influences how polymers modify the flow characteristics within the reservoir, affecting both the efficiency and economics of polymer flooding as an enhanced oil recovery method.

The addition of polymers increases the viscosity of the invading phase, enhancing the mobility ratio between water and oil, which effectively improves the macroscopic sweep efficiency. Furthermore, polymers act to reduce the relative permeability of water by filling pore spaces and creating a network that hinders the free flow of water. As the polymer flooding injection, the water cut initially decreases with a recovery increase, but it eventually rises back to a high level at the end of recovery. To date, polymer flooding has been demonstrated both in laboratory settings and field applications to increase

oil recovery (Original Oil in Place - OOIP) by 5% or more (Rai, et al., 2012) (Manrique, et al., 2007) (Kamal, et al., 2015).

b) Surfactant and Alkali flooding

At the reservoir scale, increasing flow velocity or pressure can be costly with relatively small gains, making it more practical to reduce IFT. It has been reported that if the IFT between trapped oil and displacing fluid can be reduced from the initial values of 20 - 30 mN/m to the range of 10^{-2} - 10^{-3} mN/m, oil droplets can deform and squeeze through the pores (Spildo, et al., 2012) (Deng, et al., 2021). Reed and Healy pointed out that the ultra-low interfacial tension between surfactant solutions and oil is a crucial factor in enhancing oil recovery efficiency (Reed, et al., 1977). The typical Ca for brine flooding are in the range of 10^{-7} to 10^{-6} (Howe, et al., 2015). When Ca increases by 3-4 orders of magnitude, the residual oil saturation significantly decreases, while the residual oil saturation approaches zero when Ca reaches 10^{-2} (Hou, et al., 2005) (Zivar, et al., 2021) (Guo, et al., 2022).

Surfactant and alkali flooding have been demonstrated to effectively reduce IFT, thereby enhancing oil recovery. (Samanta, et al., 2011) (Bera, et al., 2013) (Xie, et al., 2016) (Kamal, et al., 2017) (Manshad, et al., 2017) (Deng, et al., 2021) (Tavakkoli, et al., 2022).

The primary mechanisms of alkali flooding involve alkalis reacting with acidic crude oil to generate in-situ surfactants, thereby expanding the optimal salinity range and reducing IFT. They also contribute to altering the wettability from oil-wet to water-wet or from less water-wet to more water-wet conditions (Dehghan, et al., 2015) (Khlaifat, et al., 2022). This change in wettability facilitates the mobilization and recovery of trapped oil.

Moreover, surfactants can impact residual oil recovery through additional mechanisms, such as the formation of microemulsions that capture residual oil, altering rock wettability, and improving interfacial rheological properties.

Studies indicate the presence of a critical concentration of surfactants known as the Critical Micelle Concentration (CMC). Above the CMC, surfactant ions or molecules in solution aggregate into large micelles. It is below the CMC value that a reduction in interfacial tension and enhanced foam stability occur, making the CMC an important criterion to consider in Enhanced Oil Recovery (EOR) applications. Moreover, the maximum adsorption of surfactants on reservoir rock surfaces occurs at the CMC; exceeding this value does not significantly increase adsorption (Tadros, 2006) (Ahmadi, et al., 2014) (Kamal, et al., 2017).

c) Low-salinity methods

Low-salinity water flooding (LSWF) is an enhanced oil recovery (EOR) technique that involves injecting water with a lower salinity than the formation water into a reservoir to increase oil production

(Alagic, et al., 2011) (Shiran & Skauge, 2013) (McMillan, et al., 2016). This method has gained significant attention due to its cost-effectiveness and environmental friendliness compared to traditional EOR techniques. LSWF enhances oil recovery by altering the wettability of the reservoir rock from oil-wet or mixed-wet to more water-wet conditions, which facilitates the displacement of oil by water.

The effectiveness of low-salinity water flooding is influenced by several factors including the mineralogy of the reservoir rock, the composition of the resident brine, and the crude oil properties. Studies have shown that LSWF can lead to changes in the electrical double layer at the rock-fluid interface, reducing the capillary forces that trap oil and promoting its release. Moreover, the process can mobilize trapped oil by detaching it from rock surfaces through ionic exchange reactions that occur when the injection water interacts with clay minerals. These interactions can lead to the expansion of clay particles, further enhancing oil recovery by improving pore connectivity.

Field applications and laboratory experiments have demonstrated that low-salinity water flooding can increase oil recovery by several percentage points compared to conventional water flooding. The technique is particularly appealing for fields where water injection infrastructure already exists, allowing for a seamless transition to LSWF with minimal additional investment.

d) The remaining often researched area: viscoelasticity

Traditionally, there has been a prevailing belief that viscoelastic polymer flooding only intensifies oil recovery through enhancing sweep efficiency without significantly impacting S_{or} reduction, even in some specialized publications (Green & Willhite, 1998) (Lake, et al., 2014). This is primarily attributed to equivalent displacement conditions, meaning the influence of polymers on the oil-water interfacial tension can be considered negligible. Consequently, based on the CDC, theoretically, polymer flooding doesn't alter the microscopic recovery efficiency provided Sor is quantitatively correlated only with Ca. Moreover, polymers have an insignificant effect on the permeability of the oil phase, hence cannot reduce S_{or}. Some experiments suggest that the reduction in S_{or} observed in core tests might be artificially induced (Element, et al., 2001), and in micro-model experiments, it's suggested that highly viscoelastic polymers have minimal impact on Sor and can be disregarded (Wegner, et al., 2015).

However, in porous media, the influence of microstructure may exert additional effects on flexible polymer chains exhibiting viscoelastic properties. Due to the tortuosity within the porous medium, polymer solutions may experience extensive shear stresses, potentially leading to additional elastic effects during elongational flow. The recent polymer flooding experiments research (Wang, et al., 2000) (Wang, et al., 2000) (Wang, et al., 2001) (Wang, et al., 2001) and field studies (Wang, et al., 2007) (Wei, et al., 2014) indicate that viscoelastic fluids might enhance oil recovery by targeting microscale displacement within individual or a few pore sizes.

To demonstrate that displacement efficiency increases with the elasticity of HPAM, specifically, the impact of Newtonian and viscoelastic fluids on oil recovery in secondary and tertiary oil production was discussed. By comparing the oil recovery between injecting high-viscosity Newtonian fluid (glycerol) and a viscoelastic solution with similar apparent viscosity, Wang et al. found that using the polymer solution led to additional oil recovery (Wang, et al., 2000), supporting the hypothesis of improved recovery rates. Conversely, the reverse sequence (polymer-glycerol) showed no change in residual oil volume, as depicted in **Figure II-6Error! Reference source not found.**. Similar results were reported in the study by Qi et al. (Qi, et al., 2017).

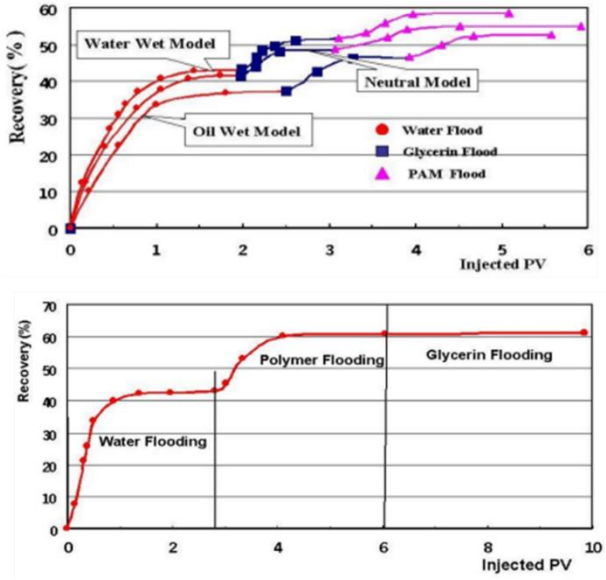

Figure II-6 *Typical core flooding tests in favor of viscoelasticity effect (Wang, et al., 2000).*

II.1.4 Diphasic Flow of Immiscible Fluids at Microscale

II.1.4.1 LogCa/logM Diagram

Within a homogeneous porous medium, immiscible fluids flow characteristic arise from the balance between viscous forces dissipation and interface displacement. This allow to build two non-dimensional numbers:

1) The capillary number that is defined as the ratio of viscous stress (τ_V) due to invading fluids ($\eta\dot{\gamma}$) and the stress rump across fluid-fluid interface (τ_{IFT}), represented as σ/R, This can be writing,

$$Ca = \frac{\tau_V}{\tau_{IFT}} = \frac{\eta\dot{\gamma}}{\sigma/R} = \frac{\eta(R\dot{\gamma})}{\sigma} \cong \frac{\eta v}{\sigma} \qquad \text{Equation 2-22}$$

where $\dot{\gamma}$ is the shear rate, R is the interfacial radius, η is the viscosity of the injected fluid, v is the velocity of the injected fluid, σ is the interfacial tension between injected fluid and displaced fluid.

2) The viscosity ratio is defined as the ratio of the viscosity of the invading fluid η_{inv} to that of the defending fluid η_{def}, with,

$$M = \frac{\eta_{inv}}{\eta_{def}} \qquad \text{Equation 2-23}$$

The flow pattern then depends on the importance of these non-dimensional numbers. Fundamentally, at low Ca, viscous effects are negligible and interfacial effects dominate, so that the flow is primarily governed by the Pc arising during displacement by invading fluid fingers, which in turn depends on the local microstructure of the porous medium.

At high Ca, viscous displacement dominates, and the pattern consequently becomes dependent on the viscosity contrast between fluids. Thus, when the viscosity ratio of the invading fluid to that of the defending fluid (M) is well below 1, displacement occurs as the invading fluid forms thin fingers through the other fluid to take place. In the opposite, when M is above unity, a uniform and stable front is built, and fluid displacement is piston-like.

This behavior was theoretically studied by Lenormand et al. (Lenormand, et al., 1988) and gave rise to the commonly used logCa/logM graphical representation, as shown in **Figure II-7**. This representation illustrates the existence of a transition zone between three regimes.

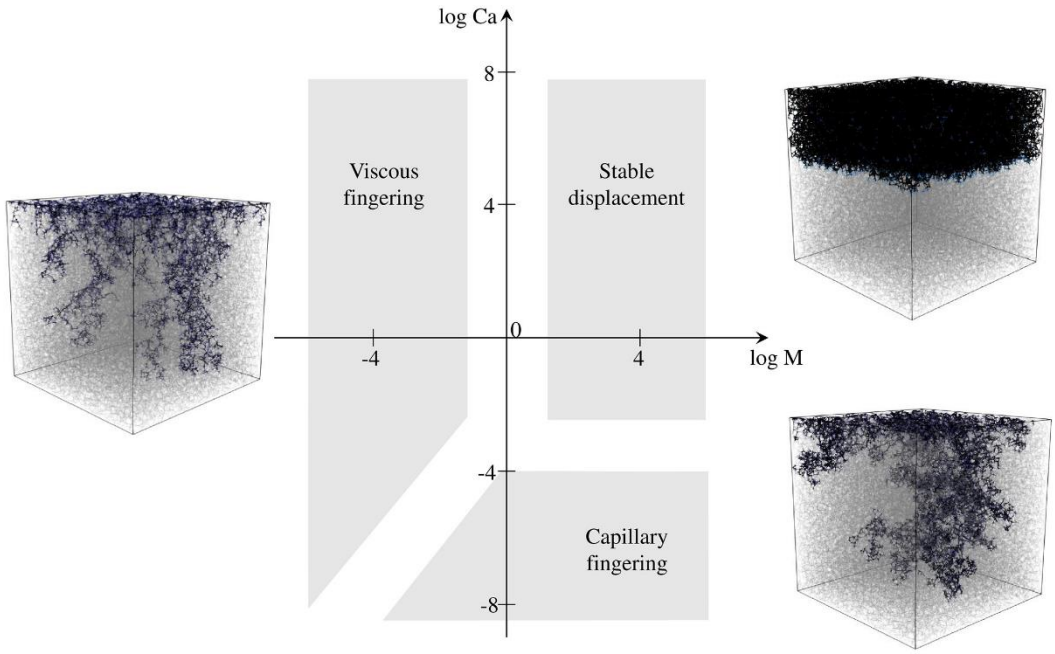

Figure II-7 *LogCa–logM stability diagram showing three flow regimes (Senyou An, 2020). The gray zones denote the stability areas indicated by Lenormand et al. (Roland Lenormand, 1988).*

Three typical displacement patterns (viscous fingering, capillary fingering, and stable displacement) were observed, each exhibiting distinct behaviors and characteristics across different zones of the porous medium.

In capillary fingering, the injected fluid invades not only towards the outlet but also radially and even in the direction of the inlet. Numerous fingers push through the less mobile defending fluid, eventually merging into larger, coarser fingers. The width size was reported by Hu et al. (Hu, et al., 2020), with a single finger is typically 2 to 3 times the pore size, while coarser fingers can be 6 to 8 times the pore size. According to invasion percolation theory, the invading fluid passes only through the largest pore throats that have the lowest capillary entry pressure.

Stable displacement regime occurs when the displacing fluid pushes the displaced fluid uniformly. Stable displacement is ideal for maximizing sweep efficiency as it minimizes the amount of residual fluid left behind. Undoubtedly, the breakthrough time in this mode is the longest among the three regimes. However, during stable displacement with less favorable viscosity ratio (logM < 0), some instabilities in the form of fingers can still emerge at the leading edge of the main flow front. These finger-like flows occur due to localized differences in fluid pressures where the fingers have lower pressures compared to the main flow front. As the displacement progresses, these unstable fingers are eventually overtaken and replaced by the subsequent main flow (Zhang, et al., 2011).

Viscous fingering predominantly follows preferential flow paths in the same direction as the injection, without backward movement. This behavior is primarily controlled by viscous forces, which are influenced by the viscosity of the defending fluid. When the velocity of the invading phase is high, the displacement front advances very quickly and soon reaches the outlet. Consequently, the saturation associated with viscous fingering is typically lower than that observed in capillary fingering or stable displacement. This results in invasion fluid saturations as the fast-moving front does not allow sufficient time for the fluid behind to fill up the pore space effectively, leading to less efficient displacement of the defending fluid.

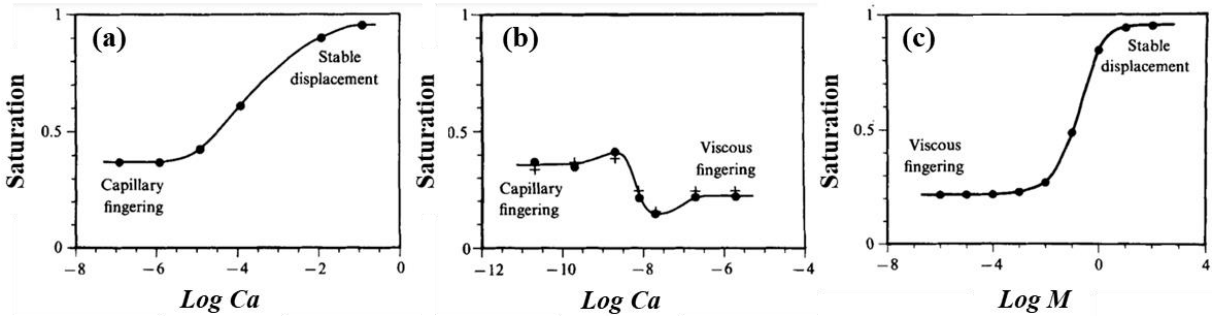

Figure II-8 *The plot of the saturation of invading fluid at breakthrough: (a) log M = 1.9; (b) log M = -4.7; (c) logCa = 0. The black dots and the crosses represent the results of the simulations (Lenormand, et al., 1988).*

Furthermore, different flow regimes lead to variations in the saturation of the invading phase, primarily due to differences in fluid flow behavior. In viscous fingering, the displacement front advances very quickly, forming thin fingering pathways and resulting in low saturation of the invading phase. According to simulations by Lenormand et al. (1988), under a low viscosity ratio (logM = -4.7), the

saturation of the invading phase at breakthrough for viscous fingering is approximately 0.22, with a minimum saturation reaching down to 0.15, as illustrated in **Figure II-8** (b). In capillary fingering, the saturation of the invading phase tends to be higher because both the defending and invading fluids are predominantly influenced by capillary forces. The average size of the pore throats invaded during capillary fingering is larger than those during viscous fingering, leading to higher saturation levels. Lenormand et al. reported that in this regime, the saturation of the invading phase at breakthrough is about 0.37, as displayed in **Figure II-8** (a) and (b), regardless of whether the viscosity ratio is higher or lower (logM = -4.7 and logM = 1.9). In stable displacement, due to the stable advancement of the invasion front, the saturation of the invading phase at breakthrough is highest. Lenormand et al. noted that when one variable (either higher M or Ca) is fixed while the other varies, the displacement mode tends to evolve towards stable displacement, characterized by a plateau. This is demonstrated in **Figure II-8** (a) and (c), where the saturation of the invading phase is approximately 0.95.

Furthermore, the boundaries and transition zones between the three flow regimes can be delineated through the effects of the M and the Ca on the saturation of the invading phase. As depicted in **Figure II-8** (a) and (b), the impact of the capillary number on the invading phase saturation under favorable (LogM > 0) and unfavorable (LogM < 0) viscosity conditions also allows for a quantitative analysis of the transition zones from capillary fingering to stable displacement and from capillary fingering to viscous fingering. Quantitatively, under favorable M conditions, transitioning from capillary fingering to stable displacement requires an increase in Ca by 3-4 orders of magnitude. Conversely, under unfavorable M conditions, transitioning to viscous fingering requires an increase in Ca by 2 orders of magnitude. **Figure II-8** (c) illustrates the process from viscous fingering to stable displacement at higher Ca levels. The saturation results are consistent with the previous discussion, and the transitioning from viscous fingering to stable displacement necessitates an increase in M by 3-4 orders of magnitude, corresponding to an approximate 70% increase in saturation. Other researchers have similarly obtained consistent conclusions in both 2D (Zhang, et al., 2011) and 3D (Senyou An, 2020) (Hu, et al., 2020)work.

The Advancement of logCa/logM Diagram

Senyou et al. (Senyou, et al., 2020) developed a 3D dynamic pore network model by altering capillary numbers and viscosity ratios, building upon the foundational results of Lenormand et al. They meticulously validated this model against micro-model experiments, both temporally and spatially, and found strong agreement between the spatial distribution of the two fluids and the temporal scales of the experiments and simulations. Furthermore, Zhang et al. (Zhang, et al., 2011) performed a series of displacement experiments in a homogeneous water-wet micromodel with log M ranging from -1.95 to 1.88 and log Ca in the range of -5.88 to 1.02, further extending the invasion pattern phase diagram in logCa/logM. In a further extension to 3D experiments, researchers (Hu, et al., 2020) used oil-wet glass beads as the packing bed medium, employing micro-CT based technic to capture 3D images under

different displacement modes. The shapes of the three flow regimes were similar to those observed in 2D periodic homogeneous pore models, though differences in boundaries were noted, manifesting as broader transition zones between any two regimes.

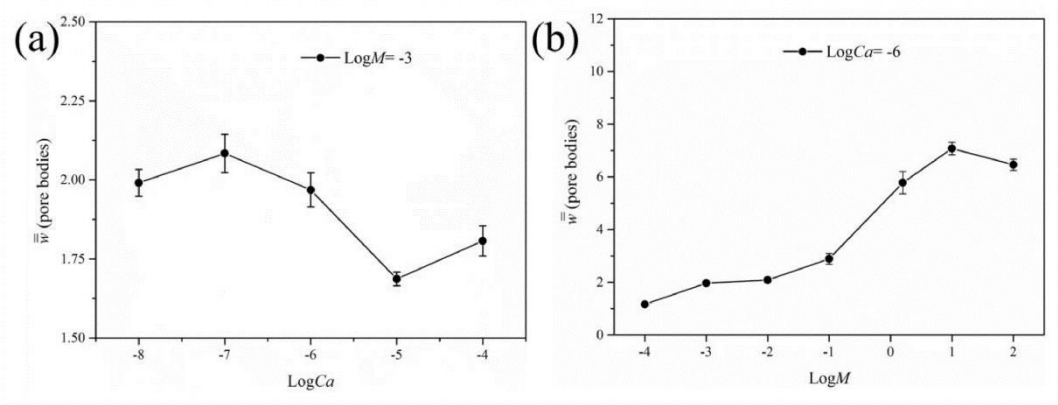

Figure II-9 *Effective finger width as a function of the (a) capillary number and the (b) viscosity ratio.*

Additionally, researchers (Chen, et al., 2023) have explored the normalized fluid-fluid interface length (l_{inv}) = interface length/width) as a function of the normalized invasion length (x_{inv}) = distance from the invasion front to the farthest boundary/length) to understand how the competition between capillary and viscous forces influences invasion morphology. In the viscous fingering regime, it has been found that l_{inv} increases linearly and slowly with x_{inv}, while in the capillary fingering regime, the change in l_{inv} with x_{inv} shows a step-like evolution due to the fluid invading forwards, horizontally, and even backwards, with forward and backward movements corresponding to plateau periods in l_{inv}. Furthermore, the distinction between capillary fingering and viscous fingering can also be made through finger width. Hu et al. (Hu, et al., 2020) proposed a statistical averaging method to estimate the width of fingers in fingering patterns, by equally dividing perpendicular to the direction of the fingers, measuring, and calculating the width of each unit, and then taking a weighted average to estimate the average diameter, resulting in an effective finger width as a function of Ca and M (**Figure II-9**). It was found that under unfavorable M (logM = -3), the finger width slightly decreases from 2 to 1.75 as Ca increases, corresponding to a transition from capillary to viscous fingering where the pathway changes from larger capillary fingers to finer viscous fingers. Conversely, at a fixed Ca (logCa = -6), the finger width significantly increases from 2 to 7 as M increases, because the flow regime transitions from viscous fingering to stable displacement, as described in **Figure II-8Figure II-8**(c), hence the substantial increase in finger width.

II.1.4.2 The Development of Microfluidic at Pore Scale

Historically, all early studies on two-phase flow have been based on core experiments. Cores are typically sampled directly from oilfield sites, providing a more accurate representation of the geological characteristics and fluid flow parameters within the rock formations, such as permeability, capillary pressure, and non-wetting phase saturation (Zhang, et al., 2007) (Humphry, et al., 2014) (Shojaei, et al.,

2015) (De, et al., 2018) (Rabinovich, et al., 2019) (Guo, et al., 2020) (Ma, et al., 2022). These parameters, traditionally defined based on macro-scale core experiments, are crucial for understanding fluid dynamics in porous media and comprehensively assessing how various variables influence fluid flow and displacement. However, a significant limitation of core experiments is that they are often "black box" experiments, meaning the internal flow behaviors and detailed interactions within the porous matrix cannot be directly observed. This limitation restricts the depth of understanding and intuitive verification and interpretation of the dynamic processes and complex interactions occurring at the pore scale. Although advancements in imaging technologies, such as X-ray micro-computed tomography (μ-CT) (Iglauer, et al., 2012) and focused ion beam scanning electron microscopy (Kizilyaprak, et al., 2014), have made capturing pore-scale flow behaviors and visualizing fluid flow possible, imaging a core is complex and scanning an entire sample can be time-consuming. Typically, imaging is only performed at a few specific stages during the drainage or imbibition process, preventing dynamic observation of the experimental phenomena as they occur.

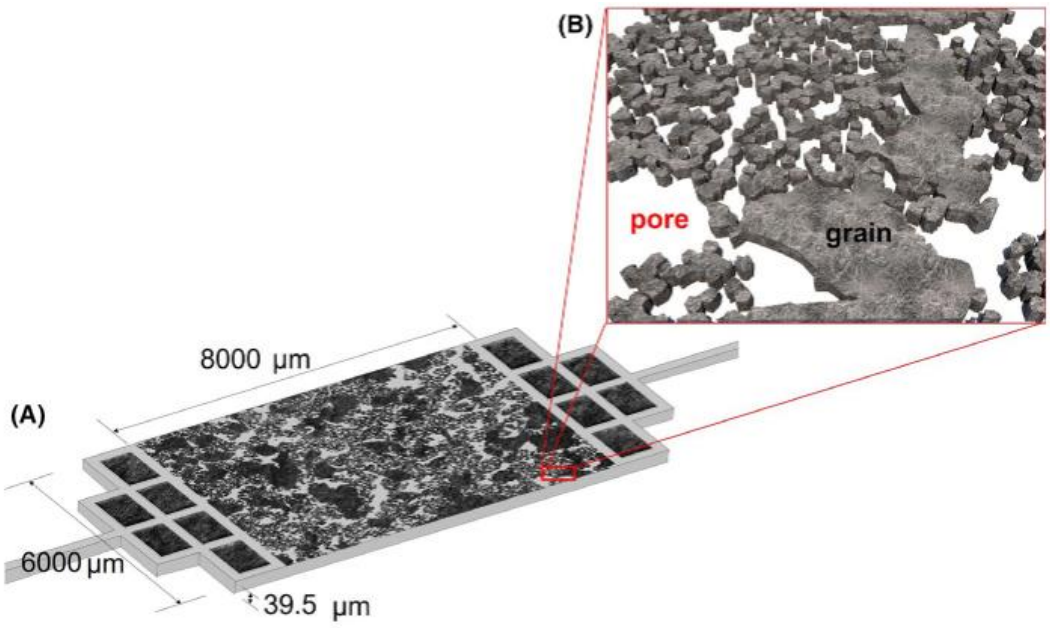

Figure II-10 *Schematic of Reservoir-on-a-Chip design. A, Overall image of the microchip; B, local image of grains and pores distribution (Lei, et al., 2020).*

In this context, elucidating the pore-scale physical processes during oil and gas extraction through characterization and experimental techniques is crucial for developing more effective EOR methods. Micromodels serve as a powerful tool for visualizing pore-scale flow dynamics and fluid-solid interactions within porous media. In recent years, there has been an increasing use of microfluidic models (Avraam & Payatakes, 1999) (Chang, et al., 2009) (Zhang, et al., 2011) (Saadat, et al., 2020) (Yun, et al., 2020) (Lei, et al., 2020), which can replicate and design complex geometric structures to simulate real rock structures, as shown in **Figure II-10**. These models are visualizable and reusable, further promoting their application in fluid displacement studies, as previously discussed.

Microfluidics is recognized as the study and application of fluid flows at microscale dimensions, integral to the fluid mechanics within fields such as colloid science (Russell & Strobel, 1989), clinical chemistry (Schulte, et al., 2002), soil science (Logsdon & Kahn, 2004), plant biology (Canny, 1977), and biomedical science (Ryan, 1980). Initially, microfluidic chip technology employed capillaries in their simplest form of one-dimensional flow to investigate interactions between fluids—such as miscibility and displacement—using capillaries of varying diameters. With advancements in microfluidic technology, sophisticated channel designs such as single pore-throat (Qi, 2018), dead-end pore (Xu et al., 2018), and T-junction structures (Xu et al., 2015) have been developed. These are used to study multiphase microfluidic flows through segmented and stratified flow architectures, facilitating research into flow formation, size adjustment, coalescence, mixing, and splitting processes (Shui, et al., 2007) (Gu, et al., 2011). This technology has found extensive applications in chemical reactions and biotechnology. The simplicity and ease of design of these models aid in qualitative research and visualization of fluid-fluid and fluid-solid interactions. Examples include corner flow, viscoelastic mobilization of residual oil, and the formation and merging of droplets or two-phase displacement mechanisms. However, these idealized micro-models are limited by their inability to replicate specific structures analogous to reservoir geological formations, thus restricting their applicability in replicating real-world geological scenarios.

The field of microfluidics is underpinned by foundational research in two-dimensional studies established on Hele-Shaw flow, initially used to investigate the behavior of fluid flow between two parallel plates. By adjusting the spacing between the plates and the viscosity of the liquid, this setup can produce various flow patterns with differing levels of confinement. In their seminal work, Saffman and Taylor (Saffman & Taylor, 1958) used a Hele-Shaw cell to explore factors influencing the instability of immiscible two-phase flow. They identified and formulated the trends and dynamic equations governing the instability of the interface between the two immiscible phases, highlighting that interface instability is primarily influenced by the viscosities of the fluids and interfacial tension. Although Hele-Shaw flow was pivotal in preliminary studies, its practical applications are limited by spatial constraints and precision control. Subsequently, the introduction of glass beads representing rock particles and matrices in narrow spaces provided a means to offer porosity in a two-dimensional structure. Allowing fluids to flow through these interspersed glass beads helps to understand the impact of system porosity and permeability. This simplistic two-dimensional structure can exhibit some fluid behaviors in complex flows more conspicuously.

With advancements in etching technology, it became possible to design homogeneously structured and larger pore-sized constructs via CAD files. These are then realized in micromodels through wet or dry etching methods, allowing for more in-depth exploration of fluid behavior and mobilization mechanisms (Bartels et al., 2017) (Perazzo et al., 2018) (Keshmiri et al., 2018). However, these models only represent a porous system and do not replicate actual reservoir rocks. The progression of lithography and imaging

technologies has enabled the capture of pore-scale fluid behaviors and the visualization of fluid dynamics. Imaging techniques such as computer tomography, focused ion beam scanning electron microscopy, or nuclear magnetic resonance are instrumental in obtaining structural images of actual porous rocks. These images can then be transformed into microfluidic chips using lithography or 3D printing technologies on transparent substrates like PMMA, PDMS, glass, or silicon-based materials (Waheed, et al., 2016) (Alzahid, et al., 2018) (Yu, et al., 2019) (Lei, et al., 2020) (Jahanbakhsh, et al., 2020) (Browne, et al., 2020). Furthermore, these techniques have been used to produce microfluidic designs that incorporate complex and smaller-sized pore structures, enhancing the simulation and study of fluid flows analogous to those in geological formations (Meybodi, et al., 2011).

Homogeneous and heterogeneous 2D micromodels based on rock layer structures have made significant contributions to understanding macroscopic fluid flow behaviors and microscopic mobilization mechanisms. However, these efforts have only increased the complexity of the horizontal pore geometry. A common drawback of these two-dimensional micromodels is their uniform etching depth, which may underestimate capillary effects present in real porous media and fail to capture certain flow dynamics induced by capillary forces in these two-dimensional models. For instance, capillary snap-off, an important mechanism for oil and bubble breakup in multiphase flow (Roof, 1970), occurs only if the throats are smaller than the pore bodies in dimensions perpendicular to the flow direction—the pressure at the “neck” must be greater than that at the droplet front (Conn, et al., 2014). This limitation is well-recognized, and studying snap-off in 2D porous media is inherently problematic due to these dimensional constraints.

To better simulate three-dimensional porous connectivity, preliminary attempts have been made with 2.5D or three-dimensional micromodels. Researchers (Bowden et al. 2010), (Sen et al. 2012), (Krummel et al. 2013) have created micromodels in the form of packed beds to mimic the complex natural porous media. However, these models, constrained by randomly or orderly stacked particle systems, fail to realistically replicate the actual pore connectivity. Moreover, several three-dimensional micromodels have been developed. Park et al. (Park et al. 2012) fabricated a three-dimensional PMMA micromodel using hot embossing techniques. However, these methods introduce complexities in manufacturing and operation, and ensuring fidelity of dimensions in three-dimensional micromodels, as well as matching the refractive indices of fluids in porous media, remains a significant challenge.

Recently, cost-effective, simpler-to-manufacture and operate 2.5D micromodels have emerged (Yu, et al., 2019). These models integrate more geometric complexity into 2D devices through controlled etching processes, designing interconnected microchannels with varying depths of pore bodies and throats. These 2.5D micromodels have successfully differentiated capillary characteristics between pore bodies and throats and have been widely applied in studies of multiphase flow in porous media (Tagavifar et al., 2017) (Yu, et al., 2019). Moreover, more realistic 2.5D micromodels that better

resemble actual rock core pore structures have been designed, comparing capillary effects in waterflooding experiments between two-dimensional and 2.5-dimensional micromodels (Yu, et al., 2019).

Although 2.5D and 3D microfluidic chips can better represent realistic pore structures and reproduce specific flow phenomena to some extent, they still do not necessarily offer significant advantages in direct observation monitoring due to the effects of light refraction. For immiscible diphasic flow phenomena, 2D micro-models suffice in depicting interface phenomena and displacement mechanisms. Therefore, in this study, we opted for more easily accessible 2D microfluidic chips for diphasic flow displacement experiments.

II.1.4.3 Correction of Key Parameters in 2D Microfluidic Models

It is important to note that many parameters were originally defined for 3-D porous media, and many experimental studies have applied these definitions to 2-D pore network micromodels, which can undoubtedly impact and misjudge the actual results. Experimental observations and theoretical analyses indicate that fluid flow in 2D pore networks significantly differs from that in 3D porous rocks. At the microscale, fluid transport in porous media depends on the geometry and topology of the network of pore throats and bodies. However, in shallow-depth etched uniform micromodels, permeability is primarily governed by channel depth, not by the geometric factors that control trapping pore networks, such as pore-throat width and pore-body diameter, while the capillary pressure is controlled by the widths of pore throats and pores, perpendicular to the etching. In addition, multiphase simultaneous flow under capillary-dominated conditions is a characteristic of three-dimensional pore networks, but not typically of two-dimensional pore networks. In water-wet micromodels, where water displaces oil, the onset of oil retention marks the start of water flowing as the continuous phase, a condition where k_{rw}~0 because the two phases cannot independently permeate the interconnected network involved in the displacement. Therefore, the k_{rw} factors in micromodels are significantly different from those in rocks, and the distribution of residual non-wetting phase is also expected to vary greatly.

In practical applications, different flow behaviours in two-phase flow directly impact changes in residual saturation, which constrains the relative permeability and capillary pressure curves at the continuum scale. We now consider that we want to displace the non-wetting phase by injecting the wetting phase, so it is typically the case for oil recovery. The most significant parameter to affect or determine *nw*-phase saturation (S_{nw}) is the *Ca*, the variation of S_{nw} with *Ca*, known as the capillary desaturation curve (CDC), is a classic empirical relationship used in reservoir engineering. The CDC demonstrates a consistent S_{nw}-*Ca* relationship, which is affected by porous media structure and fluid properties, as depicted in **Figure II-11**.

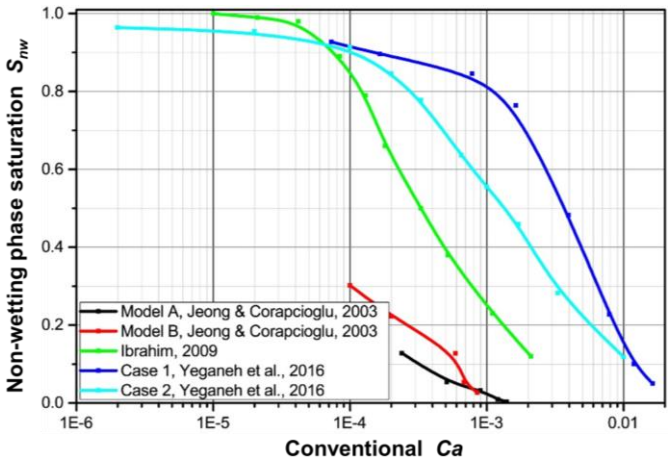

Figure II-11 *Capillary-desaturation curves using the conventional capillary number definitions (Tang, et al., 2019). All the data shown here are adapted from data in publications.*

Obviously, the data presented in **Figure II-11** demonstrates a typical CDC trend, where the non-wetting phase saturation rapidly declines as the Ca exceeds a critical threshold. In this context, Ibrahim (Ibrahim, 2009) investigated the fraction of residual oil (kerosene) remaining in place after mobilization at different Ca by increasing the flow rate at the end of waterflooding in a water-wet 2D microfluidic model with square lattice topology, and they found a substantial mobilization of residual oil beyond a critical Ca. Jeong and Corapcioglu (Jeong & Corapcioglu, 2003) employed two microfluidic models; one with uniform pore channels (Model A) and another with random grains and varying pore size distribution (Model B); to study the impact of pore structure on the displacement of residual trichloroethylene (non-wetting phase) after waterflooding. Yeganeh et al. (Yeganeh, et al., 2016) conducted experiments in water-wet microfluidic models (homogeneously formed squares and circular) with different saturations of hexadecane (Case 1) and crude oil (Case 2). After waterflooding, the Case 1 and Case 2 were flushed with surfactant solution and brine, respectively, at various Ca, resulting in variation of S_{or}.

However, it is easy to note that the CDC exhibits substantial scatter data for different works in **Figure II-11**. This discrepancy arises from variations in Ca calculation based on the 3D definition, which is influenced by the differences in experimental model systems, primarily impacted by pore structure and distributions affecting capillary forces. Consequently, Tang et al. proposed a novel definition for *Ca* in micromodels, considering the influence of pore microstructures and contact angle θ,

$$Ca = \left(\frac{k k_{rw} \left| \overline{\nabla} p \right|}{\sigma \cos\theta} \right) \frac{G}{k_{rw}} = \left(\frac{\eta v}{\sigma \cos\theta} \right) \frac{G}{k_{rw}} \qquad \text{Equation 2-24}$$

The term within the right parenthesis represents the conventional definition of Ca, considering the contact angle θ; where k and k_{rw} are the absolute permeability and relative permeability of the w-phase, respectively; and $\overline{\nabla}$p is the pressure gradient in the direction of flow. The term G represents the

geometric factor estimated through microscopic model image analysis, etch depth, and permeability values, which can writing,

$$G=\left(\frac{12}{2}\right)\left(\frac{W_t}{d_Z}\right)^2\left(\frac{L_p}{W_t}\right)\frac{1}{\left(1-\frac{W_t}{W_b}\right)(\phi\varsigma)} \qquad \text{Equation 2-25}$$

where, the d_Z is the channel depth of the micromodel; L_p is the length of one pore; W_t is the characteristic pore-throat width; W_b is the characteristic pore-body diameter; ϕ is the porosity; ζ is an adjustable factor to relate permeability and pore geometry. These parameters are schematically represented in the pore space, as illustrated in **Figure II-12**.

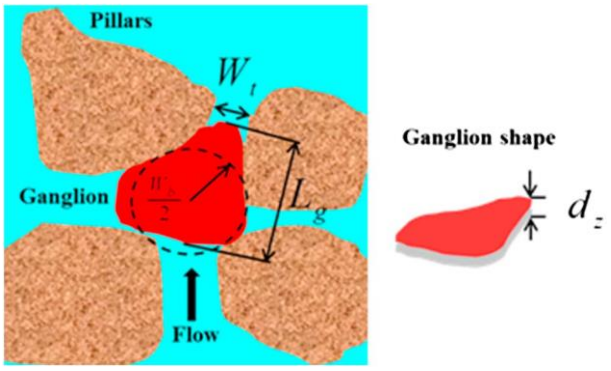

Figure II-12 *Representation of a nonwetting ganglion trapped by capillarity in a micromodel (Tang, et al., 2019).*

Specifically, the ζ is obtained knowing k, ϕ and d_Z, through the relationship,

$$k=\left(\frac{d_z^2}{12}\right)(\phi\varsigma) \qquad \text{Equation 2-26}$$

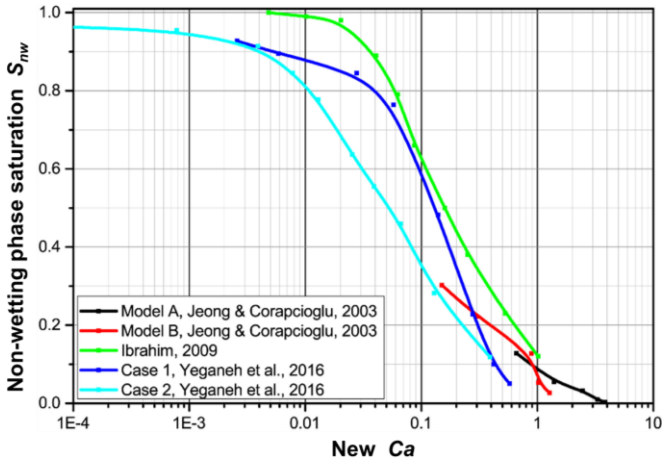

Figure II-13 *Capillary-desaturation curves using the new capillary number, using data in* ***Error! Reference source not found.***

Based on the Equation 2-24, Tang et al. performed new calculations on the data presented in **Figure II-11**. The improved fitting of the new *Ca* definition with the micromodel data suggest its validity by

yielding a consistent trend in the CDC, as shown in **Figure II-13**. This consistency makes the capillary number an important indicator for the mobilization or trapping efficiency of the nonwetting phase.

This relay on the impact of actual porous medium on capillary pressure P_c. In rock formations, a pore body can connect to one or multiple throats, but due to the complex geometry of these throats, there exists a variance in capillary pressure P_c at different-sized throats, which is related to the effective diameter of the throat (or the mean diameter of the throat), $\overline{D}_{throat}$, and the radius of curvature (R_d) for the oil/water interface in normal direction based on the Young-Laplace equation, writing,

$$P_c = \sigma(\frac{2}{\overline{D}_{throat}} + \frac{1}{R_d}) = 2\sigma(\frac{1}{\overline{D}_{throat}} + \frac{\cos\theta}{d_z}) \qquad \text{Equation 2-27}$$

whrer d_z is the depth of the model. Here, we assume that the radius of curvature of the fluid–fluid interface in the depth direction is constant and approximately equal to $d_z/2\cos\theta$ over the entire range of Ca values, resulting in a fixed contribution to the overall capillary pressure. Two extreme cases can be distingushed:

1. For $d_z >> \overline{D}_{throat}$, which means the mean diameter of the throats is much smaller than the etching depth of the chip, $P_c \approx \frac{2\sigma}{\overline{D}_{throat}}$, and the influence of chip depth on fluid flow can be neglected.

2. For $d_z << \overline{D}_{throat}$, which means the mean diameter of the throats is much larger than the etching depth of the chip, $P_c \approx \frac{2\sigma}{R_d}$, and the influence of chip depth on fluid flow dominates.

When $\overline{D}_{throat}$ and d_z are comparable, both dimensions must be considered in the analysis of capillary forces within the porous medium. In 3D structures such as rocks or fractures where the vertical depth is often substantial, both horizontal and vertical capillary forces can significantly influence fluid behaviour. In usual microfluidic chips, however, the uniformity of etched depth means that d_z and $\overline{D}_{throat}$ must be carefully considered and becomes crucial in the design of chips to accurately model fluid flow in porous media (Chen, et al., 2023). For instance, in the microfluidic chip used by Yiotis et al. (Yiotis, et al., 2021), the uniform etching depth was set to 115 μm, resulting in a significant curvature in depth. The etching depth being three times the minimum throat width implying that $\overline{D}_{throat}$ is also small, necessitating the consideration of both vertical and horizontal capillary forces. Similarly, Alzahid et al. (Alzahid, et al., 2018) also considered vertical capillary pressures in their studies, despite not providing a detailed distribution of throat sizes. The occurrence of throat widths smaller than an etching depth of 100 μm in their research indicates that both throat width and depth must be considered when calculating the equivalent pore radius. As reported by Chang, et al. (Chang, et al., 2009) and Li, et al. (Li, et al., 2022) in uniformly deep etched microfluidic chips with significant etching depths, it is generally necessary to consider the equivalent capillary forces acting in both horizontal and vertical directions. However, in chips with uniformly shallow etching depths, the interface can be approximated as planar,

leading to a curvature that is near zero, thus making d_z very large, and $1/d_z$ approaches zero. This implies that the contribution of capillary pressure in vertical direction is very low and can often be neglected (Zhang, et al., 2011) (Yu, et al., 2019). Consequently, P_c can then be simplified to the first case, where $P_c = \frac{2\sigma}{\bar{D}_{throat}}$, indicating that capillary forces are primarily influenced by the size of the pore throats. In regions with larger pore throats, there is lower capillary resistance, facilitating the initial breakthrough of the invading phase at the largest throats connected to the pores.

II.1.4.4 Microfluidic Experimental Research at Pore Scale

Fluid Dynamics in Water-Wet and Oil-Wet Porous Media

In water-wet porous medium, the oil phase primarily occupies the pore bodies, leaving the crevices at the solid surface interfaces (i.e., smaller pores and throats) unoccupied as the entry capillary pressure is not sufficient to force non-wetting oil into these spaces (Anderson, 1987). Hence, based on the geometry of pores and throats along with surface roughness, some parts of the pore space are filled with oil while others contain water. For example, the **Figure II-14** shows that in this water-wet chip water does occupies the smaller pores and forms a water film surrounding the solid surface. During water injection, water, being the preferential wetting phase, occupies the smaller pores not invaded by oil, forming thin films across all rock surfaces. Later, as the water phase progresses along the pore walls, displacement of the oil phase occurs ahead, displacing it into relatively larger pores (**Figure II-15**) (Craig, 1971). Leading to water breakthrough to occurs later, with more oil production compared to oil-wet reservoirs.

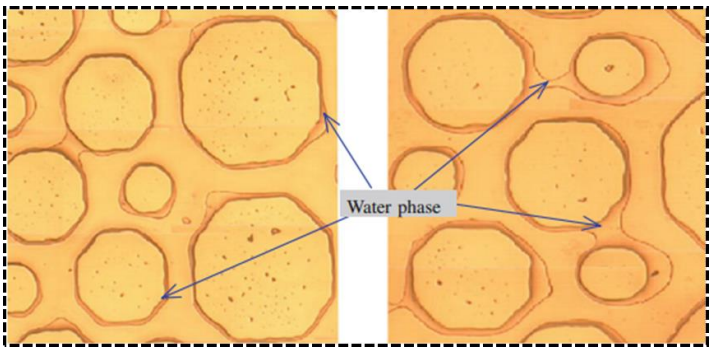

Figure II-14 *The distribution of the water and oil phases in a water-wet micromodel saturated with oil (Afrapoli, et al., 2012).*

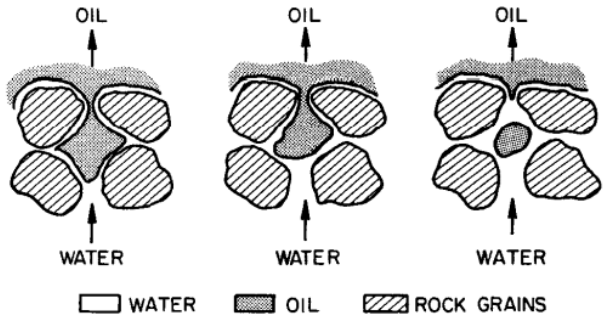

Figure II-15 *A schematic representation of water displacing oil from water-wet rock pores during the water injection process (Craig, 1971).*

As displacement moves from smaller to larger pores, water increasingly occupies the previously oil-filled spaces. At a certain location, the necks connecting oil in adjacent pores become unstable and break, resulting in oil entrapment, forming spherical oil ganglia trapped at the center of pores. The primary reason for oil entrapment is the insufficient driving pressure to overcome the capillary entry pressure of the current water-saturated pore throats. Once water displaces and captures oil, nearly all remaining oil becomes immobile (Agbalaka, et al., 2008). The disconnected residual oil exists in the form of small oil droplets (both with bended oil droplet and isolated oil droplets) at the center of pores and larger oil ganglia surrounded by water dispersed across multiple pores with big ganglion of ring shape, as shown in **Figure II-16** (Afrapoli, et al., 2012).

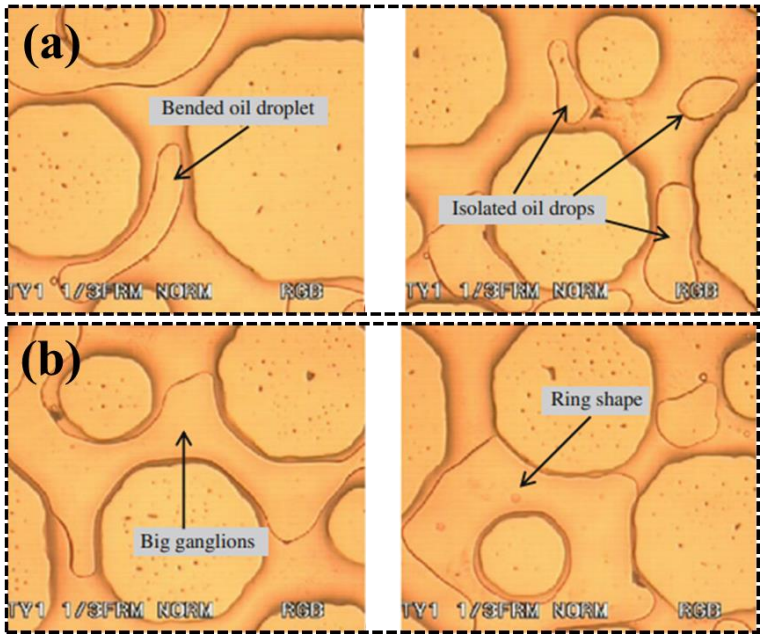

Figure II-16 *Different types of residual oil saturation after waterflooding in the water-wet micromodel (Afrapoli, et al., 2012). (a) illustrates oil droplets within the pores at the end of waterflooding, either as isolated oil droplets or in the form of bended oil droplets, lingering at the center of the pores; (b) emphasize the manifestation of residual oil in the form of ganglions connected with multiple pores, or ring shape enveloping grains.*

In oil-wet porous media, the positioning of the two fluids is opposite to that in water-wet conditions. Oil tends to adhere to surfaces, while the water phase randomly distributes within the pore centers. During water injection, water rapidly fills pathways with the highest permeability, leading to quicker breakthrough, reducing sweep efficiency. However, after breakthrough, it observe a continuous oil production to a high water cut. In other words, at the microscale and, upon water injection initiation, water saturates the centers of larger pores (with lower capillary forces), forming continuous channels or fingers that drive the oil forward, as it might be observed in **Figure II-17**. Pores with higher capillary forces hinder the advancement of the injected water interface into oil-filled pores, resulting in significant

oil retention in the form of continuous oil films on pore surfaces and entrapment within throats. Furthermore, due to the reduced sweep region, there exist substantial oil layers trapped and shielded by water in the porous media. **Figure II-18** shows the residual oil saturation (S_{or}) after waterflooding in an oil-wet micromodel (Afrapoli, et al., 2012). These combined effects lead to a decrease in the oil recovery factor (Anderson, 1987) (Agbalaka, et al., 2008) (Amiri & Hamouda, 2014) (Maaref, et al., 2017).

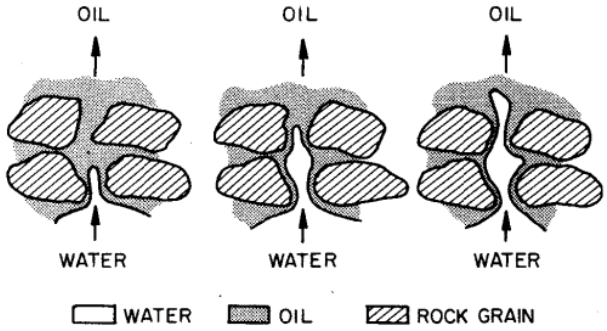

Figure II-17 *A schematic representation of water displacing oil from oil-wet rock pores during the water injection process (Craig, 1971).*

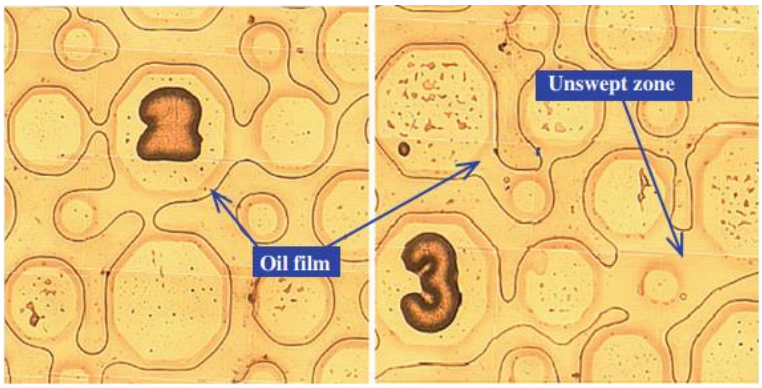

Figure II-18 *Different types of residual oil saturation after water flooding in the oil-wet micromodel (Afrapoli, et al., 2012). The number of "2" and "3" are specifically designed to mark and distinguish the locations of grains.*

To sum up, in the water-wet core, water is occupies small spaces not invaded by oil while oil is located relatively larger pores. Consequently, at irreducible water saturation (S_{wi}), oil exhibits relatively high effective permeability, closer to absolute permeability, as water doesn't significantly impede its flow (Anderson, 1987). Under natural or induced water injection, both phases are in motion. The relative permeability of oil k_{ro} decreases with decreasing oil saturation, while the k_{rw} starts increases with increasing water saturation. As water progressively displaces the previously oil-filled pores, some oil-containing pores or clusters might become isolated from the rest of the oil due to the inability to overcome capillary entry pressure, resulting in entrapment until reaching S_{or}. At this stage, the effective permeability of water becomes notably low since residual oil is trapped as globules within larger pores. Consequently, the k_{rw} at S_{or} is substantially lower than the k_{ro} at the initial S_{wi}.

In an oil-wet core, the positions of the two fluids are reversed. At low water saturations, k_{ro} is less than that of a water-wet core, as oil competes with residual water for flow within the larger pores. Initially, during water flooding, k_{ro} is relatively high and gradually diminishes, while k_{rw} starts low and gradually increases. With increasing water saturation, water rapidly traverses through the most permeable pathways, leading to a rapid decline in k_{ro}. However, water cannot trap the oil as the oil-wet surfaces provide paths for the oil to escape from the pores that are nearly filled with water. Upon reaching S_{or}, k_{rw} becomes significantly high since the residual oil resides in smaller pores, forming a thin film on surfaces with minimal impact on water flow. Consequently, the ratio of the two permeabilities can approach 1 or even greater. This disparity in saturations and behaviours of the two fluids results in contrasting relative permeability values between oil-wet and water-wet cores.

Percolation Theory

Percolation theory studies the movement and behavior of fluids through a porous network where pores are randomly filled with one or more fluids. The theory investigates how the structure and connectivity of the pore network affect the probability that a fluid will percolate, or flow through the network from one side to the other. In percolation theory, a cluster is defined as a group of connected sites or bonds that are occupied or filled with a particular phase (e.g., liquid or gas). As the occupation probability increases, these clusters grow in size, and their distribution follows a power law, especially near the critical percolation threshold. The power law behavior is expressed as:

$$N(s) \propto s^{-\tau} \qquad \text{Equation 2-28}$$

where $N(s)$ is the number of clusters of size s, and τ is a critical exponent that depends on the dimensionality of the system and other factors.

The power law relationship reflects the system's criticality at the percolation threshold, where clusters of all sizes exist, from very small to spanning clusters, as displayed in **Figure II-19**. It can be found τ governs the inverse relationship between the cluster size and the number of such clusters, indicating that as the size of the clusters increases, the frequency of such clusters decreases according to a power law distribution.

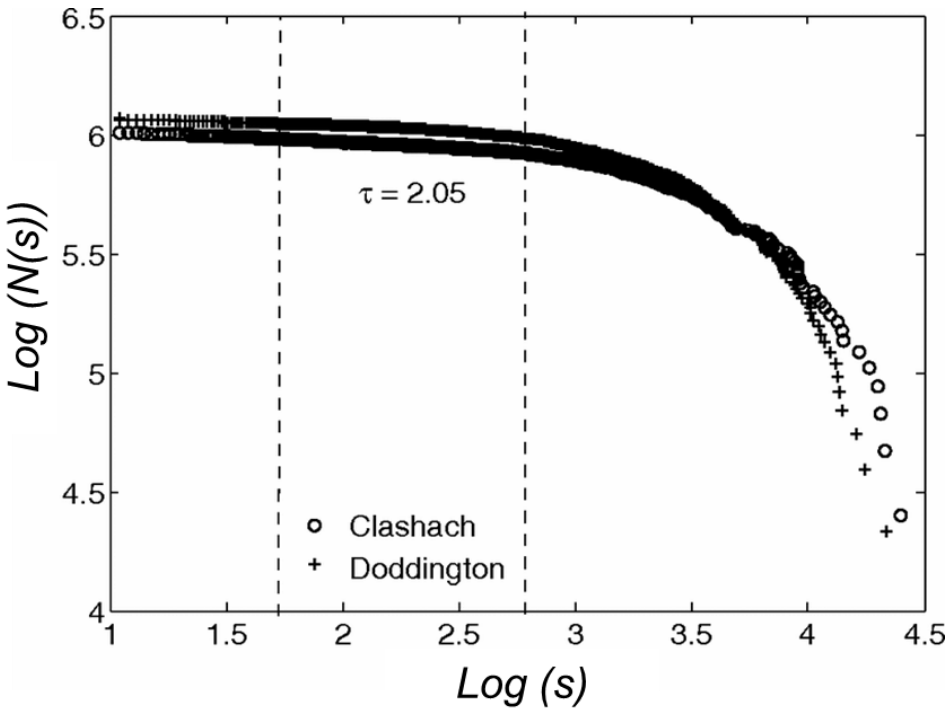

Figure II-19 *The cumulant cluster size distribution versus logarithmic cluster size (Iglauer, et al., 2010)*

The scaling exponent τ, which ranges between 1.8 and 2.3 (Iglauer & Wülling, 2016), holds significant physical implications: a smaller τ implies overall larger residual droplets, which are easier to mobilize (Herring, et al., 2013), leading to higher oil recoveries in contexts such as hydrocarbon production or solvent recovery from contaminated soil, especially when chemically enhanced recovery methods are employed (Iglauer, et al., 2010). In diphasic flow core experiments, studies have shown that the power-law cluster size distribution exponent τ measured in oil-wet systems (τ = 2.12) is higher than that in water-wet systems (τ = 2.05), indicating the presence of more small clusters in oil-wet conditions (Iglauer, et al., 2012). Moreover, it has been reported that (Datta, et al., 2014)the length L of ganglia along the flow direction and the cumulative distribution function (CDF) of ganglia lengths decay according to the power-law cluster size distribution exponent, as predicted by percolation theory. The consistency of the size distribution of residual oil clusters with a scaling law commonly observed in percolation processes suggests that the behavior of the fluid system within the porous medium can be modeled and understood within the framework of percolation theory. However, in studies where mathematical methods have been used to describe the distribution exponent τ of grain size distribution (Iglauer & Wülling, 2016), rigorous statistical analysis of the dataset revealed τ to be much smaller, approximately 1.1. This value is significantly lower than previous estimates, suggesting that traditional percolation models may not accurately predict fluid flow behavior in subterranean environments.

The Research in EOR

When discussing EOR at the pore scale, determining the fluid properties is paramount because non-Newtonian fluids, which exhibit viscosity changes under high flow rates due to shear forces within the

pores, require careful evaluation. Thus, it is crucial to test the performance of the injection fluids, which can generally be categorized into shear-thinning, shear-thickening, and shear-independent fluids, each potentially possessing or lacking a yield stress (**Figure II-20**). (Vasudevan, et al., 2008) (Sochi, 2010) (Santvoort & Golombok, 2016). Shear thickening occurs when polymer molecules are stretched and recoiled by the flow through a series of pores and throats, only when the flow rate is too high, and the polymer molecules do not have sufficient relaxation time to stretch and recoil to adapt to the flow velocity, causing an excessively high apparent viscosity due to the elasticity of the polymer chains. This behaviour helps drive the rapid displacement of fluids that are difficult to displace or recover more effectively in small-scale heterogeneities. Additionally, a high apparent viscosity is also beneficial for improving macroscopic sweep efficiency (Seright, et al., 2011).

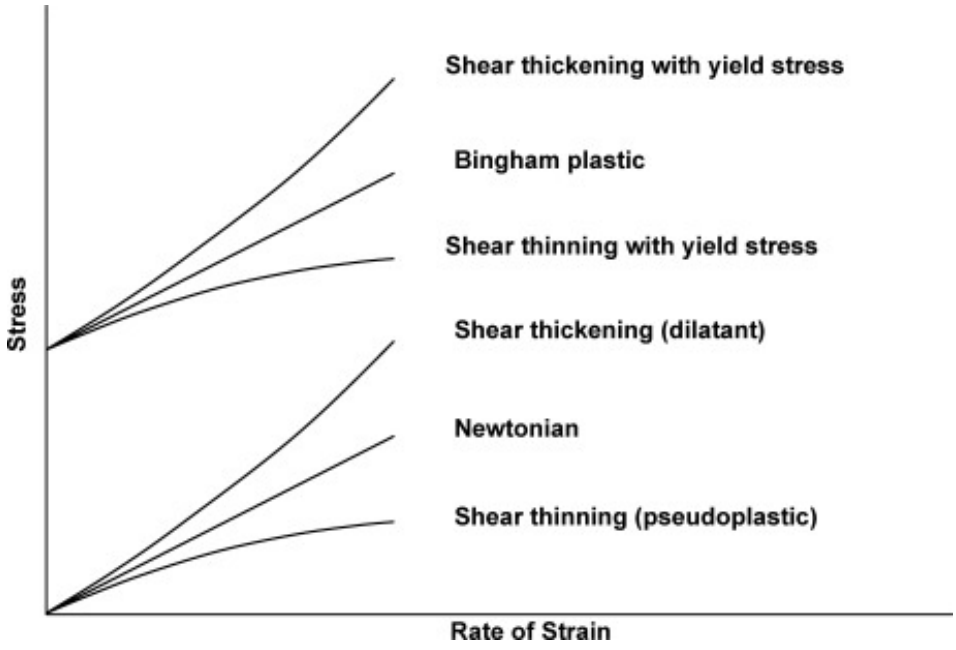

Figure II-20 *The six main classes of the time-independent fluids presented in a generic graph of stress against strain rate in shear flow.*

The development of microfluidic have led to clearer explanations and interpretations of fluid displacement phenomena and interfacial interactions within pore spaces under drainage and imbibition mechanisms. For instance, in oil-water systems, detailing the wetting and non-wetting phase filling processes during saturation increase in drainage and imbibition has explained various interfacial phenomena and displacement mechanisms, such as oil snap-off (Alzahid, et al., 2018), the Rehon and Rison effects (Yu, et al., 2019), Hele-Shaw instability, and cooperative pore filling mechanisms (Sahar, et al., 2021). Microfluidic chips have also been instrumental in studying mechanisms affecting displacement efficiency, including pore structure, wettability, interfacial tension, viscosity of displacing phases, and the viscoelasticity of polymers.

Moreover, for polymer flooding of Newtonian fluid, glycerin is commonly used, which, compared to post-waterflooding results, exhibits a more dispersed saturation distribution and smaller residual ganglia in microfluidic models. The increase in the viscosity of the injection solution leads to reduced oil bypassing at pore scale (Mejia, et al., 2020). Moreover, non-Newtonian fluids, such as shear-thinning polymer solutions, are also widely reported for oil recovery experiments in microfluidic model (Meybodi, et al., 2011) (De Castro, et al., 2016). Meybodi et al. (Meybodi, et al., 2011) investigated the effects of wettability, pore structure, and coordination number on oil recovery efficiency using shear-thinning polymer solutions in microfluidic models. The findings highlighted that the flow patterns and stability at the polymer solution front, as well as the ultimate oil recovery rates, are significantly influenced by the pore morphology, coordination number, pore shapes, and the positions of pore throats on the pore bodies. On the other hand, De Castro et al. (De Castro, et al., 2016) conducted two-phase immiscible displacement experiments in microfluidic models using shear-thinning polymer solutions to explore the impact of polymer concentration on the relationship between the Ca and M, recovery rates, and particle size distribution. Their results indicated that variations in the size and distribution of trapped phases are directly related to the polymer concentration, which affects the values of Ca and M.

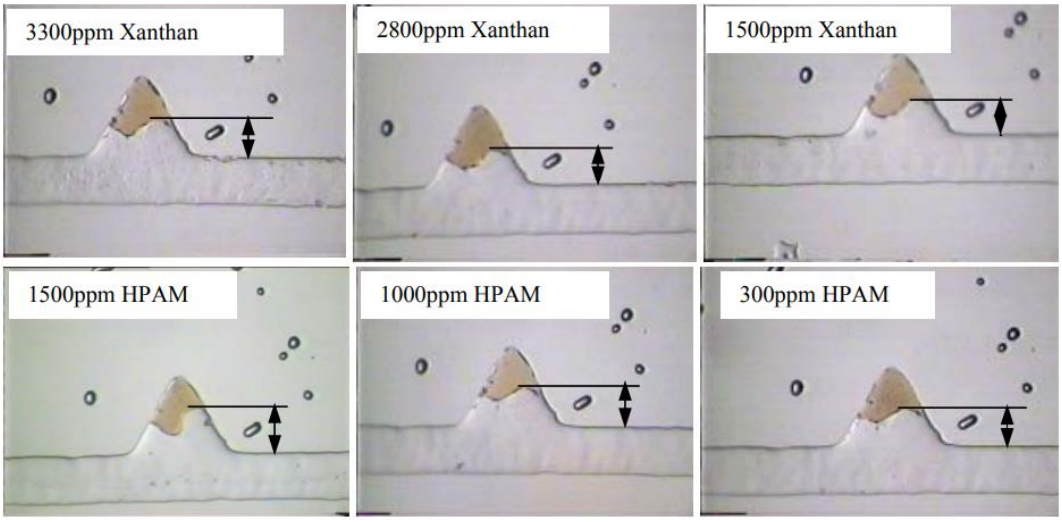

Figure II-21 *Comparison the displacement effect of HPAM and xanthan (Liu, et al., 2002).*

In most enhancement studies, shear-thinning liquids containing the biopolymer xanthan gum are utilized. Besides the viscosity effects, the elasticity of the polymers is also considered to play a significant role in oil recovery experiments. To elucidate potential differences in the oil recovery mechanisms between Newtonian and viscoelastic fluids, Wang et al. extensively studied the effectiveness of viscoelastic polymer solutions in displacing “dead-end” residual oil, residual oil films on rock surfaces, oil retained in pore throats by capillary forces, and the efficiency of unrecovered residual oil after waterflooding under various conditions (Wang, et al., 2000). In all cases, they observed a reduction in residual oil after polymer flooding. In a study by Liu et al., the experiments on dead-end pore oil displacement were replicated, revealing that HPAM, compared to xanthan gum, exhibited higher viscoelasticity and greater

mobilization capacity for residual oil (Liu, et al., 2002), which was directly proportional to its concentration (in **Figure II-21**).

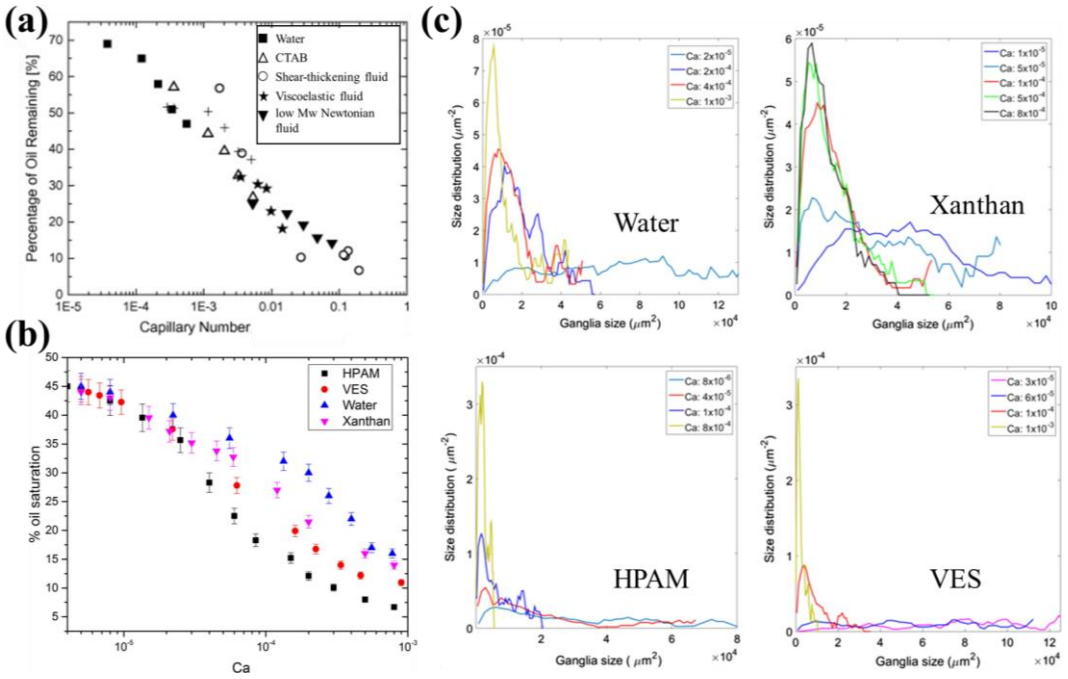

Figure II-22 *Percentage remaining oil saturation as a function of capillary number for different displacing fluids with different work (a) (Nilsson, et al., 2013) and (b) (De, et al., 2018); (c) Steady state residual oil size distribution after displacement by different fluids (De, et al., 2018).*

Moreover, Nilsson et al. compared the flow behaviour of viscoelastic fluids and shear-thickening fluids in porous media (Nilsson, et al., 2013), finding the viscoelastic fluids appeared to extract oil more effectively from dead-end pores and unrecovered volumes, showing higher oil recovery rates at similar *Ca*. Interestingly, all data appear to align closely with the main curve of *Ca* versus residual oil percentage, possibly due to experimental constraints. Furthermore, De et al. refined the analysis by examining various fluid types and Ca magnitude (De, et al., 2018), revealing that, under similar M_r conditions, displacement enhancement of HPAM was associated with its stronger viscoelastic effect compared to xanthan gum. The petroleum displacement capability of lower molecular weight viscoelastic surfactants was close to HPAM, further confirming the significant role of viscoelastic effects in enhancing petroleum recovery. This phenomenon's mechanism likely involves the reduction of pore size due to viscoelastic effects, a viewpoint validated by residual pore images in **Figure II-22** and pore size distribution histograms.

The development of microfluidic have led to clearer explanations and interpretations of fluid displacement phenomena and interfacial interactions within pore spaces under drainage and imbibition mechanisms. For instance, in oil-water systems, detailing the wetting and non-wetting phase filling processes during saturation increase in drainage and imbibition has explained various interfacial phenomena and displacement mechanisms, such as oil snap-off (Alzahid, et al., 2018), the Rehon and

Rison effects (Yu, et al., 2019), Hele-Shaw instability, and cooperative pore filling mechanisms (Sahar, et al., 2021). Microfluidic chips have also been instrumental in studying mechanisms affecting displacement efficiency, including pore structure, wettability, interfacial tension, viscosity of displacing phases, and the viscoelasticity of polymers.

In summary, microfluidic chips not only characterize parameters and outcomes similar to core flooding experiments but importantly allow observations and analyses of flow phenomena at the pore scale during displacement. This ability significantly aids in deepening our understanding of fluid flow in porous media. Despite considerable progress in studying fluid displacement within microfluidic chips, the influence of polymer flooding in CEOR on displacement efficiency remains unclear. In the experimental section of this study, we consider the overall oil recovery process and specifically investigated the impact of injected fluid viscosity on the mobilization capability of trapped oil after waterflooding period. We statistically analyzed the size and position of residual oil, probing its flow dynamics and mechanisms. Concurrently, we captured and elucidated fluid flow behaviour at the pore scale during drainage and water imbibition.

II.2 Numerical Simulations for the Multiphase Flow in Porous Media

The immiscible two-phase flow within rocks is governed by the interplay between capillary, gravitational, and viscous forces (Detwiler, et al., 2009). These interactions, in turn, are influenced by wetting conditions and changes in pore size related to the roughness of the rock (Auradou, 2009) (Yang, et al., 2016). In large-scale dimensions, such as fractures and reservoirs, fluid flow within pores is predominantly influenced by gravity and viscosity. Conversely, at smaller pore scales, the impact of gravity on fluid dynamics is minimal, and the behaviour is primarily governed by capillary forces and viscous effects. The physical and chemical properties of both displacing and displaced fluids like viscosity, interfacial tension, and contact line effects become crucial factors in studying fluid dynamics under these conditions.

The diphasic flow within porous media can induce unstable flow due to the competition between the capillary and viscous forces, resulting in fingering as we discussed in section II.1.3. While core and transparent replicas are used in flooding experiments to study displacement mechanisms, certain experiments may be challenging or unattainable due to complexity and high costs. Consequently, numerical methods have been introduced to simulate flow displacement patterns and mechanisms during immiscible displacement processes within porous media. In this section, we will delve into some fundamental concepts of numerical modeling, the mathematical model, and simulation methods in detail.

II.2.1 General Information

II.2.1.1 The Different Scales of a Porous Medium

Multiphase flow in porous media can be described at different scales, this allows researchers to choose the appropriate level of description based on the specific research objectives and computational resources available.

1. Pore Scale (Microscale): This is the smallest scale for describing fluid flow in porous media, typically ranging from micrometers to millimetres. At this scale, the characteristic sizes are the particle diameter for unconsolidated media and the average pore diameter for consolidated media. This scale explicitly considers the complex geometric shapes of the solid skeleton and the multiphase nature of flow, where each phase and interface can be identified. Despite its small size, continuum mechanics remains applicable for most materials under consideration.

2. Darcy Scale (Maroscale or Local Scale): This is the usual scale for describing porous media, covering a range from several millimeters to centimeters. Due to the relatively large size, a pore-scale explicit description of porous medium properties or the computational challenges posed by complex pore geometries. Therefore, at the Darcy scale, macroscopic state variables are employed. Physical quantities are averaged over minimal volumes within the porous medium, chosen to represent the medium's

properties. In the case of multiphase flows, interfaces are not visible, and pore space occupation is described in terms of mass or volume fractions.

3. Large Scale (Global scale): This scale considers macroscopic properties over distances ranging from a few centimeters to kilometers. The study of such environments typically combines geostatistical data with numerical simulations of Darcy-scale averaged equations for areas with constant properties.

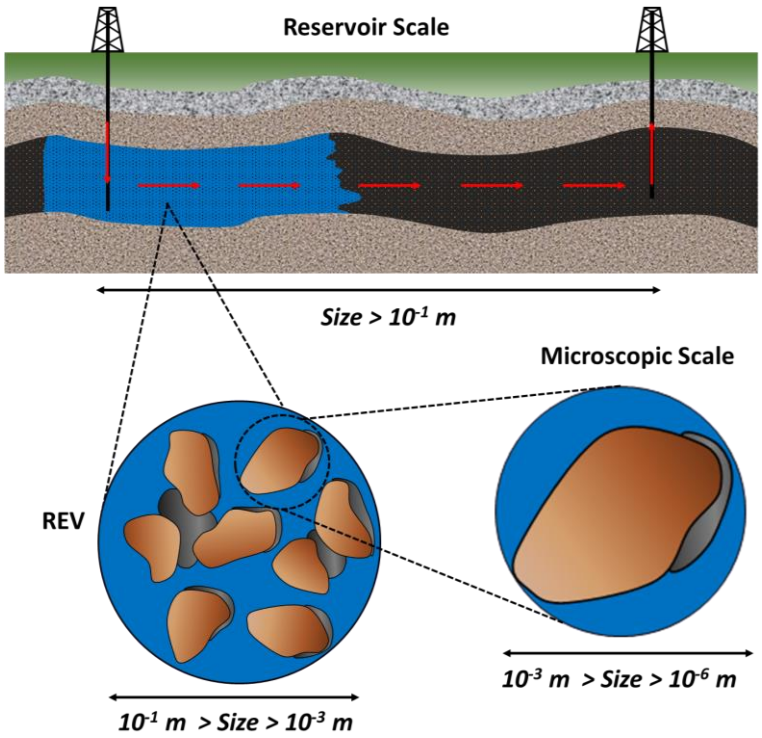

Figure II-23 Description of the different scales of porous medium

Flow can be simplified as a two-phase displacement process where the wetting phase (in blue) displaces the non-wetting phase (in black) in **Figure II-23**. In the context of continuum mechanics, the physical models used must account for all complexities at lower scales while describing phenomena at larger scales. Failure to capture the intricacies at lower scales during modeling can result in inadequate models.

II.2.1.2 Representative Elementary Volume

Multiple mathematical models can describe the same phenomenon, each with different spatial resolutions. When transitioning from the pore scale description to larger-scale models, an intermediate-scale representation becomes necessary. This intermediate scale serves as a bridge between the two scales, establishing a clear link between the descriptions of porous media at different scales. It ensures that regardless of the observer's scale, the introduced models remain consistent. In other words, macroscopic descriptions must account for the complexity of physics at the pore scale to be satisfactory. Similarly, reservoir-scale descriptions must incorporate lower-scale dynamics in a relevant way to be representative.

Depending on the volume size considered, the geometric parameters of porous media exhibit significant differences. This discrepancy is even more pronounced at smaller scales due to the specific arrangement of microchannels around observation points. However, it can be assumed that there exists a minimum size such that, for any volume size at least this large, the values of the considered geometric parameters become approximately constant, and the characteristic curves do not exhibit significant changes as the mesh volume increases. This minimum volume is referred to as the Representative Elementary Volume (REV).

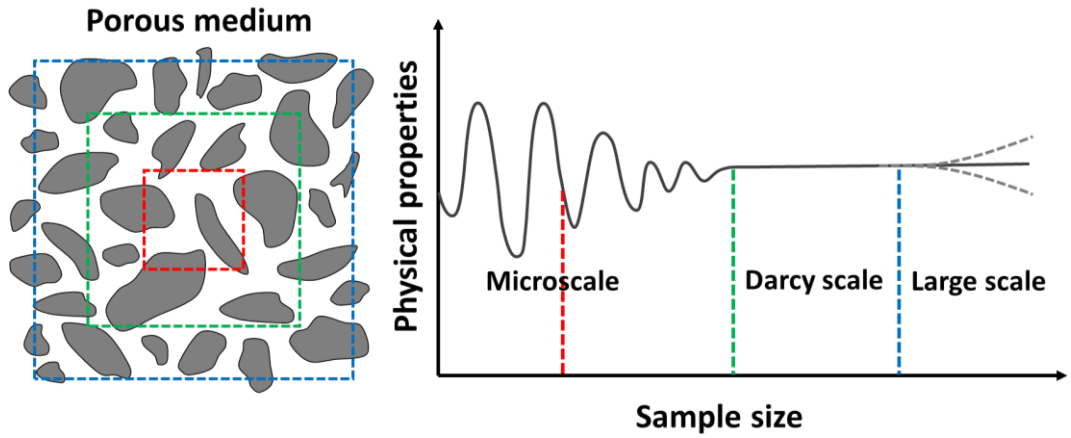

Figure II-24 *Representative elementary volume (REV). At the initial scales of description, variations in physical properties are evident, depending on the zones within the material (illustrated by red dotted lines). However, when observed over a sufficiently large volume (indicated by the green dotted line), these properties exhibit minimal variation from one point to another. This consistency is also observed when considering arbitrarily larger volumes. Nevertheless, for heterogeneous media, variations can reemerge at larger scales due to the medium structuration and macroscopic heteroploidy.*

The transition from a microscopic to a higher-scale description relies on the assumption that the physical properties of the material remain constant once the unit of description reaches a sufficient size. Consequently, the microscopic dynamics within a REV around various points in the material exhibit strong similarities. This assumption justifies employing an averaged description of physics at the Darcy scale, under the presumption that the elementary volume of the domain indeed functions as a REV, and thus, the underlying microscopic physics experiences minimal variation.

However, it's important to note that despite this assumption, practical observations reveal that physical properties may indeed depend on the size of the REV, particularly for highly heterogeneous porous media, especially at larger scales (**Figure II-24**). This variation arises from the structural characteristics of porous media, which can differ based on geological events such as sediment layering or seismic activities, resulting in distinct arrangements of pore networks across different areas. At the medium scale, considering the material's heterogeneity, one may assume the presence of multiple REVs, and consequently, zones with different dynamics that need to be considered.

The assumed existence of a REV and its determination provide a suitable tool for scaling. If sufficiently representative of the porous medium, knowledge of the phenomena governing flow within a REV provides information on Darcy-scale flow; the local geometric properties of the microstructure sufficiently approximate those of the REV so that the effects driving the flow dynamics remain the same.

II.2.2 Governing Equations for Fluid Flow in Porous Media

With the geometrical features influencing the fluid transport properties in a porous medium presented, it is now possible to derive macroscopic flow models by averaging the microscopic equations with the Thermodynamically Constrained Averaging Theory (TCAT) (Gray & Miller, 2005) (Gray & Miller, 2006) (Jackson, et al., 2009). The purpose of multi-scale models is twofold. Firstly, to link the dynamics at the microscopic scale with the description at the scale of interest. However, these mathematical procedures reveal a large number of relationships that are often unknown. Therefore, a second objective of these methods is to identify the approximations needed to close the resulting system. TCAT is not the only existing scaling method (Whitaker, 1996) (Lasseux, et al., 2019), but it has served as the basis for the macroscopic description presented in the thesis. The establishment of a multiscale porous media flow system using this method involves several step (Gray & Miller, 2006) s:

1. Formulation of the conservation equations for the extensive variables and the thermodynamic relations at the pore scale.

2. The relations are then averaged over REVs to be formulated at the Darcy scale.

3. Introduction of macroscale conservation equations into the entropy inequality using Lagrange multipliers. In this way, the flow through porous media is formulated as an optimisation problem: the solution must minimize the entropy production while verifying the macroscopic conservation equations derived earlier. Since the result of the latter is always zero, the conservation laws are added without changing the second member of the principle of thermodynamics. The result is the “constrained” entropy inequality (CEI).

4. The Lagrange multipliers are chosen specifically to make the time terms disappear. Then the remaining terms are grouped into flow/force pairs of the same origin under the desired assumptions (single phase flow, incompressible etc...). The resulting inequality is then called the simplified “constrained” entropy inequality (SEI), in the sense that it is a particular form of the CEI. This inequality is composed of a sum of products, each expressing a force-flow relationship, which are all equal to 0 at equilibrium.

5. The closure relationships linking the variables of interest are derived from the SEI. In the way they have been derived, these laws respect the thermodynamic principles of porous media and, depending on the model and the complexity of the physics introduced at the pore scale. Experimental or numerical relationships may be required to obtain a complete system.

In the following, only step 1 will be discussed in detail as the work in this thesis is mainly concerned with the microscopic scale. The final forms of the Darcy scale flow laws resulting from step 5 and the assumptions necessary to obtain a closed system will also be presented. The notations introduced follow those of (Jackson, et al., 2009). We study here the flow of one or two immiscible fluids wetting (*w*) and non-wetting (*nw*) within an undeformable solid (*s*). The fluids involved are assumed to be incompressible and to be composed of only one chemical species.

II.2.2.1 Conservation Equations at the Pore Scale

The governing equations for conservative flow at the pore scale are the Navier-Stokes equations and the continuity equation. In other words, the premise of the research is that fluid flow adheres to the principles of continuum mechanics: by considering various fluxes entering and leaving, source terms, and species transfer, the study investigates the conservation of extensive variables over time at each point. First, we analyze the flow of a single fluid through the porous medium to understand the characteristics of such flows. Subsequently, we will explore the distinctions that arise when one or more additional phases are introduced at the pore scale.

Single-phase Flow at the Pore Scale: Governing Equations

Let us first consider a single fluid *w* flowing in a porous medium whose solid matrix is denoted as *s*. For such a system, the conservation of mass laws can be written as follows:

$$\frac{\partial \rho_\alpha}{\partial t} + \vec{\nabla}\bullet\left(\rho_\alpha \mathbf{v}_\alpha\right) = 0 \quad \text{with } pour\ \alpha \in \{w, s\} \qquad \text{Equation 2-29}$$

For an incompressible fluid and an undeformable solid skeleton, the previous can be simplified as an incompressibility assumption:

$$\begin{cases} \vec{\nabla}\bullet\mathbf{v}_\alpha = 0 \cdots (a) \\ \vec{\nabla}\bullet\mathbf{v}_w = 0 \cdots (b) \\ \vec{\nabla}\bullet\mathbf{v}_s = 0 \cdots (c) \end{cases} \qquad \text{Equation 2-30}$$

Similarly, the conservation of angular momentum allows us to write on a microscopic scale:

$$\frac{\partial\left(\rho_\alpha \mathbf{v}_\alpha\right)}{\partial t} + \vec{\nabla}\bullet\left(\rho_\alpha \mathbf{v}_\alpha \mathbf{v}_\alpha\right) - \rho_\alpha \mathbf{g}_\alpha - \vec{\nabla}\bullet\underline{\mathbf{t}}_\alpha = 0 \quad \text{with } pour\ \alpha \in \{w, s\} \qquad \text{Equation 2-31}$$

If the solid phase is totally undeformable $\mathbf{v}_s = 0$, and Equation 2-31 for the solid reduce to:

$$-\rho_s g_s - \vec{\nabla}\bullet\mathbf{t}_s = 0 \qquad \text{Equation 2-32}$$

Under the stated assumptions ($\mathbf{v}_s = 0$), it is therefore not necessary to explicitly deal with the conservation equations in the solid phase; the latter only interacts with the system through the fluid-solid contact surfaces. Similarly, it is possible to simplify Equation 2-31 in the fluid phase under the

assumption of Newtonian constraints (which will be discussed in more detail in the chapter dedicated to numerical modelling) and incompressibility derived from Equation 2-30 (a):

$$\frac{\partial \mathbf{v}_w}{\partial t} + \mathbf{v}_w \bullet \vec{\nabla}\mathbf{v}_w - \mathbf{g}_w - \frac{1}{\rho_w}\vec{\nabla}\bullet\left(-p\mathbf{I} + \eta_w\left(\vec{\nabla}\mathbf{v}_w + \vec{\nabla}^T\mathbf{v}_w\right)\right) = 0 \qquad \text{Equation 2-33}$$

The system formed by equations Equation 2-30 (b) and Equation 2-33 forms the Navier-Stokes system, which governs fluid flows in continuum mechanics. This means that at the pore scale, the flow equations do not take into account the porous character of the material because the microscopic geometry of the medium is explicitly taken into account thanks to an approximate spatial discretization (only the space occupied by the fluid is taken into account) and the boundary conditions. For viscous fluids, non-slip conditions are usually introduced at the fluid-solid interface.

In many applications, if the velocity is relatively small, the non-linear term in Equation 2-33 can be neglected. In the derivation of macroscopic flow equations at the Darcy scale, this assumption is often considered (Gray & Miller, 2006) (Whitaker, 1986).

Diphasic Flow at the Pore Scale

Generally, as the system are reduced in size, phenomena such as viscosity, diffusion, surface tension, and contact lines become increasingly important. Therefore, it is necessary to consider the variation of these parameters at the microscale. Compared to the single-phase case, the flows of two immiscible fluids are distinguished by the existence of contact zones between the different entities that make up the system: the interface between the two fluids, but also between the solid *s* and the *w* phase and the *nw* phase. Each phase is separated by interfaces, which deform, rupture, and merge as the fluids flow. As previously mentioned, at the microscopic scale, these effects must be taken into account explicitly. For the sake of simplicity, in the following, the flow of the two fluids will be considered in an undeformable and immobile porous skeleton.

d. The description of the interface

The challenge in predicting immiscible two-phase flow lies in determining the interface dynamics Due to the difficulty of real-time capturing and recording of interfaces, interface-resolving numerical simulations are the preferred method at the microscale. Standard continuum methods and models for simulating interface two-phase flow include the Volume-of-Fluid (VOF) (Aniszewski, et al., 2014) (Ferreira, et al., 2015), Level-Set (LS) (SHARMA, 2015) (Fushui, et al., 2017), Front-Tracking (FT) (Pivello, et al., 2014), and Phase-Field (PF) methods (Jacqmin, 1999) (Chiu & Lin, 2011) (Heider, 2021). **Figure II-25** shown the different continuum methods for describing the evolution of deforming interface.

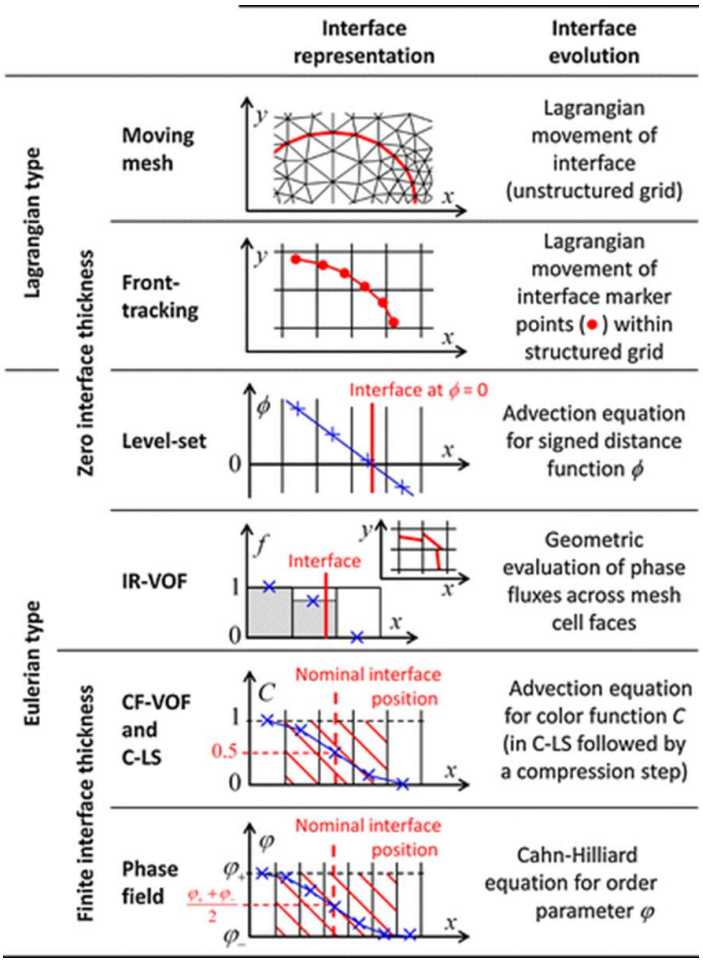

Figure II-25 *Illustration of the different continuum methods for describing the evolution of deforming interfaces (Wörner, 2012). For methods with zero interface thickness the interface position is indicated by a solid red line. For methods with finite interface thickness, the nominal interface position is indicated by a dashed red line. The interface thickness (as indicated by the red hatched area) is typically 2–3 mesh cells for the CF-VOF and C-LS methods and is larger (up to 10 mesh cells) for the PF method*

Traditionally, the interface is considered a thin boundary layer separating two distinct phases of matter (which could be solid, liquid, or gas), possessing properties different from the materials it separates. Continuum methods can be categorized into methods with zero-thickness interfaces (sharp interfaces) or finite-thickness interfaces (diffuse interfaces). In sharp interface methods, the physical interface is a zero-thickness function interface, with physical quantities like density and viscosity discontinuous at the interface (Quan, et al., 2009) (Santis, et al., 2021). To accurately describe the interface, adequate grid resolution is required to capture changing curvatures. These methods are sensitive to interface changes, particularly during fluid splitting and merging, necessitating complex algorithms and longer computational times.

In the diffuse-interface approach, the interface possesses a finite thickness, and physical quantities undergo continuous changes across the interface (Ding, et al., 2007) (Shahab, et al., 2017) (Jain, et al., 2020). Unlike the infinitely thin separation boundary in the sharp interface limit between immiscible

fluids, a small but finite-width transition region replaces it, as shown in **Figure II-28**. Within this transition zone, physical properties vary sharply yet continuously, simplifying the treatment of interface topological changes. This approach grants the composition field physical significance both at the interface and in the bulk phase, applicable to both miscible and immiscible physical states. Moreover, it eliminates the explicit tracking of interfaces while solving all governing equations, enhancing simulation accuracy when describing complex multiphase fluid interfaces and interactions, making it easier to implement and apply.

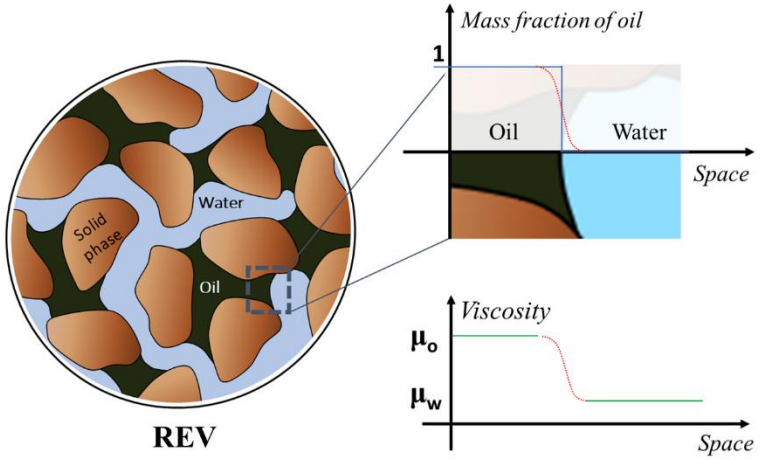

Figure II-26 *The variation of physical quantities at the diffuse interface (red line). The blue line refers to sharp interface.*

e. Conservation equations

As for the single-phase case, conservation equations of mass and momentum be written for each phase,

$$\frac{\partial \rho_a}{\partial t} + \vec{\nabla} \bullet \left(\rho_a \mathbf{v}_a \right) = 0 \ \ pour\ \alpha \in \{w, nw, s\} \qquad \text{Equation 2-34}$$

$$\frac{\partial \left(\rho_a \mathbf{v}_a \right)}{\partial t} + \vec{\nabla} \bullet \left(\rho_a \mathbf{v}_a \mathbf{v}_a \right) - \rho_a \mathbf{g}_a - \vec{\nabla} \bullet \underline{\mathbf{t}}_a = 0 \ \ pour\ \alpha \in \{w, nw, s\} \qquad \text{Equation 2-35}$$

Furthermore, equivalent conservation equations must be formulated for interphases (TCAT). These equations take into account the planar aspect of the interface, and include, in addition to the terms already present in the previous conservation equations, mass and momentum exchange terms. The introduction of capillary forces is then done by stress couplings at the interface. Another point of view is to take into account capillary forces through a volume force term (Jacqmin, 1999) (Jacqmin, 2000). Finally, other methods consider the interface as a boundary separating two subdomains: one occupied by the w phase and the other by the *nw* phase. In this case, boundary conditions on pressure and velocity are imposed (Whitaker, 1986). The mathematical treatment of capillary forces in the development of our numerical model will be discussed in more detail.

Here, we used phase field method to describe phase transitions in incompressible, immiscible two-phase flow. It transforms the problem of phase interface movement and evolution into a partial differential equation problem, enabling tracking and description of the phase interface. The fundamental idea involves introducing a conserved order parameter or phase field φ to characterize two distinct phases (Wörner, 2012). This ordered parameter changes rapidly and smoothly within the diffuse interface region, representing the distribution of different phases throughout the system, being mostly uniform within the bulk phase. The phase interface is represented by the spatial distribution of the phase field variable. The phase field equation can be solved throughout the computational domain without explicitly knowing the position of interface. This approach completely avoids explicit interface tracking and naturally handles topological changes without any special procedures. The equations in the phase field method come in two forms: the Cahn-Hilliard equation (Cahn & Hilliard, 1958) (Hosseini, et al., 2017) (Xia, et al., 2022) and the Allen-Cahn equation (Allen & Cahn, 1976) (Jeong & Kim, 2017). The interface dynamics is modeled by an evolution equation for φ, thus the Cahn-Hilliard equation ensures mass conservation (Furihata, 2001), and in this work, we utilize it to compute the incompressible Navier-Stokes flow for the two-phase system. It can be described as,

$$\frac{\partial \varphi}{\partial t} + \left(\mathbf{u} \bullet \vec{\nabla}\right) = \vec{\nabla} \bullet \left(M_e \vec{\nabla} \mu_\varphi\right) \qquad \text{Equation 2-36}$$

Here, **u** is the velocity field; M_e is the mobility; μ_φ is the chemical potential, which represents the rate of change of free energy with respect to φ and is given by (Wörner, 2012),

$$\mu_\varphi = \frac{d\Phi}{d\varphi} - \varepsilon_\varphi^2 \vec{\nabla}^2 \varphi \qquad \text{Equation 2-37}$$

For the bulk energy density $\Phi(\varphi)$ different formulations are used in the literature which depend on the choice for $\varphi_\pm$, such as the case of $\varphi_\pm$=±0.5, so the $\Phi = (\varphi + 0.5)^2(\varphi - 0.5)^2$; or at the case of φ+=1, φ-=0, the $\Phi = \varphi^2 (1 - \varphi^2)/4$ (Jacqmin, 1999).

II.2.2.2 Darcy Scale Modelling

At the macroscopic scale (Darcy scale) at each point we have more than one phase each one characterized by its own volume fraction, velocity and stress tensor.

Single Phase Flow Law at Darcy Scale

When the porous medium is saturated with the *w* fluid phase, as shown in **Figure II-27**, at each point, both the *w* phase and the *s* phase coexist. Therefore, the volume fractions of the *w* (ε^w) and *s* (ε^s) phases have the relationship $\varepsilon^w + \varepsilon^s = 1$. In addition, porosity is denoted as $\varepsilon = 1 - \varepsilon^s$. The mass fraction equation of the fluid phase can be described as,

$$\frac{\partial \rho^w \varepsilon^w}{\partial t} + \vec{\nabla} \bullet \left(\rho^w \varepsilon^w \mathbf{v}^w\right) = 0 \qquad \text{Equation 2-38}$$

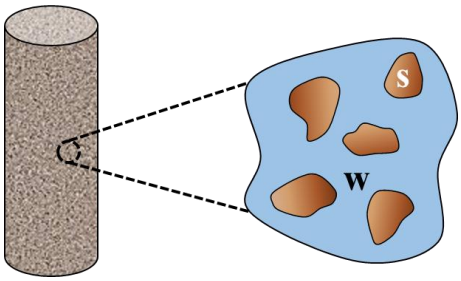

Figure II-27 *Diagram of porous media (core) saturated with w phase*

By assuming that the fluid is uncompressible and the porosity constant, this equation can be reduced to,

$$\vec{\nabla}\bullet\left(\rho^w\varepsilon^w\mathbf{v}^w\right)=0 \quad \text{with } \mathbf{v}^w=-\frac{\underline{\underline{\mathbf{K}}}^w}{\varepsilon^w\eta^w}\left(\nabla p^w-\rho^w\mathbf{g}^w\right) \qquad \text{Equation 2-39}$$

where, $\mathbf{v}^w$ represents the Darcy velocity, and p^w denotes the average pressure of the liquid phase. $\underline{\underline{\mathbf{K}}}^w$ stands for the permeability tensor, which is an intrinsic physical property of the porous medium. It quantifies the ability of the rock to allow fluid to flow through it, particularly in anisotropic media where flow properties can vary in different directions.

Macroscopic Models of Two-phase Flow in Porous Media

When we model two-phase flow at the macroscale, each point within the porous medium three phases coexist (**Figure II-28**): the solid phase, wetting fluid and non-wetting fluid, and the volume fraction ε^α of each them has,

$$\varepsilon^w+\varepsilon^{nw}+\varepsilon^s=1 \qquad \text{Equation 2-40}$$

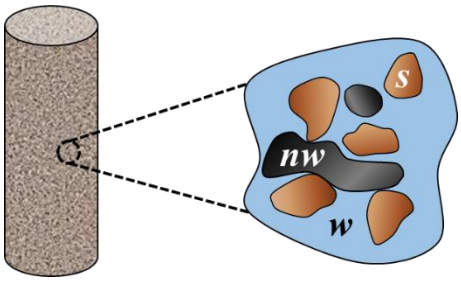

Figure II-28 *Diagram of two-phase flow within porous medium*

The porosity is also denoted as $\varepsilon = 1 - \varepsilon^s$ in this case. A measure of the relative occupancy of the pores by the fluids present must be introduced for multiphase flows. This variable is the degree of saturation *S*. The saturation of a fluid measures the ratio between the volume occupied by a fluid and the pore volume of the REV:

$$S^\alpha=\frac{\mathcal{E}_\alpha}{v_\varepsilon} \quad \text{with pour } \alpha = (w, nw) \qquad \text{Equation 2-41}$$

This allow us to rewrite Equation 2-40 as,

$$S^{w} + S^{nw} = 1 \qquad \text{Equation 2-42}$$

In the absence of chemical reaction terms, the mass conservation equations Equation 2-34, averaged over the REV in each fluid phase, are then written as (Gray & Miller, 2006),

$$\begin{cases} \dfrac{\partial\left(S^{\alpha}\varepsilon\rho^{\alpha}\right)}{\partial t} + \vec{\nabla}\bullet\left(S^{\alpha}\varepsilon\mathbf{v}^{\alpha}\right) = 0 \cdots for \cdot \alpha = (w, nw) \\ \dfrac{\partial\left(S^{\alpha}\varepsilon\rho^{\alpha}\right)}{\partial t} + \vec{\nabla}\bullet\left(S^{\alpha}\varepsilon\mathbf{v}^{\alpha}\right) = 0 \cdots (a) \\ \dfrac{\partial\left(S^{\alpha}\varepsilon\rho^{\alpha}\right)}{\partial t} + \vec{\nabla}\bullet\left(S^{\alpha}\varepsilon\mathbf{v}^{\alpha}\right) = 0 \cdots (b) \end{cases} \qquad \text{Equation 2-43}$$

This Equation measures the temporal evolution of the saturation of each phase as a function of the porosity of the medium, as well as the relative velocity of each fluid present. However, the number of unknowns in the system can be reduced thanks to Equation 2-42, which allows us to know the saturation of *nw* phase by modelling only the evolution of the saturation of *w* phase.

Following TCAT, a generalised Darcy's law can be obtained that relates the macroscopic fluid velocity $\mathbf{v}^{\alpha}$ to the pressure gradient p^{α} as well as to the volume forces $\mathbf{g}^{\alpha}$ acting on it,

$$\mathbf{v}^{\alpha} = -\frac{\underline{\mathbf{K}}^{\alpha}}{S^{\alpha}\varepsilon\rho^{\alpha}\eta^{\alpha}}\left(\vec{\nabla}p^{\alpha} - \rho^{\alpha}\mathbf{g}^{\alpha}\right) \quad pour\ \alpha = (w, nw) \qquad \text{Equation 2-44}$$

In the previous equation Equation 2-44, η^{α} represents the macroscopic dynamic viscosity of the fluid considered and $\underline{\mathbf{K}}^{\alpha}$ the effective permeability tensor. It is through this term that the affinities of one of the phases with the medium considered are taken into account: the higher the effective permeability, the more easily the fluid flows within the porous medium. It can be added that the effective permeability of a phase is generally written in the following form,

$$\underline{\mathbf{K}}^{a} = k^{a}\underline{\mathbf{K}} \quad \text{pour } \alpha = (w, nw) \qquad \text{Equation 2-45}$$

Where k^{α} is the relative permeability factor of the phase α and $\underline{\mathbf{K}}$ the intrinsic permeability of the porous medium. Thus, in tensor form, the effective phase permeability in Equation 2-44 has the same characteristics as the absolute permeability tensor in terms of isotropy (or not). It is simply corrected by the factor k^{α} to take into account the coexistence of phases within the pores. This coefficient is an unknown in the problem, and varies both according to geometric factors of the porous medium (such as

porosity) and the properties of the fluids in question. Analytically, it is usually determined by introducing a permeability law. We will discuss this aspect in more detail in the dedicated sections. Following this assumption, the phase velocity obeys a Darcy law where the factor $\underline{\mathbf{K}}^{\alpha}/\eta^{\alpha}$ often called the phase mobility factor.

Several extensions of the generalised Darcy equations allow to complexify the underlying pore-scale physics in Equation 2-44. An averaging derivation of the macroscopic equations brings out coupling terms between the phase velocities thus allowing for momentum transfers that take place on the interface between the *w* and *n* fluids (Whitaker, 1986) (Pasquier, et al., 2017). Taking this phenomenon into account can correct the modelling given by Equation 2-44 in very permeable media, where the contact surfaces between the phases in presence are important.

$$\mathbf{v}^{a} = -\frac{\underline{\mathbf{K}}^{a}}{S^{a}\phi\eta^{a}}\left(\nabla p^{a} - \rho^{a}\mathbf{g}^{a}\right) + \underline{\mathbf{K}}^{ak}\mathbf{v}^{k} \quad \text{for } \alpha,\ k = w,\ nw;\ \alpha \neq k \qquad \text{Equation 2-46}$$

The tensor $\underline{\mathbf{K}}^{\alpha\kappa}$ being the viscous coupling tensor. This is a new unknown of the problem that needs to be determined with new closure equations.

Macroscopically, the capillary pressure is introduced into the equation system and corresponds to the pressure jump between the fluid phases $p^{c} = p^{nw} - p^{w}$ The relationship between capillary pressure and saturation must be specified to close the system. Examples of commonly used relationships will be discussed later in the section II.2.3 "Capillary Pressure Function of Saturation" part. Taking the capillary pressure and the pressure of the non-wetting phase as primary variables, it is possible to treat the system formed by Equation 2-43 (a) and (b) by injecting the expressions for the phase velocity into the continuity equation. For a two-phase flow consisting of phases *w* and *nw*, Equation 2-43 become:

$$\begin{cases} \varepsilon\dfrac{\partial}{\partial t}\left(S^{w}\right) - \vec{\nabla}\cdot\left(S^{w}\varepsilon\dfrac{k^{w}}{\eta^{w}}\underline{\mathbf{K}}\left(\nabla p^{nw} - \nabla p^{c}\left(S^{w}\right) - \rho^{w}\mathbf{g}^{w}\right)\right) = 0 \\ -\varepsilon\dfrac{\partial}{\partial t}\left(S^{w}\right) - \vec{\nabla}\cdot\left(\left(1-S^{w}\right)\varepsilon\dfrac{k^{nw}}{\eta^{nw}}\underline{\mathbf{K}}\left(\nabla p^{nw} - \rho^{nw}\mathbf{g}^{nw}\right)\right) = 0 \end{cases} \qquad \text{Equation 2-47}$$

We find a closed system of two unknowns p^{nw} and p^{w} with two equations to determine them, provided that the law of fluid permeability is known, as is the law of capillary pressure.

II.2.3 Constitutive Equation

A research line of interest in multiphase flow involves seeking parameterizations to determine relative permeability and capillary pressure through laboratory experiments and numerical methods. The main

objective is to advance the understanding of two-phase flows in porous media by comparing parameterization methods and conducting parameter estimation to address flow problems. Several models of varying complexity exist to characterise the permeability law of a porous medium. Currently, two commonly used parameterization models for simulating the relationship between saturation, capillary pressure, and relative permeability variables in porous media are the Brooks-Corey (BC) (Brooks & Corey, 1964) and Van Genuchten (VG) (Van Genuchten, 1980) parameterization models. Next, we will discuss the constitutive equations of these parameters in different models.

II.2.3.1 Generalized Darcy's Model-Law of Relative Permeability

The relative permeabilities of the phases in the macroscopic system Equation 2-47 play an important role in the shape of the solution, allowing the characterisation of the effective permeability of the porous medium for a given fluid given the presence of the other fluid. The relative permeability of a phase is a monotonic function of its saturation (the more a fluid is present in the pores, the easier it will be to flow and therefore the higher its relative permeability).

The widely used model for its ease of use is the empirical BC model (Brooks & Corey, 1964). This model involves the residual saturation of each fluid present in the porous medium S_{min}^{a} which is the minimum saturation of the phases (α = *w* and *nw*). It is the lowest volume fraction that the fluids can reach inside the pores. When the saturation value tends towards the residual saturation, the permeability tends towards 0. The relative permeability factor k^{α} of a fluid is written as a function of the maximum permeability k_{max}^{α} (Brooks & Corey, 1964) (Schroth, et al., 1998) (Horgue, et al., 2015) (Slompo, et al., 2023):

$$\begin{cases} k^{w} = k_{\max}^{w}\, \bar{S}_{\alpha}^{\frac{2+3\lambda_d}{\lambda_d}} \\ k^{nw} = k_{\max}^{nw} \left(1-\bar{S}_{\alpha}\right)^{2} \left(1-\bar{S}_{\alpha}^{\frac{2+\lambda_d}{\lambda_d}}\right) \end{cases} \qquad \text{Equation 2-48}$$

where, $\lambda_d > 0$ is related to the distribution of pore sizes. A more uniform porous medium is expected to have a narrower pore size distribution, resulting in a higher λ_d (typically greater than 2), whereas the broader pore size distribution lead to a small λ_d parameter. Generally, the range for λ_d is between 0.2 and 3, with Corey suggesting a typical value of around 2 (Corey, 1994).

Finally, the $\bar{S}_{\alpha}$ is the effective saturation of the fluid phase and can be described as,

$$\bar{S}_{\alpha} = \frac{S^{\alpha} - S_{\min}^{\alpha}}{1 - S_{\min}^{w} - S_{\min}^{nw}} \qquad \text{Equation 2-44}$$

In immiscible two-phase flow, the saturation of each phase, minimum saturation, and relative permeabilities need to be obtained through laboratory experiments.

In addition, the VG model in two-phase flow can be modified to capture the unique behaviour associated with each fluid phase (Van Genuchten, 1980). In the VG parameterization, relative permeabilities of the *w* and *nw* phases can be expressed as (Van Genuchten, 1980) (Horgue, et al., 2015) (Slompo, et al., 2023),

$$\begin{cases} k^{w} = \overline{S}_{\alpha}^{\frac{1}{2}} \left[1 - \left(1 - \overline{S}_{\alpha}^{\frac{1}{m}} \right)^{m} \right]^{2} \\ k^{nw} = (1 - \overline{S}_{\alpha})^{\frac{1}{2}} \left(1 - \overline{S}_{\alpha}^{\frac{1}{m}} \right)^{2m} \end{cases} \qquad \text{Equation 2-45}$$

where, m is the Van Genuchten coefficient relating to the pore size distribution with $m < 1$. The higher asymmetric pore size distribution of the porous medium, the lower the m value. Slompo et al. found a significant linear relationship between λ_d and m, which is expressed as (Slompo, et al., 2023),

$$\lambda_d = 0.51 \left(\frac{1}{1-m} \right) - 0.7986 \qquad \text{Equation 2-46}$$

This expression establishes a relationship between the free parameters of each parametrization. They further introduce several typical values, with a representative case being $m = 0.5$, $\lambda_d = 0.28$, as $m = 0.5$ represents the realistic situation of highly asymmetric pores. The permeability-saturation relationship is illustrated in **Figure II-29** (left), where it is observed that the area between the relative permeability curves of the two models is significant. Additionally, a typical parameter $\lambda_d = 2$ is used, as mentioned above, revealing a smaller area between the curves (**Figure II-29**, right). However, in practical applications, calibration of the models based on laboratory experimental parameters is required, and further optimization of the algorithms may be necessary.

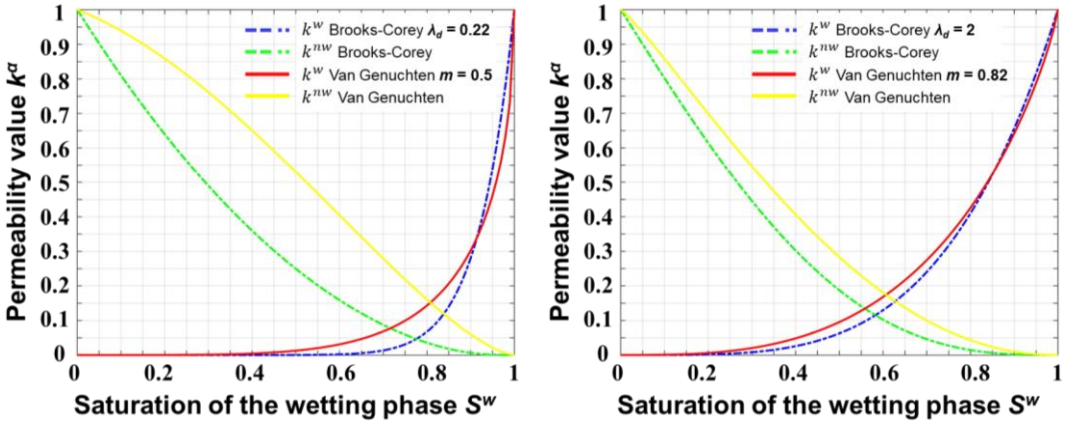

Figure II-29 *Variation of relative permeability with saturation of the wetting phase.*

From the previous examples, it can be seen that despite the determining role played by the relative permeability coefficients of each fluid, these parameters are intrinsic properties of the porous medium considered. The analytical laws developed now are largely based on BC and VG model's analytical

work and are adapted posteriori to the case considered. Alternatively, the emergence of scale change methods has contributed to the search for ways to determine the permeability tensor as a function of the microstructure of the medium. Indeed, on porous media resulting from the repetition of the same pattern (media formed by stacking of identical grains for example), symmetry conditions inherent to the geometry of the pores at the microscopic scale allow to find satisfied relations for each of the relative permeabilities (Whitaker, 1986) (Lasseux, et al., 1996) (Lasseux, et al., 2008). The averaging of variables over a REV then provides numerical permeability values.

II.2.3.2 Capillary Pressure Function of Saturation

The last relationship to be characterised in order to close the system Equation 2-47 is the dependence of the capillary pressure on saturation. As with the relative permeability models, the laws used are generally based on empirical arguments, and are adapted to the cases studied. The most widely used model is the Brooks and Corey model, although other more complex models exist (Brooks & Corey, 1964) (Abdallah, et al., 1986) (Lomeland & Ebeltof, 2008). To a first approximation, this law can be stated as,

$$p^c = p^d \overline{S}_\alpha^{-\frac{1}{\lambda_d}} \qquad \text{Equation 2-52}$$

where p^d is the displacement pressure. In the VG parameterization, the capillary pressure with saturation relationship is defined by,

$$p^c = p^e \left(\overline{S}_\alpha^{-\frac{1}{m}} - 1 \right)^{\frac{1}{n}} \qquad \text{Equation 2-47}$$

where p^e is entry capillary pressure and represents the critical pressure required for the non-wetting phase to enter the larger pores of the medium; n is empirical parameter which related to the symmetry in the distribution of pore sizes and m is often related to n by $m = 1\text{-}1/n$.

The typical dependences of the capillary pressure on the saturation of the wetting phase for both the BC model and the VG model are plotted in **Figure II-30**. Although the shape of the capillary pressure function depends on the model, this function is an increasing function of the non-wetting phase saturation independently from the model. The BC model and the VG model allows the experimental data associated with the different media to be modelled qualitatively.

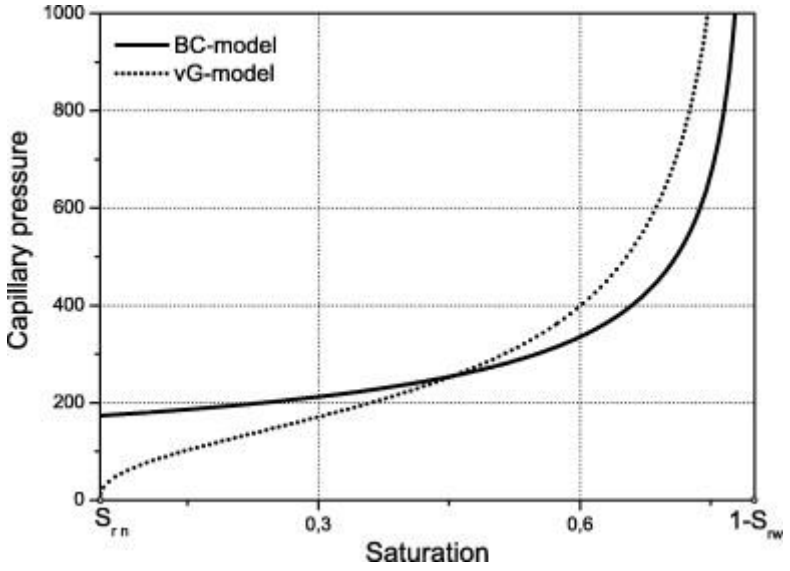

Figure II-30 *The functional relationship between capillary pressure and wetting phase saturation in porous media with different permeabilities*

II.2.3.3 Hysteresis in Relative Permeability

Relative permeability, like capillary pressure, depends on the distribution of two fluids at the pore scale. Under the same saturation conditions, there can be multiple distributions in equilibrium, resulting in several pairs of relative permeabilities.

Hysteresis in relative permeability refers to the phenomenon where the relative permeability of fluids in porous media depends on the history of saturation changes, showing different values during drainage and imbibition. Suppose we saturate a medium with a wetting fluid *w* and partially displace it with a non-wetting fluid *nw* until both fluids can flow simultaneously in diphasic system. We can then measure the relative permeability. Fluid *w* is displaced by fluid *nw*, and the relative permeability is measured again, and this process is repeated. Initially, saturation is reduced, and then it is increased. The relative permeability of the wetting fluid remains relatively consistent with changes in saturation, while the relative permeability of the non-wetting fluid exhibits significant variations between imbibition and drainage processes.

III. Materials and Methods

Our work includes physical experiments and in-silico experiments.

III.1 Physical Experiments

We have set up an instrumented microfluidic system that allows us to observe in live the flow behaviors within microfluidic chips and monitor the size distribution of oil clusters in real-time. Furthermore, the ΔP and flow rate can be recorded in all the experiments. In this study, we have observed and recorded the macroscopic flow behaviors of wetting and non-wetting phases during both drainage and imbibition processes, and analyzed the interactions at the fluid interfaces on a microscale. In addition, we have focused on exploring the saturation and mobilization mechanisms of the non-wetting phase by adjusting the Ca through changes in Q and the viscosity of the injection fluid. We have also examined the number, volume, and distribution of residual oil clusters. In this section, we will primarily discuss all materials and instruments involved in the experimental protocol, operational methods, image processing and data post-processing, as well as plans for subsequent experiments.

III.1.1 Fluids

III.1.1.1 Oil

The oil we used in the experiment was a commercially available rapeseed oil that was dyed with Oil Red O dye obtained from Sigma-Aldrich at a concentration of 0.01 % w/w (100 ppm), to make positive differentiation of various phases during the fluid displacement process. The dyed oil was passed through a 3 μm filter. The density and viscosity of the rapeseed oil are 0.91 g/cm^3 and 80 mPa·s, respectively.

III.1.1.2 Aqueous Mixture

Brine

The water used in the experiment is deionized water that was beforehand filtered through a 0.22 μm pore size acetate filter. The pure water was used in experiments not only serves to displace other phases but also is vital for cleaning and preparing the chip between runs to ensure consistency and prevent cross-contamination of results. This preparation helps maintain the integrity of each experimental cycle and allows for reproducible conditions that are essential for systematic study and comparison.

Moreover, it is noted that in the experiment the shallow etching depth of the chip ensures sharply defined fluid interfaces. However, this also results in limited optical differentiation among the three phases (water, oil, and solid), making it challenging to distinguish them clearly in captured images. Therefore, enhancing visibility through appropriate dyeing techniques becomes essential for effective visualization. These techniques involve adding specific dyes to the fluids, which enhances contrast and helps in accurately identifying and tracking the behavior of each phase during experiments. Here, water was

dyed in black using Ecoline liquid water colour in a 30 mL bottle, Noir 700 from Royal Talens. This not only aids in observing the fluid dynamics and displacement mechanisms but also facilitates subsequent image processing. The concentration of dying colour particles in water was 8% w/w. After filtration through the 0.22 μm pore size filter paper, the dyed water is sealed and stored.

In the experiment, we observed that the dyed water tends to form aggregates and its stability decreases after being stored for a period of time. Therefore, to ensure stability and dispersion of this water phase dispersion, sodium chloride (NaCl) (ACS reagent, ≥99.0%, from Sigma-Aldrich) was added, thereby facilitating solid particles dispersion. For that purpose, we investigated the influence of NaCl concentration on aggregate size. The results are shown in **Figure III-1**. The diameter of aggregates in the dyed water without NaCl varies from 25 to 50 μm. At a NaCl concentration of 6 g/L, the size of aggregates notably decrease and reaches a diameter of 10 to 20 μm. With increasing NaCl concentrations of 10 g/L and beyond, the aggregates disappear, and the dye within the solution disperses uniformly, exhibiting a diameter of approximately 4.7 μm. Consequently, brine with 10 g/L was utilized in the waterflooding and was subsequently used for preparing the other aqueous mixture (see below section). The density and viscosity of brine are 0.998 g/cm^3 and 1 mPa·s at 20 °C, respectively.

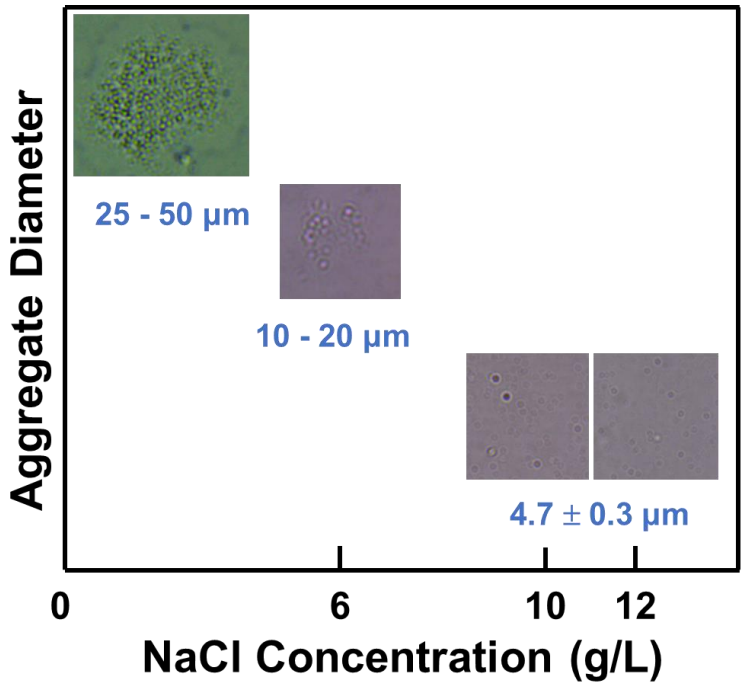

Figure III-1 Variation of aggregate diameter with NaCl concentration

Glycerol/Water Mixtures

The glycerol, purchased from Sigma-Aldrich (≥99.0% GC), was used to improve the viscosity of injected aqueous fluids with different *M* by increasing the concentration of glycerol in glycerol/water mixture. Based on the reported literature, a comprehensive evaluation was conducted concerning the density and viscosity of aqueous solutions with varying glycerol concentrations at 20 °C.

A specific volume of water was initially measured using a graduated cylinder and added to a vessel. The desired glycerol quantity was then incorporated to achieve the targeted glycerol/water mixture ratio. The density of the solution was determined by measuring its mass with an electronic balance. The dynamic viscosity of the mixture was calculated using an Oswald viscometer. This preparation included pure glycerol and glycerol/water mixtures. Since this work follows waterflooding, the invading phase used here is a glycerol/water mixture, while the defending phase is brine. The remaining oil is encased by the water phase, and the mixture acts to displace the brine, thereby mobilizing the remaining oil. Therefore, the glycerol/water mixtures we set with different viscosity ratios (M) relative to water: 1, 4, 8, 20, and 80 (Table III-1).

During the mixture preparation, to enhance contrast and identifying and tracking the behaviour, Ecoline liquid watercolor, Bluish Violet 548 from Royal Talens, was added to achieve the same dye concentration and salinity level as in the brine. The required amounts of glycerol, water, pigment, and NaCl for each M ratio were precisely weighed using an electronic balance and then transferred into a clean beaker. The mixture was stirred at room temperature for 8 h at 600 rpm to ensure thorough mixing. After stirring, the solution was transferred to a transparent container, labeled accordingly, and sealed for future use.

Finally, the interfacial tension (IFT) between rapeseed oil and the various glycerol/water mixtures of different M was measured using a Force Tensiometer - Tensíío from KRÜSS. For these measurements, precise volumes of the aqueous mixtures and oil were added into a glass dish positioned on a temperature-controlled sample stage, following the guidelines. The IFT between the oil phase and each aqueous mixture was then automatically measured at room temperature using the Du Noüy ring method, providing accurate assessments of the fluid interactions under controlled conditions.

Table III-1 The mass fraction of aqueous solutions with different M

Viscosity of mixture/water	***M* = 1**	***M* = 4**	***M* = 8**	***M* = 20**	***M* = 80**
Mass fraction of glycerol (% w/w)	0	46	54	68	82

III.1.1.3 The Cleaning Fluids

For cleaning, we used surfactants, absolute ethanol, sodium hydroxide (NaOH) and hydrochloric acid (HCl) sequentially. After flushing out the fluids within the porous medium, deionized water was used to rinse the porous medium to remove any residual cleaning chemicals. Subsequently, nitrogen gas was utilized for thorough drying of the porous medium chips. The surfactant used in this process is Enordet O332 from Shell Chemicals, diluted to a mass concentration of 5%. HCl was purchased from Sigma-Aldrich at a concentration of 25% mol/L, which was further diluted to 10% mol/L for use. NaOH from

Scharlau was purchased at a concentration of 20% (w/v) and was diluted to 10% (w/v). Absolute ethanol, also procured from Scharlau, required no further dilution and was directly used for cleaning purposes.

III.1.2 Porous Medium

III.1.2.1 The Geometry and Parameters

The porous medium used in our work are microfluidic chips from Micronit (Netherlands), made of glass with a size of 45 mm × 15 mm × 20 µm (length × width × depth), and supplied in a black polypropylene box, as shown in **Figure III-2**. They are water-wet and of distinct pore network structures, to investigate the displacement dynamics of immiscible two-phase flow driven by the heterogeneity of porous medium: 1) The first type is the "Physical Rock Structure chip", designed based on real rock pore structure scan results, and referred to as the "random chip". 2) The second type is the "Uniform Network chip", featuring a uniform network structure with clearly distinguishable pore bodies and throats (specific parameters will be presented in the following section). This chip is named as the "regular chip".

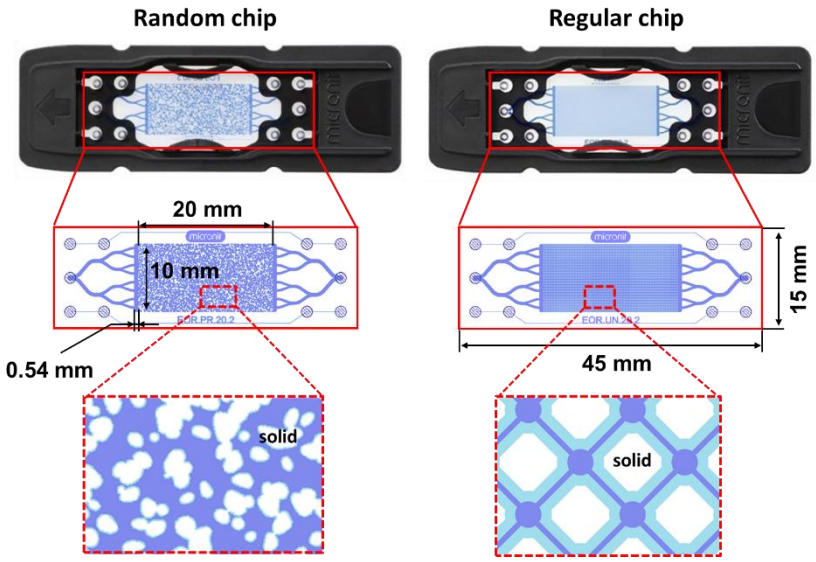

Figure III-2 *Exterior view of the two chips (top). Below, schematic representations of the geometric structures of the porous media and flow channels within the entire glass substrate are shown. Notably, on each side of the porous media, there is a 0.54 × 10 mm fracture. In the porous media, the white regions represent the solid phase, while the other areas correspond to the pores*

In detail, the porous medium of Regular and Random chips, each with an identical size of 20 × 10 mm and a 20 µm etch depth, shows contrasting pore network distributions and geometric structures, as detailed in **Figure III-3**. The Random chip features irregularly shaped grains, while the Regular chip comprises repetition of a single geometric structure. Notably, a distinguishing feature lies in the details of the pore structures, as illustrated in **Figure III-3**. Specifically, at the upper end of each pore body, there exists an etched pore diameter of 90 µm, accompanied by a mask width diameter of 50 µm. The

separation between adjacent pore bodies measures 200 µm. Similarly, at the apex of the pore throat, there exists an etched diameter of 50 µm, accompanied by a mask width of 10 µm.

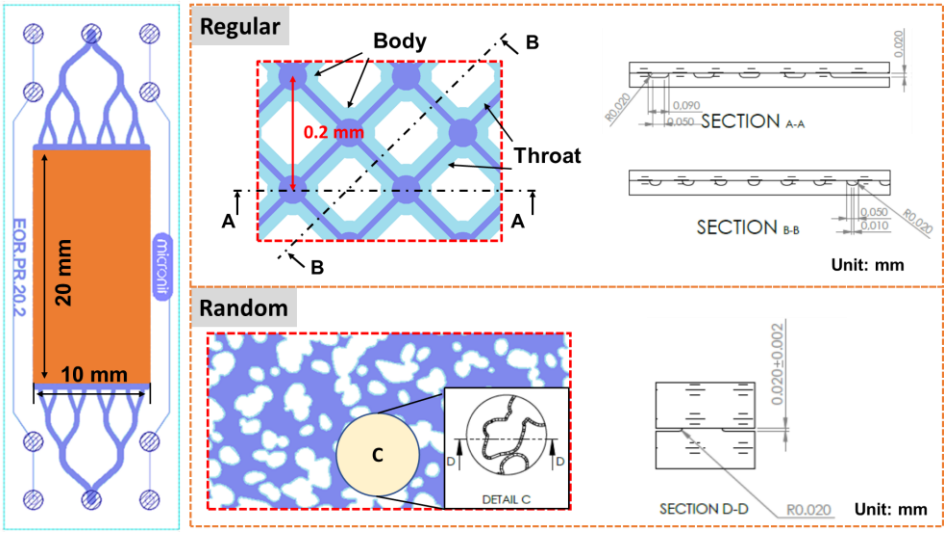

Figure III-3 *The dimensions of the porous medium region within the microfluidic chip, as well as the details of the geometric distribution and dimensions of the porous medium in both types of chips. With the porous medium distribution areas highlighted in orange.*

In the study of porous media as represented in **Figure III-2** and **Figure III-3**, the regular chip displays a uniform structure with easily distinguishable pore bodies (circular areas) and pore throats (rectangular-like areas). Conversely, the random chip exhibits a non-uniform distribution of pore diameters, closely mimicking the porous structure of real rocks. To accurately analyze the variation in pore sizes within the random chip, we employed watershed segmentation and circle-fitting methods to evaluate the diameter distribution.

Watershed segmentation is a widely used image segmentation technique that is particularly valued for its simplicity, speed, and effectiveness in completely segmenting images, even in cases of low contrast and weak boundaries (Hamarneh & Li, 2009) (Beucher & Meyer, 2018) (Kornilov, et al., 2022). This method ensures the provision of closed contours around each target area. Following segmentation, the image reveals various pore regions, each regarded as an individual pore which can then be quantitatively analyzed for characteristics such as size, shape, and distribution.

Initially, the binary images of the chip were segmented using watershed techniques to create approximately 2200 closed contours. Subsequently, each pore was analyzed using circle-fitting methods to determine the equivalent circular diameters. This step was implemented through MATLAB algorithms, and the distribution of pore diameters was statistically analyzed. As shown in **Figure III-4**, the pore sizes on the surface typically range from several micrometers to over 600 µm. This distribution is approximately normal, with an average size of 200 µm, albeit skewed towards larger sizes due to the presence of several larger pores.

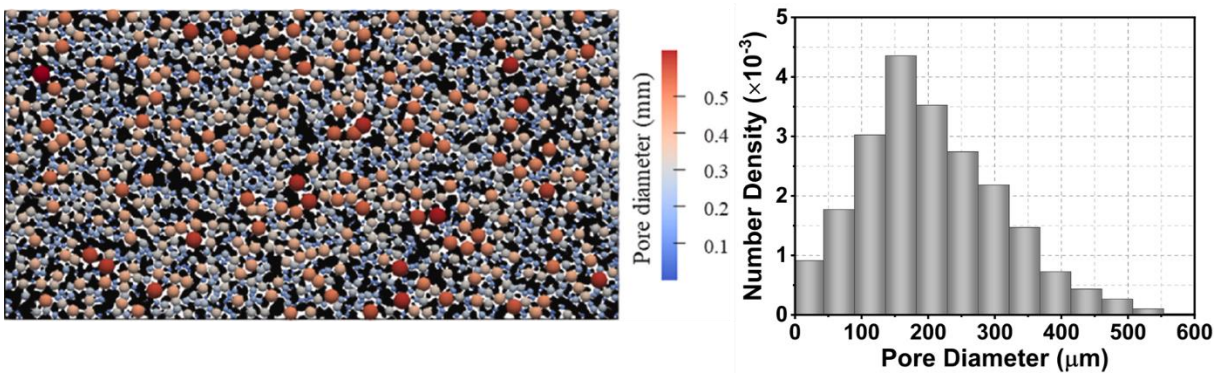

Figure III-4 *The diagram of random chip filled with circle fittings (left) and the distinguished data of pore diameter (right)*

III.1.2.2 Porous Medium Characterization

Before starting the flood experiments, the parameters of the chips such as porosity and pore volume (PV) were measured. Specifically, the pore volume and porosity of both microfluidic chips were determined using two methods: an indirect approach based on image analysis and a direct method involving optical volume calculations and permeability, was determined after saturating the chip with water and varying injection rates, and measuring the corresponding steady state pressure gradients.

For the image analysis method, pure water was injected into the chip, while paying attention to avoid the presence of any air bubble inside. When the chip was fully saturated with water, the image analysis methodology was used to obtain a binarized image where pores were depicted as white and grains as black or vice versa (as shown in **Figure III-6**). By determining through a threshold level for the pore surface and knowing the total surface, the surficial porosity of the chip can be calculated. Generally, for a 2D chip, the relationship between surficial porosity and effective porosity ϕ can be described as $\phi = V_{pore}/V_{total} \approx S_{pore}/S_{total}$.

Due to the uniformity of etching depth, the value of surficial porosity is equal to the effective porosity. However, the chip we used underwent smoothing at the corners of the pores, where a curved surface with a radius equal to the etching depth (20 μm) replaced the right-angled wall to improve experimental precision, as shown in **Figure III-5**. Therefore, there is a slight difference between the values of surficial porosity and effective porosity.

Figure III-5 *The diagram of local chip cross-section. The black part is solid, and the white part is pores.*

With reference to the provided geometric parameters of the porous medium, the total volume of the porous medium section amounts to 20 × 10 × 0.02 mm^3, which is equivalent to 4 μL. Compared with the total size, the depth of the chip is very small, the rounding of pore walls hence has a negligible impact, as confirmed by direct optical measurement results (below). Therefore, in this work, the porosity

value we used is obtained through the calculation of surficial porosity, given its consistency. Multiplying the total volume by the porosity yields the pore volume.

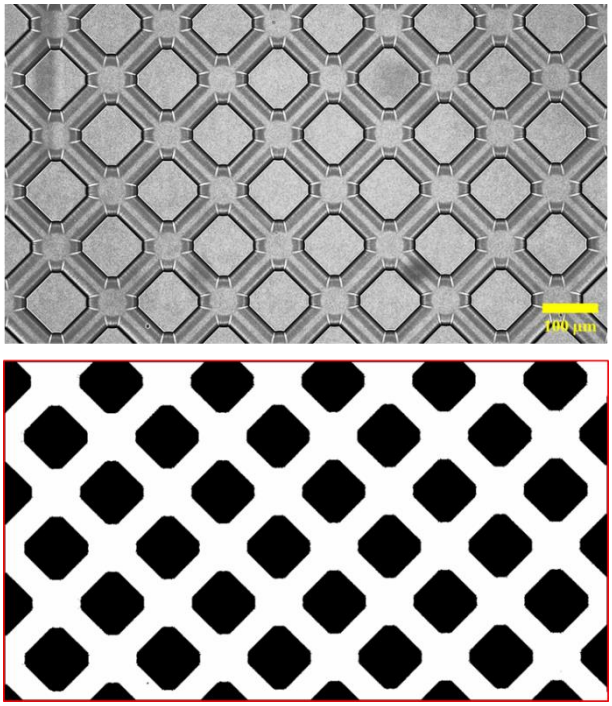

Figure III-6 *The local images of the regular chip captured by the microscope (top) and their corresponding binary images after processing (bottom). In bottom images, the black regions represent grains, while the white areas depict the pores, encompassing both the pore bodies and pore throats.*

The direct optical method involved recording the time taken for a stable fluid front to fill the porous medium under a given flow rates. At a Q of 0.5 µL/min, the fluid required roughly 290 s to flood the porous medium entirely and steadily. Multiplying the Q by the time yielded a pore volume. Consequently, porosity of the chip, calculated by dividing the pore volume by the total volume. However, it is essential to note that this method is not suitable for random chips, given the random distribution of pore positions and structures, which includes dead-end pores, posing challenges for complete pore saturation and affecting measurement accuracy.

III.1.2.3 Cleaning of the Porous Medium

The cleanliness of both the internal porous medium and the external surface of the chips are crucial. Specifically, internally cleaning the chips ensures undisturbed fluid dynamics, while the externally cleaned surface facilitates monitoring and proper storage.

Before first use, clean the internal chip with the HCl (10% mol/L) and NaOH (10% w/v) solutions under a pressure drop of 2 bar. Thereafter rinse the chip with deionized water several times with the same conditions to clean up any solutions that may be left. Subsequently, the absolute ethanol and deionized water were used to clean the chip surface next. Finally, nitrogen gas (N_2) was flushed to ensure a completely dry chip. It must be completely dry and dust-free before it is put to use for the experiments.

Post-experiment, the surfactant, ethanol, deionized water, NaOH, HCl and deionized water were utilized to clean the chips successively, to remove any remaining liquids in the porous medium. Moreover, in details, the volume of each cleaning fluid, excluding water, typically ranges between 5-8 mL, maintaining an optimal liquid pressure of 2 bar. Deionized water is extensively utilized, exceeding 10 mL at each stage, to cleanse residual ethanol and HCl. Surface cleaning remains consistent with previous procedures. Finally, N_2 is flushed at pressures exceeding 4 bar, recommended for a cleaning duration of 30-60 mins. Once thoroughly dry and free from dust, the chips are stored in a sealed bag or container to prevent secondary contamination.

III.1.3 Experimental Set-up

The experimental set-up of laboratory microfluidic system used in this work is displayed on Figure III-7. It comprises the following devices:

(1) The microfluidic chip that is securely held by a chip holder.
(2) A pressure pump system is used for precise control of fluid flow.
(3) Complement by an intelligent flow unit for real-time measurements of flow rate and pressure drop within the porous medium.
(4) The microscope is employed to observe fluid dynamics and display images or videos of the fluids within the microfluidic chip on the computer.
(5) A computer equipped with software for image capture and data recording facilitates the monitoring and display of images, pressure drop, and flow rate.

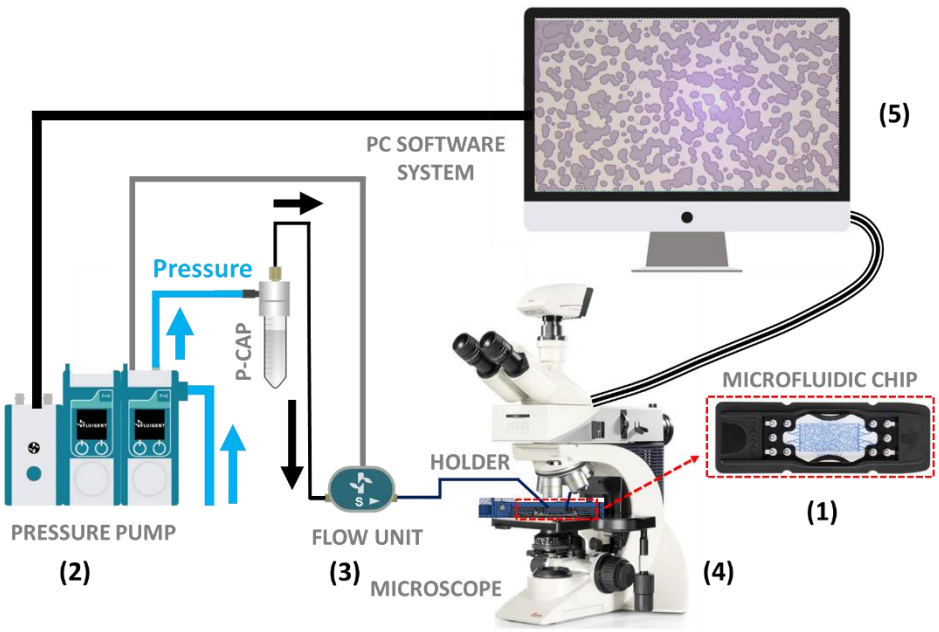

Figure III-7 Diagram of the experiment set-up

III.1.3.1 Pressure Pump System

Presentation

The pressure pump system, provided by FLUIGENT, primarily includes a pressure system controlled through the Microfluidic Software Control (LINK UP™) (the left of Figure III-7 (2)) and the Microfluidic flow controller (FLOW EZ™) (the middle and right of Figure III-7 (2)), and a smart microfluidic flow control sensor (FLOW UNIT, S-type). The FLOW EZ™ is linked to the FLOW UNIT so that we can monitor and control either the pressure drop (0-2000 mbar) or the flow rate (0-8 µL/min). Simultaneously, the real-time flow rate and pressure are displayed graphically and recorded on the computer via LINK UP™. Furthermore, it offers the convenience of using standard lab vials (15 mL Falcon) equipped with air-tight tube metal caps (P-CAP series) for filling purposes. The gas source, after passing through the pump, enters the sealed lab vials under specific pressure, propelling the fluid within the lab vials into the microtube and then is chip. This process is monitored and controlled effectively by the interlinked FLOW UNIT, regulating the flow rate, and further providing feedback to the FLOW EZ™ and PC system for display and recording.

Cleaning

The components of the pressure pump system, including tubes, connectors, P-CAP airtight vials, and the FLOW UNIT, must be thoroughly cleaned before starting an experiment also. After completing an experiment, we first remove any remaining liquid from the P-CAP, involving cleaning of both the inner and the outer surface of the airtight vials using cleaning agents and multiple rinses with deionized water. The connectors between components undergoes also the same cleaning process. The procedure for connecting the airtight vials and tubes involves the use of ethanol to eliminate any remaining solution, followed by thorough rinsing with deionized water, repeated twice. Subsequently, the cleaned components undergo an additional rinse with deionized water.

The P-CAP is then connected to the FLOW UNIT using the cleaned tubes and connectors, and a deionized water rinse is conducted within the FLOW UNIT at its maximum pressure range (2000 mbar). This step primarily targets the removal of any accumulated dyes within the FLOW UNIT. Since the experimental process involves introducing oil and aqueous phases into the system through the tubing connecting the FLOW UNIT and chip, this comprehensive cleaning protocol effectively ensures the absence of introduced impurities within the FLOW UNIT. The high level of cleanliness achieved is solely maintained through the use of filtered deionized water.

III.1.3.2 Microscope System

The microscope is the Leica DM2700 M, which, in conjunction with lab PC system software, enables real-time observation and recording of the states of the different phases within the chip, whether in the form of HD images or videos. The microscope comprises several components, primarily including

Objectives, Eyepieces, Digital cameras, LED light, Stage control, and Focus, as shown in **Figure III-8**. The Objectives consist of five sets: HC PLAN 1.25×/22, 2.5×/22, 5×/22, 10×/22, and 20×/22, allowing observation of phenomena within porous media at different scale. The Eyepieces are HC PLAN 10×/22. The digital cameras enable high-definition imaging of fluid flow details within porous media. These images are visualized on the computer screen using system software and facilitate the recording of images or videos. The LED light serves as the illumination source for visual field imaging. The microfluidic holder was placed on the stage. Adjusting the Focus and Stage control, the chip was moved to the center of the field of view for observations. The stage stroke is 25 mm, indicating the maximum distance the stage can move along its axis. Additionally, the imaging software within the system allows for the free modification of image parameters, such as contrast and RGB values. The obtained images can be used individually or stitched together to conduct dynamic and mechanistic analyses.

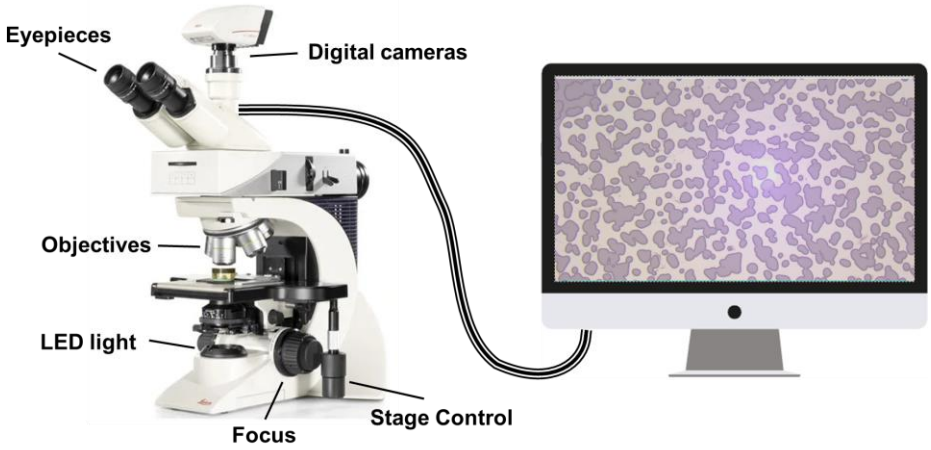

Figure III-8 *The diagram and main components of the Leica DM 2700 microscope*

III.1.3.3 Microfluidic Chip and Holder

The microfluidic chip necessitates secure fixation using a chip holder, serving to both shield against leakage and simplify the experimental procedure for interfacing the chip with other components. Liquid injection follows the directional arrow (red) indicated on the chip holder, as depicted in Figure III-9, where injection occurs from left to right. For sealing connections between different components and tubing, connection kits sourced from Micronit, along with microtubes, are employed.

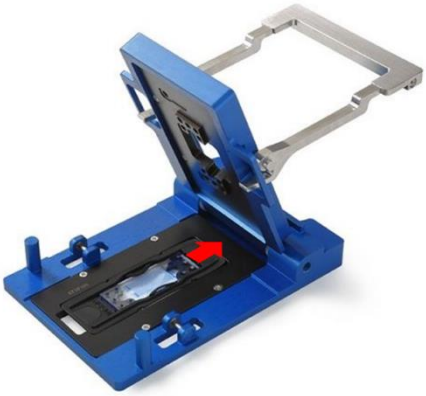

Figure III-9 The microfluidic holder and the chip be placed

III.1.3.4 Software System on the Lab PC

The Lab PC, linked to the pressure pump and microscope systems, enhances the observation and recording of fluid dynamics and displacement mechanisms. It also displays and records the pressure drop and flow rate during the injection process. This integration of components forms a robust and versatile system for conducting microfluidic experiments.

III.1.4 Typical Experimental Protocol

The typical experiment in our work consists of three steps: oil drainage, waterflooding imbibition, and a tertiary step. In the following, we introduce the protocol for each of them.

III.1.4.1 Oil Drainage

Oil was introduced into a chip fully saturated with water (the wetting phase) at a low flow rate (Q), starting from 0.1 µL/min. During this procedure, the progression of oil saturation and displacement dynamics, such as the stability of the fluid front, were closely monitored and analyzed using image analysis. This involved capturing detailed phase information within the chip at various total injection volume intervals (N PV), immediately following the injection of a specified equivalent volume (dN PV) of the non-wetting phase (oil).

In our microfluidic system, this acquire process took approximately 4 mins, necessitating a temporary halt in oil injection to obtain images corresponding to each volume of injection. Due to the significant changes in oil saturation with increasing injection volumes, images were acquired at smaller intervals of dN (0.2PV) until to N up to 1 PV to monitor the initial breakthrough flow behavior of oil. Each set of images was stored in a separate folder for ease of subsequent image processing.

As the experiment progressed and the variation in saturation with increased injection volumes became less pronounced, the intervals for capturing images were adjusted to reduce experimental complexity. Specifically, for injection volumes of N between 1 to 2 PV, dN was set to 0.25 PV; for volumes of N between 2 and 3 PV, dN was increased to 0.5 PV; and beyond this, up to the final total of 6 PV, the

interval dN was standardized to 1 PV (refer to **Figure III-10** for details on the 0.1 µL/min step). Concurrently, all flow rates and corresponding pressure drops (ΔP) were recorded and documented.

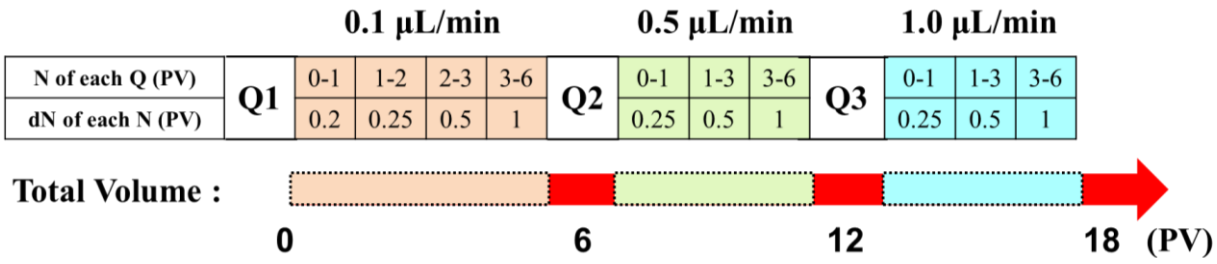

Figure III-10 *The total volume injected and image acquisition intervals at different flow rates during the drainage*

When the volume of oil injected reached 6 PV, both the ΔP and the water saturation (S_w) stabilized, indicating a plateau in the dynamics of the system. To further explore the impact of Ca, which increases with the Q, on the distribution and saturation of the remaining water phase, the flow rates were sequentially increased to 0.5 µL/min and then to 1.0 µL/min. As with the initial experiments at a Q of 0.1 µL/min, the intervals of injection volume (dN) were adjusted according to the flow rates for these new conditions.

The adjustments made to dN at flow rates of 0.5 and 1.0 µL/min mirrored each other. For injection volumes (N) less than 1 PV, dN was set at 0.25 PV; for N between 1 and 3 PV, dN was increased to 0.5 PV; and beyond this, until to 6 PV, dN was maintained at 1 PV, as detailed in **Figure III-10**. It is important to note that the choice of 6 PV as the injection volume under each Q was based on literature reports and preliminary experimental results, which will be discussed in the following section. We hypothesize that an injection volume of 6 PV reaches the irreducible water saturation (S_{wi}), although achieving an absolute S_{wi} is challenging and typically requires extensive PV injections.

When the total injection volume reached 18 PV, the S_{wi} was attained. At this point, by reducing the injection rate from 1 µL/min back to 0 µL/min and measuring the corresponding steady-state ΔP, the permeability of the oil phase at S_{wi} ($K_o(S_{wi})$) could be calculated using Darcy's Law. This methodical change in flow rates only occurred once ΔP had reached a steady state at each respective Q.

III.1.4.2 Waterflooding Imbibition

During the waterflooding imbibition step, we start by injecting brine at a low flow rate of 0.1 µL/min that correspond to usual sweep velocity in EOR waterflooding. The observation and analysis focused then on pores invasion and the dynamics of the gradual saturation of the porous medium by brine, while simultaneously recording the pressure drop. The brine rapidly saturated the pores along the wall, with a thin of flow path and an early breakthrough due to its lower viscosity compared to that of oil. To closely monitor fluid dynamics, we acquired images within the chip at every 0.1 PV of injected brine during the N less than 1 PV. However, due to the faster breakthrough (~ 0.2 PV), to better observe the displacement behaviour, the image acquires as dN with 0.05 PV before the breakthrough occurred. Afterwards, the N

and dN set as we reported previous drainage, dN was 0.25 PV for N from 1 to 2 PV; 0.5 PV for N between 2 and 3 PV; and 1 PV for the last 3 PV injected, as illustrated in **Figure III-11**. The flow behaviour at pore scale as well as spatial and tempered fluids saturation were hence followed.

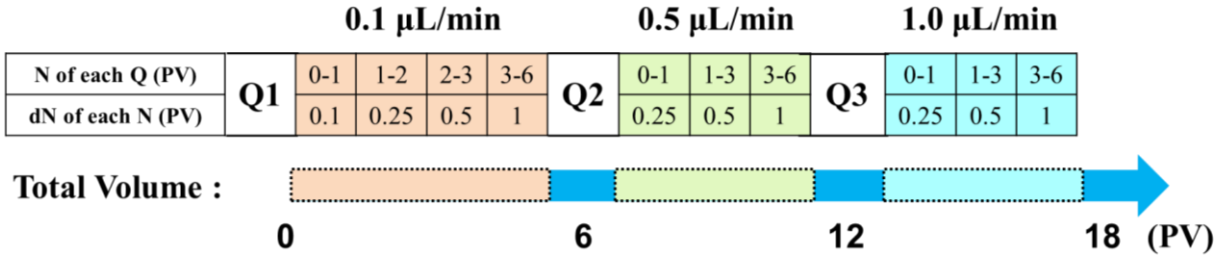

Figure III-11 *The total injected volume and intervals for image acquisition at different flow rates during the waterflooding imbibition*

After this waterflooding period at 0.1 µL/min was over at injected 6 PV of brine, a steady state was reached, the flow rate was increased to 0.5 and 1.0 µL/min to explore the influence of Ca (by flow rates) on the residual oil saturation and distribution. The image acquisition intervals for both flow rates were identical to the drainage, as detailed in **Figure III-11**, ultimately reaching residual oil saturation (S_{or}). Indeed, the S_{or} is also presumed to be a state of equilibrium, inferred from the stabilization of ΔP at a plateau and the observation that no significant movement of the oil phase occurs within the chip. In an ideal scenario, achieving a truly complete S_{or} would require the injection of an infinite volume of brine. However, in practical laboratory settings, we establish that injecting 6 PV of brine achieves a relatively stable state, as determined by preliminary results from waterflooding experiments. This experimental approach aims to replicate the dynamic equilibrium condition by ensuring that after 6 PV of brine injection, both the pressure and oil movement indicate that no further significant oil displacement is expected.

Moreover, the permeability of brine at S_{or} ($K_w(S_{or})$) state were measured. We gradually reduced the Q from 1 to 0 µL/min and recorded the corresponding ΔP to calculate it by Darcy's law. Each change of flow rates occurred again after reaching a stable plateau in ΔP.

III.1.4.3 Tertiary Step

After the waterflooding period, we move to the tertiary step, where aqueous mixtures of given viscosities were injected. During this step, we adopt the same procedure as that presented in previous paragraph to investigate the influence of Ca by M on the residual oil clusters size and distribution. Therefore, the Q was fixed here at 1 µL/min also, only increasing the viscosity of injected fluids with different M. Following the results of waterflooding, five independent experiments were performed with different aqueous glycerol mixtures as we presented at Section III.1.1. This means that the drainage and waterflooding steps are the same and the only tertiary step is different for the independent experiments with five M.

During tertiary experiments, the intervals for image acquisition were similar to these used in waterflooding imbibition during the first 6 PV injected. However, for the subsequent N of 6 to 12 PV, the dN was extended to 2 PV; and for 12 to 18 PV, dN was further increased to 3 PV, as illustrated in **Figure III-12**. The variations in ΔP and Q for the five sets of experiments were recorded continuously. The image acquisition and analysis procedures remained identical to the aforementioned process.

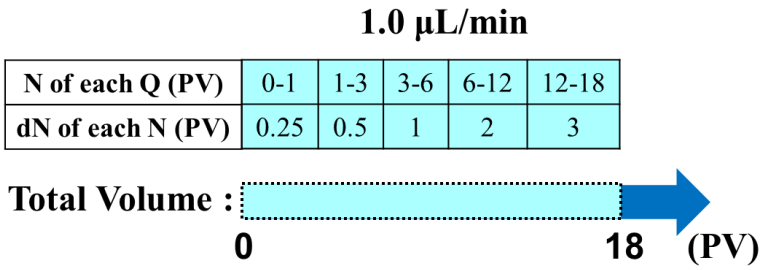

Figure III-12 The total injected volume and intervals for image acquisition during the tertiary step

III.1.4.4 Validation of the methodology

The method presented were above reveals that capturing images from different regions successfully provides a whole chip image, suitable for subsequent image analysis. It's worth noting that stitching the whole chip requires capturing 12 to 14 independent images, taking approximately 4 mins. However, this process brings about two challenges: potential disruption in fluid dynamics and displacement continuity during image capture, and probable fluctuations in flow rates due to stage movement. Consequently, stopping the pump during image capture to obtain detailed images from various areas becomes essential. This arise a fundamental question: does interrupting of fluid injection for images capture significantly influence the obtained results and corollary; what should be the maximum of the stopping term laps time to ensure a permanent live state? This section aims to address this critical inquiry through validation.

To that end, we performed a comparison of ΔP under two scenarios: continuous injection (constant flow rate Q) and start-and-stop injection for various stopping time (named "interval Q"). To begain, experiments were carried out at a constant Q of 0.5 µL/min for both drainage and imbibition. A sufficient volume of displacing fluid (22 PV) was injected, and corresponding time variation of ΔP was recorded. Subsequently, similar controlled experiments were performed except that flow rate was regularly stopped to acquire whole chip image information. In the experimental setup where the Q is paused to acquire images, as demonstrated by the red lines in **Figure III-13**, these vertical lines during both drainage and waterflooding phases are equivalent to the moments of image acquisition. These red vertical lines represent moments in the experiment where there is no incremental injection volume (PV).

By comparing the changes in ΔP during the drainage and imbibition between the two sets of experiments, it is clear that no significant impact is observed and curves are similar in shape. During drainage, the ΔP rapidly increases with the injection volume, then increases slowly after breakthrough, ultimately reaching a stable plateau (**Figure III-13** left). However, a slight difference in the ΔP of approximately

20 mbar is observed. During waterflooding imbibition (**Figure III-13** right), the ΔP increases rapidly before breakthrough followed by a rapidly decrease and gradually stabilize for higher injected volumes. This suggests that the influence of our methodology on ΔP is minimal, and this difference can be disregarded for both steps. Moreover, the final saturation of fluids on both methods was similar.

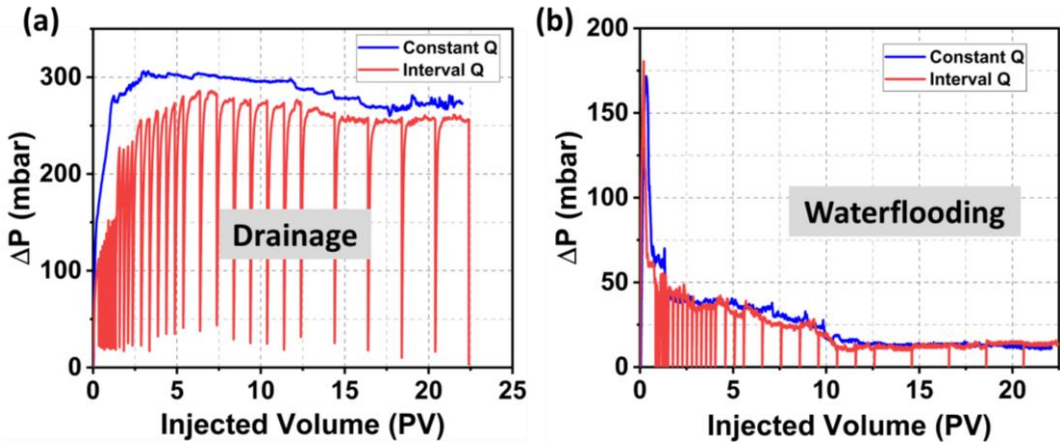

Figure III-13 *The curve of pressure drops within the porous medium against the pore volume injected during the drainage (left) and imbibition (right) for both constant Q and interval Q experiments. It's worth noting that the vertical red lines in the interval Q case represent invalid data points obtained during image acquisition.*

Therefore, the experimental methodology proposed in this work is feasible, although minor errors may be present. Nevertheless, the images acquired using this method can accurately reflect the saturation and distribution of different phases within the chip at various injection volumes. This approach provides valuable insights into flow behavior and displacement mechanisms, serving as a robust basis for analyzing the dynamic interactions between the non-wetting and wetting phases.

III.1.5 Experimental Image and Data Analysis

In this section, we primarily present the image processing techniques used for data analysis, providing specific details through a flowchart.

III.1.5.1 Image Acquisition and Pre-processing

The assessment of displacement mechanisms and fluid dynamics in microfluidic experiments relies on optical images capturing fluid phases within the porous medium. However, the microscope-PC system in the experimental setup can only observe and record limited areas because the size of observation area is inversely proportional to the microscope magnification. Consequently, it is essential to manage the microscope "Stage" to capture image data from different regions of the chip.

Specifically, this process involves adjusting the "Focus" and "Stage Control" to place one side of the chip at the center of the field of view. Subsequently, we move the "Stage" along the axis to capture all image data on this side (as shown in **Figure III-14**, where 1 and 2 represent the image numbers of two adjacent fields of view on the left side). It is worth noting that each image should overlap with a portion

of the adjacent image (about one-fourth), as indicated by the red dashed box between 1 and 2 in **Figure III-14**, since the algorithm for the automatic stitching process requires a certain reference, such as the position and size of grains/pores, to reduce small errors caused by "Stage" movement during the experimental operation, ensuring the accuracy of the stitching. Following this, the "Stage Control" operates to capture image data from the region on the other side of the chip (as shown in **Figure III-14**, where 3 and 4 represent the image numbers of two adjacent fields of view on the right side, and the red dashed box indicates the overlapping region). The images on the right side of **Figure III-14** show the results of the stitching process for images 1 and 2, and 3 and 4, respectively named "Left 1-2" and "Right 3-4". It can be observed that the red dashed box regions overlap completely after stitching.

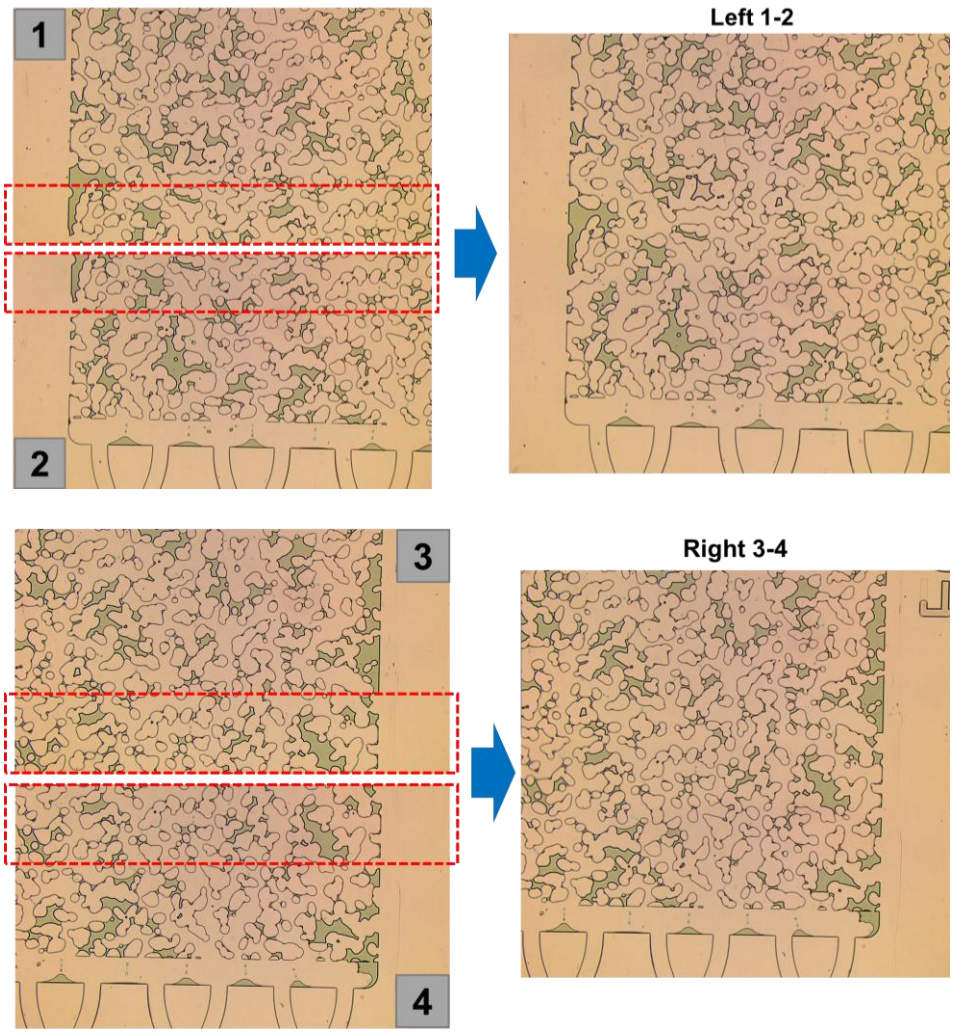

Figure III-14 *The partial images captured by the microscope-PC system (left; images of 1, 2, 3, 4) and the stitched images with overlapping regions merged (right; images of Left 1-2, Right 3-4).Images 1 and 2 correspond to partial captures when the left side of the chip was in the field of view, while images 3 and 4 pertain to the right side. The red dashed-line boxes indicate the overlapping sections obtained when manually moving the "Stage" along its axis.*

Meanwhile, similar to the principle mentioned above, there should also be an overlapping region when moving the chip to the left and right sides, as demonstrated by the black dashed box in **Figure III-15**. At the bottom of **Figure III-15**, we provide an example of the stitching results for the partial images obtained in **Figure III-14** on the left and right sides, showing the complete stitching of the overlapping part between "Left 1-2" and "Right 3-4". Next, we will detail the specific steps of the image stitching process.

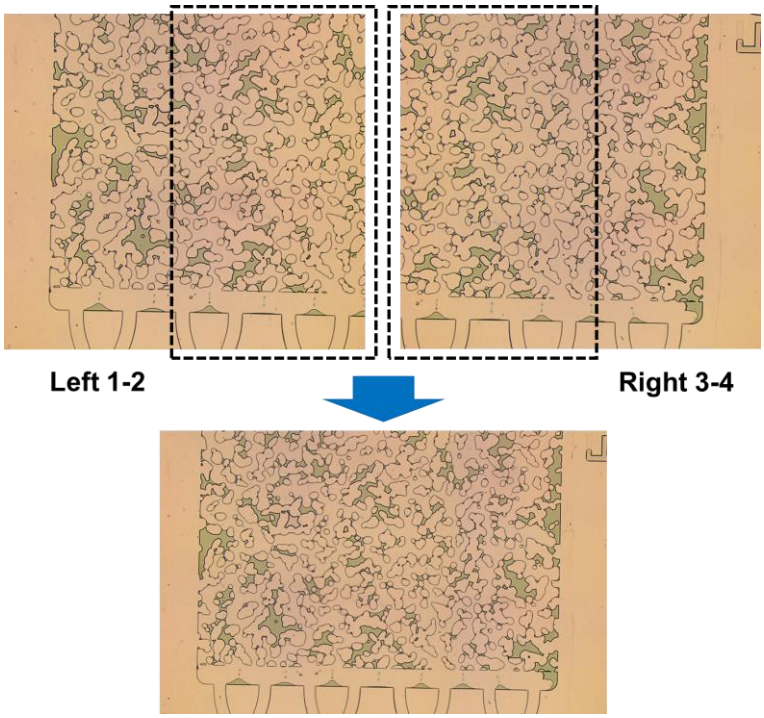

Figure III-15 *The stitched image with the overlapping regions merged (top; Left 1-2, Right 3-4) of obtained from* ***Figure III-14*** *and the image further merged with the overlapping regions from the left and right sides (bottom). The black dashed-line boxes indicate the overlapping sections obtained when manually moving the "Stage Control".*

Each acquisition point captures a series of images, necessitating image stitching and compilation to gather whole chip data. ImageJ software was used for image stitching, since it can recognize information within the images, such as the structure and position of pores and grains. In this work, we used two stitching methods: 1) manual stitching method, applicable to both types of chips; and 2) automated stitching method, exclusively suitable for random chip.

1) Manual stitching method: In this work, we first stitch all the images on the left and right sides separately, obtaining independent "Left images" and "Right images", and then combine them in the final stitching process. Therefore, we first opened adjacent left or right images and used the rectangular tool in ImageJ to select the overlapping region (an approximation, not requiring perfect alignment), as discussed above and shown by the black dashed box in **Figure III-14** and the red dashed box in **Figure III-15**. Subsequently, the "Pairwise stitching" function (black dashed box in the step 2 of **Figure III-16**)

was used to create stitched images, and this process was repeated for each subsequent image until all images on one side were stitched. After performing the same process on the other side, the complete images from both sides were stitched together, and results were shown in **Figure III-17**. It is worth noting that we added a layer of transparent letters "mark" around the regular chip (the bottom image of **Figure III-17**) to facilitate software recognition of image positions and information, preventing complete overlap of the uniform pore structure. No such modifications were made for the random chip.

2) Automated stitching method: Due to the random distribution of grains and pores, ImageJ software can recognize information in random chip images, allowing for automated stitching of the whole chip. Specifically, as shown in the step 3 of **Figure III-16**, selecting "Unknown Position" in the "Grid/Collection stitching" function as the "Stage" movement during image capture was not a fixed value. Subsequently, the folder containing all images and parameters were selected from the acquisition point (red dashed box in the step 4 of **Figure III-16**), and automated stitching was performed to generate the complete image, which is same with the image shown in **Figure III-17** (top). Conversely, for regular chips, this function could not effectively recognize the positions of uniformly distributed pore structures, even with markings. Therefore, manual stitching was the only viable option.

The automated stitching method is faster and more convenient, so we used this method for random chip images, while manual stitching was employed for regular chip images.

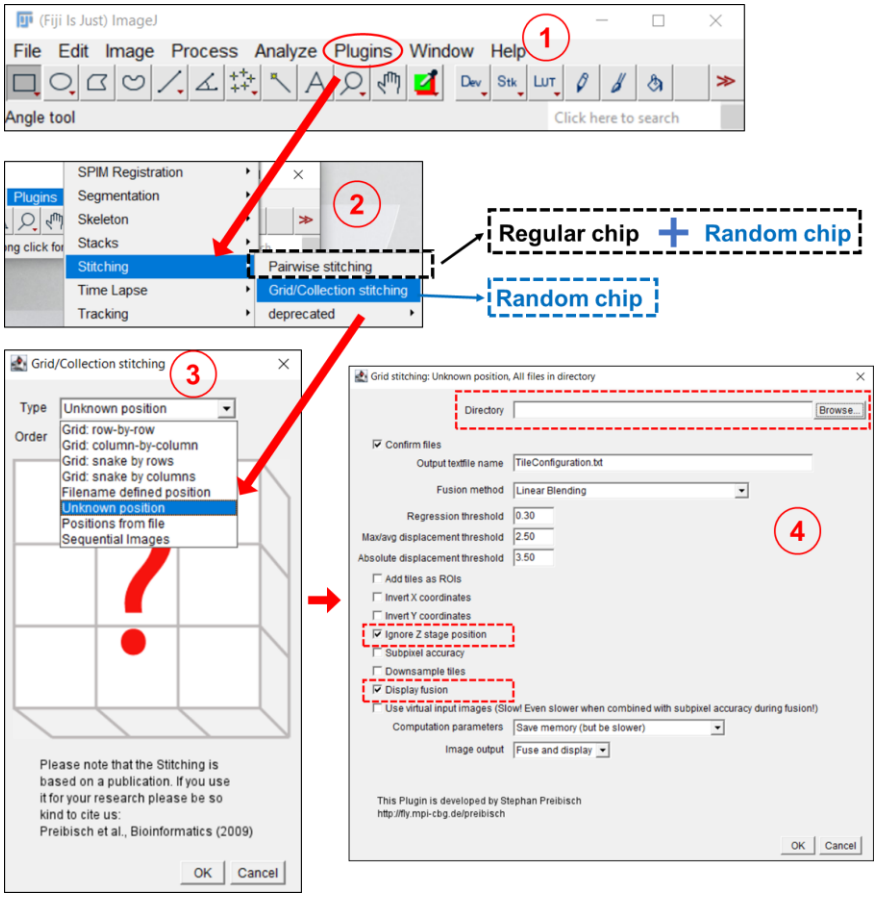

Figure III-16 *The diagram of image stitching process by ImageJ. In step 2, the "Pairwise stitching" was used for manual image stitching, applicable to both random and regular chip images; while "Grid/Collection stitching" was used for automated image stitching, only suitable for random chip images.*

Figure III-17 *The completed stitching of the random chip (top) and regular chip (bottom), both saturated with dyed water.*

The obtained image of the entire chip needs to undergo angle adjustments to align the edges horizontally and to crop out the non-porous medium areas, facilitating subsequent calculations from image data. The result is illustrated in Figure III-18.

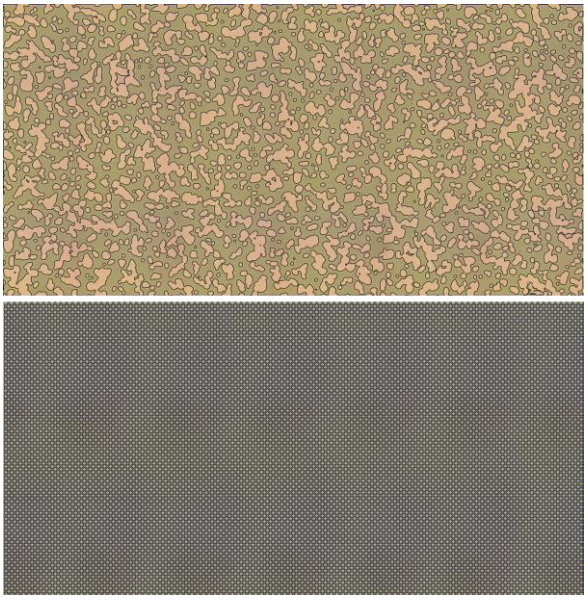

Figure III-18 The cropped and adjusted chip images of Figure III-17

III.1.5.2 Image Data Analysis

The stitched and cropped images provide a visual representation of the chip, showcasing microscale interface phenomena and spatial fluids saturation. However, for quantitative analysis, further image processing is necessary to highlight and analyze the saturation and distribution details of all fluid phases within the chip.

Binarization methods

The key to image processing lies in binarization, wherein an image is converted into a binary image containing only two grayscale levels (typically black and white). This not only helps highlight specific targets in the image but also facilitates image calculations. Applying the image pre-processing methods from the above section, we obtain an image of fully saturated air for the random chip, analogous to that at the top of Figure III-18. Subsequently, the "Stack Splitter" is used to split it into three channels (red, green, blue) for ease of subsequent image calculations and to expedite the image processing speed. For images representing the saturation of immiscible two-phase flow, it is essential to select the one that retains the most comprehensive original image information. Here, we take the image of saturated air as an example, and thus, the three cases are indistinguishable (using the green channel as an example in **Figure III-19**).

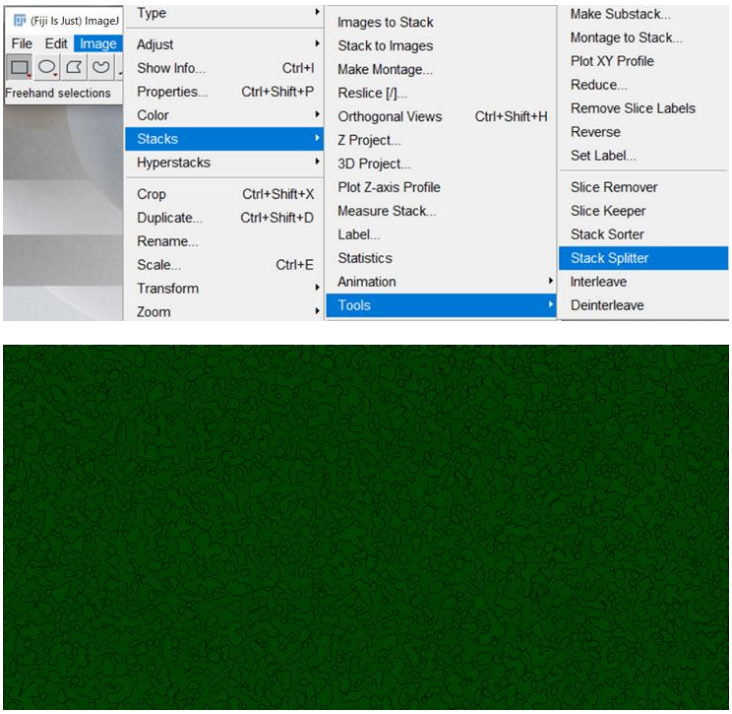

Figure III-19 The process of image split and the representation of the results

Then, adjust the grayscale range of binarization in the "Threshold" (red dashed box) to select the grain area (**Figure III-20**). It is worth noting that the termination value (bottom) should be chosen as the

minimum value under the condition that it is continuous with the boundary line of the grains (red solid line). This helps reduce optical grayscale value errors.

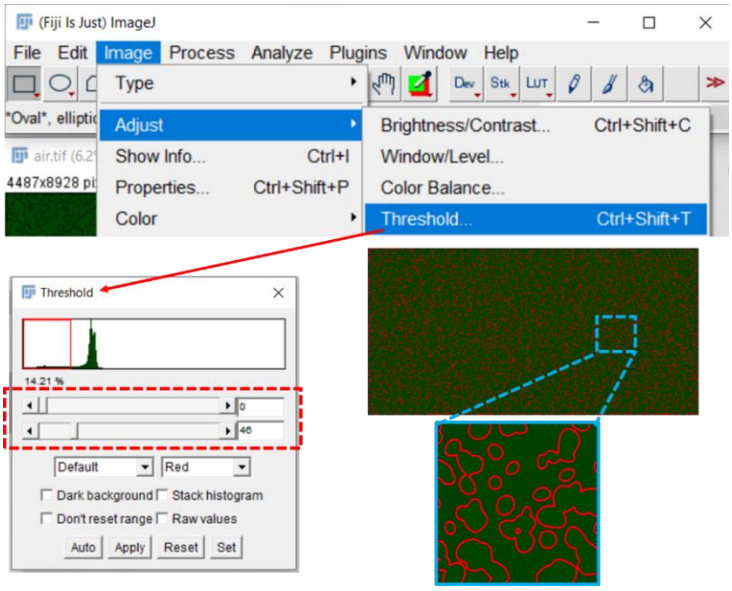

Figure III-20 *Adjust the grayscale values in "Threshold" to select the grain area.*

Afterward, in "Analyze Particles", apply "Masks" processing to the thresholded area, obtaining the binary image of saturated air "Air image" (**Figure III-21**), which will be used for subsequent image analysis.

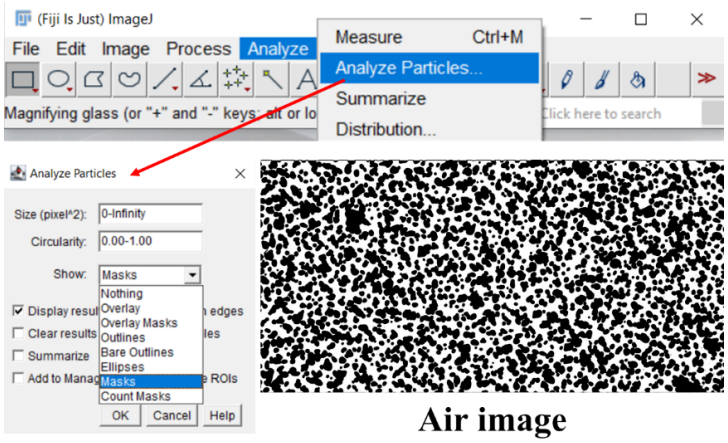

Figure III-21 *Apply Masks to the grains region to obtain a binary image "Air image".*

The images of saturation with different stages of immiscible two-phase flow are also subjected to binary processing before subsequent image analysis. The difference lies in the "Threshold" selection, which includes both the grains region and the regions saturated with aqueous mixture.

Image analysis of saturated with two phase fluids

The specific process, illustrated in **Figure III-22** taking the random chip as an example, starts by preparing reference images of "Water image" and "Air image". The "Water image" was obtained by

splitting the image that fully saturated water, analogous to that at the top of Figure III-18 by using the "Stack Splitter". Here, we use the image in the brine imbibition before breakthrough as an example. During the image analysis process, initially, in the Image Calculator, the "Whole image" is subtracted by the "Water image" to obtain the "Image 1", and then the "Air image" is minimized. Subsequently, "Threshold" is used to binary select the oil phase area from the Whole image after these operations, generating "Image 2."

Next, the "Remove Outliers" function is applied to eliminate some optical noise points (**Figure III-23**) within "Image 2," resulting in "Image 3," which better represents the information in the Whole image. Utilizing the Image Expression Parser, subtracting half of the "Air image" from "Image 3" yields different grayscale values for the oil phase, aqueous phase, and grains. This step facilitates the quantitative analysis. To enhance the image's visibility, different grayscale colors can be chosen or customized in the Lookup Tables. The final "Color image" presents the oil phase in red, the water phase in blue, and the grains in black.

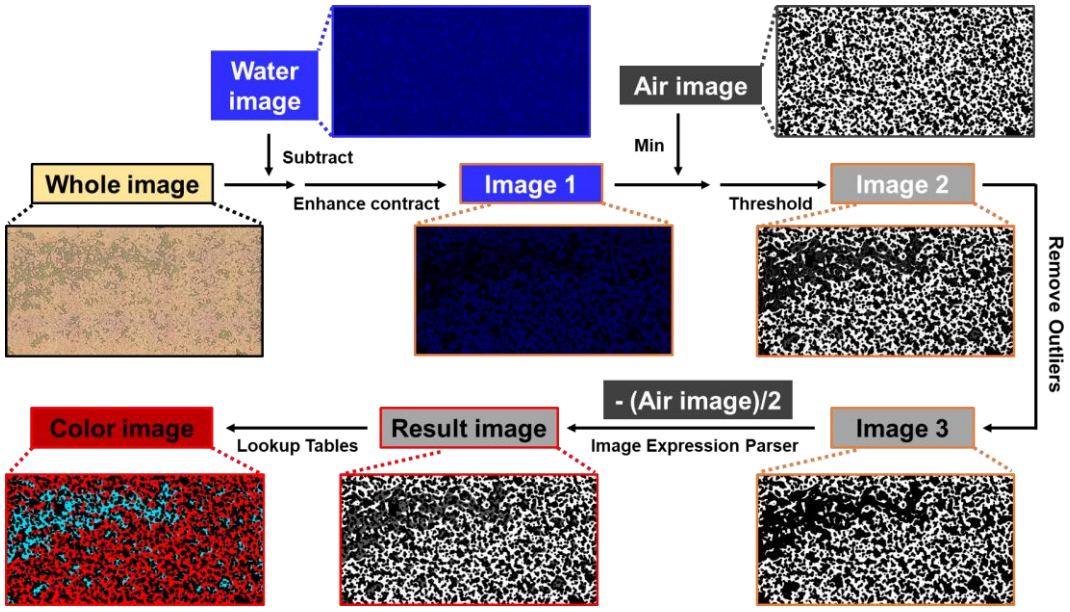

Figure III-22 *The diagram of the image analysis process by ImageJ*

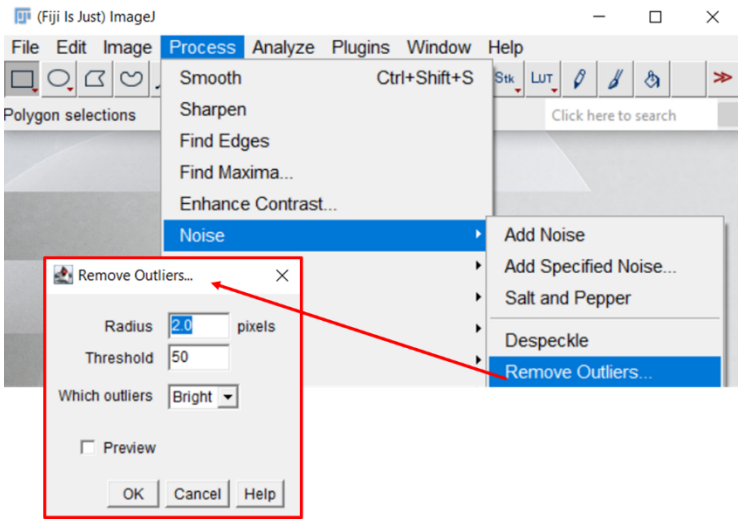

Figure III-23 Reducing optical noise illustration.

The Definition and Differentiation of Oil Clusters

In drainage, waterflooding, and tertiary step mixture flooding, images are acquired after different volumes of injection (dN) to explore the distribution of phases within the chip. After obtaining the "Color image," adjustments can be made in the “Threshold” settings to select the phases needed for analysis. For example, in drainage, we tracked and analyzed the saturation and distribution of remaining water, noting its tendency to be trapped in smaller pores and to form a water film on the surface of solid grains. During waterflooding and mixture flooding, the focus shifted primarily to the saturation, size, and distribution of oil clusters.

The calculation of residual oil saturation is straightforward, similar to that in drainage, and can be performed using the “Threshold” function. Of particular interest at the pore scale are the size and distribution of oil clusters, and how these change with the Ca. As discussed in Section III.1.1, we initially analyzed the original pore size diameter distribution and employed the same methodology to statistically assess the distribution of residual oil within these original pore sizes, aiding our understanding of oil trapping and mobilization mechanisms. The specific steps include: 1) Binary processing of the image analysis results, where the oil phase is one extreme, and the aqueous phase and solid grains are another; 2) Applying “watershed” segmentation to the oil phase and using circle-fitting methods to calculate the corresponding distribution of the original pore sizes.

Moreover, residual oil is influenced by geometric within the chip and distributed in various sizes and shapes, categorized into droplets, blobs, and ganglia:

Droplets are clusters smaller than the pore body; Blobs occupy one pores; Ganglia occupy multiple pores.

In ImageJ, the differentiation process in data analysis is shown, with the definition of these three types of clusters based on experimental results and literature references (Zarikos, et al., 2018) (Yang, et al., 2019). In the binarized image, the oil phase is selected, and in "Analysis Particles," the "Size" and "Circularity" settings are adjusted to filter different types of clusters (as shown in **Figure III-24**), displayed using Masks and Display results:

Droplets are defined as having a size of 0-0.002 mm² and circularity between 0.7-1; Blobs have a size range of 0.002-0.004 mm² and circularity from 0.3-1; Ganglia are larger than 0.004 mm² with circularity from 0-0.7.

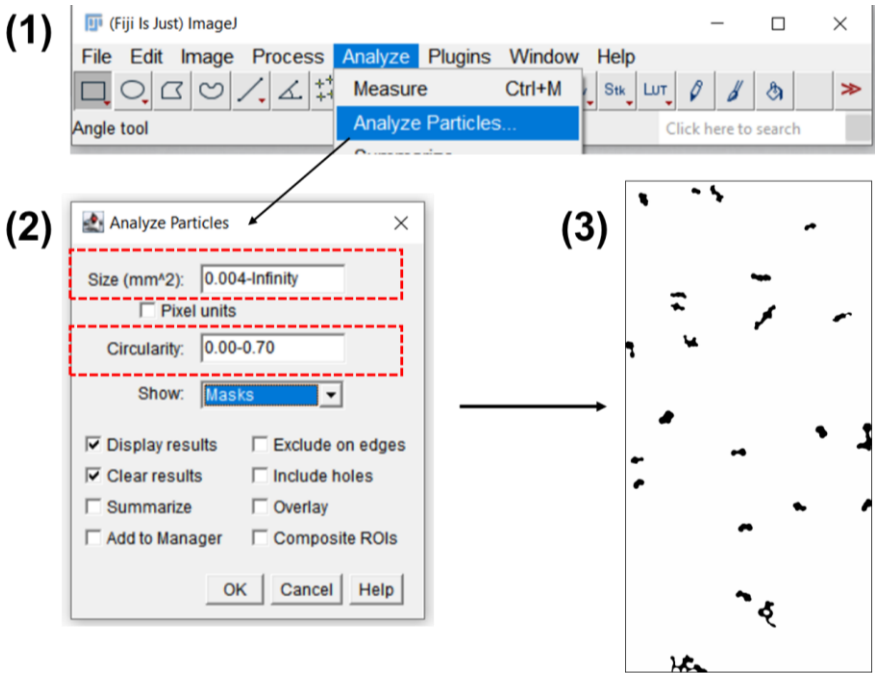

Figure III-24 In ImageJ, the process for differentiating clusters, here exemplified by ganglia

The differentiation process for ganglia during the steady state of mixture flooding at M=20 is showcased in **Figure III-24**. However, it is important to note that this setting might not perfectly categorize clusters, and manual adjustments might be needed based on the locations of clusters. For example, a blob in a small pore might be incorrectly categorized as a droplet due to its small size and high circularity, though such errors are rare and typically only occur in the definition of blobs.

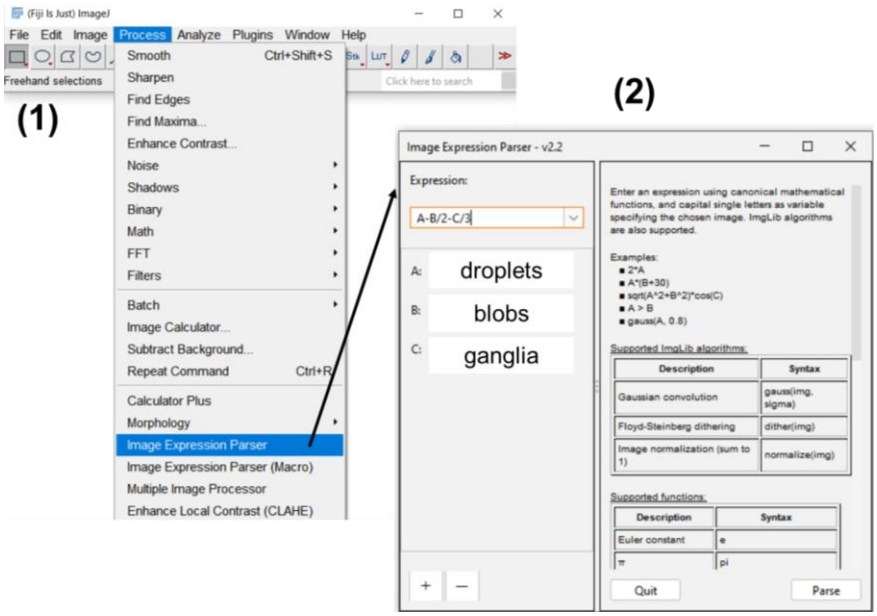

Figure III-25 The image analysis process for calculating characteristics of three types of clusters in ImageJ

Ultimately, three separate images containing only droplets, blobs, and ganglia can be obtained, and through image processing calculations as shown in the process and formulas in **Figure III-25**, these distinct clusters can be identified. In **Figure III-26**, we display images before and after processing from the mixture flooding steady state at M=20, clearly distinguishing the three types of clusters: black for droplets, red for blobs, and pink for ganglia. The number and volume of these clusters can also be easily obtained using our methodology in ImageJ.

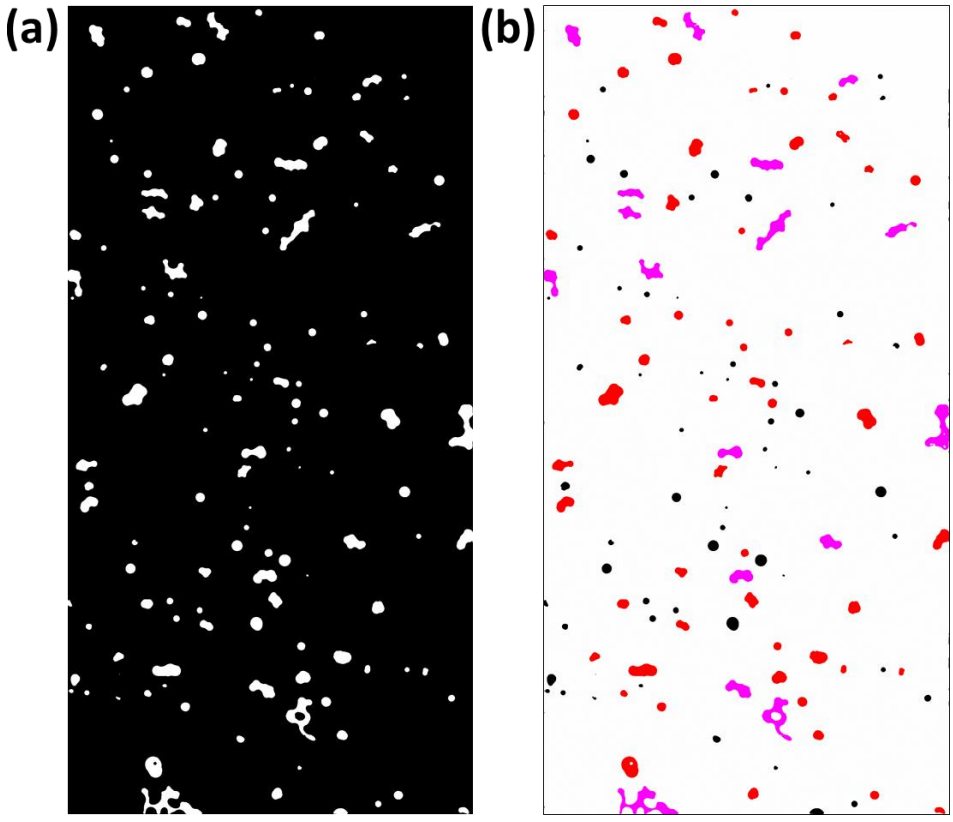

Figure III-26 *Image of clusters before processing (a) and after processing showing three easily distinguishable types of clusters (b). In the image (b), black represents droplets, red represents blobs, and pink represents ganglia.*

III.1.6 Planning of Experiment Parameters

All the aforementioned experiments were performed under water-wet conditions, using both random and regular porous structures in the chips. In subsequent research endeavours, replicating experiments using oil-wet conditions on both types of chips could be considered to explore the impact of altering the wettability of the porous medium on fluid dynamics and displacement mechanisms.

Furthermore, in the tertiary step, we investigated the influence of M on fluid dynamics and ultimate recovery using Newtonian fluids. The next phase could involve studying the effect of polymer-based (viscoelastic fluids) displacement, examining how polymer-based displacement affects the behaviour of fluids. Specifically, designing experiments under identical drainage and waterflooding conditions and maintaining the same Ca during the tertiary step would allow for an exploration of the impact and mechanisms of Newtonian fluids versus viscoelastic fluids injected sequentially into the porous medium.

III.2 *In-silico* Experiments – The Mathematical Model

Describing the fluid-fluid interface dynamics is crucial to model immiscible, incompressible two-phase flow due to the presence of surface tension which induces a pressure difference between the two fluids. To this aim we have coupled the Navier-Stokes and Cahn-Hilliard equations (NSCH) which are used in the PhD thesis to simulate the flow of biphasic fluids at the microscale under different conditions. The C-H equations address the diffusion problem of the interface, allowing for the tracking of interface positions and providing an evolution equation for the concentration field. Meanwhile, the N-S equation governs the overall fluid dynamic behaviour. This section introduces the mathematical model.

III.1.1 Advantages of the Adopted Phase-Field Approach

This work employs a phase-field approach coupled with the Navier-Stokes equations to simulate the flow of two immiscible and incompressible fluids (aqueous phase-oil system). The densities (ρ) and viscosities (η) of the aqueous and oil phases utilized in this study are constant, and, being the densities of the two phases close, they are assumed equal. In our model, the two-phase system forms a mixture, where each fluid phase consists of a distinct component due to their immiscibility. Hence, any point of the domain can be considered as composed of an aqueous phase (*a*-phase), an oil phase (*o*-phase) or a mixture if is we consider a point at the interface between the two phases. Traditionally, interfaces in two-phase flow numerical simulations have been described using a sharp-interface model, depicting a narrow region that separates the immiscible fluids as a discontinuity, resulting in discontinuities in physical quantities such as viscosity and pressure. Although grids can be employed to track the moving interface within this discontinuous surface, handling fluid interface evolution might lead to topological changes. Thus, formulating a proper generalized solution concept becomes intricate and challenging, especially in regions of high curvature where numerical convergence faces significant challenges.

To overcome these difficulties, we employ a diffuse-interface model based on the Cahn-Hilliard equations (phase-field approach). The interface is considered as a thin layer with finite thickness, where the oil and the aqueous solution diffuse, facilitating a smooth transition of viscosity, pressure, and fluid phases. Moreover, it's noteworthy that the diffuse-interface surrounding the contact line between a liquid-liquid interface and solid surface induces effective slip due to diffusive fluxes between bulk fluids, effectively mitigating stress singularities even when a no-slip velocity boundary condition is imposed in the model. This underscores the necessity to address the slip velocity with an appropriate boundary condition. In our approach the slip velocity comes out naturally and is intrinsically linked to a mobility parameter, akin to the local mass diffusion rate between the two fluid phases at the molecular scale on the interface. Further details regarding the mathematical model will be discussed in subsequent paragraphs.

III.1.2 Definition of the Multi-constituent System

In the proposed mathematical framework, the two-phase system is modeled as a mixture of an oil species, *o*, and an aqueous species, *a*, each one characterized by its own mass fraction. The two fluid species are intrinsically not miscible so the computational domain areas where the mass fraction of oil has the value 1 are those occupied by the oil phase, conversely areas where the mass fraction of oil is null are occupied by the aqueous phase. The zones where 0 < mass fraction of oil < 1 characterize the interface between the two phases. The model is developed within the frame of a Cahn-Hilliard-Navier-Stokes formulation which allows us to consider both effects related to capillarity and wettability. The proposed model is an extended version of the one previously developed in (Le Maout, et al., 2020) for modeling of confined growth of encapsulated cell aggregates. In this new version, the hypothesis of a negligible convective velocity of the mixture is released so the momentum conservation equation does not reduce to the hydro-static case. Consequently, the Cahn-Hilliard system of equations must be solved in a coupled fashion with Navier-Stokes equations.

If a properly representative elementary volume (REV) of mixture is defined, each point of the domain is characterized by a certain mass fraction of *o* and *a*, ω_o and ω_a respectively. Obviously the following constraint must be respected

$$\omega_o + \omega_a = 1 \qquad \text{Equation 3-1}$$

If we consider a point in the oil area the mass fraction of the oil species is the unity ($\omega_O = 1$) while in the aqueous phase area the mass fraction of the oil species is null ($\omega_O = 0$). At the interface between the two phases $0 < \omega_o < 1$ with the mass fraction which evolves smoothly between 0 and 1. Each point of the mixture is also characterized by a certain mixture velocity, **v**, defined as the weighted sum of species velocities

$$\mathbf{v} = \omega_o \mathbf{v}_o + \omega_a \mathbf{v}_a \qquad \text{Equation 3-2}$$

The deviations of species velocities with respect to mixture velocity are the diffusion velocities and read

$$\mathbf{u}_i = \mathbf{v}_i - \mathbf{v} \qquad i = o, a \qquad \text{Equation 3-3}$$

Combining equations (3-1 to 3-3) the following condition holds

$$\sum_i \omega_i \mathbf{u}_i = 0 \qquad \text{Equation 3-4}$$

III.1.3 Governing Equations

A species moves due to advective transport (related to mixture velocity **v**) and diffusive transport (related to its own diffusive velocity, $\mathbf{u}_i$). So the spatial form of the mass conservation equations of the oil species reads

$$\frac{\partial(\rho\omega_o)}{\partial t} + \nabla\cdot(\rho\omega_o\mathbf{v}) + \nabla\cdot(\rho\omega_o\mathbf{u}_o) - r_o = 0 \qquad \text{Equation 3-5}$$

where ρ is the mixture density and r_o is an exchange of mass to account for chemical reactions inducing mass transfer from other species of the mixture to *o* species. An analogous equation governs mass conservation of the aqueous species, *a*

$$\frac{\partial(\rho\omega_a)}{\partial t}+\nabla\cdot(\rho\omega_a\mathbf{v})+\nabla\cdot(\rho\omega_a\mathbf{u}_a)-r_a=0 \qquad \text{Equation 3-6}$$

Where, as in equation 3-5, r_a is a source or sink term to account for mass exchange between species. Mass created in one species has to come from other species due to mass conservation so having two species in our mixture the following constraint must be respected

$$r_o+r_a=0 \qquad \text{Equation 3-7}$$

Summing mass conservation equations of the two species of the mixture (*o* and *a*), and accounting for constraints equations (3-1), (3-4) and (3-7) give the mass conservation equation of the mixture as

$$\frac{\partial\rho}{\partial t}+\nabla\cdot(\rho\mathbf{v})=0 \qquad \text{Equation 3-8}$$

The mixture behavior has also to obey to its momentum conservation equation which reads

$$\rho\frac{\mathrm{D}\mathbf{v}}{\mathrm{D}t}=\nabla\cdot\mathbf{t}+\mathbf{b} \qquad \text{Equation 3-9}$$

where $\frac{\mathrm{D}\mathbf{v}}{\mathrm{D}t}=\frac{\partial\mathbf{v}}{\partial t}+(\mathbf{v}\cdot\nabla)\mathbf{v}$ is the total time derivative of the velocity vector, **b** is the volumetric force, and **t** is the stress tensor which reads $\mathbf{t}=-p\mathbf{1}+\mathbf{t}_\mu$ (p is the fluid pressure and $\mathbf{t}_\mu$ is the stress related to viscous forces).

Table III-2 *Summary of the model independent variables.*

Entity	index	Associated variables	Equivalent scalar variables
Oil species	*o*	ωo, $r o$, $\mathbf{u} o$, $\mathbf{v} o$	8
Aqueous species	*a*	ωa, $r a$, $\mathbf{u} a$, $\mathbf{v} a$	8
Mixture	—	ρ, p, $\mathbf{v}$, $\mathbf{t}_\mu$, $\mathbf{b}$	14
		Tot. number of scalar unknowns	30

III.1.4 Constitutive Equations

In the previous subparagraph the equivalent of 16 scalar independent equations have been presented:

- the scalar constraint on mass fractions (3-1);
- the definition of the mixture velocity vector (3-2) (corresponding to 3 scalar equations);
- the definition of the species diffusive velocities (3-3) (corresponding to 6 scalar equations);
- the scalar mass conservation equation of oil species (3-5);

- the scalar constraint on the reaction terms (3-7);
- the scalar mass conservation equation of the mixture (3-8);
- the momentum conservation equation of the mixture (3-9) (corresponding to 3 scalar equations);

Note that the mass conservation equation of the aqueous species (equation (3-6)) and the condition (3-4) are not included in the previous list, since these can be obtained combining the other equations.

The total number of independent variables is 30 (see **Table III-2**) so 14 scalar equations are needed for model closure. These 14 scalar equations correspond to 5 closure relationships:

The Newtonian rheological model (6 scalar equations). We assume that the oil, the aqueous solution and their mixture behave as a Newtonian fluid so the following constitutive relationship is adopted

$$\mathbf{t}_{\mu} = \mu\left[\nabla\mathbf{v} + (\nabla\mathbf{v})^{T}\right] \qquad \text{Equation 3-10}$$

where the mixture Newtonian viscosity, μ, reads

$$\mu = \omega_o\mu_o + (1-\omega_o)\mu_a \qquad \text{Equation 3-11}$$

with μ_o and μ_a viscosities of pure oil and aqueous phases.

The equation for the diffusive velocity of the oil species (3 scalar equations). The diffusion of the oil species is driven by a mobility M_e coefficient times the gradient of the chemical potential, ϕ,

$$\omega_o\mathbf{u}_o = -M_e\nabla\phi \qquad \text{Equation 3-12}$$

As anticipated a diffuse interface approach is used to track the interface between the oil and the aqueous solution. Hence, the interface's thickness and the composition profile through the interface are set by the competition between individual motion and reciprocal attraction/repulsion of fluid molecules which are accounted in the expression of the chemical potential, ϕ

$$\phi = \frac{\alpha\sigma}{\varepsilon} f'(\omega_o) - \alpha\sigma\varepsilon\Delta\omega_o \qquad \text{Equation 3-13}$$

where σ is the interfacial tension between the oil and the aqueous phase, α and ε are a normalization coefficient to recover Young-Laplace law ($\alpha = 6\sqrt{2}$) and a measure of the interface thickness respectively (Le Maout, et al., 2020). In equation (3-13) we assume that the function $f(\omega_o)$, bulk free energy density of the mixture, has the following form

$$f(\omega_o) = \frac{1}{4}\omega_o^2(1-\omega_o)^2 \qquad \text{Equation 3-14}$$

As the oil and the aqueous species are immiscible the assumed form of bulk free energy density has two minima one at $\omega_o = 0$, the other at $\omega_o = 1$.

The expression of the volumetric force (3 scalar equations). The body force in equation (3-9) which allows to account for the pressure difference between the two phases is given by the chemical potential,

ϕ, times the gradient of the oil mass fraction, ω_o (Le Maout, et al., 2020),

$$\mathbf{b} = \phi \nabla \omega_o \qquad \text{Equation 3-15}$$

The state equation for the mixture density (1 scalar equation). The pure oil and the aqueous phases are assumed as not compressible fluids so also their mixture is non compressible. In addition to this hypothesis in our application cases the density of the two pure phases have a close value. This allows us to assume them equal and then to assume a constant density for the mixture

$$\rho = \rho_i \qquad i = o, a \qquad \text{Equation 3-16}$$

where ρ_o and ρ_a are the bulk density of the oil and aqueous phases respectively.

The expression of one of the two reaction term (1 scalar equation). In the modeled examples we assume no chemical reactions so the r_O is zero (consequently also r_a is zero, *cf.* equation (3-7)).

III.1.5 Final System of PDEs for the CH-NS Model

According with the previous constitutive relationships (and simplifications) the final system of Partially Differential Equations (PDEs) has the following form

$$\frac{\partial \omega_o}{\partial t} + \nabla \cdot (\omega_o \mathbf{v}) - \nabla \cdot (M_e \nabla \phi) = 0 \qquad \text{Equation 3-17}$$

$$\phi = \frac{\alpha\sigma}{\varepsilon} f'(\omega_o) - \alpha\sigma\varepsilon\Delta\omega_o \qquad \text{Equation 3-18}$$

$$\nabla \cdot \mathbf{v} = 0 \qquad \text{Equation 3-19}$$

$$\rho \frac{\partial \mathbf{v}}{\partial t} = \nabla \cdot \left\{ -p\mathbf{1} + \mu \left[\nabla \mathbf{v} + (\nabla \mathbf{v})^T \right] \right\} + \phi \nabla \omega_o \qquad \text{Equation 3-20}$$

Where in equation (3-22), as the Reynolds number in the modeled cases is relatively small, we neglected the term $(\mathbf{v} \cdot \nabla)\mathbf{v}$ in the total derivative which reduces to the derivative with respect to time. The primary variables of the mathematical model are: the mass fraction of the oil species, ω_o; the chemical potential Φ, the pressure of the mixture p and its velocity vector $\mathbf{v}$.

III.1.6 Weak Form of the Equations for the Implementation in Fenics

To implement the equations in the finite element code Fenics their weak form must be derived. The weak form and boundary conditions for the CH part is first presented followed by that of the NS part.

Weak form of the CH part of the system. The governing equations of the CH problem are the mass conservation equation of the oil species, equation (3-17) and the equation of the chemical potential, equation (3-18), which are rewritten below in a proper rearranged form to enable a pedagogical and clear derivation of the weak form.

$$\frac{\partial \omega_o}{\partial t} + \nabla \cdot (\omega_o \mathbf{v}) + \nabla \cdot \mathbf{q}_\phi = 0 \qquad \text{Equation 3-21}$$

$$\nabla \cdot \mathbf{q}_o = \frac{1}{\varepsilon^2}\left[\frac{\varepsilon}{\alpha\sigma}\phi - f'(\omega_o)\right] \qquad \text{Equation 3-22}$$

With

$$\mathbf{q}_\phi = -M_e \nabla \phi \qquad \text{Equation 3-23}$$

$$\mathbf{q}_o = -\nabla \omega_o \qquad \text{Equation 3-24}$$

This system of equation can be solved with respect of two primary variables: the mass fraction of the oil species, ω_o, and the chemical potential, Φ.

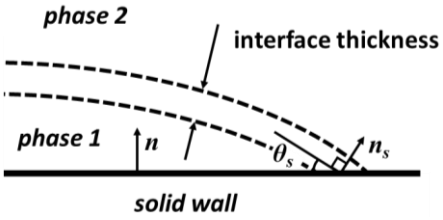

Figure III-27 *Diffuse-interface interpretation of the contact line and the contact angle*

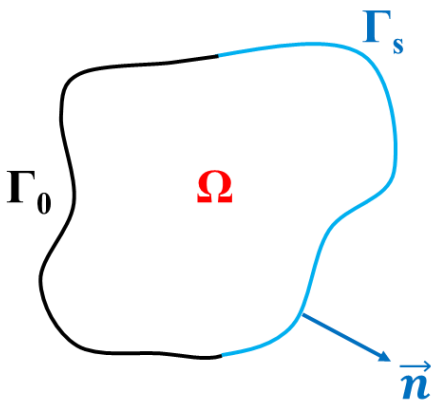

Figure III-28 *Computational domain and boundaries for the Cahn-Hilliard equations*

Let's call Ω the geometric domain and Γ its boundary and **n** and **τ** the unitary normal and tangent vectors to the boundary. On the boundary Γ Dirichlet type or Neumann type boundary conditions can be applied independently for each one of the primary variable. Very interesting is the physical meaning of boundary conditions related to equation (3-22) since they allow us to model the relative wettability of the two fluid with respect of the whole bound or part of it. More precisely if the oil wet (or does not wet) the bound, a Dirichlet boundary condition prescribing $\omega_o = 1$ (or $\omega_o = 0$) must be applied. Conversely in the case of a partial wettability a Neaumann condition fixing the wetting angle θ_s (see **Figure III-28**) must be applied as done in (Ding & Spelt, 2007). If we call Γ_0 the wetting (or non-wetting) portion of the boundary and Γ_s the partially wet one (with $\Gamma_0 \cup \Gamma_s = \Gamma$), the two types of boundary conditions read

$$\omega_o = 1 \quad (or \quad \omega_o = 0) \quad \text{on } \Gamma_0 \qquad \text{Equation 3-25}$$

$$\mathbf{q}_o \cdot \mathbf{n} = \cot(\theta_s)\left|\boldsymbol{\tau} \cdot \nabla \omega_o\right| \qquad \text{on } \Gamma_s \qquad \text{Equation 3-26}$$

For the chemical potential in the presented examples we set a natural condition on the whole boundary

$$\mathbf{q}_\phi \cdot \mathbf{n} = 0 \qquad \text{on } \Gamma \qquad \text{Equation 3-27}$$

which ensures that the oil do not diffuse thought impermeable surfaces.

To derive the weak form we introduce two weight functions, $v_{\boldsymbol{\phi}}(x,y,z)$ and $v_o(x,y,z)$ associated to the chemical potential and the mass fraction of oil respectively. Then we multiply equations (3-21) and (3-22) times $v_{\boldsymbol{\phi}}(x,y,z)$ and $v_o(x,y,z)$ respectively and we integrate over the domain Ω.

$$\int_\Omega v_\phi \frac{\partial \omega_o}{\partial t} d\Omega + \int_\Omega v_\phi \nabla \cdot (\omega_o \mathbf{v}) d\Omega + \int_\Omega v_\phi \nabla \cdot \mathbf{q}_\phi d\Omega = 0 \qquad \text{Equation 3-28}$$

$$\int_\Omega v_o \nabla \cdot \mathbf{q}_o d\Omega = \int_\Omega v_o \frac{1}{\varepsilon^2}\left(\frac{\varepsilon}{\alpha\sigma}\phi - f'(\omega_o)\right) d\Omega \qquad \text{Equation 3-29}$$

Applying the green formula to the last term of the left side of equation (3-28) and to the left side of equation (3-29) gives

$$\int_\Omega v_\phi \nabla \cdot \mathbf{q}_\phi d\Omega = \underbrace{\int_\Gamma v_\phi \mathbf{q}_\phi \cdot \mathbf{n} d\Gamma}_{\text{= 0 due to BC eqn (3-29)}} - \int_\Omega \nabla v_\phi \cdot \mathbf{q}_\phi d\Omega \qquad \text{Equation 3-30}$$

$$\int_\Omega v_o \nabla \cdot \mathbf{q}_o d\Omega = \underbrace{\int_{\Gamma_s} v_o \mathbf{q}_o \cdot \mathbf{n} d\Gamma}_{\text{BC eqn (3–28)}} + \underbrace{\int_{\Gamma_0} v_o \mathbf{q}_o \cdot \mathbf{n} d\Gamma}_{\text{= 0 due to the FEM}} - \int_\Omega \nabla v_o \cdot \mathbf{q}_o d\Omega \qquad \text{Equation 3-31}$$

Introducing equations (3-30) and (3-31) in equations (3-28) and (3-29) gives

$$\int_\Omega v_\phi \frac{\partial \omega_o}{\partial t} d\Omega + \int_\Omega v_\phi \nabla \cdot (\omega_o \mathbf{v}) d\Omega - \int_\Omega \nabla v_\phi \cdot \mathbf{q}_\phi d\Omega = 0 \qquad \text{Equation 3-32}$$

$$-\int_\Omega \nabla v_o \cdot \mathbf{q}_o d\Omega + \int_{\Gamma_s} v_o \cot(\theta_s)\left|\boldsymbol{\tau} \cdot \nabla \omega_o\right| d\Gamma = \int_\Omega v_o \frac{1}{\varepsilon^2}\left(\frac{\varepsilon}{\alpha\sigma}\phi - f'(\omega_o)\right) d\Omega \qquad \text{Equation 3-33}$$

Using equations (3-23) and (3-24) in the previous two equations and rearranging the terms we finally obtain

$$\int_\Omega v_\phi \frac{\partial \omega_o}{\partial t} d\Omega + \int_\Omega v_\phi \nabla \cdot (\omega_o \mathbf{v}) d\Omega + \int_\Omega M_e \nabla v_\phi \cdot \nabla \phi d\Omega = 0 \qquad \text{Equation 3-34}$$

$$\int_\Omega \nabla v_o \cdot \nabla \omega_o d\Omega = \int_\Omega v_o \frac{1}{\varepsilon^2}\left(\frac{\varepsilon}{\alpha\sigma}\phi - f'(\omega_o)\right) d\Omega - \int_{\Gamma_s} v_o \cot(\theta_s)\left|\boldsymbol{\tau} \cdot \nabla \omega_o\right| d\Gamma \qquad \text{Equation 3-35}$$

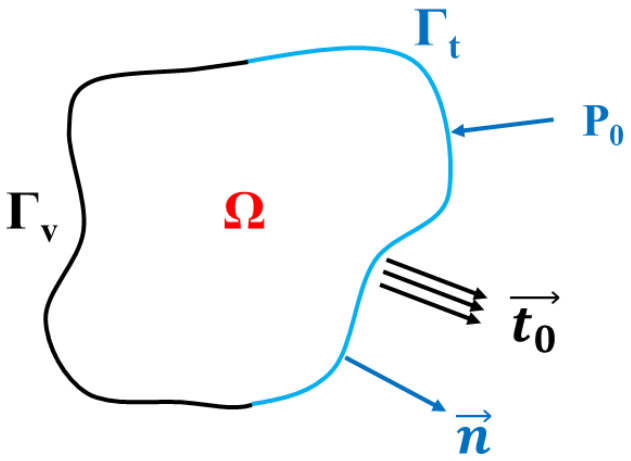

Figure III-29 Computational domain and boundaries for the Navier-Stokes equations

Weak form of the NS part of the system. The governing equations of the NS problem are the mass and momentum conservation equations of the mixture (*i.e.* equations (3-19) and (3-20)). The primary variables are the mixture pressure, *p*, and the velocity vector, **v**. Two types of boundary conditions can be applied: either the velocity vector (or some of its components) is prescribed either a traction condition is applied. In the following we will assume that in the portion of the boundary, Γ_t, where we assume a traction condition, the traction vector has not tangential component. The other part of the boundary where we set the velocity vector is indicated as Γ_v. Hence the boundary conditions for the NS equations are,

$$\mathbf{v} = \mathbf{v}_0 \quad \text{on} \quad \Gamma_v \qquad \text{Equation 3-36}$$

$$\mathbf{t}\cdot\mathbf{n} = -p_0\mathbf{n} \quad \text{on} \quad \Gamma_t \qquad \text{Equation 3-37}$$

To derive the weak form we define two weight functions: a vector one **w**(x,y,z) associated to the momentum conservation equation and a scalar one q(x,y,z) associated to the mass conservation equation. Then we multiply equation (3-9) times **w**(x,y,z) and we integrate over the domain Ω.

$$\int_\Omega \left(\rho\frac{\mathrm{D}\mathbf{v}}{\mathrm{D}t}\right)\cdot\mathbf{w}d\Omega - \int_\Omega (\nabla\cdot\mathbf{t})\cdot\mathbf{w}d\Omega = \int_\Omega \mathbf{b}\cdot\mathbf{w}d\Omega \qquad \text{Equation 3-38}$$

Applying the green formula to the second term of the left side of equation (3-38) and splitting the boundary integral give

$$-\int_\Omega (\nabla\cdot\mathbf{t})\cdot\mathbf{w}d\Omega = \int_\Omega \mathbf{t}:\nabla\mathbf{w}d\Omega - \underbrace{\int_{\Gamma_v}(\mathbf{t}\cdot\mathbf{n})\cdot\mathbf{w}d\Gamma}_{=0 \text{ due to the FEM}} - \int_{\Gamma_t}\underbrace{(\mathbf{t}\cdot\mathbf{n})}_{\text{BC eqn [3-37]}}\cdot\mathbf{w}d\Gamma \qquad \text{Equation 3-39}$$

Introducing this relation in equation (3-38) and using equation (3-37) in the last term of the previous equation give

$$\int_\Omega \left(\rho\frac{\mathrm{D}\mathbf{v}}{\mathrm{D}t}\right)\cdot\mathbf{w}d\Omega + \int_\Omega \mathbf{t}:\nabla\mathbf{w}d\Omega - \int_{\Gamma_t} p_0\mathbf{n}\cdot\mathbf{w}d\Gamma = \int_\Omega \mathbf{b}\cdot\mathbf{w}d\Omega \qquad \text{Equation 3-40}$$

Expressing **t** as in equation (3-20) and introducing equation (3-15) give

$$\int_{\Omega}\left(\rho\frac{\mathrm{D}\mathbf{v}}{\mathrm{D}t}\right)\cdot\mathbf{w}d\Omega-\int_{\Omega}p\mathbf{1}:\nabla\mathbf{w}d\Omega+\int_{\Omega}\mu\nabla\mathbf{v}:\nabla\mathbf{w}d\Omega+\int_{\Omega}\mu\left(\nabla\mathbf{v}\right)^{\mathrm{T}}:\nabla\mathbf{w}d\Omega+$$
$$-\int_{\Gamma_t}p_0\mathbf{n}\cdot\mathbf{w}d\Gamma=\int_{\Omega}\phi\nabla\omega_c\cdot\mathbf{w}d\Omega \qquad \text{Equation 3-41}$$

The weak form of the mass conservation equation of the mixture is obtained by multiplying equation (3-19) times q(x,y,z) and integrating over the domain Ω

$$\int_{\Omega}q\frac{\partial\rho}{\partial t}d\Omega+\int_{\Omega}q\nabla\cdot\left(\rho\mathbf{v}\right)d\Omega=0 \qquad \text{Equation 3-42}$$

IV. Results and Discussions

In this Chapter, we will present and discuss the results we obtained. The first part of this chapter is devoted to what we called as "physical experiments", which are reservoir-on-chip experiments, while those related to numerical simulations named "*in-silico* experiments", are presented in the second part. Both types of experimental methods and procedures were presented in **Section III.1.4**. However, certain aspects of these will be periodically recalled throughout this chapter to ensure a thorough understanding of our purposes and objectives.

IV.1 The Physical Experiment Results

The objective of these experiments was to investigated the oil mobilization mechanisms at the pore scale during waterflooding period and tertiary step as well. Specifically, this protocol involved the use of two types of water-wet chips: random chips and regular chips. Here, we will initially pay more attention to the results corresponding to the random chip due to its closer replication of the real reservoir structure. Subsequently, the specificity of regular chip will be highlighted in a second time by comparing the principal findings for each of them and discussing any observed discrepancies, if they exist.

Moreover, as we put forward well before, such investigations predominantly focus on the influence of Ca and M. However, from literature review, we emphasized that in most cases, the focus is placed on the influence of Ca by varying the flow rate (Q), while investigations on the influence of M are scarcer. Therefore, in the present study more attention will be paid to the influence of M by carrying out tertiary experiments with a flooding Newtonian fluid of increasing viscosity. Before proceeding with those experiments, we start by characterizing the chips and the fluids used.

IV.1.1 The Characterization of Fluids and Chips

IV.1.1.1 Oil

The oil used is a commercial rapeseed oil which density is 0.910 g/cm^3 and a measured viscosity of 80 mPa·s at 20 °C. Additionally, the measurements performed after its dyeing yielded close results to the aforementioned values, indicating that the dye concentration did not influence its physical properties.

IV.1.1.2 Aqueous Mixture

The dyed brine used in the waterflooding period also contained 10 g/L of NaCl to ensure good dispersion of dye particles. However, the addition of dye and NaCl has a minimal impact on the physical properties of the brine, with the density and viscosity of the brine being 1.005 g/cm^3 and 1.01 mPa·s at 20 °C, respectively.

The density and viscosity of the glycerol used are 1.261 g/cm^3 and 1460 mPa·s at 20 °C, respectively. Different proportions of glycerol and water were mixed to obtain glycerol aqueous mixtures, which

density and viscosity are functions of the glycerol concentration, as shown in the **Figure IV-1**. The density of the mixture exhibits a linear correlation with the concentration of glycerol in **Figure IV-1** (a), indicating that the aqueous mixtures are homogeneous and the density of the mixture follows a simple additive relationship (Equation 1).

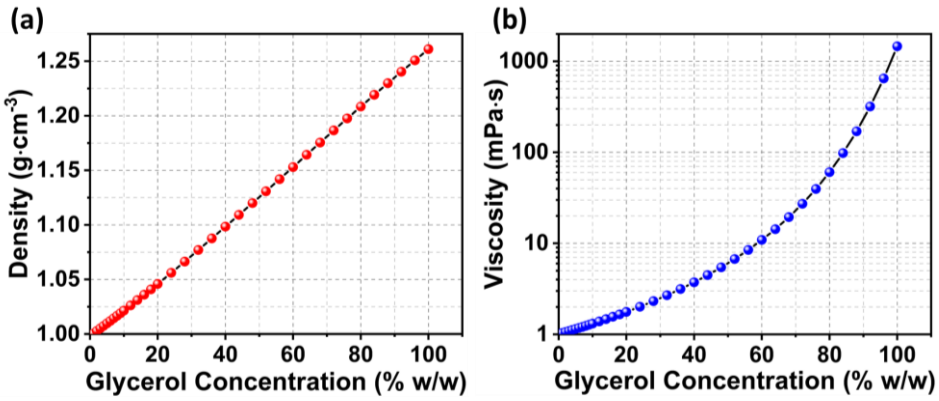

Figure IV-1 *The density (a) and viscosity (b) of the aqueous mixtures in function of glycerol concentration.*

$$\rho_{mixture} = \rho_{glycerol}\omega_{glycerol} + \rho_{water}(1-\omega_{glycerol}) \qquad \text{Equation 4-1}$$

where, $\rho_{mixture}$, $\rho_{glycerol}$ and ρ_{water} are the density of mixtures, glycerol and water at 20 °C, respectively. $\omega_{glycerol}$ is the weight glycerol by weight concentration in the mixture.

However, as shown in **Figure IV-1** (b), the viscosity of the mixture is quite nonlinear with glycerol concentration, but all of them are Newtonian. Here, we recall that M is the ratio of viscosity of displacing fluid to the viscosity of displaced one. As we said, in the tertiary step, the investigation of the mobilization mechanism of the nonwetting phase and flow dynamics were performed mainly by injecting glycerol/water mixtures of various viscosities giving five M values, spanning over two decades.

The characterizations of these five aqueous fluids, including their interfacial tension (IFT) σ with rapeseed oil are summarized in **Table IV-1**. We see therefore that the IFT decreases only slightly (a difference of approximately 2 mN/m) with M due to the reduction in interfacial interaction forces between the oil and aqueous mixture caused by glycerol molecules at the interface. Consequently, the influence of IFT (σ) on the flow dynamics of immiscible Newtonian fluids can be disregarded compared to that of the other parameters by taking σ = 55 mN/m in the present work.

Table IV-1 The properties of all aqueous mixtures

Mass fraction of glycerol (% w/w)	**0**	**44**	**54**	**68**	**82**
Density of mixtures (g/cm^3)	1	1.109	1.137	1.175	1.214
Viscosity of mixtures (mPa·s)	1	4.48	7.82	19.4	79.95
IFT σ (mN/m)	55.87	54.56	54.28	53.9	53.66
M (viscosity of mixtures to water)	**1**	**4**	**8**	**20**	**80**

IV.1.1.3 Parameters of the Chips

The characterization of the chip involves the measurement of porosity, pore volume, and permeability.

Porosity and Pore Volume

The porosity ϕ and the pore volume V_{pore} are related through $\phi = V_{pore} / V_{total}$, where V_{total} is the total volume that is equal here to 4 μL. ϕ can be determined knowing the geometric details of the chip. So, we firstly used the image analysis method of dry chips to set their pore volume and porosity, and obtained results are presented in the **Table IV-2** showing that pore volume and porosity are identical for each of chip type. Here, we used the unit of pore volume as PV for all subsequent work as well.

Table IV-2 The porosity and pore volume of both types of chips

Parameter	ϕ	V_{pore} (μL)
Random chip	0.6	2.4
Regular chip	0.6	2.4

In addition, we can calculate the pore volume by recording the time taken for a liquid to completely saturate a chip under stable displacement at a constant flow rate. It should be noted that the heterogenous distribution of pores in the random chip leads to a significant number of pore spaces remaining unsaturated during the initial stable displacement, resulting in a large error in the calculation of the pore volume for the random chip using this method. Therefore, this method is only used to measure the pore volume of a regular chip, as its uniform pore structure ensures almost complete saturation of the pores by the fluid during a stable displacement process. Three sets of experiments were performed, and data were averaged. The calculated pore volume of the regular chip is approximately 2.4 μL, corresponding to a porosity of 0.6, consistent with the results obtained from image analysis method.

Pore size Distribution

We performed statistical analysis on the pore size distribution within the random chip. Firstly, we used the watershed method to segment the binary image of the empty chip, allowing us to obtain different regions based on the size and structure of the pores. Next, we fitted circles to the obtained regions and calculated the size of each circle corresponding to each region. Finally, we obtained the pore size distribution of the random chip, as shown in **Figure IV-2**, which exhibits a right-skewed distribution.

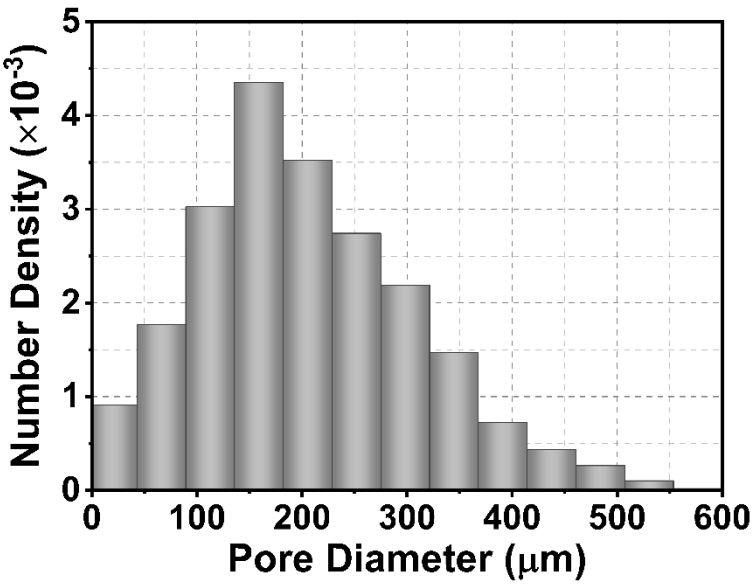

Figure IV-2 The statistical data of the pore size distribution of the random chip

Permeability

After the chips were completely saturated by water, monophasic experiments were conducted by injecting water at various flow rates and recording the corresponding pressure drop (ΔP). In these experiments we strat at Q = 4 μL/min and successively decrease it. Five independent experiments, named as E_{PW1}, E_{PW2}, E_{PW3}, E_{PW4}, and E_{PW5}, respectively, were performed on the same chip, which was beforehand cleaned and dried according to the procedure described in the **Section III.1.2**. The results are presented in terms of ΔP versus Q on **Figure IV-3**. It is evident that all data (the points with different color) are scattered within the gray region, as a consequence of instrumental sensitivity and operational factors during the measurement process such as temperature fluctuation, for example. However, in average a linear function of ΔP versus Q can be drawn, as shown by the pink line. Based on Darcy's law, the mean absolute water permeability K_w was approximately 2.7 Darcy, with a standard deviation of 0.18 Darcy for random chip.

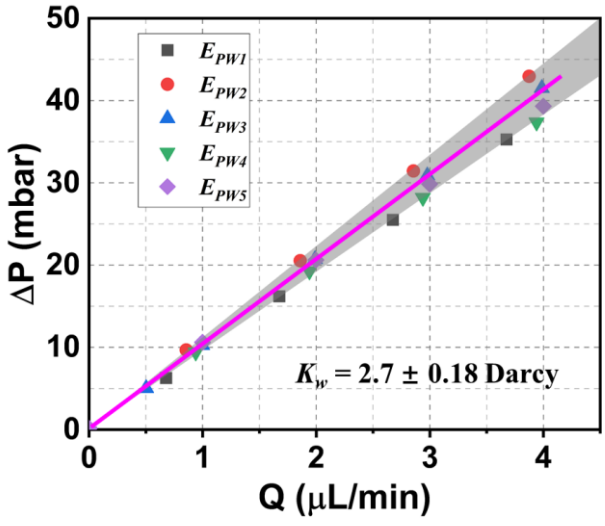

Figure IV-3 *The pressure drop ΔP versus flow rate Q for random chip from five independent experiments (data points within the gray region).*

Similarly, we used the same procedure to measure the water permeability K_w of the regular chip. Here again, five independent experiments, named as E_{PW6}, E_{PW7}, E_{PW8}, E_{PW9}, and E_{PW10}, were performed and the results are displayed on **Figure IV-4**. The K_w = 3.6 ± 0.13 Darcy, a value that is significantly higher than that of the random chip, which was 2.7 Darcy. The reason behind this disparity is the regular structure of the porous space, so that while the porosity is the same, the water flow is easier, thereby resulting in higher water permeability.

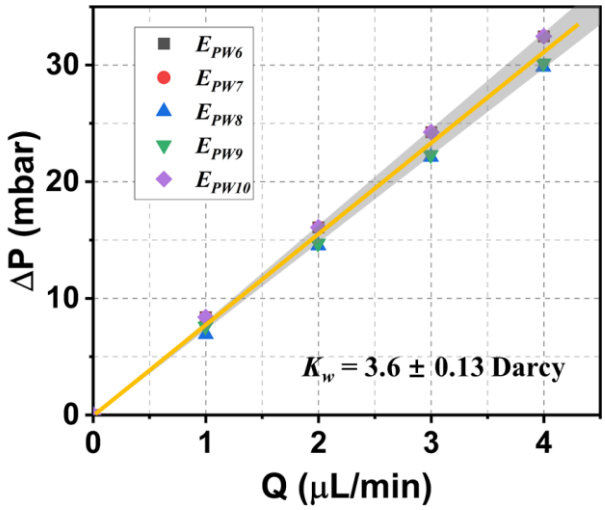

Figure IV-4 *The pressure drop ΔP versus flow rate Q for regular chip from five independent experiments (data points within the gray region).*

The images of the saturated chips were acquired and processed using image processing methods that were described in **Section III.1.4** to clearly distinguish the different phases by their grey level values, and colors were then assigned accordingly. Those images of random chip and regular chip are displaced on **Figure IV-5** (a) and (b), respectively, where water is represented in blue, and solid grains are in black.

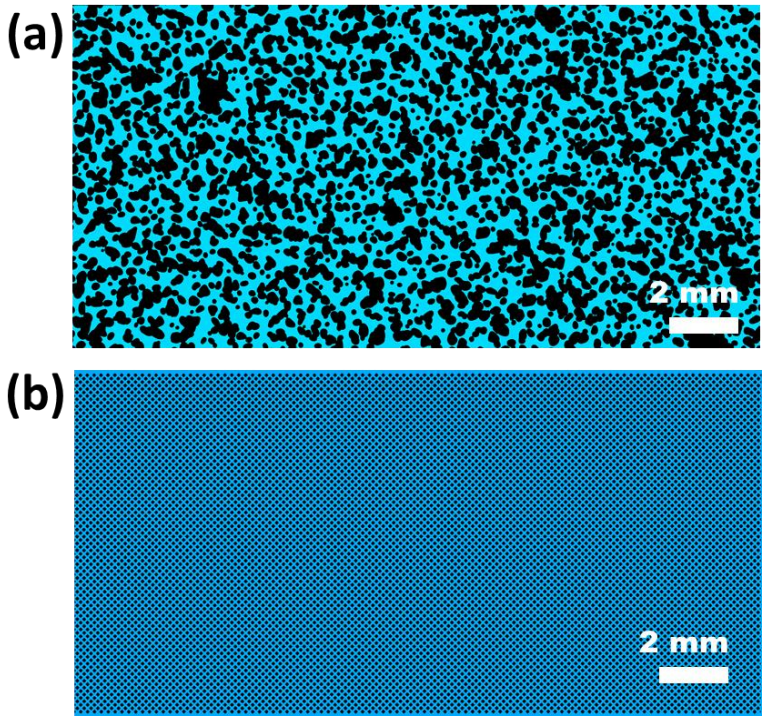

Figure IV-5 *Color-assigned image of micromodel fully saturated with water for random chip (a) and regular chip (b). The black colors are solid grains, and blue is for pores filled with water.*

IV.1.2 Oil Drainage

Five independent experiments were performed, and simultaneously, the correspond ΔP was recorded with the injection Q. In these oil drainage experiments, we studied the flow patterns and monitored and recorded microscopic flow phenomena during the oil invasion process, such as Haines jumps. The connection between microscopic phenomena and dynamics can help us better understand the invasion mechanism. Furthermore, we quantified the variation of wetting phase saturation with injected pore volume (PV) of oil through image analysis. In addition, we investigated the influence of pore structure on flow phenomena and mechanisms. Finally, we discussed the influence of Ca on remaining water saturation and dynamics by increasing Q.

IV.1.2.1 The Fluid Dynamic of Drainage

The oil was injected into the water-saturated chip at Q = 0.1 μL/min to reproduce a low invasion velocity, allowing for a clearer and more accurate observation of the details of the displacement process. In this experiment, M is equal to 80, and Ca is 1.2×10^{-5} when calculated by the classic formula Ca = μv/σ, where μ is the viscosity of the oil, v is velocity, and σ is the IFT. The flow regime is indicated by a green circle on logCa/logM diagram (**Figure IV-6**). Accordingly, the flow mode falls within the capillary fingering-stable displacement crossover zone, leaning towards the capillary fingering side. This suggests that capillary forces dominate over viscous forces, despite the higher M allowing for the neglect of the viscous ΔP in the displaced phase during drainage.

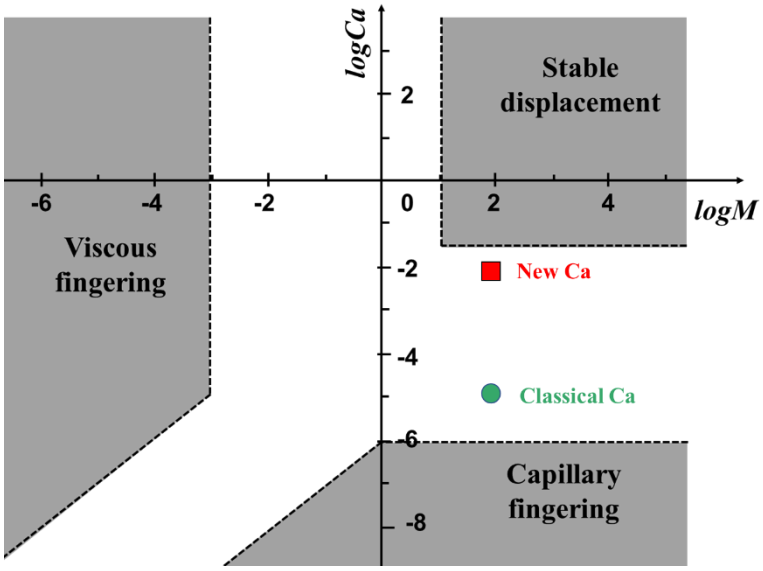

Figure IV-6 *LogCa/logM diagram. Grren circle represents the Ca calculated by classical equation number of 1.2×10^{-5}, the red square represents Ca calculated by new method (Tang, et al., 2019). The boundaries of the displacement patterns according to Lenormand et al. (Lenormand, et al., 1988).*

Moreover, during the drainage, visual images of the chip were sequentially acquired and processed as previously described in **Section III.1.4**. Some of them are shown in **Figure IV-7**, illustrating the phase distribution at successive values of injected oil volumes. Examination of these images shows that the fingering mechanism of oil is effectively dominant, though it is damped by the highly favourable viscosity ratio. Moreover, at the macroscopic scale, the stability of the overall movement of the invading front is maintained due to the viscosity of the injected fluid, consistent with the findings reported by Lenormand et al. That is to say, the pattern before oil breakthrough exhibits a relatively stable fluid interface invasion at the macroscopic level due to favorable invading viscosity ratio, while at the microscopic level, it demonstrates capillary fingering due to the capillarity (Lenormand, et al., 1988) (Zhang, et al., 2011).

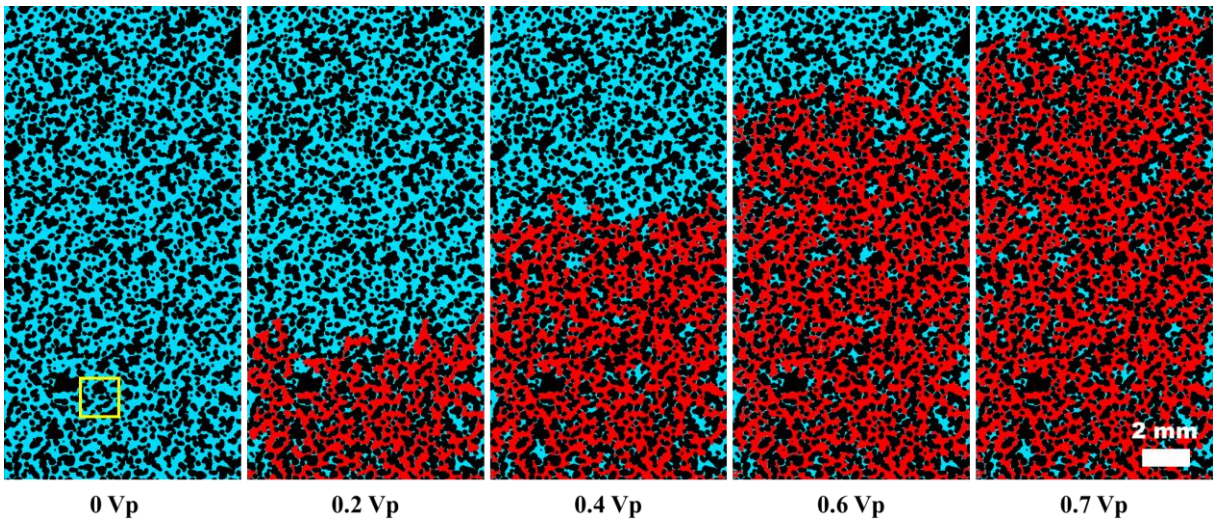

Figure IV-7 *Successive snapshots of oil investing water saturated chip during the drainage period.*

In this experiment, the oil breakthrough occurs at approximately 0.7 PV, well below 1 PV that correspond to perfect piston-like displacement. After breakthrough, the oil phase occupies a large portion of pores, and local water remnants of small size are left behind. This outcome is consistent with results reported in the literature for both 2D and 3D experiments under similar conditions of Ca and M. Zhang et al. (Zhang, et al., 2011) reported an invading phase saturation of approximately 0.8 in a 2D uniform micromodel chip under conditions of logM=1.88 and log Ca=-4.57. Similarly, Hu et al. (Hu, et al., 2020)reported an invading phase saturation of about 0.73 in 3D porous media under drainage conditions with logM=2 and log Ca=-5, demonstrating a close stable displacement with high saturation.

To show how the oil invasion process depends on the structure of the porous medium, a small space of the chip was randomly selected. In that area, indicated by a yellow box in **Figure IV-7**, a video was recorded over time. Some snapshots have then been extracted from this video and are displayed in **Figure IV-8**. In these snapshots, the solid grains are depicted in grey, the water is represented in yellow, and the oil is shown in white. This figure clearly shows, as indicated by blue arrows, that the oil follows pathways with a preferential flow through large pores saturating pore bodies instead of flowing through small pore throats. As the oil content increases, the pressure in smaller pores becomes large enough to oil passthrough. This is schematically illustrated in **Figure IV-9**, where the oil fills large pores by passing through large pore throats, while smaller ones are still filled by water. Moreover, in all situations, a water film is in contact with solid phase since the porous medium is water-wet.

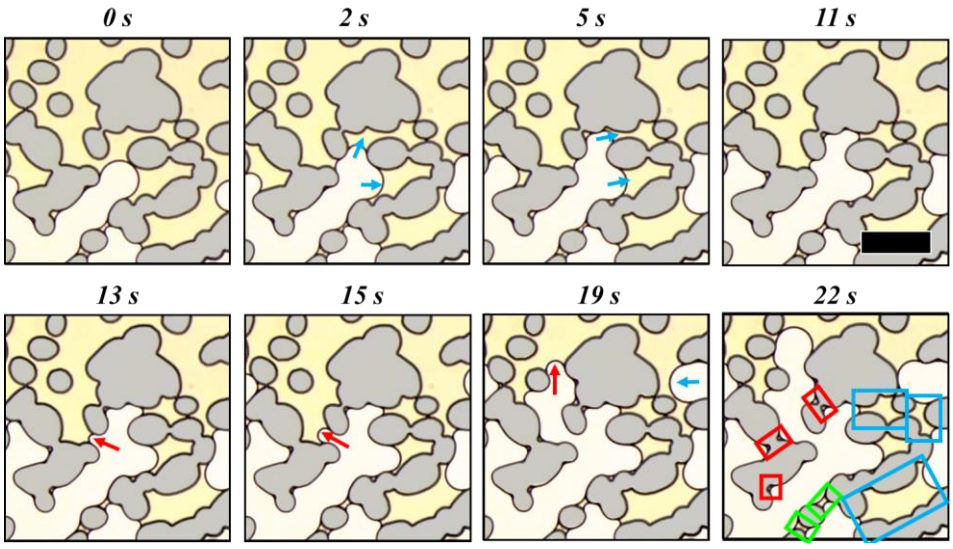

Figure IV-8 *Temporal change of phases saturation in yellow box of* ***Figure IV-7****. Oil is on white color, water in yellow and solid grains in gray. The scale bar is 500 µm.*

We can also see that admission of oil through a single narrow throat can induce a cascade of filling wider regions of the pore space. After saturating those pore bodies, oil is obstructed by larger capillary forces at narrow throats (red arrows in **Figure IV-8**), until the ΔP within become sufficient to overcome it. Once the oil breaks through the pore throat, it is no longer constrained by geometric limitations,

leading to a weakening of capillary effects and enabling it to quickly pass through the throat and saturate the next pore body. This phenomenon, known as Haines jumps, occurs due to the size of pore bodies and pore throats determining the duration required to saturate the pore bodies and overcome the critical capillary forces at throats (Armstrong & Berg, 2013) (Singh, et al., 2017). Moreover, the video observations establish that pore drainage events are cooperative and that the individual dynamics, i.e., the time at which a pore is drained, depends on the fluid configuration in adjacent pores beyond the next neighbours, that is, critical capillary forces.

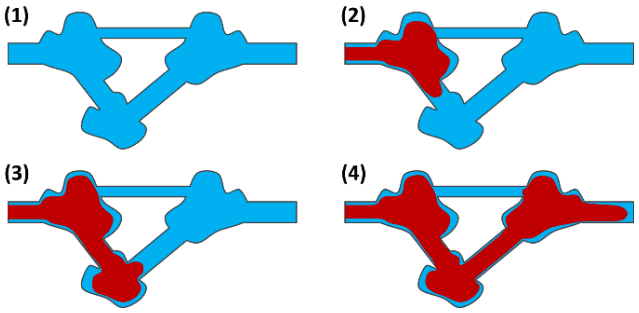

Figure IV-9 *Schematic illustrating of the drainage process of the non-wetting phase (red) within wetting phase saturated pores (blue). The remaining water located in narrow throats and smaller pores.*

The critical capillary pressure represents the minimum capillary pressure required for breakthrough, directly influenced by the curvature radius of the interface and the throat diameter of the pores. As discussed by Tang et al. (Tang, et al., 2019), for the shallow-etched chip we use, which has a depth of 20 μm, the curvature in the depth direction is minimal, meaning the radius of the interface curvature is relatively large. Thus, the influence of depth direction on capillary pressure (P_c) can be considered negligible, allowing us to focus primarily on the effects of the throat diameter. This relationship can be described by the Young-Laplace equation,

$$P_c = \frac{2\sigma\cos\theta}{\overline{D}_{throat}} \qquad \text{Equation 4-2}$$

where, the σ is interfacial tension; θ is the contact angle; $\overline{D}_{throat}$ is the mean diameter of the throat. The mean throat diameter of our chip is 82.3 μm.

During the invasion process, the oil phase follows the path of least resistance, sequentially invading pore bodies along pathways that correspond to the positions of minimum P_c. As the ΔP exceeds critical P_c, pores containing water are expelled and subsequently filled with oil, with the largest pores typically being drained first. This results in the displacement of the remaining water, which exits the micromodel through the connectivity pathways of the wetting phase located at the pore throats and on the surfaces of pore bodies.

In the invaded regions, oil primarily occupies the larger pores, while remaining water predominantly resides in smaller spaces, as the corners of the invaded pore bodies highlighted in the red rectangle in

Figure IV-8. However, it should to be noticed that some pore bodies still remain filled with water as they are surrounded by pores of much smaller size, as depicted in the blue rectangle, in **Figure IV-8**. Moreover, for isolated pore throats, the remaining water exists in the form of more or less thick films connecting neighboring solid obstacles as shown in green rectangle, in **Figure IV-8**. This remaining water will be immobile and constitute what is called the irreducible water saturation, S_{wi}.

To provide a clearer depiction of the details of remaining water, we randomly selected a localized area of the invaded region after image processing. The result is shown in **Figure IV-10** where the red color represents oil, water is in blue, and black color represents solid grains. We can distinctly observe the "trapped water" surrounded by multiple small pores, as well as the remaining water existing in the form of a "water film", including thin layers of water on the surface of solid grains, water in the corners of pore bodies, and water films connecting neighboring solid obstacles.

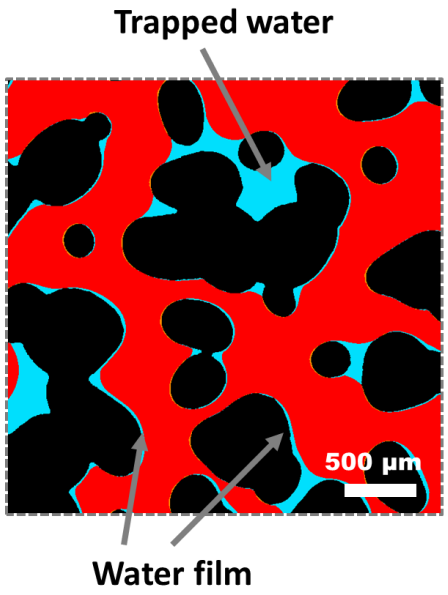

Figure IV-10 *The distribution of remaining water in the micromodel at steady state, with oil in red, water in blue, and black is the solid grains.*

IV.1.2.2 The Remaining Water Distribution and Water Saturation

The transport of fluids in porous media is characterized by parameters like permeability and relative permeability. As oil saturation increases during oil drainage, the relative permeability of oil (k_{ro}) rises sharply. Concurrently, the relative permeability to water (k_{rw}) decreases until continuous water pathways are disrupted. Eventually, k_{rw} approaches zero when the remaining water becomes immobile at the irreducible water saturation (S_{wi}). This dynamic showcases the intricate interplay between the two fluids under varying saturation levels within the porous medium. The corresponding k_{ro} at the end of oil injection is typically estimated using the Kozeny-Carman and Van Genuchten relation, which yields k_{ro} values of 0.797 and 0.853, respectively. Averaging the results from both methods, k_{ro} was approximated to be 0.82.

On a microscopic scale, however, the transport of fluids in porous media is influenced by the geometry and topology of the network consisting of connected pore throats and bodies. Although it is well recognized that the relationship between permeability and pore geometry varies across different types of porous media, in etched micromodels of shallow depth, permeability is predominantly governed by channel depth rather than the geometrical factors like pore-throat width and pore-body diameter that typically influence trapping in porous rock. Despite theoretical predictions situating the flow regime within the capillary fingering-stable displacement crossover zone (more close the capillary fingering zone), based on the classical formula for calculating the Ca, experimental observations indicate a mechanism that more close stable displacement pattern. This observation is further supported by the volume of the invading phase at the breakthrough time, with the saturation reaching 0.7 PV. Similar conditions in drainage experiments reported in the literature (Zhang, et al., 2011) (Hu, et al., 2020) have also confirmed a stable displacement with a comparable saturation at breakthrough. This indicates that the traditional method of calculating Ca may not adequately represent the dynamics in 2D micromodels. Consequently, some authors have suggested that the formula for calculating Ca should be adjusted for scenarios involving shallow pore depths, such as 20 μm.

In that respect, we adopted an alternative approach that was detailed in Tang et al. (Tang, et al., 2019) as outlined in **Section III.1.3**. The Ca in case of 2D microchip drainage experiments can be calculated by the Equation 4-3. This method incorporates a geometric factor (G) to account for microscale variations in the structure of micromodels. This factor helps to explain why the Ca required to mobilize the nonwetting phase in micromodels is significantly lower compared to that in natural rock. This approach allows for a more accurate representation of fluid transport phenomena under controlled experimental conditions, highlighting the impact of microstructural variations on fluid dynamics in porous media. Using the specific pore structure and dimensions of our micromodel, we calculated and measured all relevant parameters, the results of which are summarized in **Table IV-3**.

$$Ca = \left(\frac{\eta v}{\sigma \cos\theta}\right)\frac{1}{k_{ro}}\underbrace{\left(\frac{12}{2}\right)\left(\frac{D_t}{d_z}\right)^2\left(\frac{L_p}{D_t}\right)\frac{1}{\left(1-\frac{D_t}{D_b}\right)(\phi\varsigma)}}_{G} \qquad \text{Equation 4-3}$$

Table IV-3 *The parameters included in the geometric factor, θ and the relative permeability of the oil phase k_{ro}.*

θ	ϕ	ζ	d_z	D_t	D_b	L_p	k_{ro}
22.4°	0.6	1.62	20 μm	82.3 μm	223.5 μm	223.5 μm	0.82

where, d_z is the channel depth of the micromodel; L_p is the length of one pore; D_t is the characteristic pore-throat width; D_b is the characteristic pore-body diameter; ϕ is the porosity; θ is the contact angle; ζ is the adjustable factor to relate permeability and pore geometry. Among these parameters, D_t, D_b, and

L_p represent the average values of the micromodel, and the calculation methods for ζ and k_{ro} are detailed in **Section 2.1.3**.

Combining the parameters from **Table IV-3**, we can compute the value of G as 449.3. Then, by substituting this value along with θ and k_{ro} into Equation 4-3, we obtain the new capillary number Ca_{new} during drainage experiments at flow rate of 0.1 µL/min (η and σ are represented in **Section** IV), which is calculated as 7.1×10^{-3}. So capillary number is now 2 order of magnitude greater than that previously calculated. This new result is represented on **Figure IV-6** by a red square the lies now within the crossover region between the stable displacement regime and capillary fingering, proximal to the boundary of stable displacement. This characterization elucidates the macroscopic manifestation of more stable displacement observed prior to breakthrough, while microscopically, localized phenomena indicative of capillary fingering are discernible. Such a scenario underscores the suitability of this methodology for calculating the Ca.

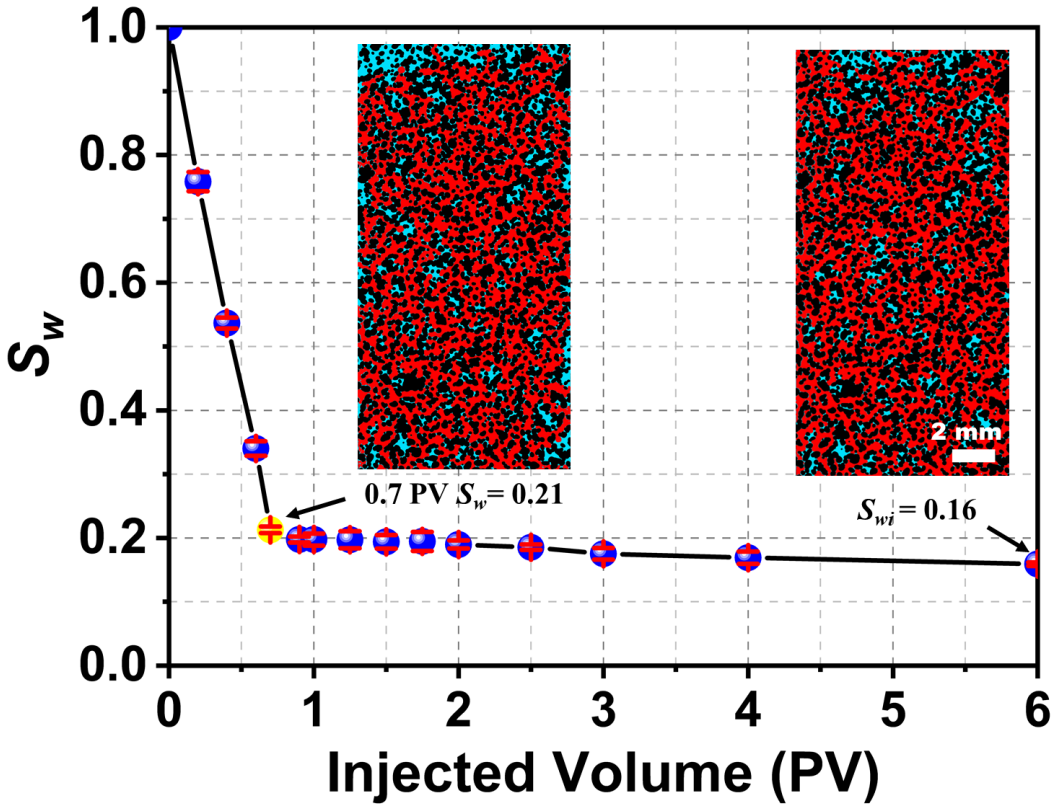

Figure IV-11 *Water saturation (S_w) in function of injected oil pore volume at Q=0.1 µL/min. The yellow point indicate the breakthrough at ~ 0.7 PV, and at steady state, S_{wi} is ~ 0.16.*

Anyway, the acquired images during the oil drainage allowed us to quantitatively analyze the successive temporal changes of water and oil saturation during the process. In **Figure IV-11**, we represent the evolution of water saturation S_w in function of the volume of injected oil expressed in terms of pore volume. As we can see, at initial stages of drainage, the S_w decreases rapidly (following an almost linear shape) until oil breakthrough occurs at 0.7 PV (indicated by the yellow dot), with S_w reaching 0.21. After

breakthrough, S_w continues to decrease slowly and slowly, reaching a final value to 0.16 for 6 PV of oil injected at that flow rate of 0.1 µL/min.

Comparing the images corresponding to oil breakthrough and the end state, we observe some changes in the location and proportion of remaining water. That is, during drainage, the oil phase preferentially breaks through and flows along paths with the smallest capillary forces. After breakthrough, the oil phase continues to invade transverse pores under favorable conditions of M.

Moreover, image processing allows also us to determine the precise location of the remaining water and oil phase by specifying the corresponding pore size distribution. These distributions are displayed on the **Figure IV-12** together with the original pore size distribution of dry chip. Water-filled pores are shown in blue, while oil-filled ones are in red. As expected, remaining water is seen to be mainly located in small pores while oil is preferentially located in large pores. The original pore size distribution is represented by the dashed line in **Figure IV-12** (a) and is, of course, the sum of water and oil filled pore types. So the proportion of pores containing the remaining water obvious show that water is predominantly retained in smaller pores, with over half of the water occupying pores smaller than 150 µm in diameter, as depicted in the blue region in **Figure IV-12** (b). However, a noticeable amount of water is also observed in larger pores, as indicated by the red rectangle area. Besides the limited confidence in statistics, another reason for this observation could be the presence of very small pores surrounding some large pores, preventing oil from filling them. In oil-wet media, the situation is indeed reversed, and therefore the remaining water should occupy large pores. Of course, in that case, an oil film coats the solid surfaces.

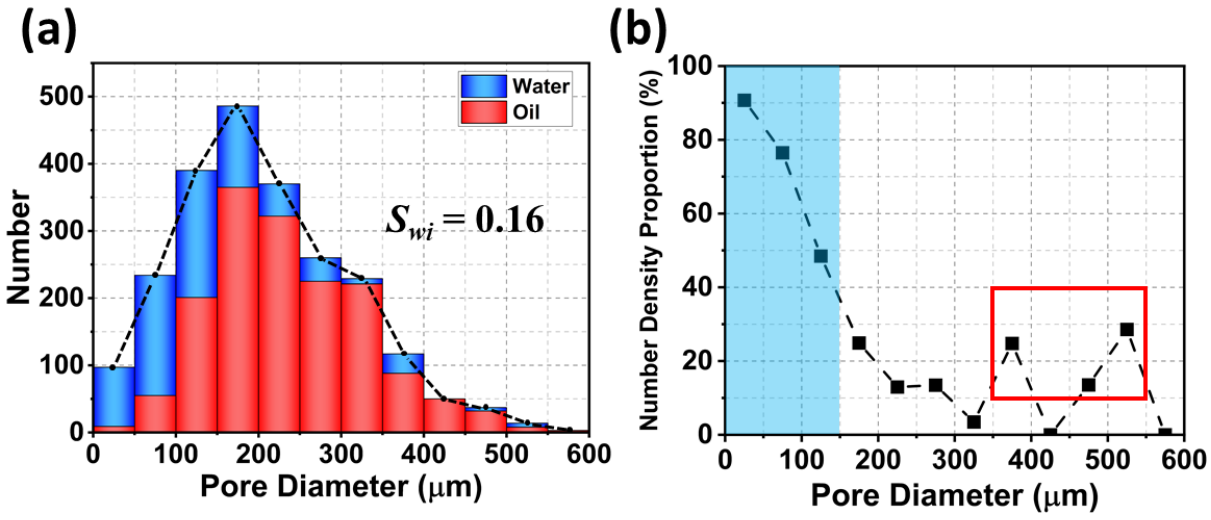

Figure IV-12 *(a) the statistical distribution of oil and water in the original pore sizes at steady state; (b) the proportion of pores containing remaining water at steady state.*

To accurately quantify the drainage displacement behavior, we used differential pressure sensors to measure the ΔP across the chip during the oil drainage. This approach was conducted in parallel with

image capture and processing to ensure comprehensive data collection, enhancing our understanding of the displacement behavior under experimental conditions. The results, depicted in **Figure IV-13**, show the envolution of ΔP over time during continuous oil injection. The line represents the ΔP that was effectively recorded during continuous injection of oil, while the data points represent the steady ΔP averaged over the time slots needed to image the whole chip. Fortunately, the two sets of data are in good agreement and almost coincide. These results indicate that the drainage can be divided into three periods, namely the stable displacement before breakthrough (pink region), the arrangement period after breakthrough (blue region), and the steady-state period (grey region). It is important to note that the increase in ΔP before 0 PV is attributed to the period when oil invades the channels and fractures upstream of the saturated porous medium. However, our experimental procedure records data starting when the oil begins to invade the water-saturated porous medium networks. So, the initial ΔP started from a relatively high value, say approximately 50 mbar.

During the drainage, pores initially filled with a wetting fluid can be drained and subsequently filled by a non-wetting fluid when the local capillary pressure exceeds the threshold entry pressure, leading to a reduction in the S_w and a corresponding increase in the ΔP. In details, as the Q is constant, during the stable displacement period, the quantity of oil invading the chip per unit time or per volume remains constant, resulting in an almost linear increase in ΔP, corresponding with the linear decrease of S_w shown in **Figure IV-11**. Following the initial breakthrough, the oil continues to invade pores along the transverse regions, further displacing the wetting phase within these pores, with a slowly and slowly increase in ΔP until it reachs a steady state when the remaining water in the chip no longer flows.

Moreover, we find that the ΔP was not directly increased with the increase of injected volume, but rather showed a “step-like” increase, as shown in the bottom plot of **Figure IV-13**, corresponding to the periods displayed in the snapshots. Therefore, we can analyze this phenomenon in conjunction with the observations in **Figure IV-8**. Because the Haines jumps in the drainage, the fluid flow contains the steps of slowly obstructed and “trapped” by pore-throats and fast saturated the pore-bodies after pass through the throats. In details, the obstructed of pore-throats lead to the increase of capillary forces until it overcome the critical capillary forces at the throats accompanied by the increase of the recorded ΔP, as the pink interval shown in the bottom plot of **Figure IV-13**. Particularly, when encountering a narrow throat, a larger ΔP is needed to overcome the critical capillary force. However, during the period when the oil interface invades the pore throat with the larger diameter and accelerates abruptly towards the adjacent pore body, the energy accumulated to pass through the pore-throat is released. This energy is sufficient to saturate the next-adjacent pore body, resulting in a small plateau in the ΔP. Exactly, during the initial invasion, the discrete pressure increase corresponds to the events of pore-throats invasion, while the plateau corresponds to the invasion events of the pore-bodies. In addition, as observed in the snapshots, “Haines jumps” can occur simultaneously at multiple pore structures. This phenomenon is reflected in the ΔP curve as distinct rising- plateau intervals.

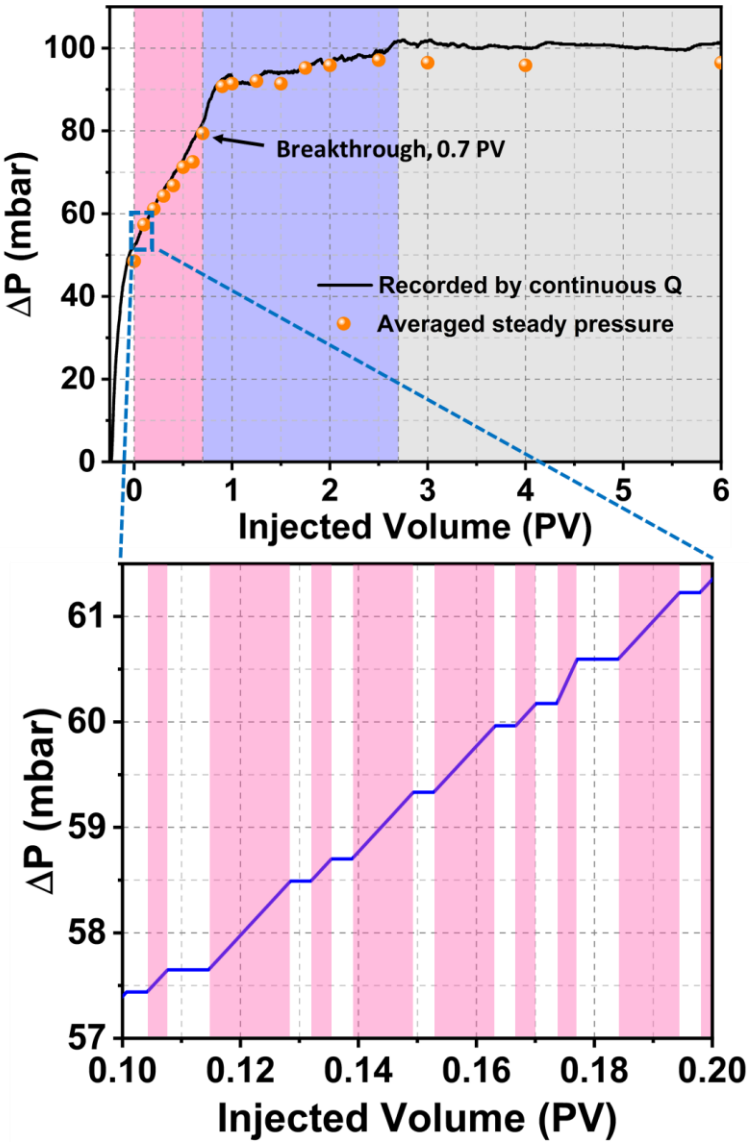

Figure IV-13 *The recorded pressure drop (ΔP) in function of injected volume at Q=0.1 µL/min (top), and a magnified view of local ΔP at the stable displacement (bottom). The results recorded for continuous Q (black line) compared to the average pressure recorded by image analysis (orange point), respectively. The pink region represents the stable displacement period, the blue region represents the arrangement period, and the grey region represents the steady state.*

IV.1.2.3 Influence of Subsequent Increase of Flow Rate

Unlike the multiple independent experiments previously reported on the effect of Q on invasion stability (Yiotis, et al., 2021) (Chen, et al., 2023), to explore the variation of the remaining water and phase distribution with the imposed flow conditions, we incrementally increased the Q. After the drainage at 0.1 µL/min was over, we sequentially injected 6 additional PV of oil at flow rates of 0.5 and 1.0 µL/min, while recording the ΔP and acquiring the images of each corresponding period to analyze the changes in fluid distribution and dynamic behavior within the micromodel. **Figure IV-14** shows the saturation of water plotted as a function of the injected volume of oil at three different Q. It is then observed that as the Q increases, the S_{wi} decreases from 0.16 to 0.11 after a one-decade increase in Q. This reduction

in S_{wi} is reflected in the corresponding steady-state chip images at different Q, where the volume of remaining water is usually smaller and smaller, with more red regions and fewer blue regions.

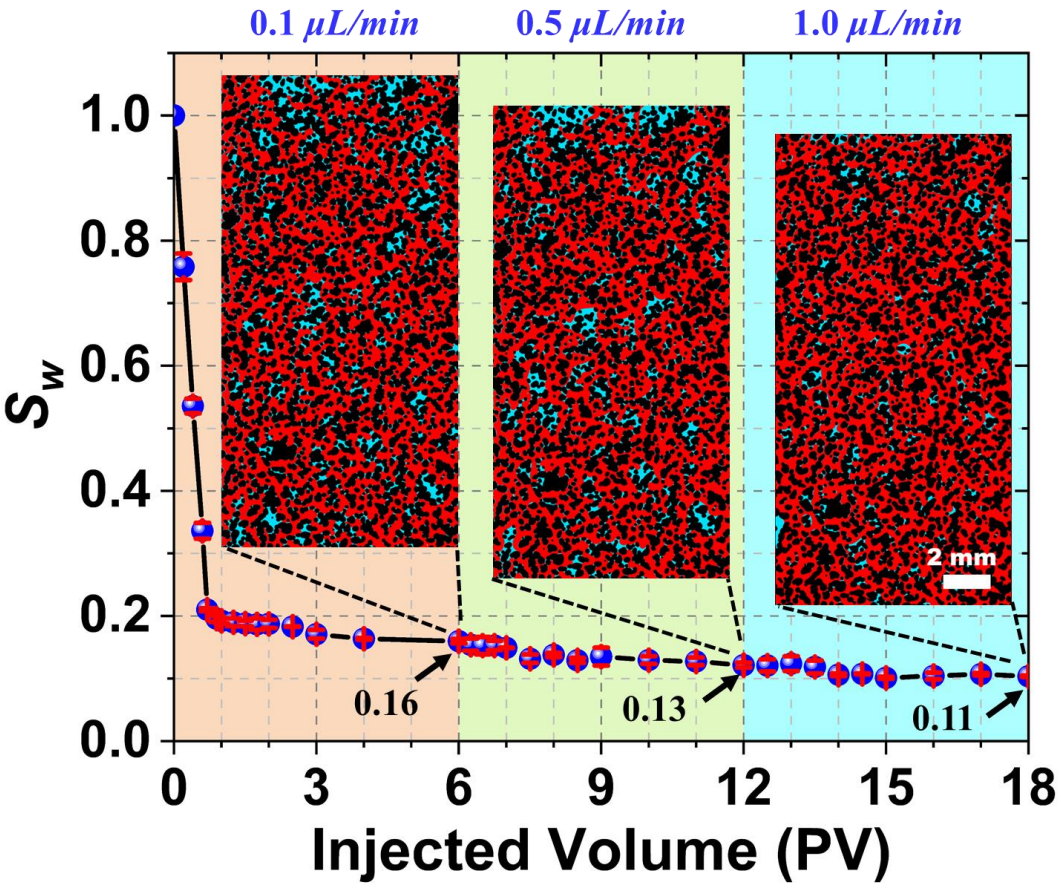

Figure IV-14 *S_w in function of the injected oil pore volume for three different flow rates: 0.1 μL/min, 0.5 μL/min, and 1.0 μL/min. The chip images and S_{wi} at steady state for each period are also displayed.*

By doing so, while M remains fixed, Ca_{new} increases from 7.1×10^{-3} to 7.1×10^{-2}, by increase in viscous force and the resulting increase in local pressure make that many smaller pore necks may now be overpassed. As the diagram displays in **Figure IV-15**, when these two additional experiments are reported, increasing Q moves us to a more state of displacement, leads to a more continuous flow in the pores, resulting in a decrease in the quantity of trapped phase as the end-state images shown in **Figure IV-14**. This observation holds true even when considering the boundary regions defined by Lenormand. As a consequence, S_w decreases.

In oil-wet microchips, the saturation and flow behavior of the wetting phase differs significantly from that observed in water-wet experiments. Typically in drainage processes of oil-wet medium, the oil phase, which is more viscous, acts as the wetting phase, while the less viscous water serves as the non-wetting phase. Therefore, when using the same solutions as in water-wet experiments, lower Ca and unfavorable M lead to a flow regime characterized by either viscous fingering or capillary fingering. This results in earlier breakthroughs and lower saturations of the invading phase. However, a larger proportion of the wetting phase gets trapped within the pores due to capillary forces, leading to

significantly higher saturations of the wetting phase compared to water-wet scenarios, both at breakthrough and at the final steady state (Meybodi, et al., 2011) (Yu, et al., 2019).

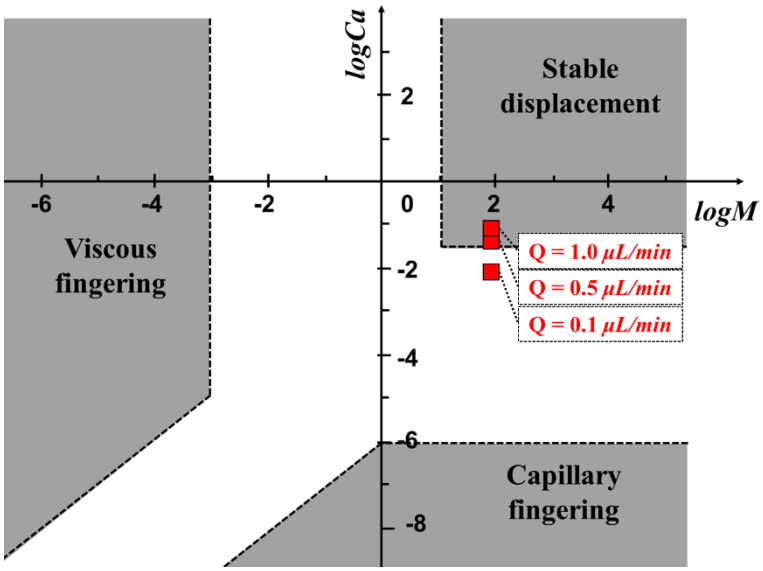

Figure IV-15 *Position of the 3 flow rates experiments (red square) on the logCa/logM diagram.*

Also, as before, and through image processing, we determined the location of the remaining water under the end state of each Q and the corresponding distributions are displayed on **Figure IV-16** (a-c). Comparing the results with the original pore size distribution, a change in water distribution is detected even it is so small. Subsequently, to gain a more precise understanding of how the remaining water changes with Q at steady state, we calculated the proportion of pores number occupied by water in different size ranges of the original pore sizes. As shown in **Figure IV-16** (d), the number of pores containing water decreases in overall as Q increases. Due to the increasing pressure within the pores with Q, which can overcome the minimum pressure required to displace water from smaller pores. Consequently, not only is the water in the "water film" in smaller pores displaced, but some of the "trapped water" surrounded by smaller pores is also displaced. Furthermore, at steady state, the majority of remaining water is found in smaller pores (<100 μm), with more than half of it remaining even after a decade increase in Q. These water film and trapped water within these small pores still exist in the form of continuous pathways.

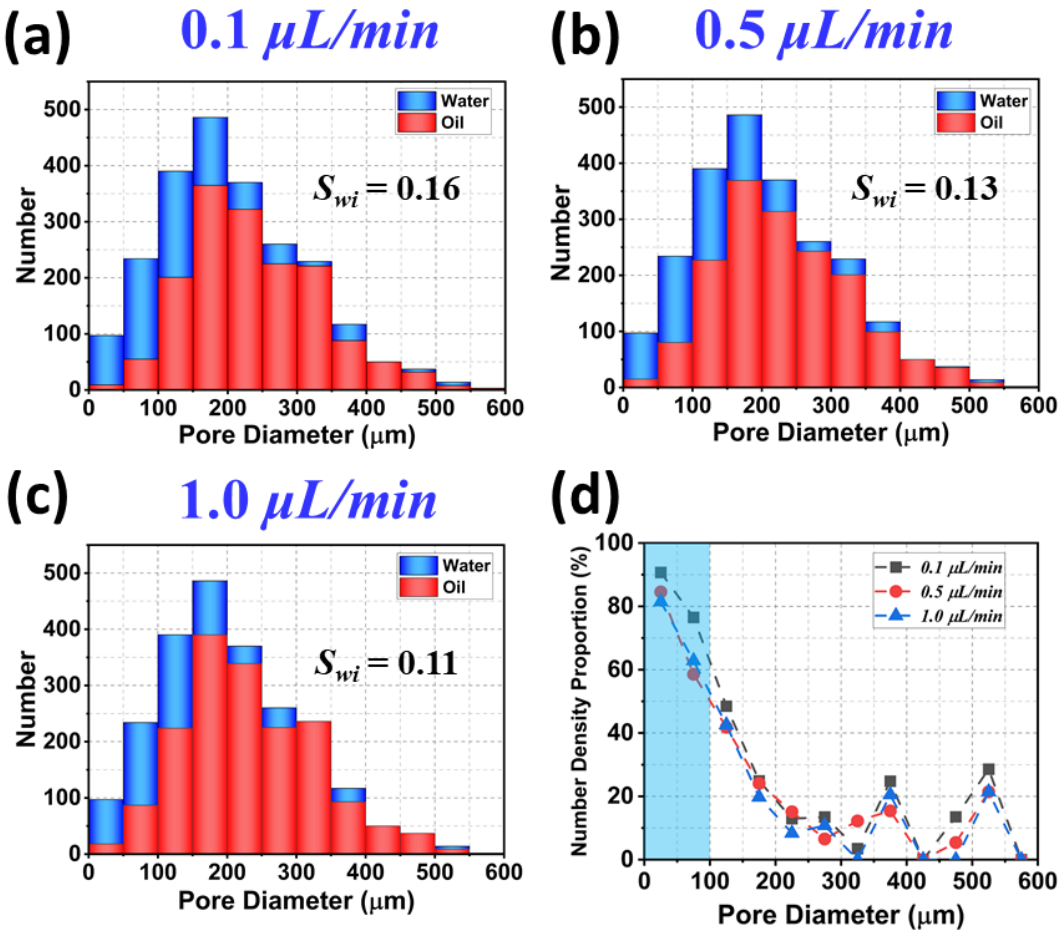

Figure IV-16 *the statistical distribution of oil and water in the original pore sizes at steady state with flow rate for (a) 0.1 μL/min; (b) 0.5 μL/min; (c) 1.0 μL/min; and the corresponding proportion of remaining water pores in different pore sizes.*

Therefore, we speculate that the direct cause of the transformation of the remaining water is the change in ΔP within the chip, where larger ΔP result in the breakage of water ganglia. This is corroborated by the ΔP plotted as a function of the volume of injected oil at successively increased Q on **Figure IV-17**. The ΔP has a significant increase after increased the Q until reach a plateau, which means that the invading oil phase, as Q increases, continuously overcomes larger critical capillary forces, displacing the remaining water from smaller-sized pores.

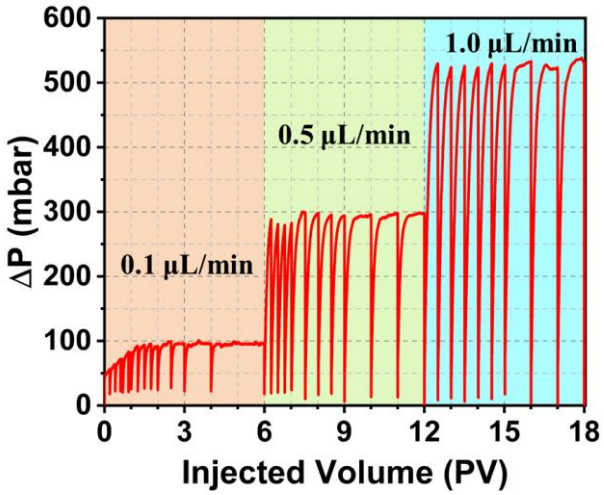

Figure IV-17 *In live ΔP plotted as function of injected oil volume for the 3 flow rates from 0.1 to 1.0 µL/min. The red verticals represent the flow stop to acquire images.*

IV.1.2.4 Permeability of Oil at S_{wi}

After achieving steady state at Q of 1.0 µL/min, the permeability to oil at S_{wi}, $k_o(S_{wi})$, was measured by decreasing Q from 1.0 µL/min to 0 and recording the corresponding ΔP. Five independent experiments, denoted as E_{KOD1}, E_{KOD2}, E_{KOD3}, E_{KOD4}, and E_{KOD5}, were conducted and the time averaged ΔP obtained for each Q during steady state are presented in **Figure IV-18**. As it may be seen, all data points of different colors, do lies within the gray region, which accounts for the normal deviation caused by instrumental sensitivity and operational factors during the measurement process. By calculating the average of all measurement data, a linear repression of ΔP versus Q can then be obtained and by using Darcy's law the effective permeability $k_o(S_{wi})$ is found to be as 4.5 ± 0.18 Darcy. So, the value of $k_o(S_{wi})$ is significantly higher than the 2.7 Darcy value for pure water K_w. Indeed, the water film covering the pore surfaces reduces the resistance to oil that more easily flow in the center of pores that are filled by oil.

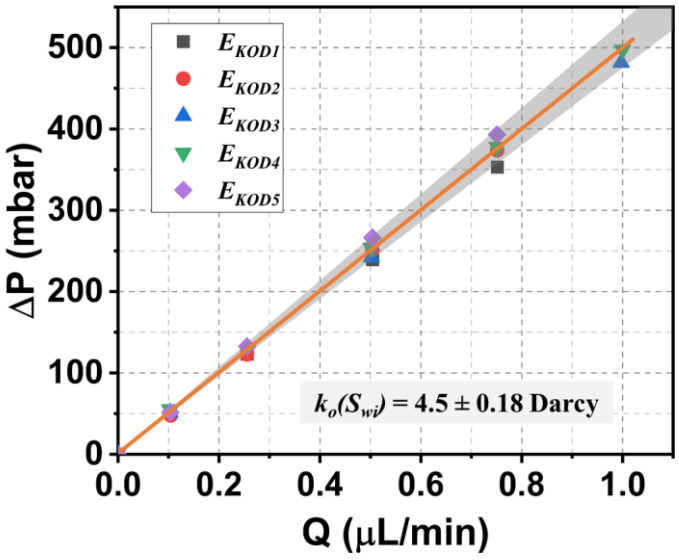

Figure IV-18 *ΔP versus Q at steady state for five different experiments. Data are represented by symbols (within the gray region), the continuous line is a linear regression.*

IV.1.2.5 The Influence of Network Structure

Figure IV-19 and **Figure IV-20** respectively illustrate the oil drainage of the random chip and the regular chip, as well as the micro-model images of oil breakthrough in the random chip and the regular chip. On contrary to the random chip, in the regular chip, a clear delay of oil breakthrough and smaller water saturation can be observed, even with the successive increase in flow rate from 0.1 to 1.0 µL/min. Since the same experimental procedure was conducted in this experiment, indicating that the viscosity of fluid and Ca remained unchanged, fluid flow is only influenced by the network structure. In the regular chip, due to the advantageous viscosity of the oil phase invasion, the oil phase invades and saturates the pore bodies and pore throats step by step with a relatively stable interface. Moreover, due to the nearly non-existent pressure difference between each pores, the capillary resistance experienced by the oil front during invasion is uniform, resulting in a higher invaded efficiency and requiring a smaller pressure drop for oil invasion. Consequently, this leads slow down breakthrough and lower the remaining water saturation. This observation is further confirmed by the micro-model image at the breakthrough moment in **Figure IV-20**, where remaining water is barely visible in the invaded region in regular chip. With the presence of localized capillary fingering at the micro-scale, as shown in **Figure IV-21**.

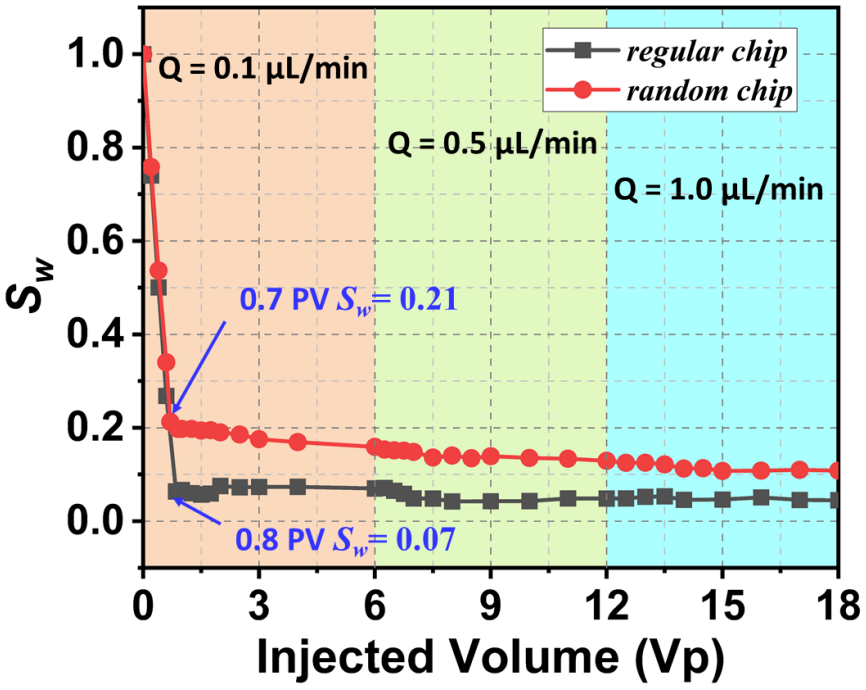

Figure IV-19 *The oil drainage performance at three different flow rates, for the random chip in red, and the regular chip in black. The arrows indicate the breakthrough volume and the corresponding water saturation (Sw).*

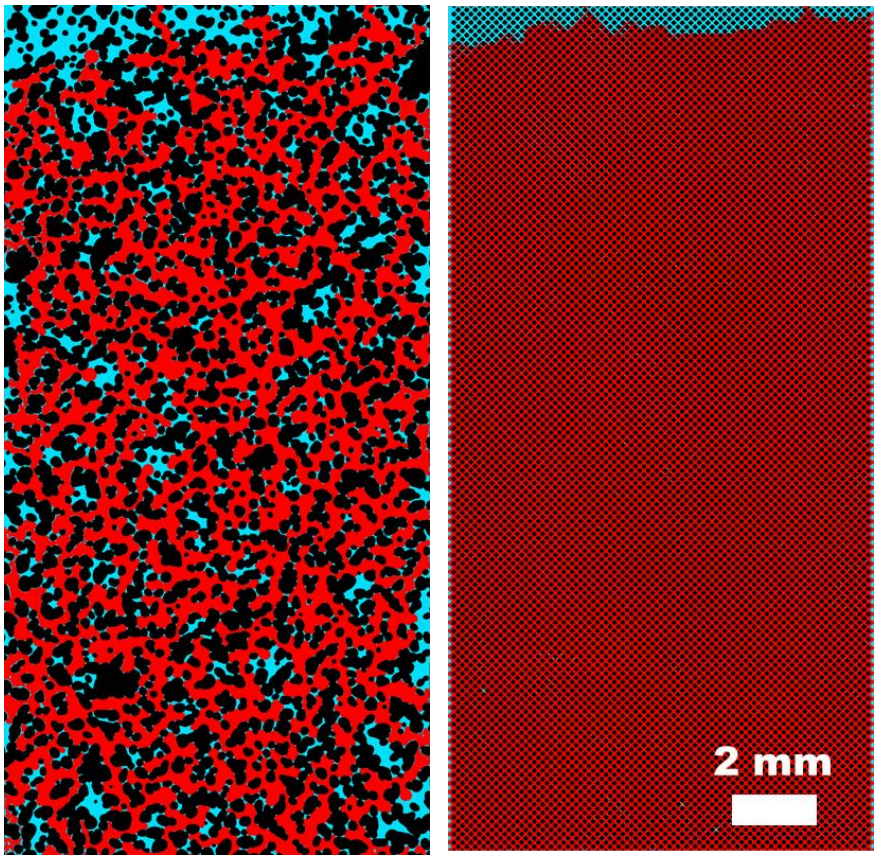

Figure IV-20 *The color-modified image illustrates the distribution of remaining water and oil at oil breakthrough in random chip (left) and regular chip (right). Blue represents water, red is the oil, and black is the solid grains. Both scale bar is 2 mm.*

Of course, similar to the random chip, we can observe a similar flow regime in the regular one before oil breakthrough. In **Figure IV-21**, we display the local flow patterns at the fluid front interface when injecting 0.2 PV of oil. It can be observed that compared to the random chip,

At the microscale, the regular chip, due to its simpler pore structure, exhibits a more stable invading front, with only a few noticeable capillary fingers. In contrast, the random chip, with its complex pore structure, allows oil to invade through wider flow paths. Therefore, within the same field of view, we can only observe limited fingering. Moreover, significant differences are observed in the oil invasion region as it may be seen in the right image of **Figure IV-21** since only a small amount of water of small size is trapped in the pore throats in the regular chip (the blue point in the red area and corner of the grains), similar with other reported works (Saadat, et al., 2020). On contrary, in the random structure shown in the left image, the amount of remaining water is significantly higher and is also trapped in large pores that are surrounded by very small one. However, it is worth noting that both structures have a water film coating the pore surfaces, although it may not be easily observed.

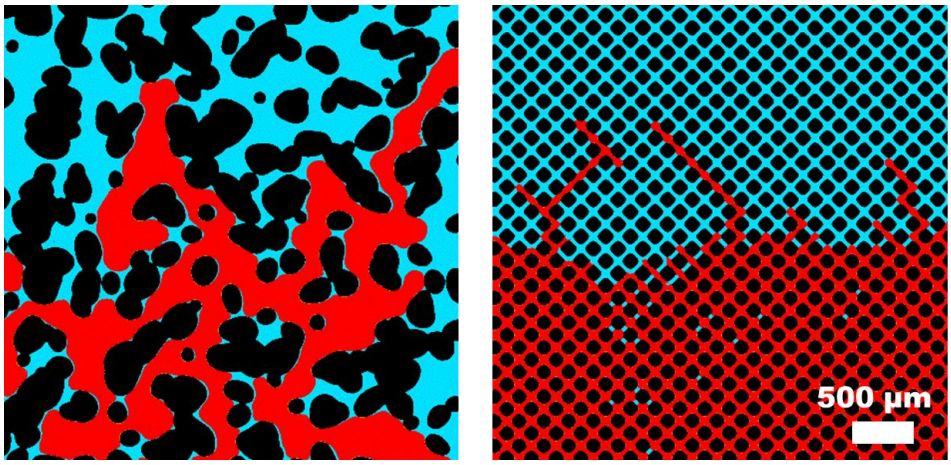

Figure IV-21 *A magnified comparison of the oil invasion between the random chip (left) and the regular chip (right).*

Finally, after achieving steady state at a flow rate of 1.0 µL/min, we similarly measured the oil permeability at S_{wi} by decreasing the flow rate from 1.0 to 0 µL/min using the same procedure as in the random experiments. As shown in **Figure IV-22**, the averaged ΔP for each Q case exhibited a linear correlation for both chips. By using Darcy's law, the oil permeability of the random chip at S_{wi} was determined to be 4.5 ± 0.18 Darcy, while that of the regular chip is 5.1 ± 0.15 Darcy. The reason for the higher $k_o(S_{wi})$ value of the regular chip is that its uniform structure imposes less hindrance and more uniformity on the invasion of the oil phase, allowing the oil phase to flow more easily within the chip, thereby resulting in a higher value.

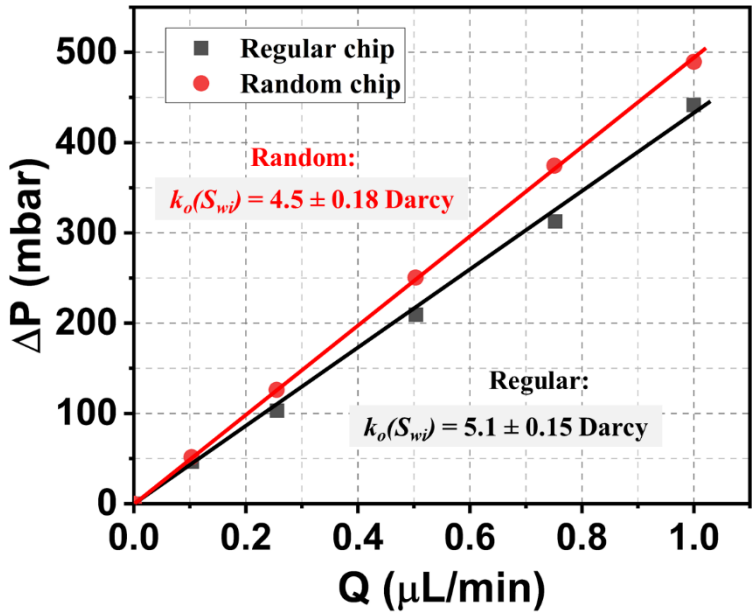

Figure IV-22 *The averaged ΔP versus Q at steady state symbols represents average experimental data for 5 independent experiments for regular chip (in black) and random chip (in red).*

IV.1.2.6 Discussion of Oil Drainage

In the drainage experiments carried out at a Q of 0.1 μL/min and M of 80 in a water-wet chip saturated with water, we focused on observing the macroscopic fluid flow and pore-scale fluid dynamics during the invasion of oil, and analyzed displacement mechanisms.

Through image analysis, we obtained the macroscopic flow states at different injected volumes and observed an almost stable fluid front. Then we calculated the Ca using classical method worth 1.2×10^{-5} with corresponding M of 80, it was observed fall within transition zone between the capillary fingering and stable displacement regime on the logCa/logM diagram, leaning closer to the capillary fingering region. However, this contrasts with the close stable displacement flow behavior observed experimentally. Therefore, we discussed a more suitable method for calculating Ca for microfluidic chip models and used a correction factor (G ~ 449.3), resulting in a new Ca value ($Ca_{new} = 7.1\times10^{-3}$). This adjustment moved the flow regime closer to the stable displacement region on the logCa/logM diagram, though it still remains within the transition area. The Ca_{new} not only maintains consistency between microfluidic experimental results and the logCa/logM diagram, but also aligns our findings with results from two-phase flow experiments in 3D porous media using classical calculations of Ca (Hu, et al., 2020).

Furthermore, to demonstrate how the oil invasion process depends on the porous medium structure, we selected a localized region in the chip and recorded a video of oil invasion over time. Analysis of the video snapshots revealed the cyclic invasion process of oil into pore bodies, hindered by pore throats, known as Haines jumps, which also corresponded to observed changes in ΔP. Specifically, after oil was hindered by pore throats, the ΔP gradually increased until it overpassed the critical capillary force at that throat, which is solely influenced by throat size. Subsequently, oil rapidly passed through the throat and saturate the pore body, without requiring additional potential energy, leading to a stable ΔP. Oil invaded sequentially along the path of least resistance in pore bodies, resulting in a rapid linear decrease in S_w before breakthrough at 0.7 PV. Following breakthrough, drainage entered an arrangement period, where oil continued to invade larger pores along non-flow paths initially missed, causing a slow increase in ΔP until reaching steady state, corresponding to S_w decreasing from 0.21 to 0.16.

In the post-invaded porous medium, the remaining water reside in smaller pores, as quantitatively analyzed from the original pore size distribution. This observation was confirmed in the video results, where remaining water was mainly observed in water films on pore surfaces, small spaces at pore edges, throats, and smaller pores. To mobilize remaining water, higher pressure is required to overcome the critical capillary force, prompting an investigation of the influence of Ca, that was achieved by increasing Q by one decade. The logCa/logM phase diagram indicated therefore that all three cases considered were located in the stable displacement regime, with larger Q resulting in a more piston-like front and consequently lower S_w. Additionally, the statistical distribution of oil and water in the original

pore sizes at steady state of the three cases showed that as Q increased, remaining water in intermediate-sized pores was preferentially mobilized and discharged along continuous paths on the chip surface, leading to a decrease in S_{wi} from 0.16 to 0.11.

In the drainage experiments, five independent experiments were conducted. After reaching S_{wi} at Q = 1.0 µL/min, Q was successively decreased from 1.0 µL/min to 0, and the corresponding ΔP was recorded. The linear correlation between Q and the corresponding steady state ΔP was observed and according to Darcy's law, the permeability of oil at S_{wi} $k_o(S_{wi})$ was determined to be 4.5 Darcy, significantly higher than the initial permeability of pure water (K_w = 2.7 Darcy). Due to the water film at solid surface letting oil to flow in central zone of pores.

IV.1.3 Waterflooding Imbibition

After reaching S_{wi} during the drainage, the waterflooding experiments were performed. Five independent experiments were conducted, and the results were averaged to obtain representative data. In these experiments, we observed and analyzed the mechanism of "snap-off" during brine imbibition in waterflooding. We also investigated the macroscopic flow patterns and the microscopic effects on oil clusters influenced by capillary forces and geometric structures during brine invasion. The capillary forces have been considered as important forces impacting the mechanism of immiscible fluid displacement (Chang, et al., 2009). Moreover, the saturation of the oil (S_o) as a function of injected brine pore volume (PV) determined through image analysis, and shows the corresponding change of recorded ΔP. We also consider again the steady-state distribution of the water and oil phases within the original pore sizes at residual oil saturation (S_{or}). Finally, we discussed the influence of Ca on residual oil saturation and recovery efficiency by increasing Q. This experiments series end with measurement determination of the water phase relative permeability at S_{or} ($k_w(S_{or})$). Our expectations extend beyond simply monitoring macroscopic flow behavior and calculating saturation; we aim to delve deeper into the pore-scale mechanisms that mobilize oil clusters by increasing Ca. We seek to understand the distribution and variability in the ease of mobilizing different oil clusters, preparing for tertiary step operations.

IV.1.3.1 The Fluid Dynamics of Waterflooding Imbibition

After the detailed oil drainage process discussed in the previous section, we carried out waterflooding experiments in the chip by injecting dyed brine at a Q of 0.1 µL/min, corresponding to a viscosity ratio M of 1/80 and a Ca_{new} of 8.89×10^{-5}. This flow rate was selected based on field data from actual oilfield operations to enhance the controllability, repeatability, and better simulate real conditions in underground oil reservoirs. These experiments are clearly located within the transition area between viscous fingering and stable displacement regime but they are very close to the viscous fingering zone on the logCa/logM diagram (see **Figure IV-23**). This indicates a combination of flow conditions where viscous fingering is more important in determining displacement of the interface between the injected

brine and the displaced oil. While the logCa/logM diagram provides a comprehensive overview of the flow regime, it may lack detailed insights into specific dynamics. Fortunately, our experimental setup allows us to observe the waterflooding process to investigate the effects of capillary and viscous forces on the brine invasion.

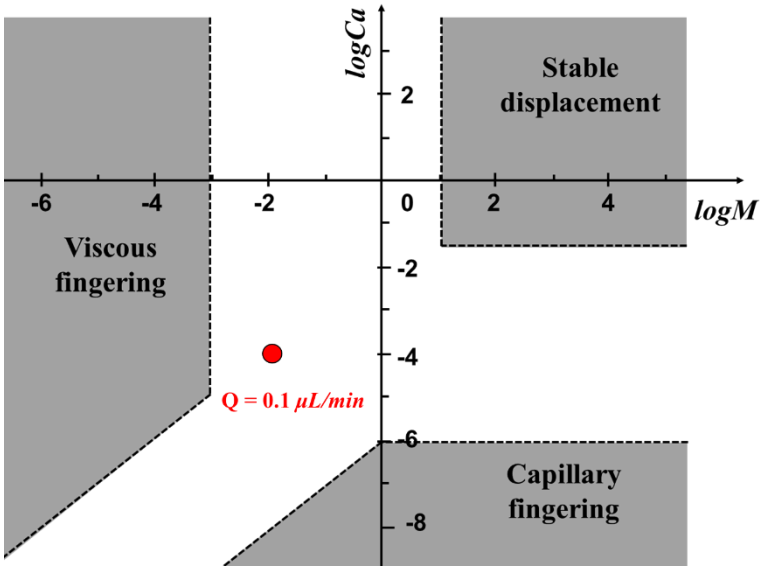

Figure IV-23 *Position of imbibition experiment at Q = 0.1 μL/min on logCa/logM phase diagram.*

Therefore, we conducted continuous monitoring and recording the flow of each phase within the chip during the waterflooding experiments. **Figure IV-24** displays the phase distribution patterns recorded during the experiment before brine breakthrough, showcasing how the phases evolve at intermediate stages of brine injection. Waterflooding begins at a specific initial water saturation (the irreducible water phase saturation remaining after drainage) and is conducted at intermediate capillary numbers.

Phenomenologically, at the pore scale during the initial of imbibition, the brine rapidly flows along the grain walls and smaller pores, following the previously contacted pathway. This allowed the brine to effectively snap off oil segments trapped within crevices of the porous medium, leading to oil displacement from the pores through intermittent, abrupt bursts starting at the inlet, leaving discrete oil ganglia of varying sizes in its wake.

However, macroscopically, the invasion shows viscous fingering phenomenon due to the lower viscosity ratio between the invading brine and the displaced oil. In this unfavourable situation, the brine rapidly follows the preferential flow paths, characterized by the formation of tree-like structures extending towards the outlet. However, the brine may never imbibe into all pores of a given size as a result of entrapment of the oil phase by snap-off. The early phase of the imbibition process is characterized by the development of single-branch preferential flow paths, the invading phase rapidly grew at the front position, while the bulk of the invading fluid at the near inlet area grew forward with a relatively lower speed. These paths, with a fingering width that extends approximately three to five pore sizes, are

predominantly directed towards the outlet with minimal lateral movement, leading to an early breakthrough (~ 0.2 PV). This mechanism results in a relatively low invasion saturation (S_o ~ 0.60). As the injection continues, some fingers begin to advance in transverse or even backward directions, amplifying the complexity of the flow dynamics within the chip, resulting in a wider flow path (~6-8 pore sizes). These viscous fingers, governed by the differential viscosity under significant viscous control, create an unstable interface that propels multiple brine fingers toward the outlet. After the breakthrough, a significant volume of oil clusters are trapped within the chip and this residual oil is present in the pores as bulk oil varying in size from pore scales up to macroscopic aggregates.

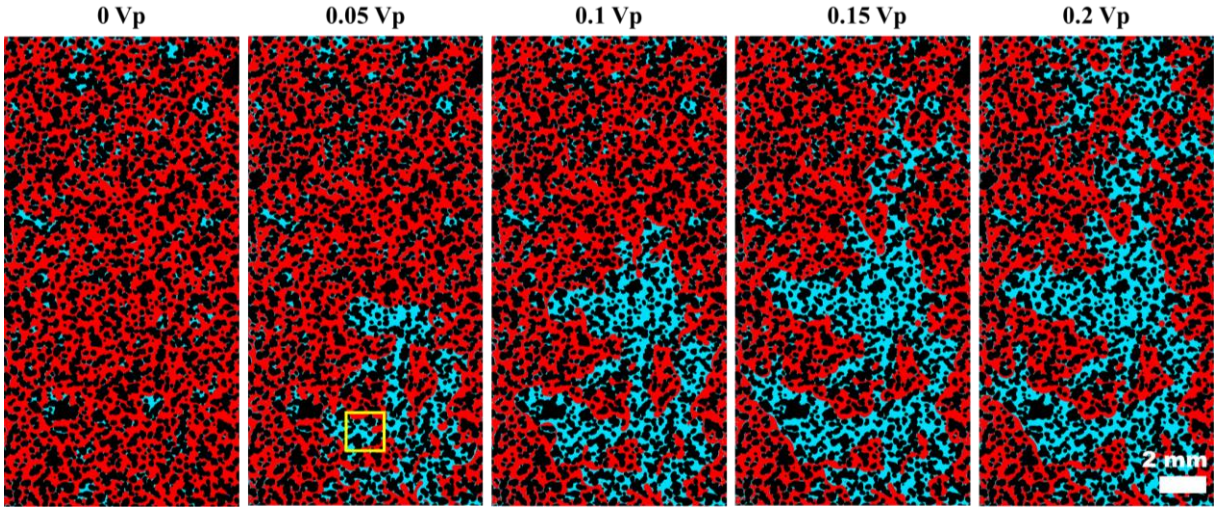

Figure IV-24 *The evolution of invasion morphologies at successive the injected volume of brine during the waterflooding imbibition.*

Furthermore, to illustrate how the brine imbibition process is influenced by the structure of porous medium, a location (highlighted by the yellow box in **Figure IV-24**) was randomly selected, and a video in this area was recorded over time. From this video, several snapshots were extracted and are presented in **Figure IV-25** to demonstrate the swelling of connate water films and snap-off in our chips. In these snapshots, the solid grains are depicted in grey, the yellow color stands for water, and the light pinkish regions represent the oil phase. In this snapshots, blue arrows indicate the water saturation way, while red arrows indicate the direction of oil movement.

The time interval from 0 to 6 seconds in **Figure IV-25** depicts the process of water saturating the pores along water coating film, and pore throats. At the beginning of the displacement, brine tends to flow through the continuous water film path, thus a swelling of the water film appears. As water imbibition continues, the filling increases, causing the original oil phase in the pores is gradually displaced with a capillary pressure decreases. This phenomenon is consistent throughout the entire microfluidic device during the water imbibition process. Subsequently, the wetting phase fluid occupies the throat and push the oil phase into pore bodies, resulting in the thinning and collapse of continuous oil phase at the adjacent pore throats. When the ΔP become lower than the local critical capillary pressure, the oil phase

breakup at the throat (highlighted in red circle), leading to oil snap-off, as shown from 6 to 7 s. At soon as oil break, it rapidly moves towards the adjacent pores, causing a portion of the water to be expelled from the pores and a transient increase in ΔP should then be observed. As the wetting phase re-saturates and reaches equilibrium, the pressure gradually returns to its original level or slightly decreases to a stable value, as the snapshots shows from 7 to 9 s.

When the local water saturation reaches a certain level of equilibrium, the pressure in pores becomes relatively stable (e.g., processes from 9 to 11 s and 19 to 23 s). The invasion proceeds spontaneously without the need for additional force until there is a sudden change in the saturation of the oil phase. Subsequently, as the saturation of the wetting phase continues to increase, localized collapse and snap-off of the non-wetting phase in pores may continue to occur (as in the process from 11 to 19 s), corresponding to a local increase in pressure drop at the breakage event; or continuous displacement of the non-wetting phase from the pores may occur (as in the process from 23 to 26 s), corresponding to a decrease in ΔP.

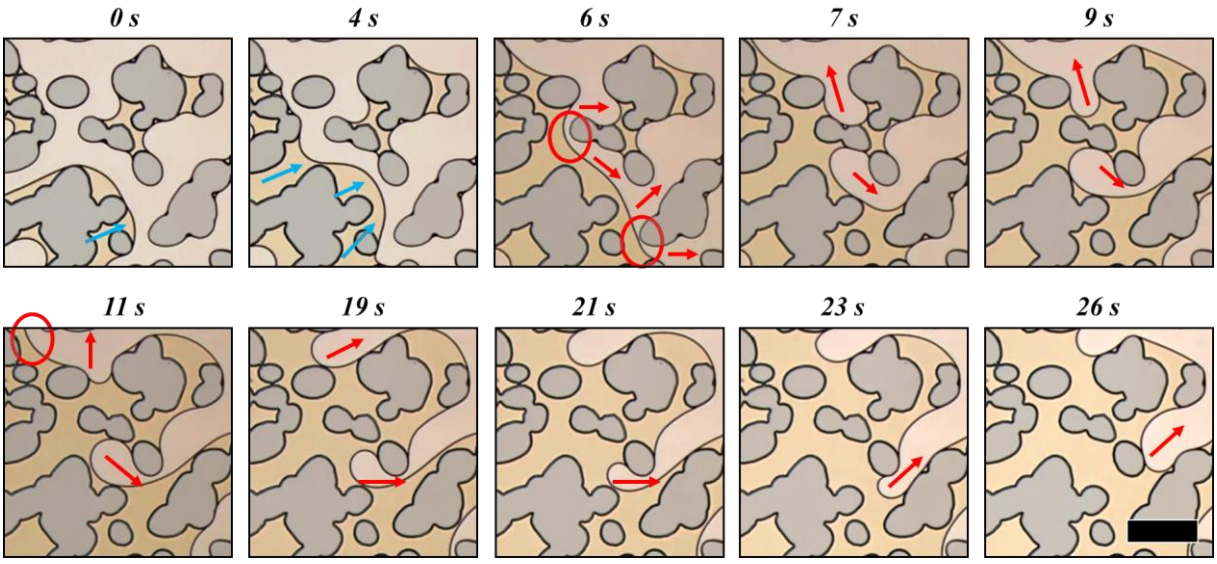

Figure IV-25 *The saturation variation and displacement details of the immiscible two-phase flow during the brine imbibition. The blue arrows indicate the saturation direction of water, while the red arrows represent the flow direction of the oil phase. The red circle denotes the throat where snap-off occurs. The scale bar is 500 μm.*

Of course, in waterflooding, sometimes, after a break or snap-off oil become trapped, forming new oil ganglia. For instance, after snap-off, one pore or a group of pores containing oil can become isolated from the rest of the oil bank. This isolation occurs because the oil phase fails to rapidly fill the adjacent pore bodies and maintain sufficient capillary pressure at the pore throats. Consequently, the oil is displaced by the invading wetting phase (brine), leading to its segregation within the porous medium. This process continues intermittently until the second pore body is filled, allowing the non-wetting phase in both pore bodies to remain connected without experiencing further snap-off events. Similarly, this "trapping" phenomenon can occur in single or multiple pores, depending mainly on the geometry of the

pore network. A small amount of oil may be broken in droplets and leave the pore as the water saturation increases until lacking sufficient driving pressure to overcome the capillary entry pressure for the now water-saturated pore throat, the oil is then trapped in place. The residual oil adopts the form of minimum interfacial energy, typically spherical or ellipsoidal, and remains at the center of the pore (as shown in **Figure IV-26**). The front of the water phase rapidly penetrates the porous medium along the path of highest hydraulic conductivity, while the areas unswept by water retain the oil phase in the form of large ganglia.

After breakthrough, the water phase flows along the swept pores as a continuum and gradually saturates the not-yet swept ones in the non-flow direction through the connection pathway. This process is accompanied by the recovery of a certain amount of oil phase until a higher water cut is reached. The smallest clusters of remaining oil are broadly spherical in shape, centered in a single pore, while the larger clusters are overall fatter and reflect the connectivity of the widest pore spaces. This observation aligns with the core experiments results reported by Ryazanov, et al (Ryazanov, et al., 2014) and Iglauer (Iglauer, et al., 2012). They also reported works in oil-wet cores, showing that the genuinely trapped oil is very low, and from the occupancy statistics, for the most oil-wet cases, oil layers are present in all pore sizes, but bulk oil is only present in the smallest pores. This is clearly due to the persistence of oil layers which allow oil drainage down to very low levels.

We will now proceed to analyze in detail the occupancy statistics of residual oil in the water-wet chip and its location and presence state within the chip.

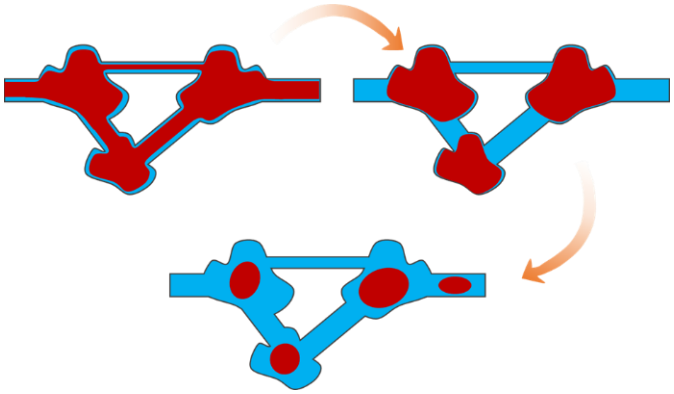

Figure IV-26 *The schematic representation of the imbibition process of the wetting phase (in blue) within pores saturated with the non-wetting phase (in red). Residual oil is trapped within the central regions of the pores within the swept area.*

As dominant mechanisms for oil entrapment in porous media, Roof (Roof, 1970) early describes oil snap-off as the formation of oil droplet due to oil being pushed through a water-wet constriction into a water-filled pore. Alzahid, et al. (Alzahid, et al., 2018) underlined that the occurrence of snap-off is also largely dependent on the specific pore geometry. Generally, snap-off occurs during the imbibition process only at pore throats due to differences in capillary pressure caused by the curvature of the pore

wall (Chang, et al., 2009) (Zhao, et al., 2019). This aligns with the results observed in our experiments as represent above. Furthermore, and as reported by Alzahid, et al. (Alzahid, et al., 2018), the collapse of the interface development leads to snap-off events, happening not only during the initial invasion of brine but also when a ganglia spans multiple pores in the porous media. During imbibition, flow instabilities damping due to the contrast of fluids properties and porous medium geometry, resulting in differences in capillary pressure. The leading and trailing ends of the oil ganglia have a certain capillary pressure, while the constriction of the pore throat between adjacent pores can result in a larger capillary pressure due to the swelling of wetting film in the neck region. Therefore, we present a case from the images acquired during waterflooding, showing a snap-off event and the resulting oil clusters (**Figure IV-27**).

Between 0.25 PV and 0.30 PV, a snap-off event occurred. Firstly, by comparing images at 0.2 PV and 0.25 PV we can see the changes in a ganglia (before snap-off are shown), undergoing a noticeable and elongation refinement at the pore throat indicated by the yellow arrows. Eventually, snap-off occurs there when the capillary force decreases to the critical capillary force and then the ganglia collapse and rearrange. At 0.3 PV and 0.4 PV, the flow details of the two ganglia after snap-off are depicted. When the larger upstream ganglion "a" exhibits a tendency of reverse flow near the snap-off (white circle area), which due to the capillary forces on both sides of the ganglion at the throat are greater than the pressure in the adjacent pores, at the moment of snap-off, this is usually named as a "form relaxation". Therefore, the oil ganglia "a" and "b" have been pushed towards regions of lower pressure (yellow elliptical areas). Specifically, the front of oil ganglion "a" shows slight reverse flow towards pores in opposite direction to the main flow, while its rear end shows no significant movement. Oil ganglion "b", on contrary, moves in overall towards next pores in the flow direction. The pressures at the throat during snap-off, as well as the pressures P_{c1} and P_{c2} at the front and rear of the oil ganglion before snap-off, are shown in **Table IV-4**. It can be observed that the pressure experienced by the ganglion at the marked throat is much higher than that at the front and rear of the ganglion. Therefore, the ganglion undergoes interface flattening at the throat under the both side pressure of the brine (the yellow arrow), leading to a significant deformation of the ganglion before snap-off. When the capillary forces decrease to the critical capillary force at the throat, the ganglion is completely break-up, splitting into two new ganglia. Generally, downstream ganglia tend to be smaller in size, making them more susceptible to subsequent mobilization, except for blocking by the solid phase, while upstream ganglia tend to be larger and are more likely to remain trapped due to continued capillary forces. After stabilization (0.4 PV), the ganglia are trapped in the pores in a low-energy state, characterized by an increase in interface curvature. In summary, the snap-off strength depends on specific pore geometries, i.e., pore wall curvature.

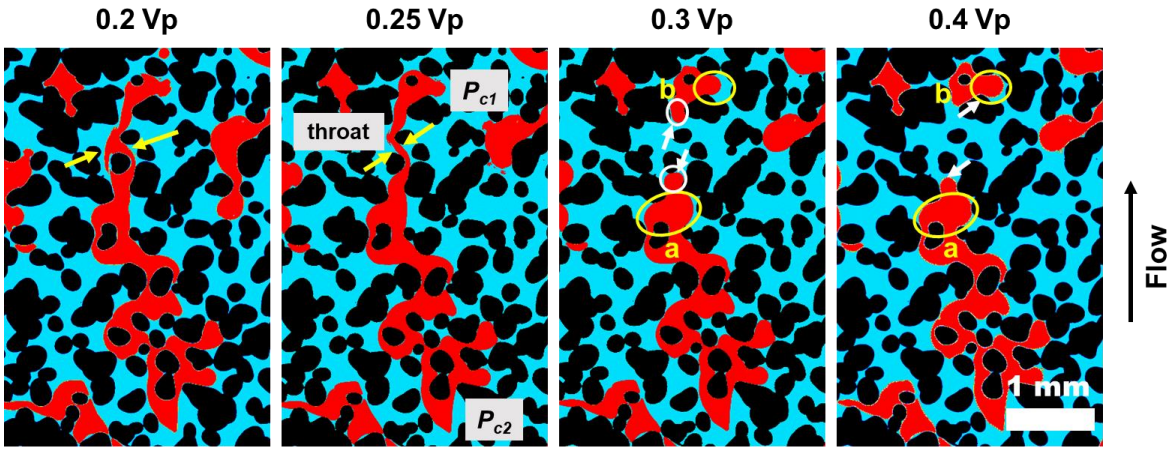

Figure IV-27 *Occurrence of the snap-off process of oil after breakthrough at the same waterflooding flow rate. The yellow arrows indicate the position of this event and the direction of brine squeezing. The white arrows indicate the subsequent movement trends of the new ganglia a and b after the snap-off. The white and yellow circles show the movement trend of the sub-ganglia after the breakage in the adjacent pores.*

Table IV-4 *Capillary pressure measurements at throats and P_{c1} and P_{c2} of front and end of ganglia before snap-off*

Location	IFT (N/m)	Curvature diameter (m)	P_c (Pa)
Throat	5.58×10^{-2}	1.15×10^{-4}	9.72×10^{2}
P_{c1}	5.58×10^{-2}	2.34×10^{-4}	2.38×10^{2}
P_{c2}	5.58×10^{-2}	1.86×10^{-4}	3×10^{2}

IV.1.3.2 The Residual Oil Distribution and Saturation

On the macroscopic scale, in the starting state, water occupies small pores that were not invaded by oil, while oil occupies large pores. Therefore, during waterflooding imbibition, the water relative permeability (k_{rw}) starts low and increases as water saturation increases. Conversely, the oil relative permeability (k_{ro}) is initially high because oil flows through the largest pores, but it decreases as oil saturation decreases. Due to wetting forces, water saturation initially increases preferentially in smaller pore spaces. As displacement progresses from smaller to larger pores, water increasingly occupies previously oil-filled pore throats, leading to snap-off events that trap oil. The onset of oil trapping marks the beginning of water flowing as a continuous phase. Eventually, all continuous flow paths become filled with water, and oil flow ceases. The final k_{rw} is lower than the original k_{ro} due to the presence of oil trapped in large pores.

Images collected during the waterflooding imbibition allowed us to quantitatively analyze the successive temporal changes of oil saturation during the process, as shown in **Figure IV-28** (only for the case of Q = 0.1 µL/min). It can be observed that the waterflooding start from the S_{wi} state, thus the initial S_o at 0 PV was about 0.9. During the initial stages of waterflooding, as the brine imbibition proceeds, the S_o in

the chip decreases rapidly until breakthrough occurred at 0.2 PV, with a S_o of 0.63. After breakthrough, as the brine continued to be injected at a constant Q, S_o slowly decreased to 0.50, which same with the works of viscous fingering case of Hu, et al. (Hu, et al., 2020). Comparing images acquired at the time of breakthrough and after injecting 6 PV, we can directly observe that the flow paths remain stable. The invading fluid continues to advance along the established flow paths, with the width of the main flow front and other fingers widening. Consequently, resulting in a decrease in S_o, consistent with the results reported in the literature (Lenormand, et al., 1988) (Hu, et al., 2020) (Chen, et al., 2023).

The brine continues to invade after breakthrough, primarily because the contribution of capillarity is essentially independent of the applied capillary pressure and depends on the relative time scales in water-wet porous media (Mason, et al., 2010) (Arab, et al., 2022). Over time, brine progressively infiltrates along existing continuous water film pathways and breakthrough paths, leading to the ongoing displacement of the oil phase, even as the rate of oil recovery diminishes. This indicates that, as reported (Ryazanov, et al., 2014), continuous injection of brine will consistently decrease oil saturation, making it challenging to reach Sor. This is a key reason for our assumption that reaching a "steady state" with the injection of 6 PV of the invading phase is an adequate endpoint for these experiments.

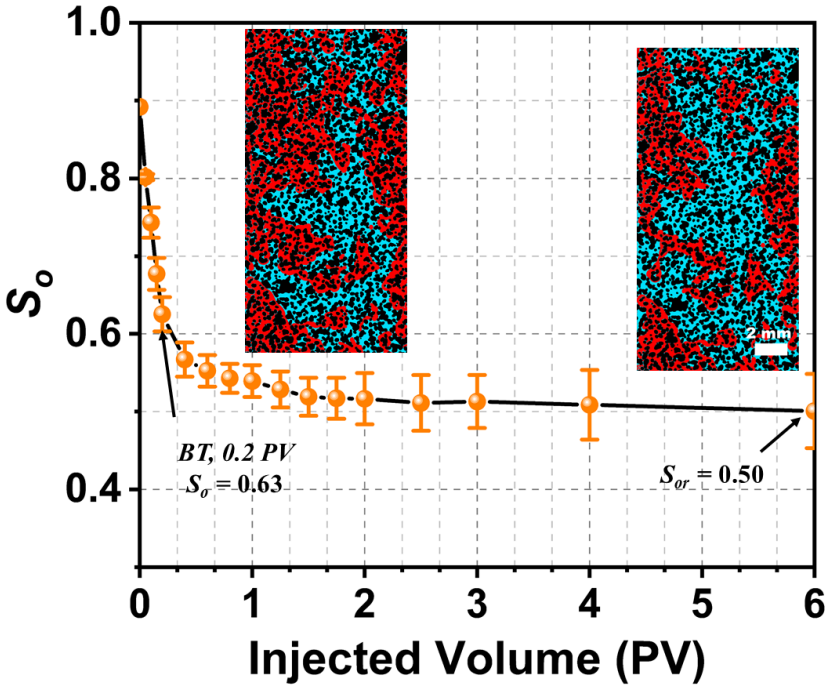

Figure IV-28 *The oil saturation (S_o) plotted as a function of injected volume of brine. Symbols are for data, averaged over five independent experiments. The images acquired at the brine breakthrough and after injection of 6 PV corresponding step reveal the details of the remaining oil saturation.*

At high injection volume of brine, the remaining oil saturation cannot be further easily reduced by additional wetting phase flow due to the complex pore network of the chip and the associated strong capillary forces, which trap the oil phase. As a result, the residual oil phase is split into many

disconnected clusters of different sizes. Hence, here we conducted a statistical analysis of the distribution of oil and water phases in the original pore sizes of the chip at steady state.

Figure IV-29 shows the proportion of original pore size distribution that are filled by water (in blue), and by oil (in red). By comparing, the proportion of pores saturated by residual oil at this steady state with those saturated by oil pores before waterflooding, it is obvious that the displacement of the oil primarily occurs in the medium-sized pores as display in **Figure IV-29** (b), with a noticeable decrease in oil content in larger pores.

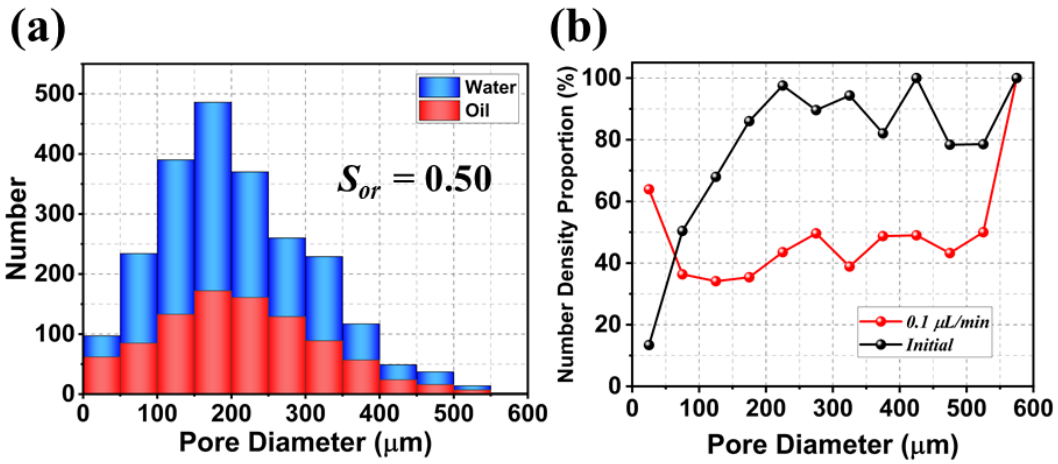

Figure IV-29 (a) The statistical steady-state distribution of oil and water in the original pores; (b) the number density of occupied residual oil phase with original pore size between the end (red line) and start of waterflooding (black line).

In parallel to image taking and processing, the ΔP was recorded in the course of time all along the waterflooding as it may be seen on **Figure IV-30**. The result indicates that the waterflooding imbibition can be divided into three periods: the viscous fingering before breakthrough (blue region), the arrangement period after breakthrough (green region), and the steady-state period (grey region). Similar with the drainage step, our recording of the injected volume in this imbibition begins when the brine starts to invade the oil-saturated porous medium. Before this, the oil phase would first invade the connected channels and fractures upstream, leading to an increase in pressure drop in the chip before 0 PV.

In the initial capillary fingering period, the rapid invasion of brine along the water film improves the overall fluids mobility and reduces the frictional resistance as the fluids passes through the chip, leading to a decrease in ΔP. In addition, besides oil saturation decrease, the continuous occurrence of oil snap-off events during the invasion process reduces the flow resistance of the oil phase, further decreasing ΔP. The combined effect of these two phenomena results in a rapid decrease in overall ΔP within the chip, even after breakthrough (0.2 PV), which is sustained for a brief period. This brief period corresponds to the transient process of brine breakthrough saturating the downstream channels filled with oil phase leading to the outlet. Following this step, the decrease in ΔP becomes significantly less

steep with minor fluctuations in ΔP. This is because, after breakthrough, brine continues to invade the pores around the flow path (transverse or backward), causing ΔP to decrease. Once the movable oil clusters are expelled from the chip along the flow path, the system reaches a stable state, where a significant amount of residual oil is trapped in the pores due to capillary effects.

It is worth noting that in water-wet chips, residual oil primarily exists as bulk with few oil layers. The absence of these oil layers allows the bulk oil clusters to break up and become trapped, hindering capillary displacement processes and resulting in a large amount of trapped oil. Conversely, in oil-wet chips, residual oil primarily exists as oil layers. The persistence of these oil layers allows for continued oil production, resulting in lower levels of trapped oil and S_{or}. When the wettability of the chip falls between these extremes, the remaining oil consists of a combination of bulk oil and oil layers. Laboratory tests on cores prepared with varying degrees of mixed-wet conditions show that slightly water-wet samples yield maximum oil recovery (Jadhunandan & Morrow, 1995).

Moreover, we also make analysis of the ΔP during the initial of viscous fingering period before breakthrough, as illustrated in the bottom part of **Figure IV-30**. We observed these existence of decreasing periods (blue) and plateau periods (white). In combination with combining the snapshots in **Figure IV-25**, the saturation of brine along pore bodies is almost spontaneous, leading to a continuous decrease in ΔP. As water saturation in the pore bodies increases, the oil phase at the pore throats collapses, and snap-off happens when ΔP decreases to the critical capillary pressure. Typically, snap-off leads to a localized increase in ΔP; however, throughout the entire chip, water continues to invade the pore bodies along the flow path, resulting in a reduction in ΔP, which offsets the fluctuations in ΔP caused by snap-off events, and the appearance of the white region with a plateau in ΔP. Exactly, during the initial invasion, the pressure decrease corresponds to the events of brine invasion in pore bodies, while the plateau corresponds to snap-off events in pore throats. Overall, as observed in the video and snapshots in **Figure IV-25**, the occurrence density of snap-off events can vary, corresponding to different intervals due to the influence of porous medium structure.

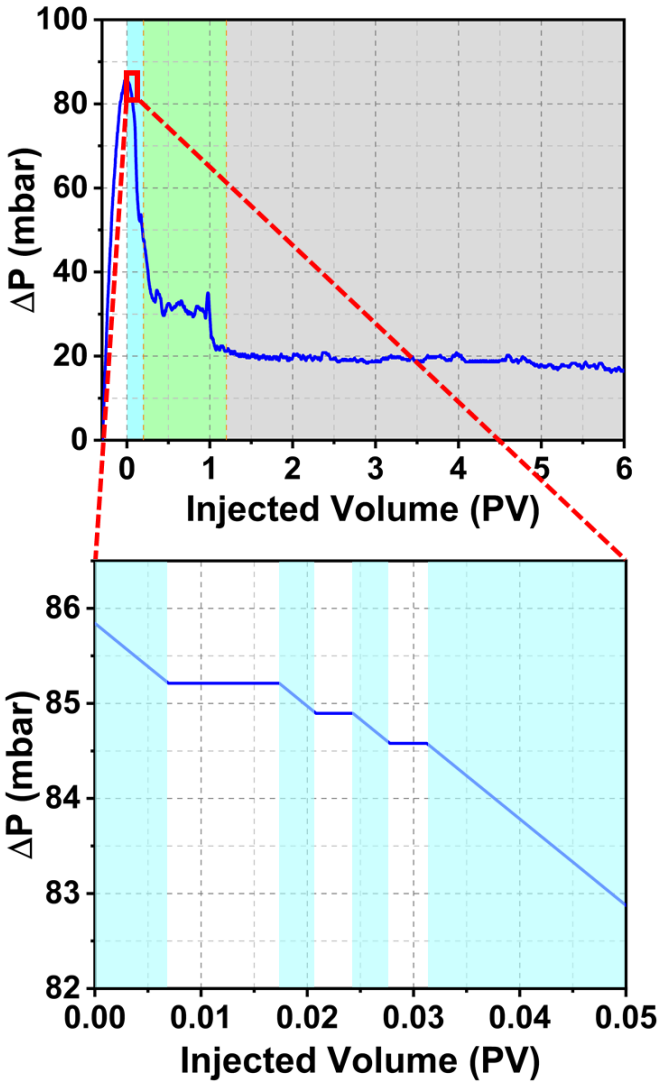

Figure IV-30 *The recorded pressure drop (ΔP) is plotted as a function of injected volume at Q=0.1 μL/min (top), and the bottom image shows the ΔP during the capillary fingering period over injected brine volume as snapshots in* ***Figure IV-25****. In the top image, the blue region represents the capillary fingering period, the green region represents the arrangement period, the grey region represents the steady state; while in the bottom image, the blue regions indicate the decrease of ΔP.*

IV.1.3.3 The Influence of Flow Rate on the Residual Oil

After the waterflooding period at 0.1 μL/min was over, we successively injected addidtional 6 PV of brine at flow rates Q = 0.5 and Q = 1.0 μL/min. Those three experiments are here named as E_{WF1}, E_{WF2}, and E_{WF3}, respectively. The acquired images were used to analyze the saturation and distribution of water and oil in the chip, and the corresponding ΔP was recorded at each Q. By analyzing the acquired images, we obtained the S_o at each period, then the S_o was plotted as a function of the injected volume of brine as displayed in **Figure IV-31**. Additionally, we presented real-time "steady-state" images of the two phases at the end the three periods. It is observed that the S_o decreases from 0.50 to 0.41, but remains at a high level. The invasion dynamics of the invading phase offer an explanation for this phenomenon. In cases of viscous fingering, under the same M, as the displacement pattern reaches equilibrium, the

saturation of the invading phase continues to increase with the injection flow rate, leading to a decrease in S_o (Zhang, et al., 2011) (Hu, et al., 2020). However, while this process enhances the ability of brine to displace or isolate the oil phase around the flow paths, completely removing all the oil remains challenging. Therefore, the S_o decrease a little.

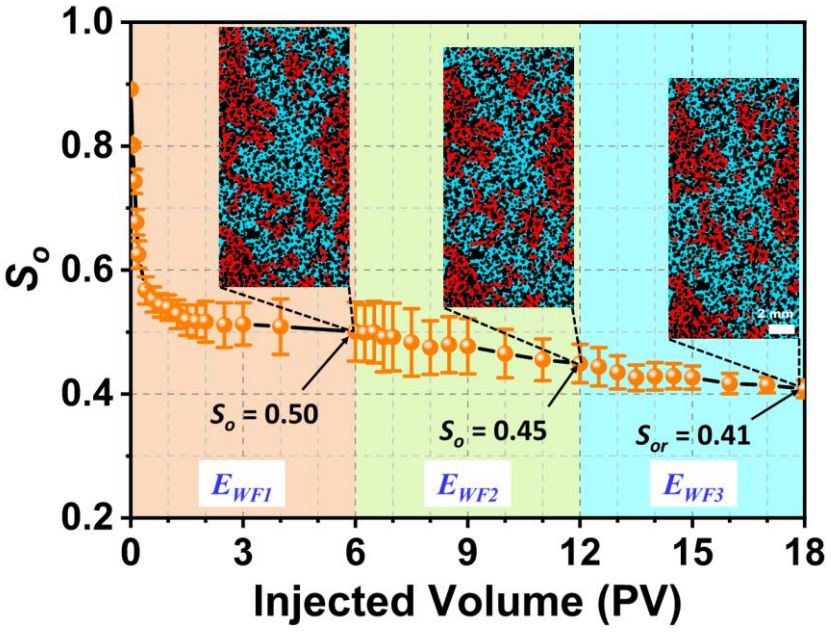

Figure IV-31 *S_o plot in function of the injected volume for three different flow rates: 0.1 µL/min, 0.5 µL/min, and 1.0 µL/min. Simultaneously, the chip images and reached S_{or} for each period are indicated as the images acquired at the corresponding step.*

By increasing the flow rate, the Ca was increased from 8.89×10^{-5} to 8.89×10^{-4} at a fixed M of 1/80, resulting in an increase in viscous forces relative to capillary forces, and as shown in the logCa/logM diagram (**Figure IV-32**), all these experiments still lies in the viscous fingering zone so that the increase in viscous forces within the chip, promote brine infiltration into the pores surrounding the flow paths, leading to a widening of the flow paths, as depicted in the acquired images at the end state in **Figure IV-31**. Consequently, there is a slight decrease in S_o.

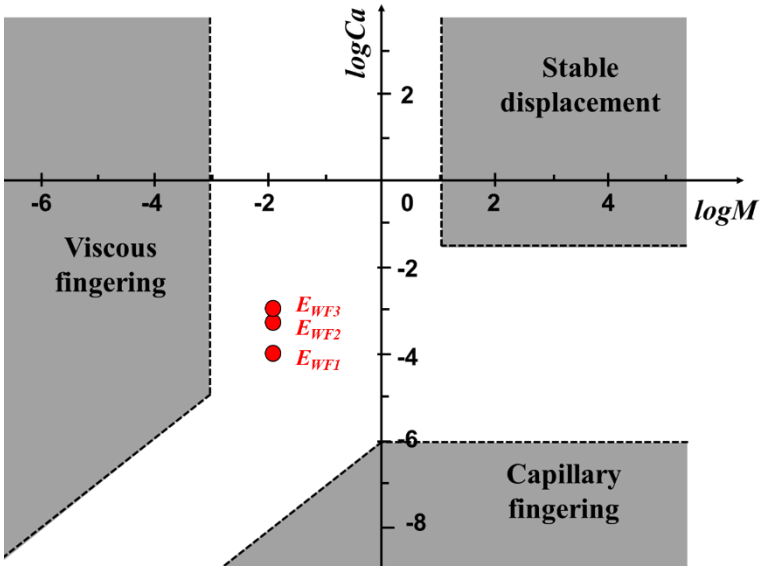

Figure IV-32 *Position of imbibition experiment at Q = 0.1 µL/min (E_{WF1}), 0.5 µL/min (E_{WF2}), and 1.0 µL/min (E_{WF3}) on logCa/logM phase diagram.*

The corresponding ΔP was plotted as a function of the volume of injected brine at successively increased Q on **Figure IV-33**, together with variation in the oil recovery. It is noteworthy that prior to breakthrough, the ΔP gradually decreased with increasing injection volume. After the breakthrough, the ΔP continued to decrease to a stable value of about 23 mbar at the end state of E_{WF1}. Then, the ΔP increased abruptly to above 60 mbar when the Q is suddenly increased to 0.5 µL/min before it reach a new steady state, at 27 mbar and soon. The sudden increase in pressure is due to partial snap-off events in the chip and mobilization of residual oil until the remaining oil became immobile. Subsequently, brine flowed along the flow paths, maintaining a stable ΔP. By increasing Q, the decrease in ΔP becomes smaller, since viscous forces are now insufficient to recover more oil. Consequently, few snap-off events are happening in large oil clusters with limited mobilization of small oil clusters; all this results in smaller changes in ΔP and less variation in S_o.

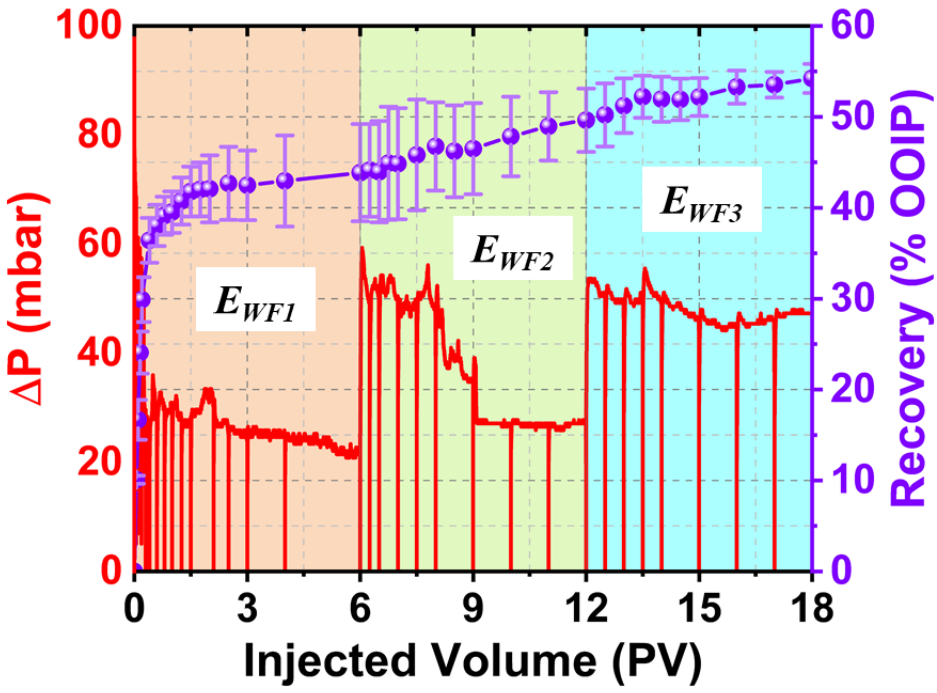

Figure IV-33 *Changes of pressure drop and oil recovery with injected volume of brine at different flow rates*

Moreover, through image processing, we determined the position of the remaining oil under the three different conditions (**Figure IV-34** (a-c)). Comparing the 3 final oil and water filling pore distributions, we only observe a small change from one Q to the other with la minor decrease in residual oil in the small-sized pores (< 50 μm) and more significantly in large sized pores (350-500 μm), while there is no change in oil content in other pores. This is because in water-wet systems, efficient oil displacement is mainly governed by capillary phenomena. The increase in Q has a relatively small impact on the pressure in the chip. Therefore, after reaching steady state at 0.1 μL/min, the effect of increasing the Q on residual oil is minimal. This may involve some snap-off of large oil clusters, as indicated by the changes observed in the 350-500 μm pores, but primarily involves mobilization and sweeping of smaller oil clusters. As a result, a noticeable decrease in the proportion of residual oil in smaller pores can be observed.

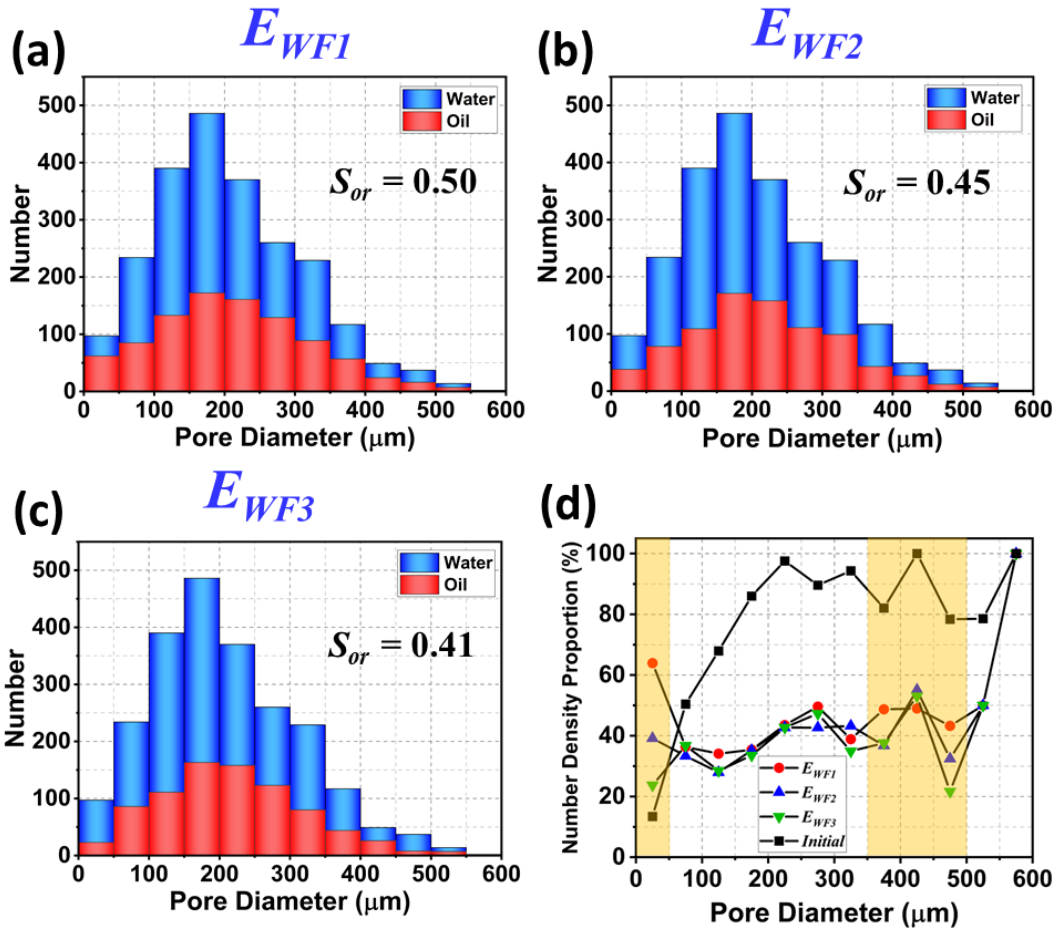

Figure IV-34 *The statistical steady state distribution of residual oil and brine in the original pore sizes of (a) 0.1 μL/min; (b) 0.5 μL/min; and (c) 1.0μL/min; (d) the proportion of oil clusters in different original pore sizes at steady state of three cases and before waterflooding.*

As described earlier, during waterflooding, the continuous oil phase experiences snap-off, breaking into dispersed clusters of various shapes and sizes. Some of these dispersed clusters undergo movement with the intrusion of brine, to some extent leading to a decrease in S_o until reaching S_{or}. To better quantify the dynamic changes of the trapped oil phase, we categorize them into three types based on their size and distribution: droplets, blobs, and ganglia, as shows in **Figure IV-35**. Droplets are smaller than individual pores and represent trapped fluid in the form of small spherical droplets. Blobs are larger than droplets and completely fill individual pores, leading to increased influence of capillary forces and complexity of momentum transfer and mobilization processes compared to droplets. Ganglia are larger non-wetting phase trapping bodies that occupy multiple adjacent pores.

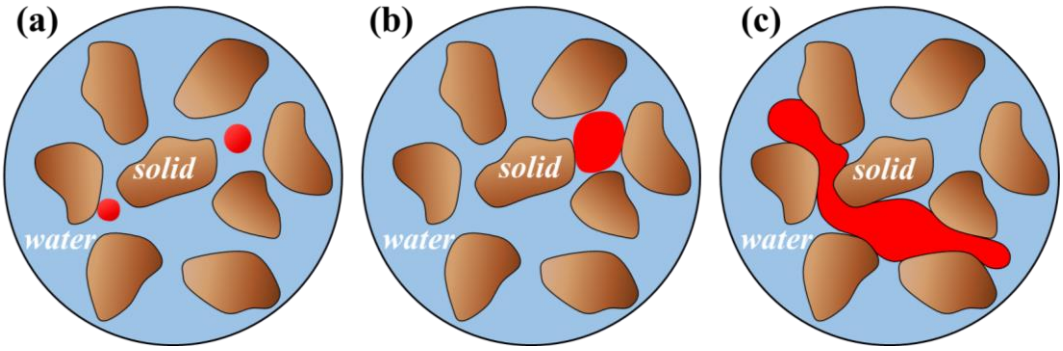

Figure IV-35 *The schematic illustration of oil droplets, oil blobs, and oil ganglia in a porous medium.*

The majority of the residual saturation is associated with the presence of large ganglia, whereas small droplets and blobs contribute less to residual saturation. Although large ganglia have a notable influence on residual oil saturation, their population is considerably smaller compared to blobs and droplets. The size of ganglia plays a crucial role in their mobilization. It has been reported that shorter and smaller ganglia tend to exhibit higher transport rates than larger ones. The primary mobilization mechanism for large ganglia involves break-up and coalescence to form new droplets and blobs that are more easily mobilized, with their numbers remaining within a certain range. However, when the capillary number within the chip is insufficient to break-up and coalescence of large ganglia, the number of droplets and blobs decreases significantly after the mobilization of movable droplets and blobs. Therefore, as displays in **Figure IV-34** (d), the proportion of residual oil remaining at the small original pore size have a significant decrease as the Ca increases, driven by the increase in Q.

IV.1.3.4 Permeability of Water at S_{or}

After achieving steady state at Q of 1.0 μL/min during the waterflooding imbibition, the permeability of water at S_{or}, $k_w(S_{or})$, was measured by decreasing Q from 1.0 μL/min successively through the injection of brine and recording the corresponding ΔP. Again five independent experiments, denoted as E_{KWF1}, E_{KWF2}, E_{KWF3}, E_{KWF4}, and E_{KWF5}, respectively, were conducted on the same chip, following the procedure described in **Section III.1.4**. The average ΔP recorded at each Q during steady state is presented in the plot of **Figure IV-36**. It is obvious that all data, represented by different colors, are scattered within the gray region, but they are in average well fitted by a linear law, as indicated by the orange line. By using the Darcy's law, we obtain $k_w(S_{or})$ = 1.1 ± 0.07 Darcy. This value is significantly lower than that of initial water permeability K_w of 2.7 Darcy, due to the immobile oil-include changes in medium topology.

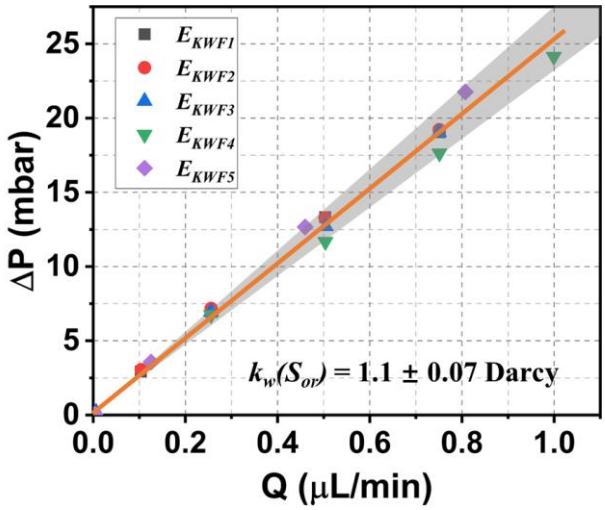

Figure IV-36 *ΔP versus Q at steady state for five different experiments. Data are represented by symbols (within the gray region), the continuous line is a linear regression.*

IV.1.3.5 The Influence of Network Structure on Waterflooding

In addition to the studies focusing the influence of Ca by modifying the Q on the displacement efficiency and trapping mechanisms of residual oil as discussed previously, the wettability, pore structure and geometry of the medium also have strong effect on flow behaviour and microscopic mechanisms of the displacement process (Meybodi, et al., 2011). Given that the chips we used are all water-wet, we will focus on the influence of pore structure and geometry of the medium on flow behavior and displacement mechanisms by comparing a random water-wet chip and a regular water-wet chip with similar characteristics, while all other operating conditions are kept unchanged.

Waterflooding was initiated following the drainage at low constant Q = 0.1 μL/min, corresponding to M of 1/80 and Ca_{new} of 3.1×10^{-5}. The image at breakthrough is depicted in **Figure IV-37**, where two fingering patterns can be observed: on the left side is a typical viscous fingering, leading to rapid breakthrough (~0.2 PV) with a narrow front, while on the right, a transverse invasion of a wide front is observed indicative of capillary fingering. The breakthrough is similar to the random chip case, but the flow pattern is clearly different, highlighting the significant impact of the porous structure in the current situation.

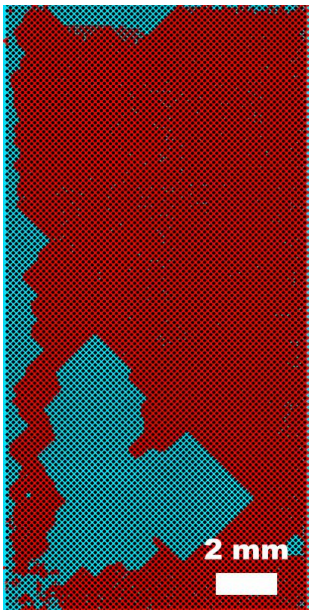

Figure IV-37 *The saturation image of water and oil at breakthrough during the waterflooding period in the regular chip. Blue represents brine, while red represents oil.*

As before, the oil saturation in the regular chip at different injection volumes of brine and flow rates was calculated from the images, and the effect of Ca on trapped oil was explored by successively increasing the flow rate after reaching steady state. The obtained results are displayed in **Figure IV-38**, with a focus on the first PV in the right figure. We observed minimal differences in S_o between the two types of chips throughout the waterflooding process. Detailed comparison of S_o in the two types of chips at the end of the three Q periods are listed in **Table IV-5**. It can be seen that at steady state, S_o is generally consistent between the two types of chips. However, differences are still observed at the initial state and breakthrough. Therefore, image (b) depicts the variation of S_o during the early stage of waterflooding at the low flow rate. It clearly demonstrates that at injection volumes less than 1 PV, S_o in the regular chip is higher than that in the random chip while both chips experience rapid breakthrough (~0.2 PV). So the rate of decrease in S_o with increasing injection volume is higher in the random chip.

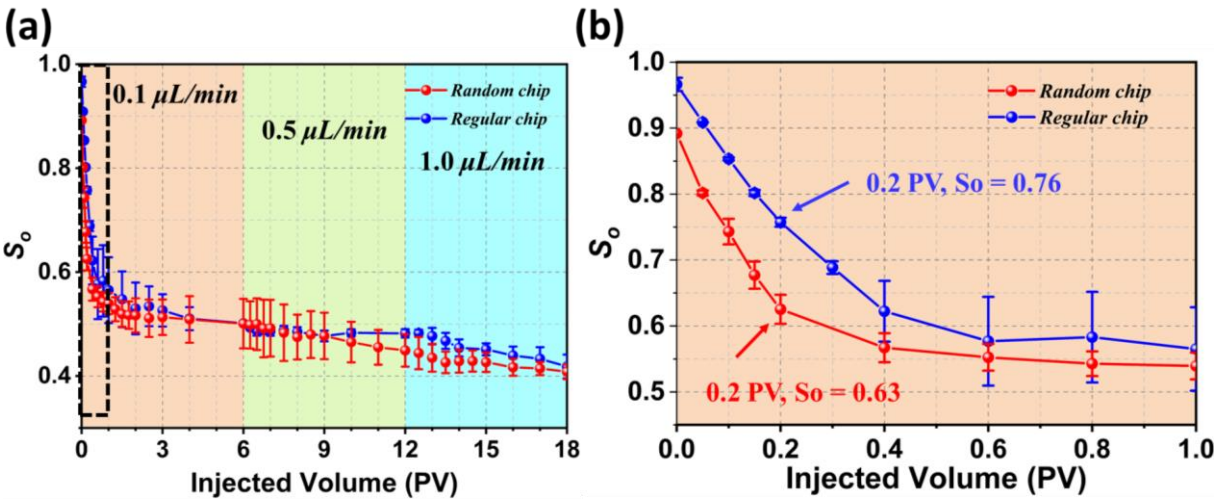

Figure IV-38 *The function of S_o versus the injected volume of brine for both types of chips at all three flow rates is depicted in panel (a), while panel (b) magnification of the initial stage at flow rate of 0.1 µL/min.*

Table IV-5 *The comparison of S_o between the two types of chips at several special injection volume points.*

	0 PV	Breakthrough	End of Q1	End of Q2	End of Q3
Random chip	0.89	0.63	0.5	0.45	0.41
Regular chip	0.97	0.76	0.5	0.48	0.42

Further analysis was conducted on oil recovery rates, as shown in **Figure IV-39** (a), where the recovery in the regular chip (blue) was found to be higher by approximately 2% to 5% compared to the random one (red) at three flow rates experiments.

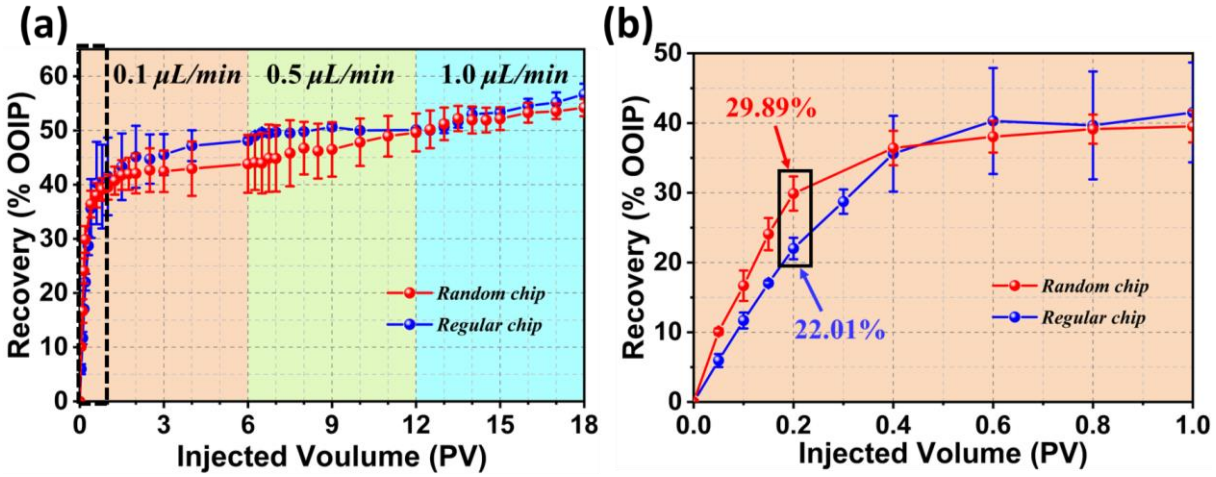

Figure IV-39 *The oil recovery versus the injected volume of brine for both types of chips at three flow rates (a); (b) magnification of the initial stage at flow rate of 0.1 µL/min.*

The reasons for these results may be twofold. On one hand, with the same etching depth, the capillary forces are primarily influenced by the size of the pore throats. In the regular chip, the distribution of pore throat sizes is uniform at 50 µm, while the average pore throat diameter in the random chip is 82.3 µm, resulting in slightly greater capillary forces in the regular chip, which can be also find in the **Figure IV-40**. This means that the invading phase needs to exert greater pressure to displace oil in the regular chip. On the other hand, the distribution of pore structures has been shown to significantly affect the mobilization of the trapped non-wetting phase (Meybodi, et al., 2011) (Lei, et al., 2020) (Saadat, et al., 2020). In the regular chip, both the pore bodies and throats are uniformly distributed; the pore bodies are dead-end-free circulars with a diameter of 90 µm, and each pore body is connected to four throats with the same size and shape. This means that at the pore throats experiences the same inlet pressure, and the round, dead-end-free pore bodies do not easily trap oil, contributing to the minimal remaining oil in the swept area of the regular chip. Conversely, each pore body in the random chip is typically

connected to two or three throats of varying sizes, causing differences in inlet pressure and making it easier for oil to become partially trapped in irregular pore bodies. Moreover, the overall structure of the random chip includes smaller-sized pore throats that are more prone to causing snap-off and trapping of the oil clusters, as well as dead-end pores where oil is directly trapped.

Balancing these factors leads to slightly higher recovery rates in the regular chip compared to the random one. As a result, the swept area in the regular chip shows very little remaining oil, while in the random chip, there remains a significant presence of various types of residual oil clusters.

Table IV-6 *The comparison of recovery (% OOIP) between the two types of chips at several special injection volume points.*

	0 PV	Breakthrough	End of Q1	End of Q2	End of Q3
Random chip	0	29.89	43.85	49.63	54.22
Regular chip	0	22.01	48.12	50.11	56.71

Table IV-6 gives the exactly recovery rates for the end of each period, revealing that, except for the breakthrough time, the recovery rates in the regular experiments are consistently higher. Therefore, we focus on the early invasion period, as shown in **Figure IV-39** (b), where it can be clearly seen that the recovery rate in the random chip is significantly higher than that in the regular chip before breakthrough. At breakthrough, the recovery rate in the random chip experiment is 29.89% OOIP, while in the regular chip experiment, it is 22.01% OOIP. The reason for this result may be as mentioned earlier, due to the larger pore size and more trapped remaining water in the random chip, the capillary forces smaller, thus the oil phase is more easily displaced at initial period of waterflooding with same conditions, resulting in a higher recovery rate before brine breakthough.

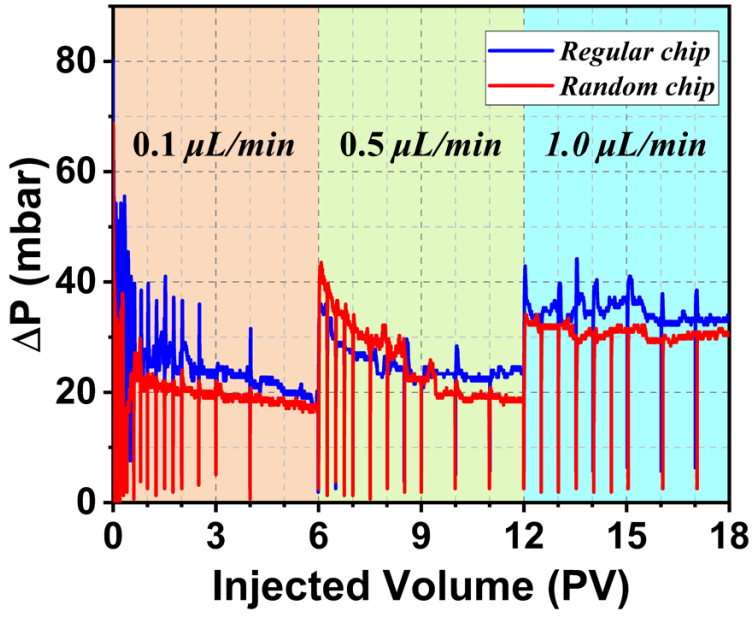

Figure IV-40 *In live ΔP for the 3 Q from 0.1 to 1.0 µL/min during waterflooding for regular chip (in blue) and random chip (in red). The red verticals represent the flow stop to capture images.*

At the end of the waterflooding period, when reaching S_{or} at Q = 1.0 µL/min, the distribution of residual oil in the two types of chips was compared and analyzed. The results, as shown in **Figure IV-41**, reveal distinct differences. In the random chip, residual oil is observed to be distributed as ganglia, blobs, and droplets within the pores (**Figure IV-42**), with their size and distribution influenced by the trapped pore size and geometric structure, as discussed above. Conversely, in the regular chip, almost no residual oil is trapped in the cleaned region, with only small blobs and ganglia forming near the inlet and outlet ends (**Figure IV-42**). The primary residual oil is trapped in the uncleared region, existing in the form of continuous large oil clusters. One possible reason for this is that residual oil in the regular chip is minimally influenced by medium geometry factors, and the smooth curved surface of the pores makes it difficult to trap oil. Thus, even though some oil may be trapped during waterflooding, its smaller size makes it easily mobilized under continuous invasion. Therefore, in the main invasion region, trapped oil is almost absent. However, around the edges of the chip, due to the lower frequency of waterflooding, some ganglia and blobs formed are left undisturbed.

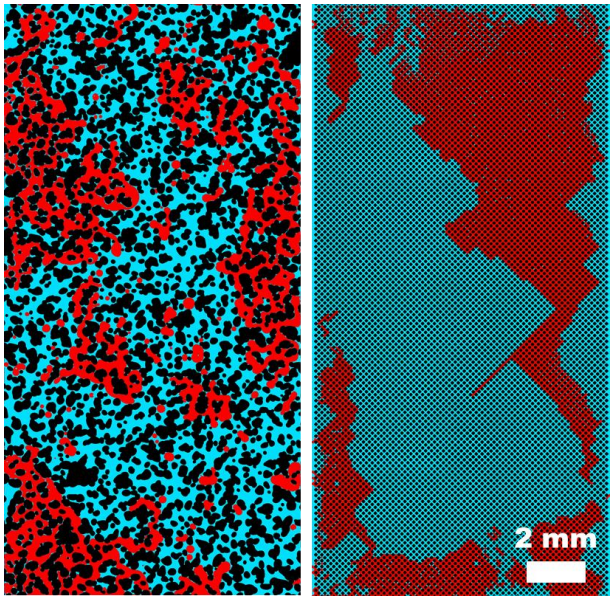

Figure IV-41 *The distribution of residual oil in both types of chips during the waterflooding after injection of 6 PV at Q = 1.0 µL/min. Oil is in red and brine in blue.*

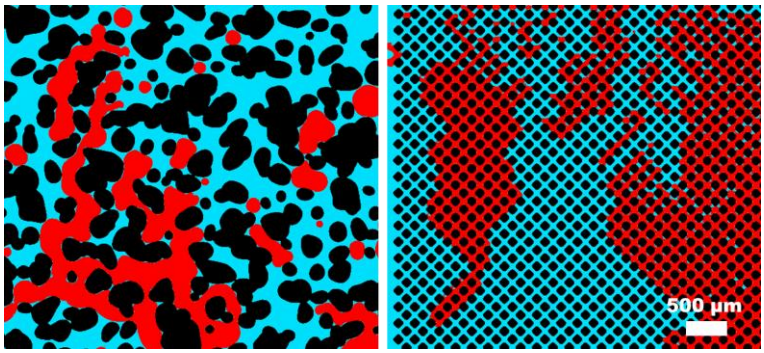

Figure IV-42 Magnification of trapped oil clusters for both chip in Figure IV-41 at steady state.

Finally, after achieving steady state at a flow rate of 1.0 µL/min, we similarly measured the brine permeability at S_{or} by decreasing the flow rate from 1.0 to 0 µL/min using the same procedure as before. As shown in **Figure IV-43**, the averaged ΔP for each Q case exhibited a linear correlation for both chips. By using Darcy's law, the brine permeability of the random chip at S_{or} was determined to be 1.1 ± 0.07 Darcy, while that of the regular chip was 1.0 ± 0.14 Darcy. The reason for the smaller $k_w(S_{or})$ value of the regular chip is that its uniform structure imposes less hindrance and more uniformity on the mobilization of the oil, allowing the water to flow the water pathway more easily within the chip.

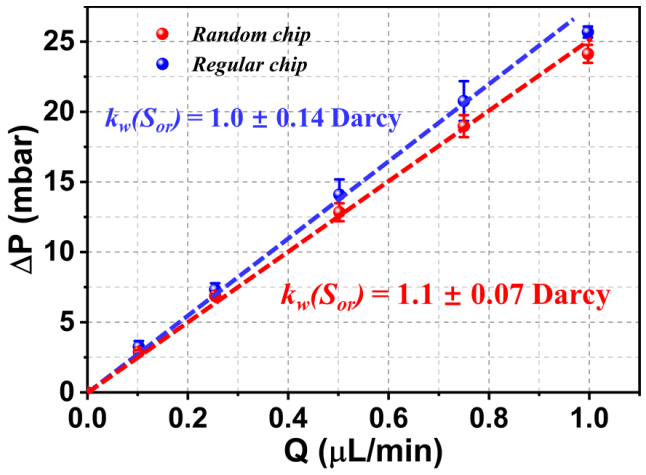

Figure IV-43 The averaged ΔP versus Q at steady state during waterflooding to regular and random chips. Dashed lines are linear regression of data.

IV.1.3.6 Discussion of Waterflooding

In the waterflooding experiments, a thorough investigation was conducted to assess the impact of various factors on oil displacement dynamics, particularly focusing on the role of structural differences of microfluidic chips and the effects of varying flow rate.

Initially, the waterflooding experiments start from an irreducible water saturation state (S_{wi}) with an initial S_o of approximately 0.9. The brine injection lead to a rapid reduction in oil saturation, reaching 0.63 at a breakthrough of 0.2 PV injected, illustrating its bad sweep efficiency. This breakthrough event

marks a typical flow pattern that is more consistent with viscous fingering. The thin fingering observed prior to the brine breakthrough also reflects this characteristic, although it is located in the regime of the viscous fingering-stable displacement crossover zone on the logCa/logM diagram. The injection process continued to evolve, decreasing S_o further to 0.50 at steady state after the injection of 6 PV. This was supported by image analysis that show that the advancing brine preferentially occupy smaller and previously oil-filled pore throats, thereby promoting oil snap-off and trapping. Moreover, the residual oil distribution at steady state revealed a significant trapping of oil within larger pore structures, with residual oil predominantly existing as isolated clusters. This distribution is a critical indicator of the efficiency of the waterflooding process and suggests that while water successfully displaced a significant amount of oil, substantial oil remains due to the heterogeneity of the pore network and the strong capillary forces within larger pores.

The ΔP measurements provided further insights into the fluid behaviors within the chip. The initial rapid decrease in ΔP during the viscous fingering period before breakthrough is indicative of reduced flow resistance due to effective oil displacement by brine. Subsequent periods showed fluctuating ΔP values which corresponded to the formation of new flow paths and the movement of oil clusters, which occasionally increased resistance and ΔP. This highlights the complex interplay of capillary and viscous forces that govern the displacement processes in porous media.

After that, we explored the impact of increasing flow rate on residual oil saturation during waterflooding experiments. Increasing the flow rate from 0.1 μL/min to 1.0 μL/min led to a decrease in S_o from 0.50 to 0.41. Additionally, the changes in ΔP with increased flow rates highlighted how dynamic pressure adjustments and oil cluster mobilization affect oil recovery. As flow rates increased to 0.5 and 1.0 μL/min, oil recovery rates improved, reaching up to 54.2%, but such gains began to taper off due to the limitations imposed by the pore structure and capillary forces within the chip. Finally, through image analysis, we observed slight changes in the distribution of residual oil in small and large pores, providing further evidence that while higher flow rates can modify flow paths and enhance recovery in specific scenarios, their overall impact on residual oil distribution is constrained by the inherent properties of the porous medium.

In separate experiments we examined the influence of pore structure and geometry on the displacement efficiency and trapping mechanisms during waterflooding in microfluidic chips of defined wettability. Our findings highlight the critical role of pore geometry in influencing oil saturation and recovery during waterflooding. The S_o at the end of various flow rates (0.1 μL/min, 0.5 μL/min, and 1.0 μL/min) remained relatively consistent between two chips, the initial S_o was higher in the regular chip due to its uniform structure, leading to more effective water displacement of the oil phase during the initial period of waterflooding. Moreover, the recovery of regular chip is higher 2-5% than random one, which influence more by the chip structure. In the regular chip configuration, the pore bodies are dead-end-

free circles with a diameter of 90 μm, and each pore body is connected to four pore throats that rectangular channels with a width of 50 μm. The presence of uniform pore structures facilitated a more homogeneous displacement of oil, characterized by an efficient sweeping of the waterflooded areas. In contrast, the random chip configuration features randomly distributed pore sizes with mean pore throat width of 82.3 μm and mean pore body diameter of 223.5 μm. The dead-end pores and irregular structure of random chip result in the oil trapped easily, leading to amount of remaining oil observed as ganglia, blobs, and droplets in waterflooded areas. Consequently, the regular chip experiments have a higher recovery than random one.

Finally, after achieving steady state at a flow rate of 1.0 μL/min, we similarly measured the brine permeability at Sor by decreasing the flow rate from 1.0 to 0 μL/min. Permeability measurements at Sor provided additional insights into the impact of pore structure on fluid dynamics within the chips. The brine permeability at Sor was slightly lower in the regular chip (1.0 ± 0.14 Darcy) compared to the random chip (1.1 ± 0.07 Darcy), indicating that the regular pore geometry imposed less hindrance hindrance and more uniformity on the mobilization of the oil, allowing the water to flow the water pathway more easily within the chip. Furthermore, when comparing these values to the initial water permeability (K_w) of 2.7 Darcy, due to the immobile oil-include changes in medium topology.

IV.1.4 Glycerol/Water Mixture Flooding

Research on immiscible two-phase flow displacement not only includes macroscopic investigations under various Ca and M conditions during imbibition and/or drainage situations and their impact on fluids saturation, but also encompasses studies at the microscopic scale on invasion mechanisms, as well as the distribution and mobilization of residual non-wetting phase (Ying, et al., 2013) (De Castro, et al., 2016) (Zarikos, et al., 2018) (Nikolaos, et al., 2019) (Chen, et al., 2023) (Anastasiou, et al., 2024). In Section **4.1.3**, we discussed how changing Ca by increasing the flow rate affects residual oil mobilization and distribution during waterflooding. In other works (Meybodi, et al., 2011) (Nilsson, et al., 2013) (De Castro, et al., 2016) (De, et al., 2018), the change of Ca can also be achieved by changing the viscosity of the invading fluid by using, for example, hydrosoluble polymers that given non-Newtonian fluids. In that case, other complexities arise from their shear-thinning behavior and their inherent elastic character.

In the present work we consider the impact on aqueous solution of improved viscosity. By this way we mimic the tertiary oil recovery methods. However, to specifically investigate the influence of viscosity ratio, only Newtonian aqueous fluids of controlled viscosity were selected. This was achieved by mixing water and glycerol at various proportions as described in terail in **Section III.1.1**, these aqueous solutions are named here “mixtures” or “aqueous mixtures”.

In the present work, we consider the impact of increased viscosity on aqueous solutions as a way to mimic tertiary oil recovery methods. However, to specifically investigate the influence of the viscosity

ratio, we selected only Newtonian aqueous fluids with controlled viscosity. This was achieved by mixing water and glycerol in various proportions, as detailed in **Section III.1.1**. These aqueous solutions are named here "mixtures" or "aqueous mixtures".

IV.1.4.1 The Fluid Dynamics of Waterflooding Imbibition

Beforehand, the date of drainage and imbibition experiments for water-wet chip that were presented before and consisting of five independent experimental series were averaged. Then after the waterflooding, we conducted additional experiments by injecting glycerol/water mixtures at a flow rate of 1 µL/min for 18PV as in the waterflooding step. Specifically, we varied the ratio of mixture viscosity over the oil viscosity, M, from 1 to 80 in five independent experiments. Those five experiments are named as E_{GM1}, E_{GM2}, E_{GM3}, E_{GM4} and E_{GM5}, respectively. As M increases, the Ca_{new} increases too from 8.89×10^{-4} to 7.09×10^{-2}, and such increase in viscous forces is expected stabilize of the fluid advancing front, thereby facilitating the mobilization and sweeping of residual oil. Consequently, there should be a significant decrease in S_o. The M and their corresponding Ca for the five experimental sets are provided in **Table IV-7**.

Table IV-7 *The value of M and correspond Ca with five experimental cases.*

	E_{GM1}	E_{GM2}	E_{GM3}	E_{GM4}	E_{GM5}
M	1	4	8	20	80
Ca_{new}	8.89×10^{-4}	3.98×10^{-3}	6.95×10^{-3}	1.72×10^{-2}	7.09×10^{-2}

Moreover, visual observation of the experiments using the microscope in the experimental setup allows for the visualization of the flow mechanisms and the movement details of residual oil during mixture flooding. The acquired images were used to analyze the saturation and distribution of aqueous phase and oil in the porous medium, giving the evolution of ultimate residual oil distribution in the chip with increasing M, as shown in **Figure IV-44**. In those acquired images, the deep blue represents the glycerol/water mixture, and the red represents. It can be observed first that for M=1 (that means continuing injection of brine), there was of course, no significant reduction in the quantity and size of residual oil observed with increasing injection volume in E_{GM1}. However, as M increases, there is a remarkable decline in both the quantity and size of residual oil, which almost vanishes at higher M values (E_{GM5}). Furthermore, after waterflooding (E_{GM1}), large oil ganglia are typically retained in easily recognizable areas of the chip, such as near the inlet and outlet regions and along the lateral boundaries. In contrast, at subsequence injection, of the glycerol/water mixture, (E_{GM2} to E_{GM5}), the micromodel exhibits a more dispersed saturation distribution, and the remaining oil ganglia are usually smaller. Regarding the mobilization mechanism of residual oil, we also observed differences compared to waterflooding under unfavorable conditions, favorable M conditions primarily lead to the breakup of

large oil clusters and the formation of small ganglia, droplets, or blobs, depending on the pore structure, that may then move out the chip. This observation was validated posteriori through video recordings.

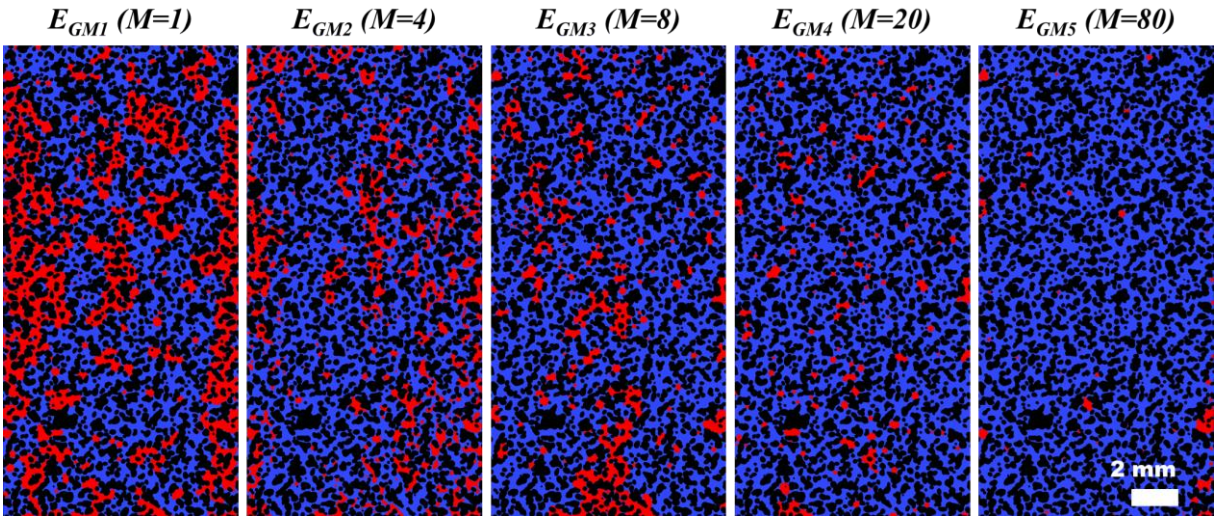

Figure IV-44 *The residual oil size and distribution at steady state after injection of 18 PV of glycerol/water mixture of five different M.*

To that end, we captured the details of residual oil mobilization during displacement processes through video recordings. On **Figure IV-45**, we present successive snapshots that illustrate the mobilization of residual oil under mixture flooding with M=1 (E_{GM5}). In these images, the light yellow color represents the oil phase, the pink region is the mixture phase, and the gray region represents solid grains. It is noteworthy that before the mobilization of oil droplets, breakage of ganglia in pore bodies (pinch-off) or at the junction of pore bodies and throats (snap-off) becomes the dominant breakup mechanism. The effective break-up of ganglia releases the local pore capillary forces, enabling the mobilization of new forms droplets or ganglia. This phenomenon can be observed in **Figure IV-45**, if we focus on two parts of ganglia within the red circle at 0 s. One second later, the ganglion on the left undergoes break-up at the pore throat, generating small oil droplets that rapidly relaxes becoming “spherical” and move forward, reaching the edge of the field of view at 3 s (indicated by the red dashed box). However, the remaining part of such ganglia is still retained; the ganglion continues to undergo break-up, releasing new droplets until almost all the residual oil cluster can be mobilized (as displayed in the black dashed box). Similar, the ganglion on the right simultaneously undergoes break-up at the pore throat and breakage within the pore body, breaking up into new droplets and ganglia, ultimately overcoming the capillary forces at the pore throat to be fully mobilized (the blue arrow at 15s). A large M favours the formation of smaller ganglia, blobs, oil droplets, and connected pathways over broader ranges of the system. Therefore, by the 22nd s, there are no original ganglia left in the porous area, and ganglia from the upstream region are re-passing through this area and being mobilized.

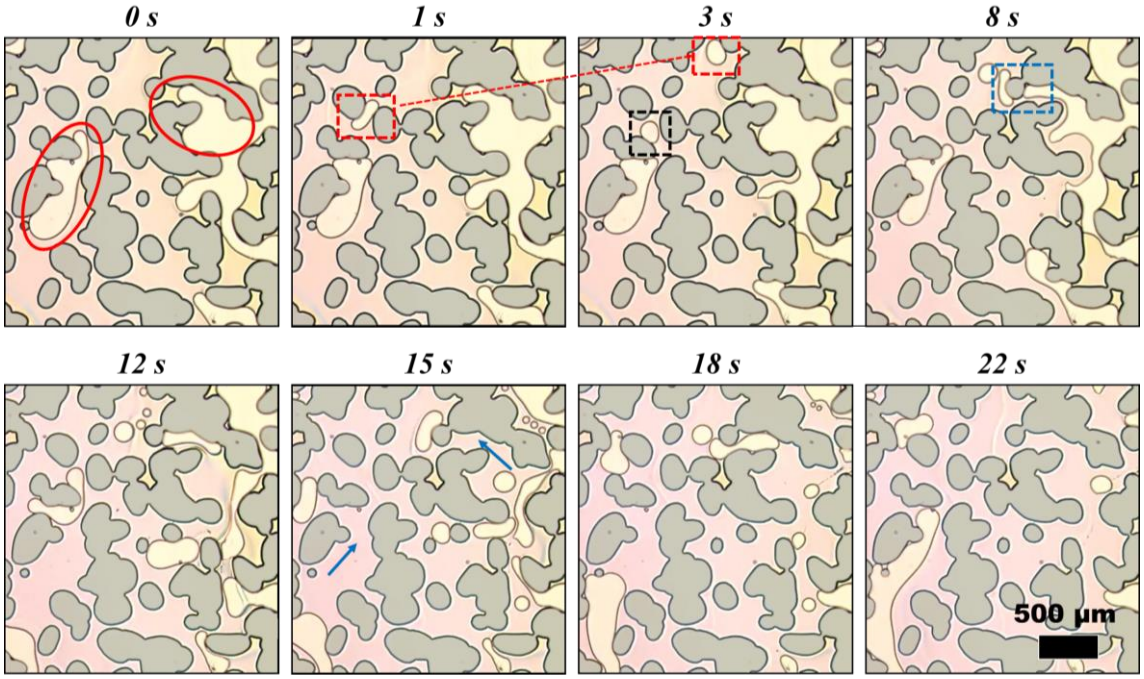

Figure IV-45 *Real-time images showing ganglia fragmentation and mobilization in the micromodel at the Q = 1.0 µL/min injected the glycerol/water mixture with the M of 80. Where light yellow color is oil, pink is for the mixture, and gray is solid grains.*

The acquired images were used to analyze the saturation of residual oil and oil recovery beside recording the corresponding ΔP for each M. In **Figure IV-46** (a), the ΔP is plotted as a function of the injected volume for both previous waterflooding at successive flow rates and the following glycerol/water mixture flooding at 1.0 µL/min. It can be seen first that for E_{GM1}, where M=1, the overall pressure remained stable, with a marginal added the increase in oil recovery since it is only a continued waterflooding period. Subsequently, during glycerol/water mixture flooding, as M increases, the ΔP in the micromodel chip undergoes a rapid increase followed by a slow return to a steady state region. The ΔP plateau values are plotted versus M on **Figure IV-46** (b).

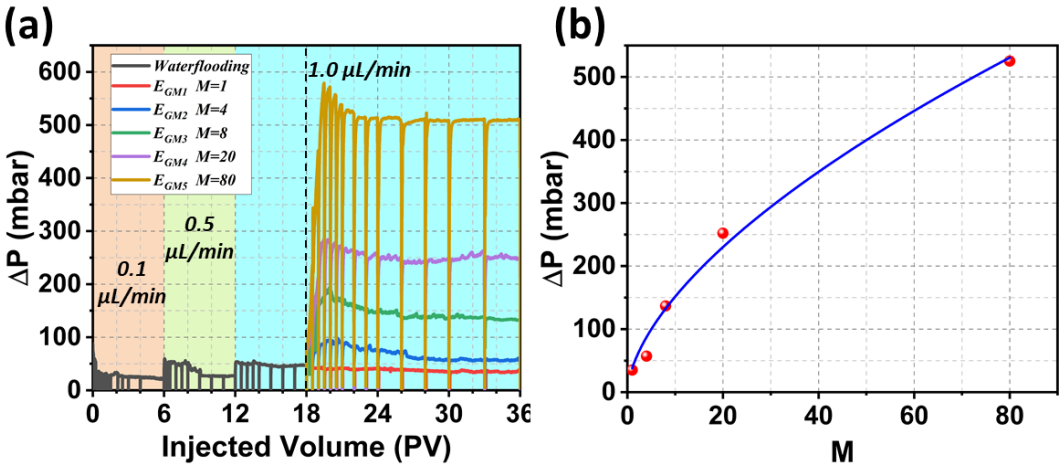

Figure IV-46 *(a) ΔP plotted in function of injected volume during the waterflooding and subsequently flooding with glycerol/water of various viscosity ratios; (b) the average steady-state ΔP plotted as function of M at the Q = 1.0 μL/min, where the blue point is the steady-state pressure of waterflooding and the red points are for the steady-state of mixtures flooding.*

If no change happens within the chip, the increment in ΔP should be linearly correlated with the increase in M, as expected from Darcy's law. However, due to the real-time mobilization of residual oil in the chip, the change in ΔP deviates from this expectation. In **Figure IV-47** (a), we assume the simultaneous presence of droplets, blobs, and ganglia in the field of view, although in reality, only one or a combination of them may exist in the local view of the chip. During the injection of the mixture flooding, as the viscosity increases, the induced increase in ΔP may mobilize some blobs and droplets, and possibly cause the breakup and mobilization of ganglia, depending on the local pore geometry. This behavior was demonstrated by Zarikos et al. (Zarikos, et al., 2018), who used micro-particle tracking velocimetry (μ-PTV) to visualize the velocity distributions inside trapped phase clusters both prior to and during mobilization. Their research elucidated the complex interplay between capillarity and momentum transfer across the two fluid phases for different trapped clusters, highlighting the varied dynamics influencing the mobilization of droplets, blobs, and ganglia within the porous medium. Following their work, we have further explored the forces acting on trapped droplets, blobs, and ganglia during their mobilization in our experiments, focusing on the energy transformations and morphological changes involved.

In **Figure IV-47** (b), we illustrate the mobilization of residual oil driven by the upstream scouring effect of glycerol/water mixture. Due to the pressure at the pore entrances exceeding the threshold capillary pressure, the droplets 1 and blobs 2 being mobilized and released within a dashed line limited area. Simultaneously, ganglia are displaced by the mixture in the upstream pores, while compressing the wetting phase in the downstream pores, thus forming the contours of the black dashed line area. As the injection of the mixture continues, the pressure within the medium keeps increasing, causing droplets 1 and blobs 2 leaving the porous medium, and the ganglia at the pore throats to be further compressed and narrowed until they make contact with the solid grains at the pore throats (indicated by the white dashed line). At that point, the ganglia undergo snap-off, rupturing into two new smaller ganglia. It is also possible for new droplets to form from the breakup ganglia, although this is not depicted here. Consequently, as shown in **Figure IV-47** (c), ganglia-3 is fragmented into two smaller ganglia (red), while the droplets and blobs have already been mobilized and leaved the medium (indicated in gray). All these processes lead to a decrease in ΔP. Therefore, accounting for the decrease in ΔP due to the mobilization of residual oil, ΔP shows then a nonlinear correlation with M. The magnitude of ΔP increases with M but at a decreasing rate, and larger M values result in faster and more extensive breakup and mobilization of residual oil, causing a larger offset in ΔP, which consequently reduces the overall rate of increase in ΔP.

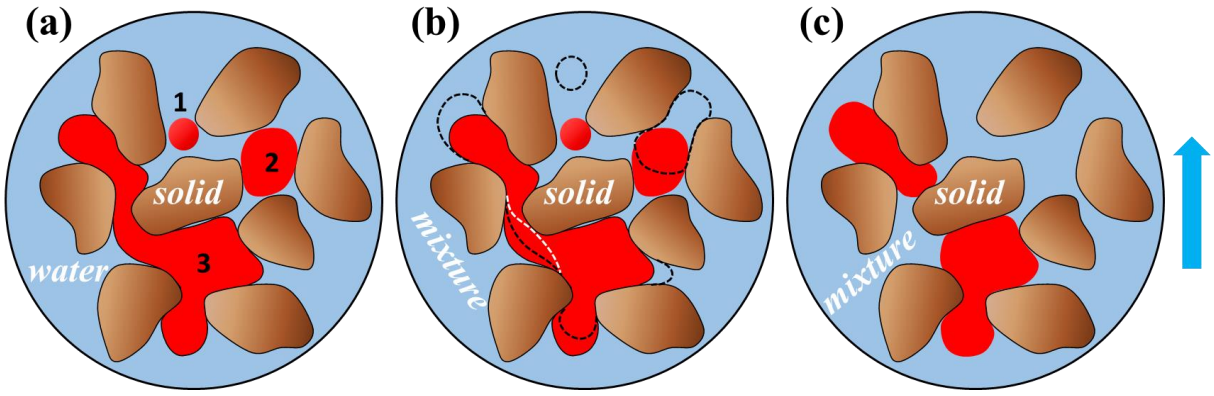

Figure IV-47: *(a) A sketch of the mobilization of different types of residual oil clusters in porous medium before mixture flooding; (b) the potential mobilization processes of three types of residual oil clusters during mixture flooding, with dashed lines indicating changes in position and shape; and the sketch of oil clusters in porous medium after mixture flooding (c). Label 1 represents droplets, 2 represents blobs, and 3 represents ganglia.*

Moreover, we also present the oil recovery as a function of the volume of injected mixture in **Figure IV-48** (a). It can be observed that except for E_{GM1}, all mixture flooding experiments resulted in an increase in oil recovery. Compared to the limited impact of continuous water flooding on oil recovery in E_{GM1} (~ 1.7%), E_{GM2} to E_{GM5} ultimately increased oil recovery by approximately 18.6%, 23.2%, 26.1%, and 37.9%, respectively, compared to the initial value of approximately 54% in the end of water flooding experiments. On **Figure IV-48** (b), we plot the ultimate oil recovery versus the M observed in mixture flooding experiments. The points data represent the results obtained from experimental image processing, while continuous line is only served as a visual guide, demonstrating how an increase of dM enhance the oil recovery with a gradual decrease of the curve slop. This suggests that while higher M values can yield higher recovery rates, considering the experimental costs, opting for a smaller M might be more efficient. This approach is well-known in petroleum engineering applications.

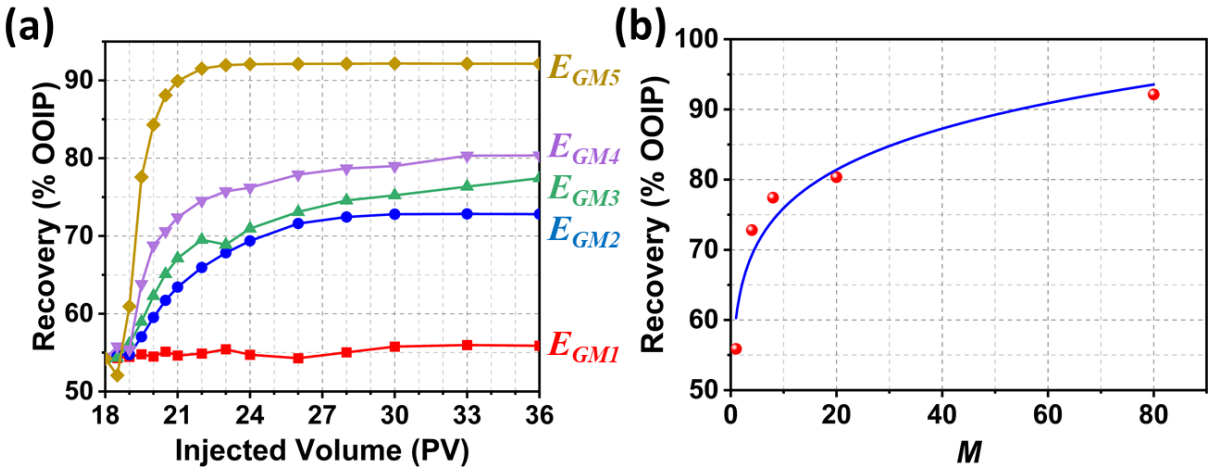

Figure IV-48 *(a) The oil recovery as the function of the volume of the mixture injected volume with different M; and (b) the corresponding steady state recovery plotted in the function of M.*

Moreover, by image processing method already presented in **section III.1.4**, we calculated the distribution of residual oil and water phases in the original pore sizes at "steady state" for the. We also calculated the S_{or} at steady state, which decreased from 0.39 to 0.02 in the experiments of E_{GM1} to E_{GM5}. In **Figure IV-49**, the red and blue colors represent the count of oil and mixture occupying the original pore size, respectively. It can be observed a significant reduction in the oil quantity and remarkable change of its with increasing M. This is more evidenced in **Figure IV-50** where we have plotted the number proportion of residual oil in different pores at steady state for the five mixture flooding experiments. It can then be clearly observed that with increasing M, the count proportion of residual oil in all original pore sizes globally decreases, except for pores smaller than 100 μm. This is because, in E_{GM1}, during water flooding, the smaller Ca and unfavorable M can only effectively displace residual oil in small pores, while residual oil in large pores under the form of ganglia are trapped due to capillary forces. When M increases to 4 in E_{GM2}, as reported earlier, favorable M and larger ΔP promote the breakage of oil clusters, resulting in an increase of droplets and blobs. These entities tend to accumulate in small pores, consequently increasing the proportion of residual oil in those pores. Subsequently, with further increase in M, favorable M promotes the mobilization of residual oil in the chip, especially for droplets or blobs, leading to a reduction in the proportion of residual oil in small pores. Moreover, an increase in M positively promotes the breakage and mobilization of ganglia, resulting in a continuous decrease in the proportion of oil in large pores to near-zero values. It also intuitively demonstrates the decrease in the maximum pore size occupied by residual oil, from 550-600 μm in E_{GM1} to 400-450 μm in E_{GM5}.

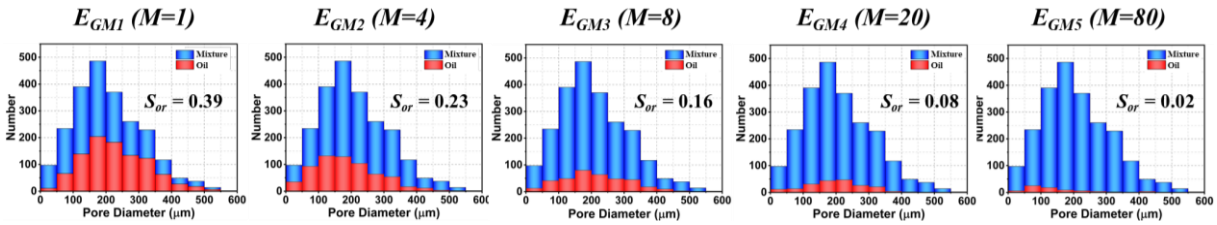

Figure IV-49 *The statistical distribution of residual oil and aqueous phase in the original pore size at steady state of the five M experiments. Blue color is for glycerol/water mixture, and red is for oil.*

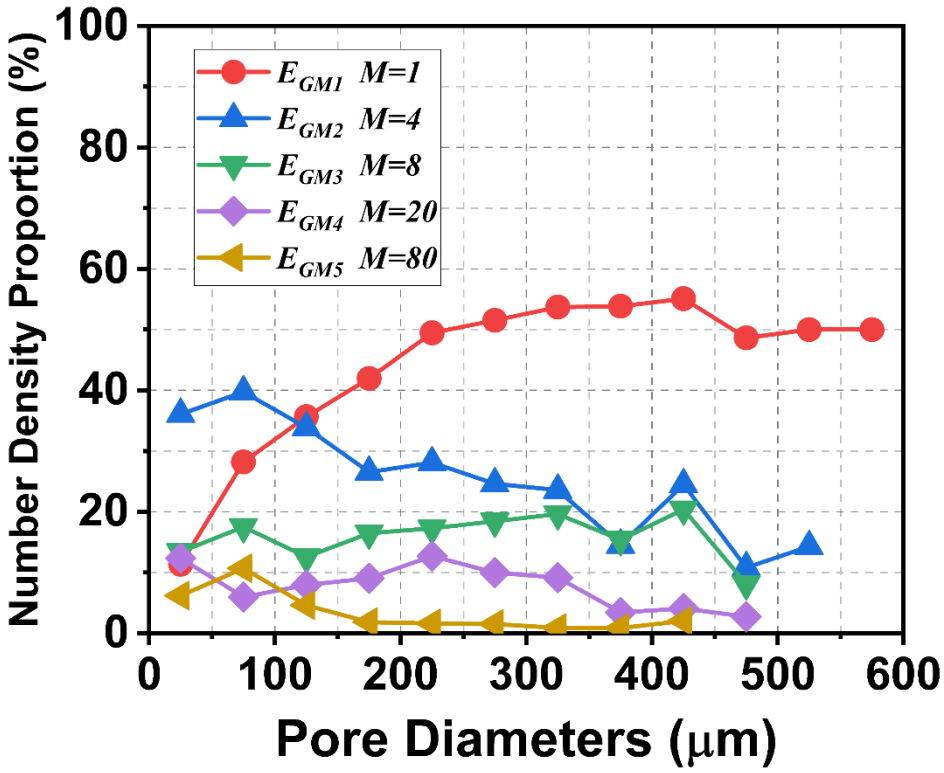

Figure IV-50 *The number density of pores occupied by oil at steady state for the five M experiments*

IV.1.4.2 The Influence of Network Structure on Mixture Flooding

Similarly, using the regular chip, we replicated all the mixture flooding experiments conducted in the random chip, building upon the results of the previous waterflooding experiments. Here the five experiments are named as E_{GM1}, E_{GM2}, E_{GM3}, E_{GM4} and E_{GM5}, respectively, with the M values and corresponding Ca values being the same as those in the random (see **Table IV-7**). After injecting 18 PV of glycerol/water mixture at a constant flow rate of 1 μL/min, significant changes were observed in the size and distribution of the residual oil within the chip. At steady state, the distribution status of the residual oil in different experimental groups can be seen in **Figure IV-51**. It was noted that as M increased, the size of the residual oil significantly decreased and its distribution became more uniform. Simple visual inspection also indicated that the number of residual oil patches increased as their size decreased.

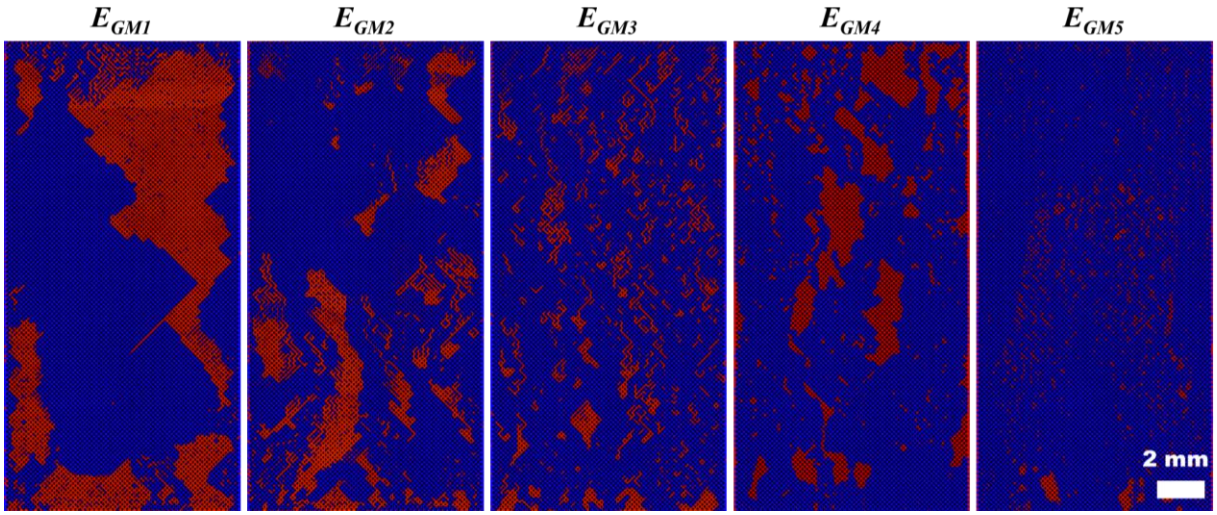

Figure IV-51 *The residual oil size and distribution at steady state after injected of 18 PV mixture with five M in regular chip.*

Image analysis was employed to calculate the saturation of residual oil within the chip, and the corresponding ΔP was recorded for each M. In **Figure IV-52** (a), we illustrate the ΔP plotted against the volume of injected fluids during waterflooding and mixture flooding experiments on a regular chip, highlighting how ΔP varies under different conditions. Similarly, compared to the results from the random chip, the experiments of regular one in the continuous water injection E_{GM1} (M=1) showed minor changes in pressure. However, in experiments E_{GM2} to E_{GM5}, ΔP noticeably increased as M increased, showing an overall trend similar to the results from the random chip. Consequently, we explored the correlation between ΔP and the viscosity of the glycerol/water mixture and compared these findings with those from the random chip, with the results presented in **Figure IV-52**(b). It has been observed that the ΔP values in random chip experiments are higher than those in regular chip experiments across all viscosity ratios. This is because the regular chip contains less residual oil, and the aqueous mixtures are more easily flow. Consequently, these smaller ganglia present less resistance to the flow of the wetting phase, resulting in lower steady-state ΔP values under all tested M conditions. This indicates that the geometric uniformity and reduced complexity of the pore structures in regular chips facilitate smoother fluid transitions and less obstructive interactions between oil and water phases, enhancing overall fluid dynamics.

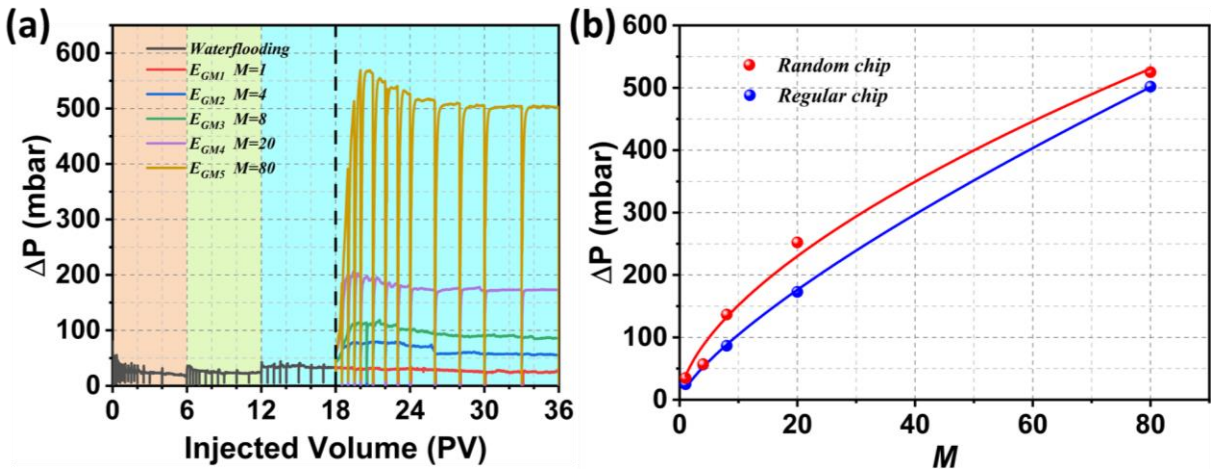

Figure IV-52 *(a) the ΔP plotted as function of M during the waterflooding and glycerol/water flooding with three flow rates; (b) the average steady-state ΔP plotted as function of M at the Q = 1.0 μL/min, where the blue one is the results of regular chip and the red one is the results of random chip during the mixture flooding.*

Figure IV-53 (a) shows the evolution of recovery versus the fluids injected PV and again beside the limited impact in E_{GM1} during continuous water flooding (approximately 2.7%), the final oil recoveries in E_{GM2} to E_{GM5} increased by about 15.9%, 24.3%, 27.4%, and 40.5% respectively, with an initial value at the end of the waterflooding experiment of about 56.7%. Compared to the random chip, which showed increases of 1.7%, 18.6%, 23.2%, 26.1%, and 37.9%, all cases except for E_{GM2} exhibited greater increments in recovery rates in the regular chip under the same experimental conditions, demonstrating that residual oil is now more easily mobilized, resulting in higher oil recovery rates than in the random chip. We also compared the impact of M on recovery rates in mixture flooding experiments between the regular and random chips, as shown in **Figure IV-53** (b). It is observed that the recovery rates in both types of chips follow the same trend, even if the sweeping efficiency is slightly greater for the regular chip.

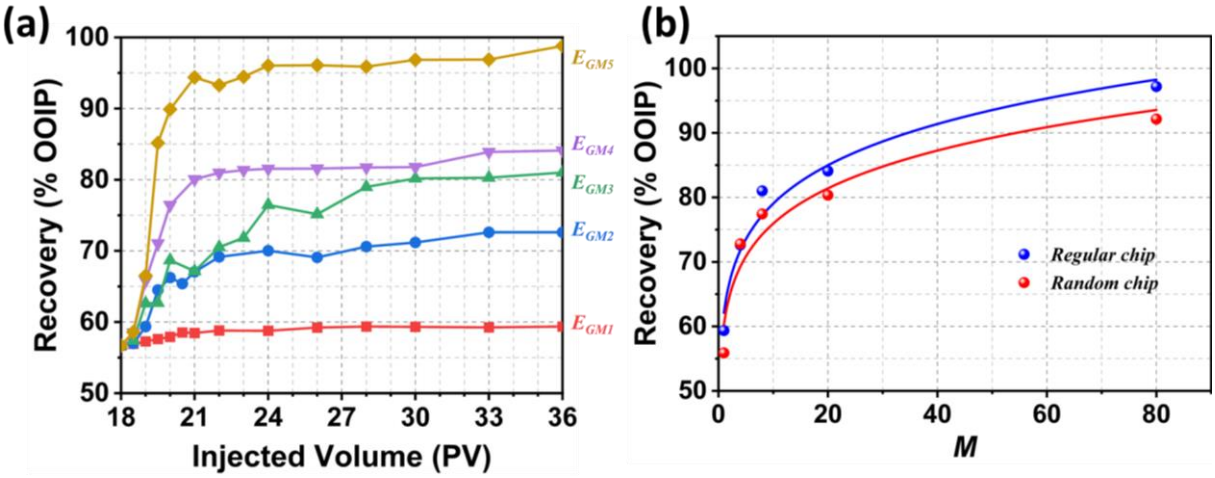

Figure IV-53 *(a) the oil recovery as the function of the volume of injected mixture with different M in regular chip; and (b) the correspond steady state recovery plotted as the function of M (blue) compared with random one (red).*

IV.1.4.3 Discussion of Dynamics and Mobilization Mechanism of Residual Oil

The fluid dynamics in porous medium, crucially influenced by the interplay between capillary and viscous forces, dictate the mobilization and trapping of non-wetting fluids. These interactions can be quantitatively analyzed through the dimensionless number, Ca, that may be adjusted by modifying Q and/or viscosity to explore various mobilization and trapping states of the non-wetting phase under different Ca conditions. Most reported studies have investigated flow regimes and displacement patterns by changing the flow rate (Saadat, et al., 2020) (Yiotis, et al., 2021) (Chen, et al., 2023) (Anastasiou, et al., 2024) or by injecting viscoelastic polymer solution or by decreasing the IFT (Avendano, et al., 2013) (De Castro, et al., 2016) (De, et al., 2018) (Lei, et al., 2020) (Yun, et al., 2020). Essentially, these methods fall under the category of secondary oil recovery. However, both in experimental and practical applications, it is crucial to focus on and understand the mechanisms of non-wetting phase trapping and mobilization, in the usual tertiary oil recovery method.

Observations indicate that the majority (65-90%) of the residual saturation of non-wetting phase in water-wet porous media is associated with large ganglia, while smaller ganglia contribute less to residual saturation (Georgiadis, et al., 2013) (Zarikos, et al., 2018). Although large ganglia significantly impact residual non-wetting phase saturation, they are considerably fewer. The size of a ganglion plays a crucial role in its mobilization potential (Lenormand, et al., 1983). Many reports suggest that larger or elongated ganglia are easier to mobilize due to local pressure differences across them (Mayer & Miller, 1993) (Georgiadis, et al., 2013). However, some studies indicate that shorter ganglia have higher transport rates than larger ones (Morrow, 1979) (Ramstad & Hansen, 2016) (Datta, et al., 2014). The primary mechanism of cluster mobilization is the splitting and merging of ganglia, a process that occurs predominantly for large ganglia and is significantly influenced by Ca and M, particularly for Newtonian fluids (Reddi, et al., 1998) (Anastasiou, et al., 2024).

Studies have shown that at low Ca values, the structure of non-wetting clusters does not change; conversely, when Ca exceeds a critical value, the largest ganglia begin to be mobilized and eventually removed from the medium (Chatzis, et al., 1983) (Datta, et al., 2014). Yet, there is controversy over the mobilization process of trapped non-wetting phase fluids as Ca increases. Some works and simulations indicate that ganglia are not immediately removed from the medium with increasing Ca; instead, they break up into smaller ganglia, only one pore in size, and remain trapped in the medium, becoming mobilized and removed only for large Ca values (Zhong, et al., 2001) (Zarikos, et al., 2018). In contrast, experiments on individual ganglia show that ganglia do not breakup; instead, all ganglia larger than a threshold size decrease with increasing Ca and are mobilized and removed (Ng & Payatakes, 1980) (Datta, et al., 2014). Thus, the change in Sor with increasing Ca is not determined by the decomposition of trapped ganglia; rather, it may reflect the mobilization and removal of the largest ganglia from the medium. Moreover, M is more crucial for the mobilization of trapped ganglia and the reduction of

residual saturation. For favorable M values, an increase in Ca leads to a greater reduction in residual saturation. For unfavorable M values, residual saturation increases before decreasing to the Ca threshold.

The physical processes and mechanism of different types of clusters as Ca increase

Despite the substantial literature on the entrapment and mobilization of ganglia, there is less focus on the impact of energy exchange and interactions between two-phase fluids on the mobilization of the non-wetting phase. Such studies are primarily conducted through the examination of the velocity field within trapped non-wetting phases (van Steijn, et al., 2009) (Zarikos, et al., 2018). Depending on the shape of the ganglia and surrounding geometric structures, the velocity field within each oil cluster differs, implying local energy disparities that could lead to the mobilization or breakup of ganglia. This necessitates a comprehensive assessment of the forces exerted on the oil clusters by the flow of the wetting phase, the frictional forces from the solid phase, capillary forces, and the pressure differences exerted by the wetting phase on the droplets.

Here, drawing from literature (Zarikos, et al., 2018) (Anastasiou, et al., 2024)and using acquired images from experimental processes, we analyze the potential energy transformations experienced by three types of clusters—droplets, blobs, and ganglia—as Ca increases. This analysis helps elucidate how changes in fluid dynamics under increasing Ca influence the behavior and displacement efficiency of various oil cluster types within porous media, providing deeper insights into the complex interactions at play in enhanced oil recovery scenarios.

Droplets

As illustrated **Figure IV-54**, one droplet is trapped at the center of pore, due to blockage by solid grains and other clusters on the bottom and left side, wetting phase primarily flowing from small pore throat on the right, as guided by the white arrows in the middle image. The larger space below the droplet allows more and easier wetting phase flow along its lower side, whereas the smaller space on the upper right results in slower flow rates, causing asymmetry in the local velocity distribution. Consequently, the greatest resistance is applied along the lower side of the droplet, where the non-wetting phase flow rate is highest. The resistance moving the non-wetting phase leftward generates a clockwise circulation within the droplet. Moreover, only a small pressure difference is expected between the top and bottom of the droplet. Therefore, the droplet remains immobile even if flow rates increase by an order of magnitude, but it will likely change its shape from spherical to elliptical under higher Ca. However, it is important to note that when viscous forces dominate, other droplets along the path of the wetting phase flow are likely to be mobilized.

During the mixture flooding phase, due to the increased viscosity of the injected fluid, viscous forces are enhanced enough to push the weting or non-wetting phase pass through the bottom throats and flow along the flow injected direction from bottom to top (indicated by orange arrows in right image of **Figure**

IV-54), applying greater upstream pressure differentials to all oil clusters. This can lead to direct mobilization of the droplet or through energy exchange with upstream residual oil, causing a significant pressure difference between the upper and lower parts of the droplet and thus mobilizing it.

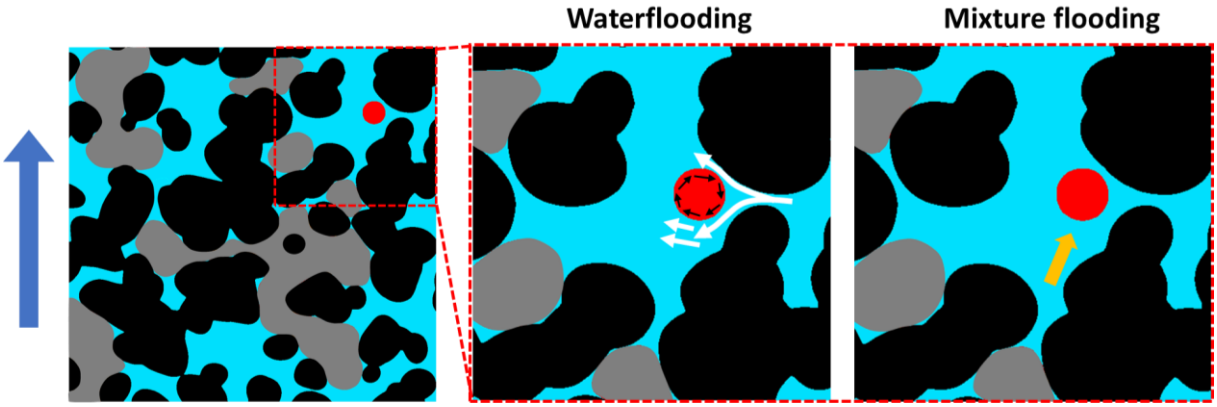

Figure IV-54 *The visualization from the waterflooding process shows the distribution of localized oil clusters within the porous medium. Focous on the the red dashed frame area, the red droplet have a internal velocity field (balck arrow) in middle image, and the brine flowdirections along with the white arrow arround the droplet during the waterflooding; while in the mixture flooding, the dropelt pushed by the viscous forces of mxiture, as the orange arrow shows in the right image. In all images, blue areas represent the wetting phase, black areas denote solid grains, red indicates the droplet, and gray signifies other oil clusters.*

Blobs

Subsequently, we consider two blobs within the porous medium, each occupying a pore space, but with distinct locations: the left blob is situated in a dead-end pore, while the right blob is located in a whole pore along a connected pathway (in **Figure IV-55**). During the waterflooding phase, similar to the previously described droplet, brine primarily enters from the right-side pore and flows in the direction indicated by the white arrows. The flow velocity above both blob slows fastest, while in other directions, the movement of the wetting phase is hindered by geometric structures and trapped clusters, resulting in few flow rates. As a result, the velocity vectors within the blobs indicate counterclockwise rotation, directly resulting from the blobs' positions and the drag forces applied by the wetting phase. In addition, due to differences in the interface area where energy exchange occurs between the phases and the positions of the captured blobs, there are variations in their internal velocity fields. However, due to geometric restrictions, the energy transferred from the wetting phase at the interface to the blobs is minimal, meaning that the pressure differential across the blobs is also small, thus making their mobilization challenging.

When considering the mobilization of captured blobs, the impact of their captured position and the effective transfer of energy from the wetting phase must be accounted for. For the two blobs presented in this document, increasing the flow rate to enhance Ca affects them only to the extent of a limited increase in brine velocity in the direction indicated by the white arrows, due to the pore structure and

behavior of other captured clusters. This would only cause an increase in the internal circulation velocity within the blobs, insufficient for their mobilization. During the mixture flooding phase, however, the effective increase in viscosity amplifies the viscous forces of the wetting phase, which could effectively mobilize other captured clusters along the flow path or reach the location indicated by the orange arrows through energy exchange. This undoubtedly causes the bottom of the right blob to experience significant upstream pressure, creating a large pressure differential with the top, leading to the breakup of the cluster into smaller droplets, or causing them to be mobilized in whole. However, for the left blob, despite experiencing significant pressure differential on the side indicated by the orange arrows, the structure of the dead-end pore hinders further mobilization possibilities, thereby keeping it trapped but allowing it to move deeper into the pore, as indicated by the contour of the orange line.

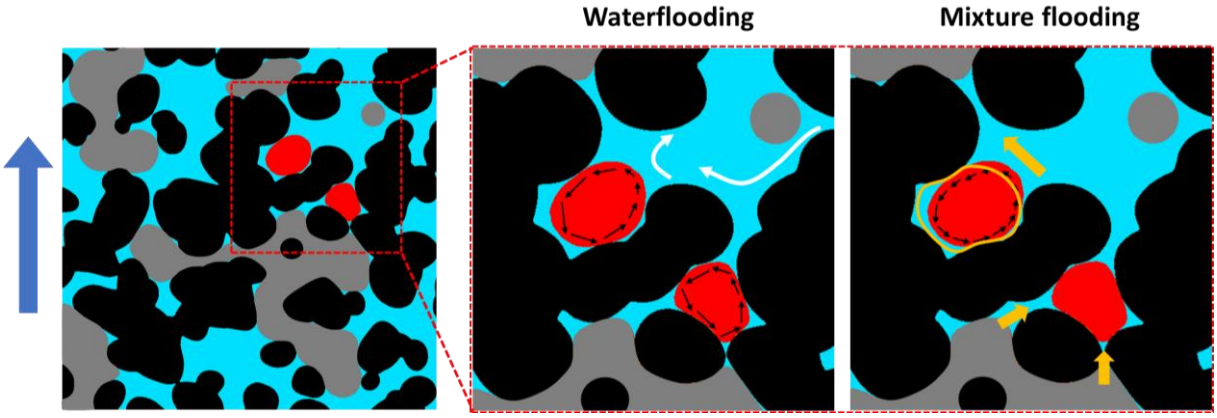

Figure IV-55 *The visualization from the waterflooding process illustrates the distribution of localized blobs within the porous medium. During waterflooding, the brine flows as indicated by white arrows in the middle image, which then causes two blobs to undergo counterclockwise internal rotation, as shown by the black arrows. Meanwhile, in mixture flooding, under the influence of higher viscous forces, the wetting phase can exert pressure on the blobs either directly or through energy transfer along the orange arrows, resulting in the deformation of the left-side blob (outlined in orange) and the mobilization of the right-side blob. In all images, blue areas represent the wetting phase, black areas denote solid grains, red indicates the blobs, and gray signifies other oil clusters.*

Ganglia

The largest clusters, known as ganglia, are often the most challenging to fully mobilize due to their size and the significant capillary forces required to maintain them within the pore spaces. As depicted in the **Figure IV-56**, a ganglion captured by capillary forces is shown; the flow direction of the wetting phase is indicated by the white arrows on the left side. Under its influence, multiple vortices form near the interface, and the overall velocity is counterclockwise. Due to the structural restrictions of the pore on the left side of the ganglion, energy exchange between phases is difficult, making the velocity field approach zero, while the highest velocity is at the liquid-liquid interface where energy exchange takes place. With the Ca increases by increase of Q, enhancing the flow velocity at the white arrow, causing significant deformation of the ganglion. The upstream interface is displaced under the pressure of the

brine, forming a flatter interface and being pushed towards the solid-liquid boundary; simultaneously, the interface curvature increases downstream through energy transfer, displacing brine, as depicted by the black dashed line in the middle image. Under strong drag forces, internal circulation within the ganglion intensifies. When the upstream interface reaches the solid-liquid boundary under high Ca, it may cause the ganglion to breakup.

In mixture flooding, under the influence of high viscous forces and pressure drops (indicated by the orange arrows in the right image), the ganglion can break through pore throat geometrical constraints downstream through energy transfer and can also rapidly push the liquid-liquid interface towards the solid-liquid interface upstream, where the ganglion breakup. Ganglion breakup is a common phenomenon that results in the partial movement of the ganglion, as described by Lenormand (Lenormand, et al., 1983). Breakup typically manifests as deformation of the ganglion and the formation of a non-wetting phase filament. Generally, after breakup, a ganglion forms two sub-ganglia; the upper half may remain in place while the lower half is mobilized, or it may briefly stay put before rupturing or being mobilized under continued wetting phase scouring. However, this is also limited by the downstream pore structure. At low Ca, it is usually trapped in the form of a blob, but at high Ca and M values, the fragmentation process is intense, allowing small ganglia to flow unrestricted by capillary forces. At this point, the internal flow velocity of the small ganglia increases rapidly, and the flow velocities are roughly equal in all areas, consistent with their main direction.

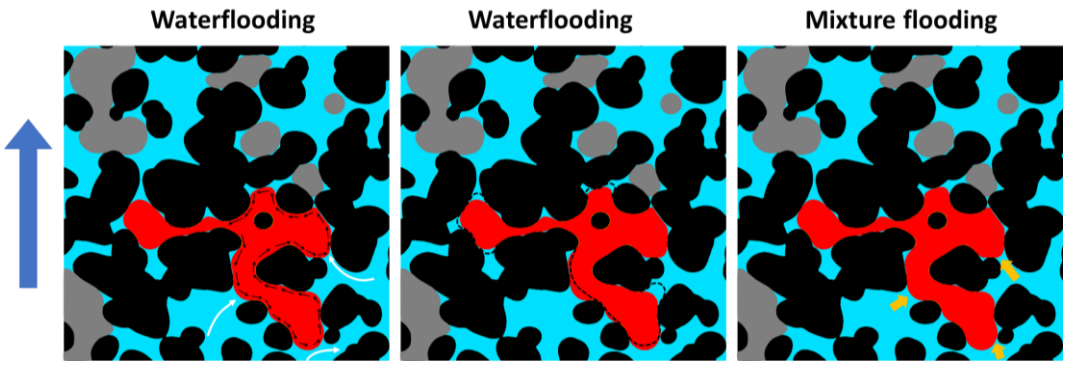

Figure IV-56 *In left image, the direction of brine flow is indicated by white arrows, while the flow direction within the ganglia is shown by black arrows during the waterflooding. Increasing the Q to raise the Ca affects the ganglia, with their deformed outlines depicted by black dashed lines in the middle image. In mixture flooding, the direction of pressure exerted by the wetting phase on the ganglia is indicated by orange arrows in the right image. In all images, blue areas represent the wetting phase, black areas denote solid grains, red indicates the ganglia, and gray signifies other oil clusters.*

The breakup, coalescence, and trapping behaviors of clusters.

Before this steady state is achieved, these three types of oil clusters are continuously generated and undergo processes of coalescence and fragmentation within the micromodel chip. To assess these dynamics, we visually examine the coalescence and fragmentation of different types of residual oil at

various locations on the chip using processed images. In **Figure IV-57**, it can be observed that the residual oil located along the flow path experienced coalescence and fragmentation within the microfluidic chip. Typically, the stranded residual oil may become mobilized when the mobile residual oil collides and coalesces with them. The collision-induced coalescence produces larger ganglia, leading to significant pressure differentials at their leading and trailing edges, thereby overcoming the capillary pressure threshold of specific pore throats and mobilizing them. Conversely, the fragmentation process generates new ganglia, blobs, or droplets, depending on geometric. The formation of new ganglion typically leads to the stranding of formed ganglia in the downstream direction (Talon, et al., 2023). In contrast, if droplets are formed, they are no longer influenced by capillary forces and can freely flow around solid obstacles (Anastasiou, et al., 2024). The mobilization of blobs resulting from fragmentation depends on the downstream geometric structures.

In **Figure IV-57** (a), we display the capture of three types of oil clusters during the waterflooding phase at a flow rate of 0.1 μL/min. The yellow square frames a ganglion that remain, stable all over the waterflooding. The yellow dashed square frames a droplet that forms after continuous injection of 0.8 PV of brine and remains captured until the final steady state. In the image, it is easy to observe that there is sufficient space on the left side of the droplet, allowing brine to pass through freely. On the right side, the droplet contacts two pore throats and three solid grains, blocking further movement, indicating an internal clockwise velocity field. Additionally, due to the no-slip condition at the solid-liquid interface, there is lower velocity, resulting in minimal pressure differential from left to right, and thus the droplet cannot be mobilized. The white ellipse frames a blob that is mobilized during the brine injection process (0.8 PV) but it then remain trapped until reaching steady state.

Figure IV-57 (b) displays the breakup and coalescence behavior of clusters observed in another set of independent waterflooding experiments when Q was gradually increased to 1 μL/min. When 0.25- 0.5 PV of brine is injected at this flow rate, breakup of a ganglion occurs at the position indicated by the yellow arrow at 0.25 PV, forming a droplet depicted in the white square at the bottom of the 0.5 PV image. The breakup of this ganglion is due to increased capillary pressure at the front of the lower ganglion under heightened differential pressure, which fractures at the pore throat. Subsequently, this droplet collides and coalesces with the blob shown in the white square above along the purple arrow direction, forming a ganglion illustrated in the white dashed box at 0.75 PV. This ganglion is then mobilized, undergoes breakup, forming a new droplet that is mobilized, while the residual part of the ganglion remains trapped as shown in the white dashed box at 1.5 PV. This ganglion remains trapped under this flow rate until reaching steady state, and we did not capture the breakup forming the droplet, as reported by Anastasiou et al. ((Anastasiou, et al., 2024)).

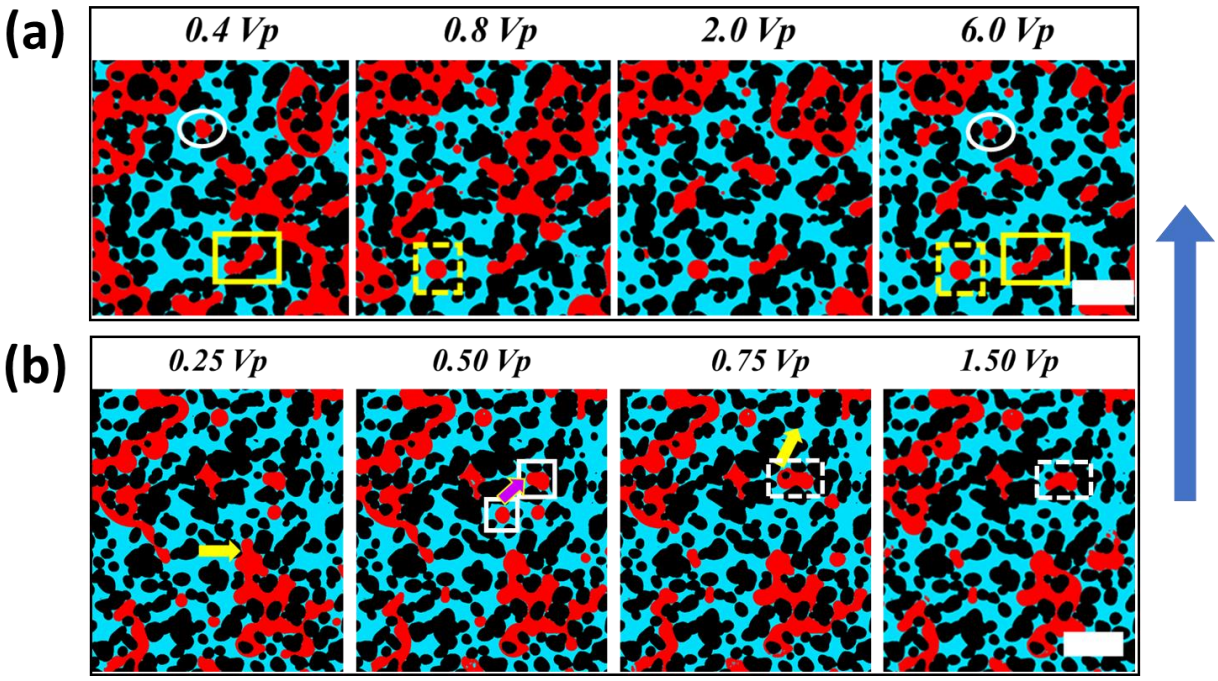

Figure IV-57 *(a) The trapping behavior of oil clusters within the chip at Q = 0.1 μL/min. The cluster within the yellow box is ganglia; in the yellow dashed box is droplet; and within the white elliptical box is blob. (b) In another independent experiment, as the Q gradually increased to 1 μL/min, the breakup and coalescence behaviors of clusters observed in the chip. Yellow arrows indicate the locations of breakup; white boxes and purple arrows represent the collision and coalescence processes between moving clusters and trapped clusters; white dashed boxes show newly formed ganglia and subsequently, ganglia that undergo breakup and are permanently trapped. The scale bar measures 1mm.*

In mixture flooding, the viscosity effect on oil recovery stems from a reduced mobility difference between the displacing and displaced fluids, as the capillary forces decrease relative to the viscous forces, favoring oil recovery. Favorable M not only improves the smoothness of the displacement front but also significantly increases viscous forces, leading to a notable rise in ΔP within the chip and effective mobilization of residual oil. Unlike waterflooding, the newly formed ganglia after fragmentation do not become stranded and trapped downstream, as their mobilizable size is sufficiently small and not affected by pore throat capillary forces.

In **Figure IV-58**, we present the mobilization results of localized residual oil in the chip after injecting different volumes of the mixture with M as 1/10. Initially, at 0.5 PV, large ganglia and bypassed residual oil are visibly present in the window, with only a small amount of droplets and blobs along the flow path. By the time 1 PV is injected, the bypassed residual oil is noticeably diminished, although the field of view still contains residual oil, but in significantly reduced sizes, present in the form of ganglia, blobs, and droplets. Upon injecting 4 PV, the larger ganglia disappear, fracturing into numerous blobs and droplets downstream, which rapidly move along the flow path, with a more multidirectional flow path observed. At the end of 18 PV, both the size and number of residual oil clusters decrease significantly.

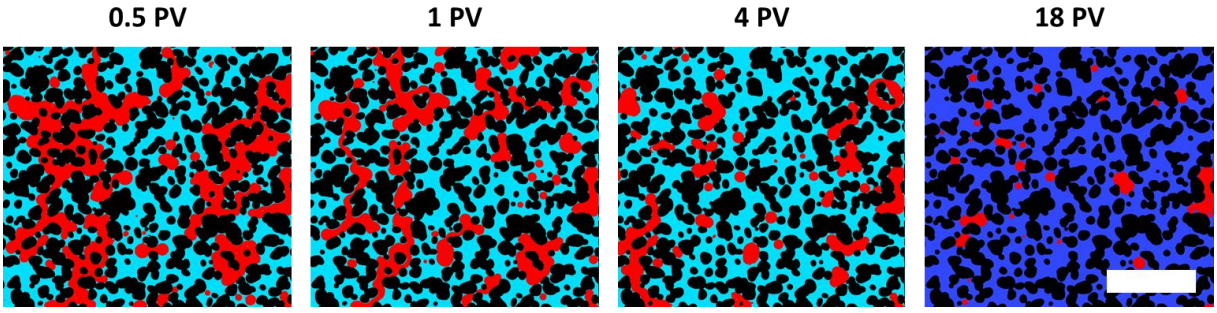

Figure IV-58 *The residual oil type and size change with the injected volume of mixture with M of 8. Where the black are solid grains; red are oil clusters; blue is mixture, and the dark blue is the final steady-state. The scale bar measures 2 mm.*

IV.1.4.4 Clusters Size Distribution and Analysis

In **Figure IV-59**, the distribution of ganglion sizes is calculated based on split images corresponding to the three Q in waterflooding and five values of M when glycerol/water mixture were injected. **Figure IV-59**(a) illustrates that during waterflooding, there is no significant change in ganglion sizes as the Q increases from 0.1 μL/min (E_{WF1}) to 1.0 μL/min (E_{WF3}), indicating that increasing Ca by a decade has a minimal influence on the size distribution of ganglion size and volume. However, the calculation of ganglia density within the original pore sizes (**Figure IV-59** (b)) reveals variations in ganglia density across different original pore sizes among the three experiments. It is observed that the distribution of ganglia density is complex and staggered among the three groups, but follows a basic pattern where ganglia density distribution decreases in larger pores and correspondingly increases in adjacent smaller pores. For example, as Q decreases, ganglia density decreases in the 450-500 μm pore size, but it increase in the 400-450 μm size range; similarly, a decrease in Q leading to reduced ganglia density in the 350-400 μm range causes an increase in the 150-300 μm range. This significant interval fluctuation is due to the large ganglia's substantial influence on residual oil saturation. When they break up into smaller ganglia, they produce several times of smaller ganglia of lower mass, and due to geometric constraints, the size and number of these breakup ganglia also have a broad distribution, thus having a big density distribution. However, for ganglia in larger pore sizes, due to their limited number, their influence on the number and size distribution of ganglia in adjacent smaller pores is minor. In smaller pores, ganglia primarily exist in the form of droplets, and when Q increases, thereby increasing Ca, it drives some droplets to mobilize, reflected by a decrease in ganglia density in this range.

Figure IV-59(c) shows the influence of M values on ganglion size under a constant flow rate of 1.0 μL/min. It is obvious that ganglia sizes do decrease progressively from E_{GM1} to E_{GM5}, with noticeable differences in the finer size distributions, with the majority of ganglia sizes ranging from $\sim 10^4$ to 10^6 μm^2. This phenomenon is likely due to unfavorable M conditions (E_{GM1}) leading to the formation of larger ganglia, which are then fragmented or mobilized under higher M to form smaller ganglia. **Figure IV-59**(d) supports this viewpoint. Unlike the effects caused by changes in Ca due to limited increased

Q, the increase of Ca by increasing M has a monotonic effect on ganglia density. Specifically, in larger pores (greater than 100 μm), their density decreases with increasing M, and the sizes of the largest filled pores gradually decrease. Whereas in smaller pores (less than 50 μm), the density significantly increases with M, and the range of sizes becomes narrower.

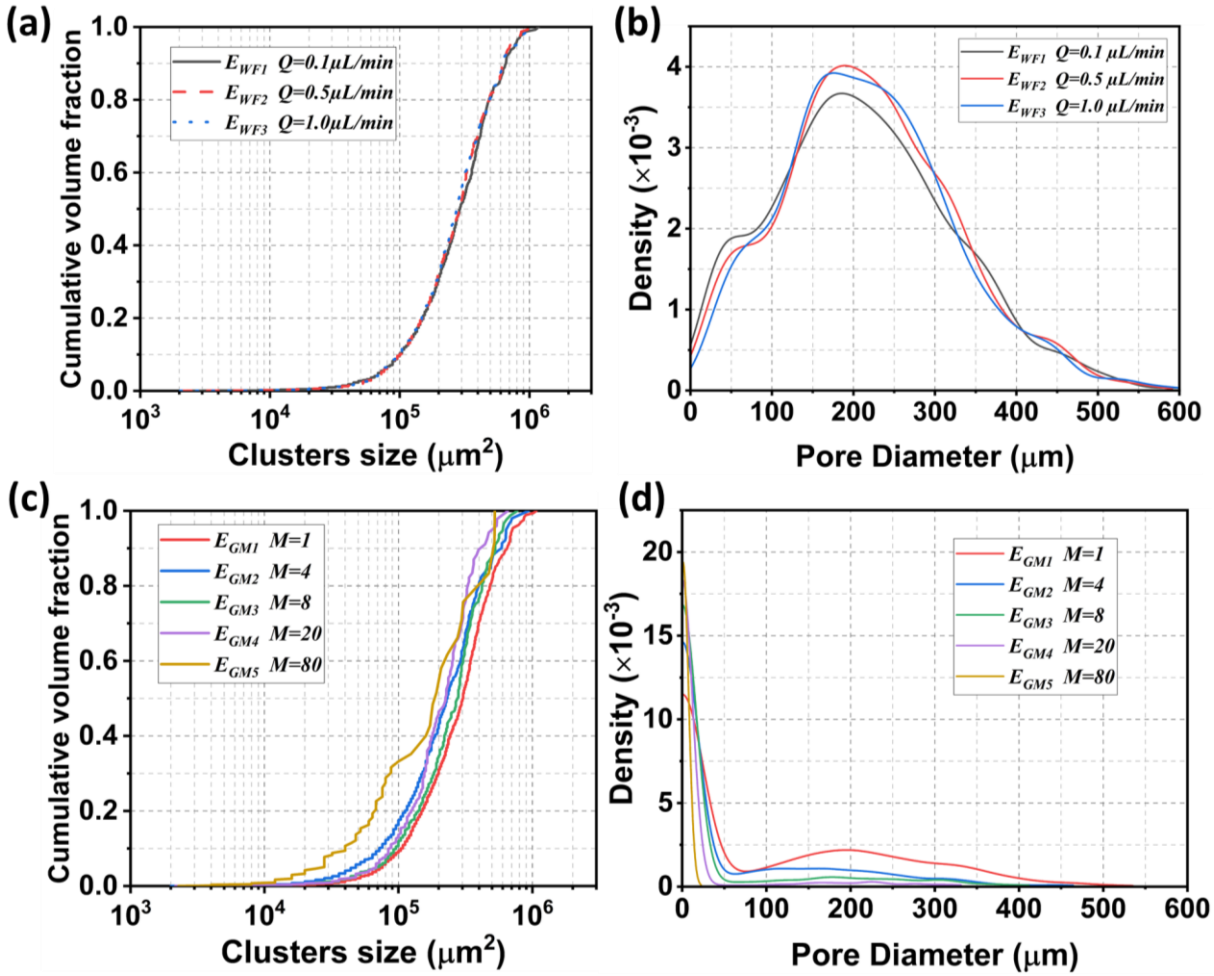

Figure IV-59 *(a) Cumulative volume fraction plot in function of clusters size during waterflooding at three flow rates; (b) the oil clusters density in function of original pore size during waterflooding at three Q; (c) Cumulative volume fraction plot in function of clusters size during glycerol/mixture flooding with five different M; (d) the residual oil clusters density in function of original pore size for glycerol/mixture flooding with five differnent M*

We perform now a statistical analysis of the number and volume of different types of clusters within the chip at steady state across five different M cases. The results, illustrated in **Figure IV-60**, show dashed lines representing the number of three types of clusters and solid lines for their volumes; droplets are indicated in black, blobs in red, and ganglia in blue. Across all cases, at steady state, the number of droplets is the highest, followed by blobs, with ganglia being the least numerous (**Figure IV-60**(a)); however, the volume distribution exhibits the opposite trend, with ganglia having the largest volume, followed by blobs, and droplets having the smallest (**Figure IV-60**(b)). This implies that ganglia

primarily impact residual oil saturation, consistently with literature reports (Mayer & Miller, 1993) (Georgiadis, et al., 2013).

Moreover, we observed that the volume of droplets and blobs changes little with increasing M, remaining within a narrow interval. In contrast, the volume of ganglia decreases more sharply with increasing M, particularly when M smaller than 4. It was usually reported that the sweep efficiency is optimal for a M near or less than 20 (Dyes, et al., 1954). At M=80, the volume of ganglia at steady state reaches a very low level. This is because ganglia are more susceptible to breakup and mobilization in a high viscosity mixture, leading to not only a dramatic reduction in their volume but also in number that effectively reduces S_{or}. In addition, the number of blobs slightly decreases as M increases expect at high M of 80, while the number of droplets remains relatively unchanged. This reaffirms that non-wetting phase saturation is predominantly influenced by ganglia.

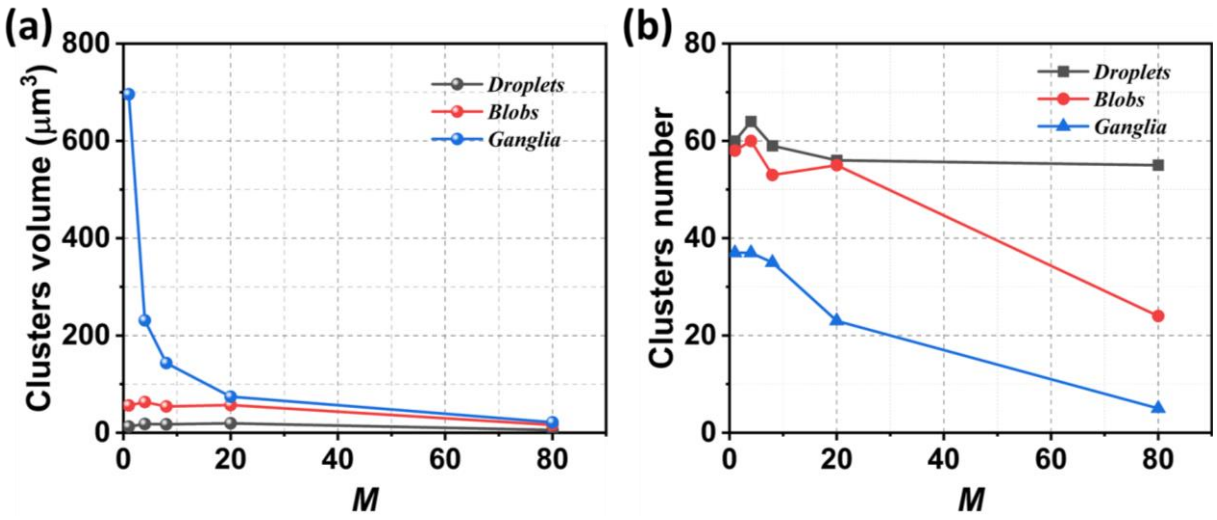

Figure IV-60: *(a) the clusters volume and (b) clusters number plot as function of M at steady state*

Otherwise, the granularity distribution of these residual oil clusters is a significant factor in assessing fluid recovery efficiency in petroleum engineering and CO_2 geological sequestration applications. In that respect, percolation theory was applied to analyze the size distribution of residual oil clusters, and it was observed that the cluster size distribution follow a power law as:

$$N(s) \sim s^{-\tau} \qquad \text{Equation 4-4}$$

where $N(s)$ represents the number of clusters of size s, and τ is a critical scaling exponent, and by combining works from the literature, the reported τ values usually range between 1.8 and 2.3.

Extensive experimental studies and data analysis have revealed that the power-law exponent in oil-wet porous media is higher than in water-wet conditions, indicating a prevalence of smaller clusters in oil-wet conditions (Iglauer, et al., 2012). In addition, the length distribution of trapped ganglia ($LN(L)$) decays consistently with a power law as predicted by percolation theory also (Datta, et al., 2014), with the size of a ganglion is related to its length (L) by the relation $s \propto L^{3/(\tau-1)}$, and therefore have, $LN(L) \propto L^{-}$

$^{3\tau/(\tau-1)+1}$. The scaling exponent has significant physical implications: a smaller τ implies larger overall residual droplets, which are easier to mobilize.

Here, using images obtained during experiments, we studied the presence of this power law in both water flooding and mixture flooding conditions. The analysis was improved by considering only ganglia sizes larger than 10 pixels and occurring more than once. It is important to note that this scaling method should be applied to the pore size of ganglia, not their surface area in pixels. However, given that the depth of the channels in our micromodel is constant, the two methods are approximately equivalent. According to the literature, normalized counts are defined as (the number of ganglia with a given surface in pixels) / (the number of the smallest ganglia), and normalized size is defined as (surface) / (surface of the smallest ganglia). In all cases, normalized counts are represented as a function of normalized size.

Form **Figure IV-61**, the average value of τ is ≈ 2.0, that is consistent with numerical predictions based on invasion percolation theory (Wilkinson & Willemsen, 1983). Additionally, despite the changes in Ca caused by different M and/or Q considered here, the obtained exponents are very close. A notable exception is the τ value predicted for E_{GM5}, which shows significant deviation from other groups, possibly because at that M value, the number of remaining clusters is very low and static calculations provide no satisfactory confidence. Moreover, studies have demonstrated through rigorous mathematical analysis of representative experimental data that the exponent τ is much smaller than previously thought (Iglauer & Wülling, 2016). It must be mentioned that the exact value of τ is influenced by the method of curve fitting and the range of ganglia sizes used for fitting the power law (De Castro, et al., 2016) (Iglauer & Wülling, 2016).

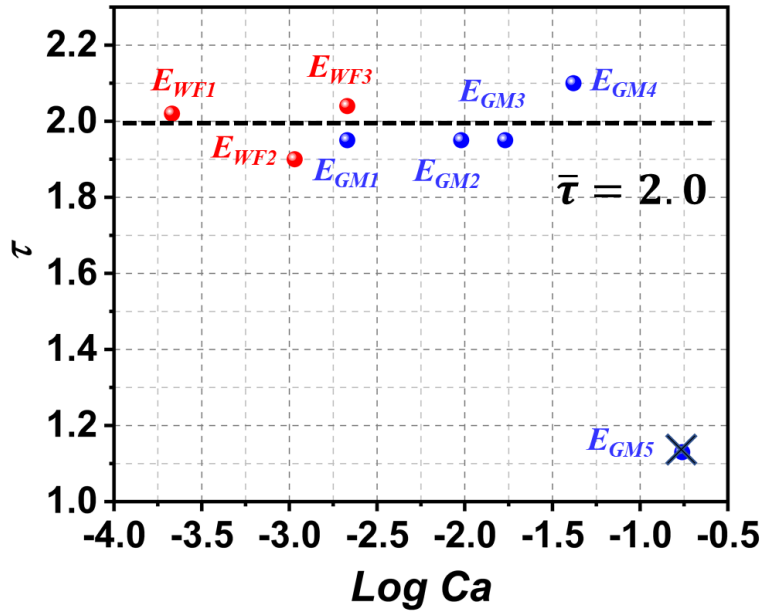

Figure IV-61 *Fitted power-law values as a function of the Ca during the waterflooding experiments (red points) and glycerol/water mixture flooding experiments (blue points)*

The residual oil number and average size

Figure IV-62 illustrates the function describing the change in number of residual oil clusters with Ca in the micromodel. In this figure, E_{WF1} to E_{WF3} represent the stepwise increase in flow rate. It can be observed that at steady state, the number of residual oil clusters significantly increases as the flow rate increases. This is because higher flow rates simultaneously increase the pressure drop and Ca in the micromodel, which facilitates the fragmentation and mobilization of larger ganglia. As a result, large ganglia fragment into smaller ganglia or blobs, leading to an increase in oil clusters number. Subsequently, the influence of M on residual oil mobilization and size was explored. E_{GM1} serves as the control group with the same M as the previous experiments, even if prolonged water injection may displace some smaller-sized residual oil such as blobs and droplets from the micromodel, resulting in a decrease in oil clusters number. However, as M values increase to 4 and 8, according to the dynamic mechanisms described earlier, M enhances flow stability, allowing the mixture to sweep more areas, while larger pressure drop that leads to continued fragmentation of ganglia into smaller residual oil entities. Therefore, the residual oil number in the micromodel rapidly increases. Nevertheless, with further increases in M, as observed in E_{GM4} when M increases to 20, the higher viscosity leads to more rapid fragmentation of larger-sized residual oil into smaller ones. Additionally, due to the further increase in pressure drop, the fragmented smaller-sized residual oil is more easily mobilized and displaced from the micromodel under the same injection volume, resulting in a decrease in oil clusters number. At the end, a few residual oil clusters number is observed in the micromodel when M is 80. This rapid decrease in residual oil number is attributed to the enhanced sweeping capability and fragmentation ability resulting from higher M compared to E_{GM5}.

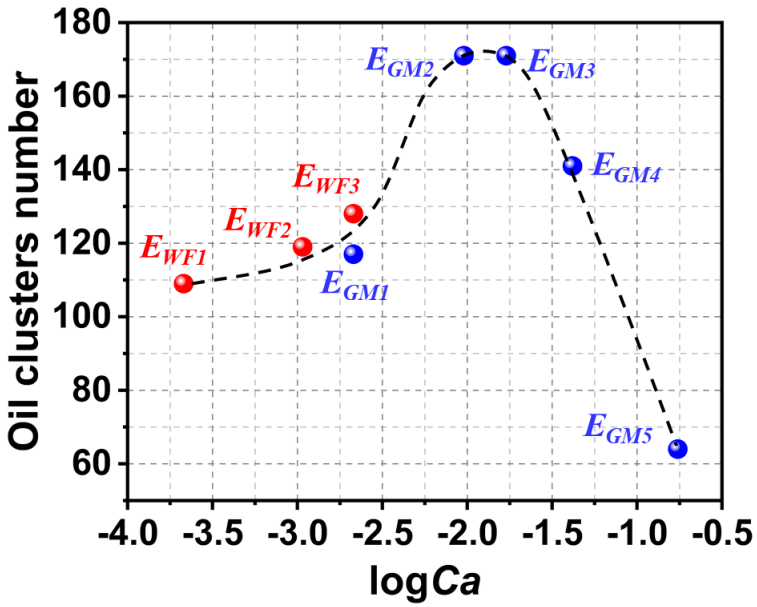

Figure IV-62 The residual oil number in function of logCa

Meanwhile, we conducted a statistical analysis of the relationship between the average residual oil size and the Ca value for different cases at steady state, and the results are shown in Figure IV-63. It appears that the relationship between the average residual oil size and Ca follows a reverse S-shaped curve, indicating that increasing Ca or M effectively reduces the average residual oil size. From the **Figure IV-63**, it is apparent that the change in average residual oil size due to variations in Ca resulting from increasing flow rates is relatively limited, with a decrease of approximately 1×10^5 μm^2. Additionally, comparing E_{GM1} and E_{GM2} reveals that even small changes in M can effectively reduce the average residual oil size, suggesting that M is more conducive to the fragmentation and mobilization of large ganglia. However, as M increases, such as in E_{GM3} to E_{GM5}, the influence of M on the average residual oil size gradually diminishes, as remaining ganglia become more and more efficiently trapped in complex poral structures.

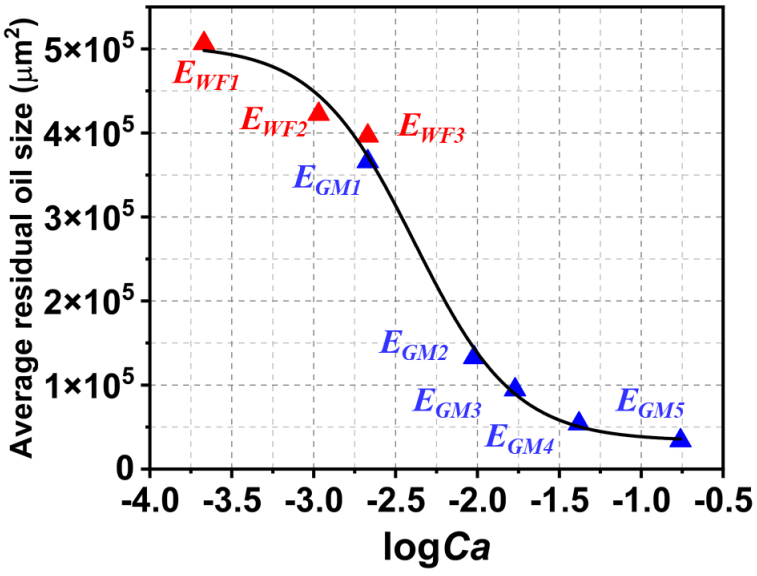

Figure IV-63 Average oil clusters size in function of logCa

The Capillary Desaturation Curve

Capillary desaturation curves (CDCs) are commonly used to describe the relationship between the saturation of residual non-wetting phase and the Ca during the imbibition phase. We analyzed and calculated S_{or} versus Ca for the two types of chips under steady-state conditions of waterflooding and mixture flooding. The CDC data obtained from our experiments coalesced almost perfectly into a single curve, consistent with the typical trends observed in CDC curves. As shown in **Figure IV-64**, triangles represent waterflooding experiments, while full circles represent mixture flooding results. During the waterflooding, it was observed that S_{or} decreases with an increase in Ca by increasing Q only when the Ca higher than 10^{-4}, which is the critical threshold Ca, indicating partial mobilization of the residual oil in the micromodel, aligning with the reported in the literature (Datta, et al., 2014). Both the size of the largest trapped ganglia and the total amount of trapped non-wetting fluid decrease with increasing Ca during the waterflooding phase, with no significant observed effects of ganglia breakup. However, during the mixture flooding, we distinctly observed the breakage and mobilization of ganglia. In this series of experiments, increasing Ca by increasing M facilitated the fragmentation of oil clusters into smaller ganglia, which were then mobilized, effectively reducing Sor. When Ca was increased to the order of 10^{-1}, Sor in the chip reached a very low value, indicating that most of the clusters were mobilized.

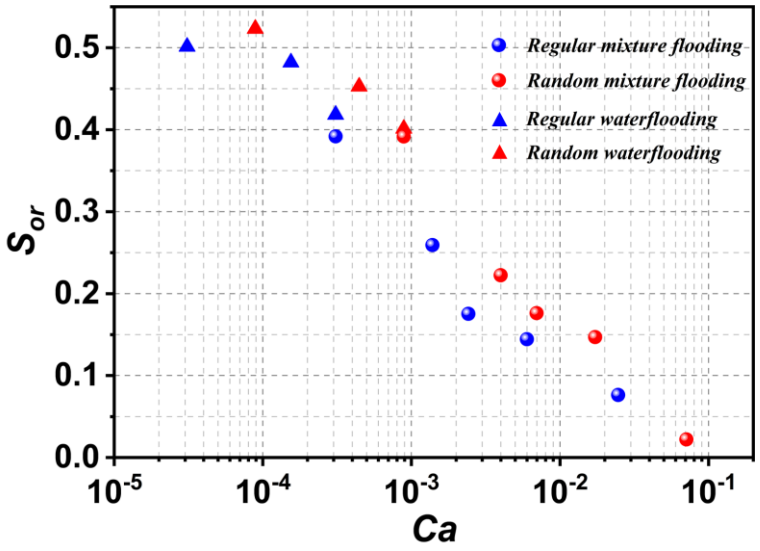

Figure IV-64 *Sor in function of Ca both for regular chip (in blue) and random chip (in red) during waterflooding and mixture flooding.*

IV.1.4.5 The Discussion of Mixture Flooding

In this section, we adjusted the viscosity of the injecting phase by using a glycerol/water Newtonian mixture, with the M ranging from 1 to 80. We explored the impact of increasing the *Ca* through changes in M on the saturation, location, size distribution, and number density of the non-wetting phase, and we conducted a detailed investigation into the mobilization mechanisms of clusters. Replication and

validation experiments were also performed in the regular chip to discuss the influence of pore structure on cluster mobilization. Finally, the functional relationship between S_{or} and the Ca_{new} at steady state was analyzed using a new calculation method for *Ca*. Below, we will report the results obtained in detail:

Firstly, from the analysis of acquired images, it was found that, aside from the case with M=1 (that means continuing injection of brine), the number and volume of residual oil clusters significantly decreased under other four M at steady state, and their distribution within the porous media became more uniform, with this effect positively correlated with the magnitude of M. From snapshots obtained through video, we captured the process of ganglia breakage during the invasion of the aqueous mixture. Under the injection of high-viscosity mixture, ganglia breakage, experiencing snap-off at pore throats, forming new blobs or droplets, and moving rapidly along the flow direction. Although the ganglia reduced in size, they remained trapped in the pores until multiple breakages reduced their size sufficiently to overcome the capillary forces and mobilize them.

We believe that the breakage and movement of clusters are due not only to the increased sweeping efficiency provided by higher M but also to the greater ΔP caused by higher viscosity, which leads to cluster breakage and rapid movement. According to Darcy's Law, for Newtonian fluids, an increase in viscosity results in a linear increase in ΔP, but the mobilization of clusters (manifested as the movement of blobs and droplets and the breakage of ganglia) tends to reduce ΔP within the chip. Moreover, as M increases and more clusters are mobilized, ΔP decreases further. Thus, the functional relationship between ΔP and M shows a trend of ΔP per unit M decreasing.

Following waterflooding, the recovery of oil exhibits the same trend, that is, recovery increases with increasing M and shows a pattern of increasing first and then reaching a steady state with the volume of injected mixture. Importantly, the interval from recovery increase to steady state is the period when clusters undergo breakage and mobilization. It can be observed that this interval value decreases with increasing M, indicating that higher M accelerate the rate at which remaining oil clusters breakage and mobilization. We also analyzed the functional relationship between recovery and M and found that the rate of increase in recovery gradually decreases with increasing M, implying that a smaller M can achieve desirable economic efficiency. This value reported in the literature is 20, consistent with our experimental results.

After the end of mixture flooding, we calculated the number density of clusters in the original pore sizes and found that it gradually decreases with increasing M. Subsequently, we quantitatively compared their proportional share of number density; the proportion of clusters number density in all pores decreases with increasing M, except at M=4, where the proportion in small pores (<100μm) rises, and it is observed that the maximum pore space occupied by clusters is also decreasing.

Subsequently, we demonstrated the forces and movement trends experienced by droplets, blobs, and ganglia during the mobilization process, influenced by the geometric structure within the pores. We

highlighted that mobilization of blobs is least likely to occur due to the presence of dead-end pores and smaller pore throats. In contrast, droplets are more prone to movement, and notably, due to the breakage of ganglia, new droplets are generated, maintaining a dynamic equilibrium of droplets. We also detailed the flow behaviors of the three types of clusters during the mixture flooding process, such as blobs and droplets being permanently trapped or mobilized by the pore structure, only to be refilled and re-trapped by new clusters. Ganglia act as transport mediums, merging with upstream colliding clusters and breaking into new clusters downstream or being mobilized themselves. This detailed illustration reveals the mobilization mechanisms of clusters during the imbibition process.

Lastly, we analyzed the cumulative volume fraction of cluster sizes and their density distribution in original pore sizes after waterflooding and mixture flooding. Results indicated that while there was no significant change in cluster sizes during waterflooding, their distribution across different pore sizes showed slight fluctuations with increasing flow rates. In mixture flooding, the cumulative volume fraction of cluster sizes showed a clear trend of overall reduction with increasing M, and their density distribution in the original pore sizes decreased in larger pores (>100 μm) and concentrated and increased in smaller pores (<100 μm). This suggests that large ganglia are being breakup to smaller clusters.

By analyzing the volume and number of droplets, blobs, and ganglia at steady state under five different M values, we found that both the volume and number of droplets are minimally affected by M, remaining stable within a constant range. The volume of blobs is also largely unaffected by M, but their number decreases at higher M, indicating a minimal impact of blobs number on residual oil. However, both the volume and number of ganglia show a significant decline with increasing M, dropping to very low values. These findings suggest that cluster volume is primarily dominated by ganglia, and reducing the volume and number of ganglia can effectively lower S_{or}, providing a strategic guide for mobilizing trapped non-wetting phases. Additionally, when we plotted the number density N(s) against the size (s) of each type of cluster, we demonstrated that it satisfies a power law with an exponent close to 2, aligning with findings from other imbibition experiments.

In the regular chip, we replicated the aforementioned experiments under the same conditions, with a focus on analyzing the relationship between ΔP and recovery with the volume of mixture injected at different values of M. We observed the same trends as in the experiments with the random chip, but the uniformity of the pore structure in the regular chip resulted in higher recovery rates. This is evident from the volume of clusters in the chip at steady state, which also showed a more uniform distribution and smaller sizes as M increased.

We employed a new method for calculating the Ca based on a 2D microfluidic chip model, and established correlation graphs between S_{or} and Ca_{new} for all imbibition conditions. These correlations are consistent with the typical CDC curve, corresponding to enhanced mobilization of residual oil due

to decreased capillary forces and increased viscous forces. This revealed a critical capillary number value of approximately 1×10^{-4}, consistent with reported literature.

IV.2 Numerical Results

In this section we first apply the mathematical model presented in Chapter III to simulate *in silico* an academic basic experiment where the instability of an oil droplet at the extremity of a glass tube is studied. Then the mathematical model is used to simulate the drainage phase of the water-wet rock type chip previously presented (*cf.* section 3). A qualitative comparison between numerical and experimental results is reported to show that the numerical results consistently reproduce the physics at play. However, the mathematical model has currently some limitations in its applicability that for the moment preclude its exhaustive validation; these limitations and the perspective of improvement of the current version of the mathematical model are discussed in the conclusion section of the manuscript.

IV.2.1 Validation of the mathematical model

Before applying the mathematical model to an EOR oriented experiment, its physical relevance is first tested on an academic experiment of an oil droplet extracted from a capillary tube (Piroird, et al., 2011). This experiment can also be considered as the retraction phase of an oil drop out of a capillary, starting from a slug to a "sphere-tongue" shape.

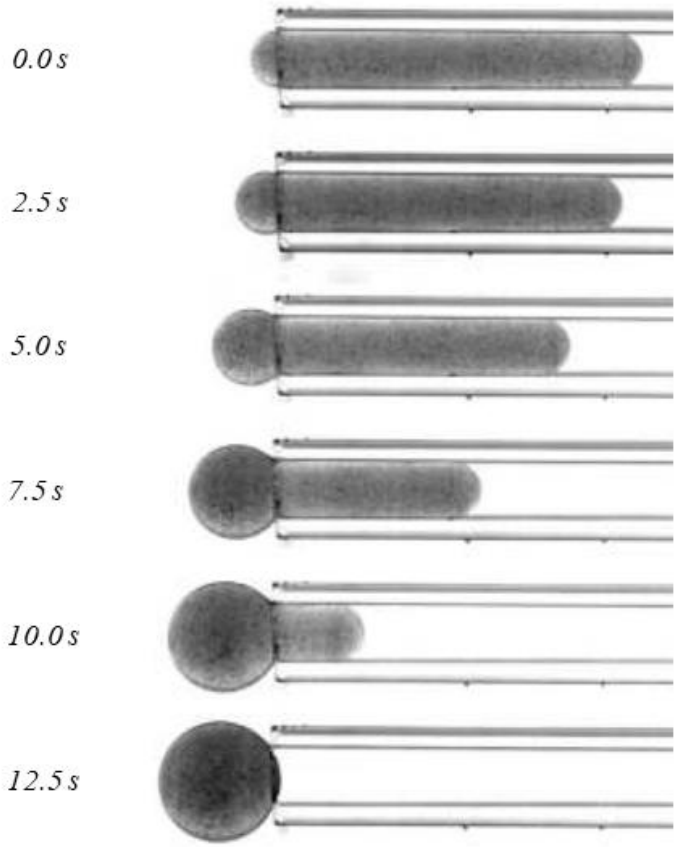

Figure IV-65 *Capillary extraction of a non-wetting oil droplet (of viscosity η_o = 1 Pa.s and density 960 kg/m^3) initially placed in a glass tube of radius R_t = 0.88 mm and length L_t = 40 mm, fully immersed in a mixture of water and ethanol of the same density: when the drop is placed at the end of the tube, a slight perturbation results in its complete extraction (image from (Piroird, et al., 2011)).*

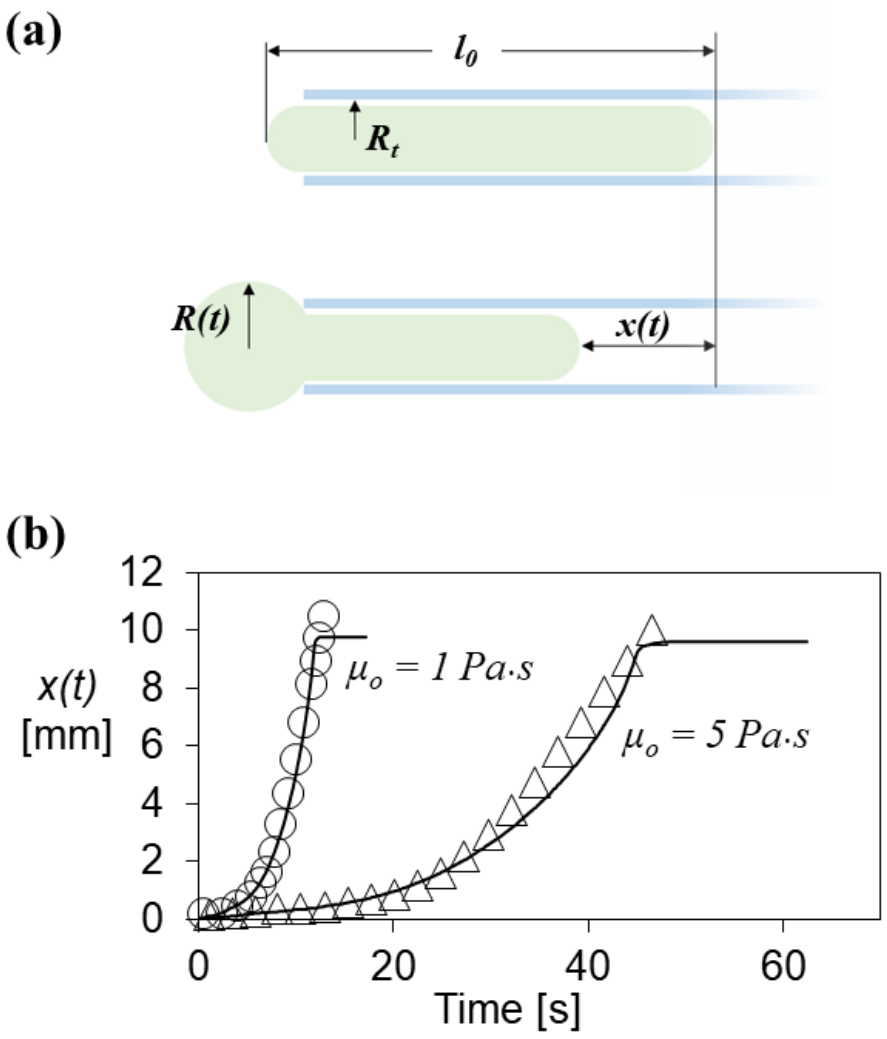

Figure IV-66 *Geometrical description of the oil retraction test (a); Comparison between numerical and experimental results for the two considered oil viscosities (b).*

A non-wetting oil drop is studied with the static contact angle (θ_s) equal to 180°. Once the drop becomes unstable (*i.e.* when the left meniscus exits the tube as shown in **Figure IV-65**, any further displacement of the liquid tongue towards the outlet reduces the surface energy of the system. The drop velocity increases gradually until it reaches a constant value. The movement stops once the drop is completely extracted at the tube exit and reaches the minimum surface shape, *i.e.* a sphere. It has been shown that the retraction dynamics primarily depends on the interfacial tension between the two fluids and on the viscosity of the oil drop. This experiment has been carried out using silicone oil. The oil drop is placed in a capillary tube having length L_t = 40mm and radius R_t = 0.88mm (see **Figure IV-66** (a)). The whole device is immersed in a bath of water-ethanol mixture of viscosity equal to 0.001 Pa.s. Water and ethanol have been properly mixed to exactly match the density of the silicone oil (*i.e.* 960 kg/m^3). The indexes *o* and *a* are used in the following of this section for the oil and the water-ethanol mixture respectively. The interfacial tension σ_{oa} between the two fluids is of 20 mN/m. Two experimental cases are studied with a silicone oil of viscosity

1. Pa.s and a silicone oil of viscosity 5. Pa.s. The experimental results are reported in **Figure IV-66 (b)** (symbols).

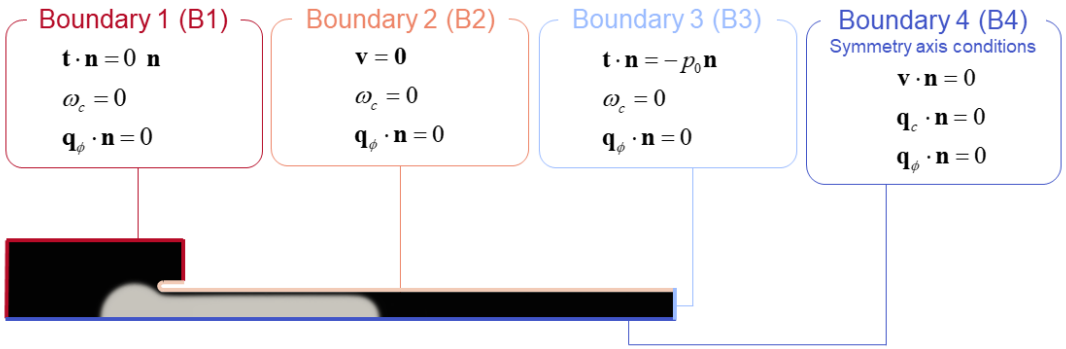

Figure IV-67 *Schematic representation of boundary condition*

Table IV-8 *Parameters of the mathematical model for the oil retraction case*

Parameter	Symbol	Value	Unit	Source
Equilibrium value of oil mass fraction	ω^{eq}	1.	-	Piroird *et al.* 2011
Interfacial tension between the fluid phases	σ_{oa}	0.02	*N/m*	Piroird *et al.* 2011
Dynamic viscosity of the water-ethanol solution	μ_a	0.001	*Pa.s*	Piroird *et al.* 2011
Density of the water-ethanol solution	ρ_a	960.	kg/m^3	Piroird *et al.* 2011
Dynamic viscosity of the silicone oil	μ_o	1.5	*Pa.s*	Piroird *et al.* 2011
Density of the silicone oil	ρ_o	960.	kg/m^3	Piroird *et al.* 2011
Mobility of the *na* interface	M_e	4×10^{-9}	$m^5\,s^{-1}\,J^{-1}$	Identified

IV.2.1.1 Boundary conditions

The boundary conditions for the modeled problem are depicted in **Figure IV-67**. For the Stokes system we have 4 types of boundary conditions for the 4 bounds B1, B2, B3 and B4:

- on B1 a normal stress equal to 0 Pa is set;
- on B2 which corresponds to the surface of the glass tube the velocity vector is set null (no-slip condition);
- on B3 which corresponds to the left extremity of the tube an over-pressure (pressure perturbation) p_0 = 2 Pa is assumed;
- on B4 the axial-symmetry of the problem is accounted by setting the velocity component vr =0.

Note that the value of the pressure on B3 is relatively small and has only the role to trigger oil extraction. Once the extraction initiates the dynamics is then governed by the interfacial tension and the over-pressure on B3 has a negligible impact.

For the Cahn-Hilliard system we have two types of boundary conditions:

- on the boundary B1 U B2 U B3 a natural condition is assumed for the chemical potential (the gradient of the chemical potential is set null) while a non-wetting condition is assumed for the mass fraction of oil;

- on B4 the boundary condition respect the axial-symmetry of the problem (natural conditions are assumed for both the chemical potential and the mass fraction of oil);

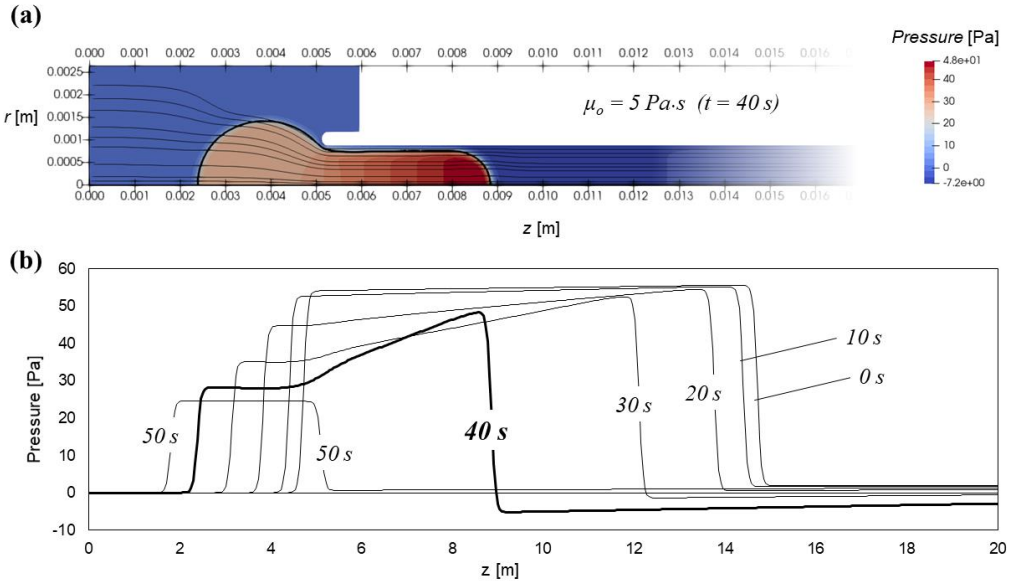

Figure IV-68 *Numerical results for the pressure after 40 seconds for the case with µo = 5Pa.s (velocity stram lines are also depicted) (a); pressure over the space coordinate z at different time stages (b).*

The drop is initially within the pipette. Then, thanks to the over-pressure applied on B3, it starts to move towards the left to get extracted. The physical parameters used in the mathematical model are summarized in the **Table IV-8**. Note that the equilibrium value of the mass fraction of the oil species is set equal to 1 since the drop consists of oil only. It is important to highlight that almost all the parameters needed in the mathematical model are provided in Piroird *et al.* (Piroird, et al., 2011), the only exception is the mobility coefficient M which has been identified by inverse analysis.

IV.2.1.2 Spatial and temporal discretization of modelled problem

The governing equation of the model are discretized in space with finite elements (FE) and in time with an implicit finite difference (FD) scheme. A typical mesh size of around 35 μm is adopted in the area where we expect the presence of the fluid-fluid interface while a coarser mesh is used in the other parts of the domain. As known in the Cahn-Hilliard approach the interface is modeled in a "smoothed" fashion so the interface area has a certain thickness. This thickness is controlled by the parameter ε in equation (3-13) which is assumed here equal to 1/30 the radius of the pipe (*i.e.* $\varepsilon \simeq 30\ \mu$m). Since the Reynold number is always relatively small (Piroird, et al., 2011), the convective part of the time derivative of the velocity vector is neglected so practically speaking an unsteady Stokes problem is resolved.

IV.2.1.3 Results of the numerical analyses

The overall retraction dynamics for the two modeled cases is depicted in the **Figure IV-66** (b) which shows the evolution of the distance *x(t)* with time for the experiments (symbols) and the numerical simulation (solid lines).

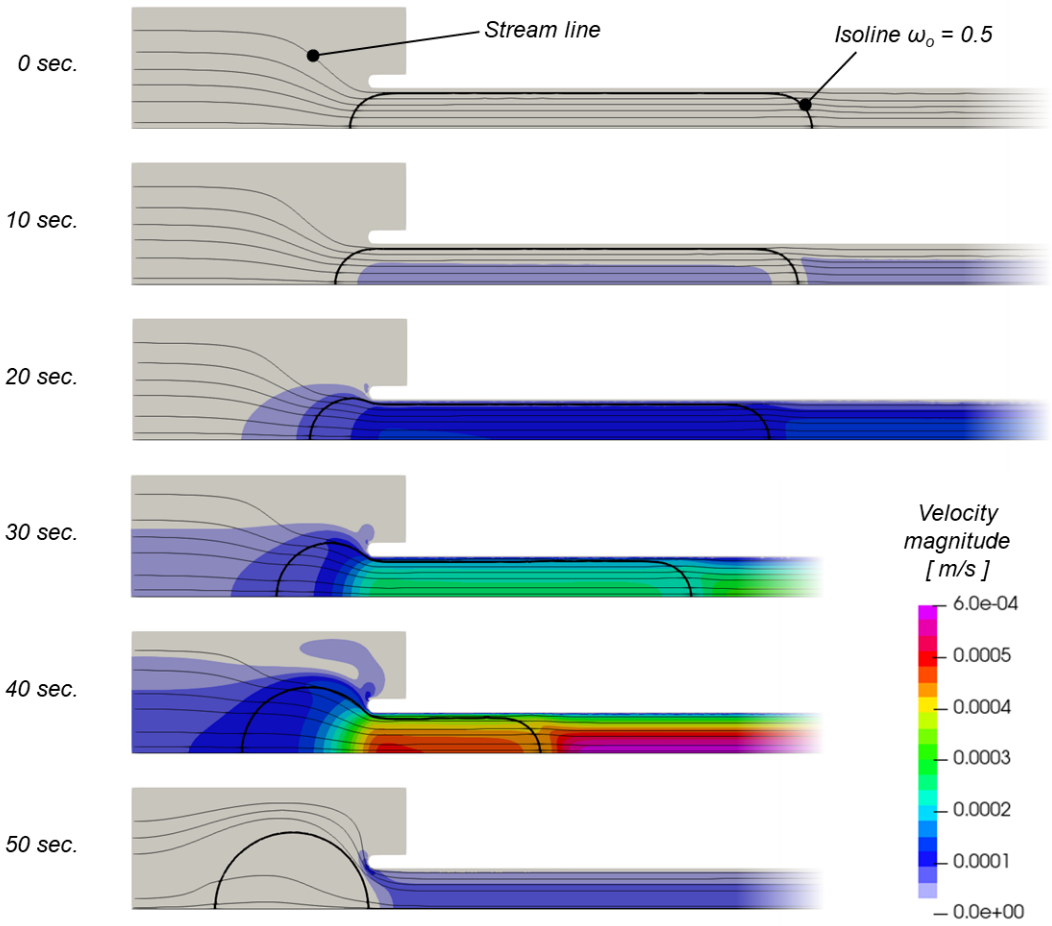

Figure IV-69 *Fluid-fluid interface, stream lines and velocity magnitude at different time stages for the case with* μ_o *= 5Pa.s*

$x = 0$ corresponds to the unstable position of the right extremity of the drop within the tube as depicted in **Figure IV-66**(a). The initial length of the oil slug within the tube is indicated with l_0 which is here 10 mm. In Piroird *et al.* (Piroird, et al., 2011) they experimentally observed that $x(t)$ increases more and more rapidly as time goes on. The retraction takes approximately 10 s for the case of viscosity μ_o = 1 Pa.s and 50 s for the case of viscosity μ_o = 5 Pa.s keeping the other parameters constant. **Figure IV-66**(b) shows a good agreement between experimental and numerical results. However, a certain discrepancy can be observed in the final phase of the case μ_o = 5 Pa.s. Actually, while in the experiment the velocity tends toward a constant value at the end, in the numerical results the drop continues to accelerate until it is totally out of the tube. **Figure IV-68**(a) shows the numerical results for the pressure and stream lines at 40 s for the case of viscosity μ_o = 5 Pa.s. The pressure in the left part of the slug is smaller than in the right part leading to a net force which together with interfacial forces drives the retraction. The pressure profile over the axis z at different times is depicted in the graph in **Figure IV-68**(a). This graph together with **Figure IV-69** (representing velocity at the same time stages) allow us to appreciate the full dynamics of the extraction process for the case of viscosity μ_o = 5 Pa.s. To conclude the description of this validation case in **Figure IV-70** we report the velocity decay over the axis z at 42 s for the case of viscosity μ_o = 5

Pa.s, and its comparison with the experimental results (symbols) reported in Piroird *et al.* (Piroird, et al., 2011).

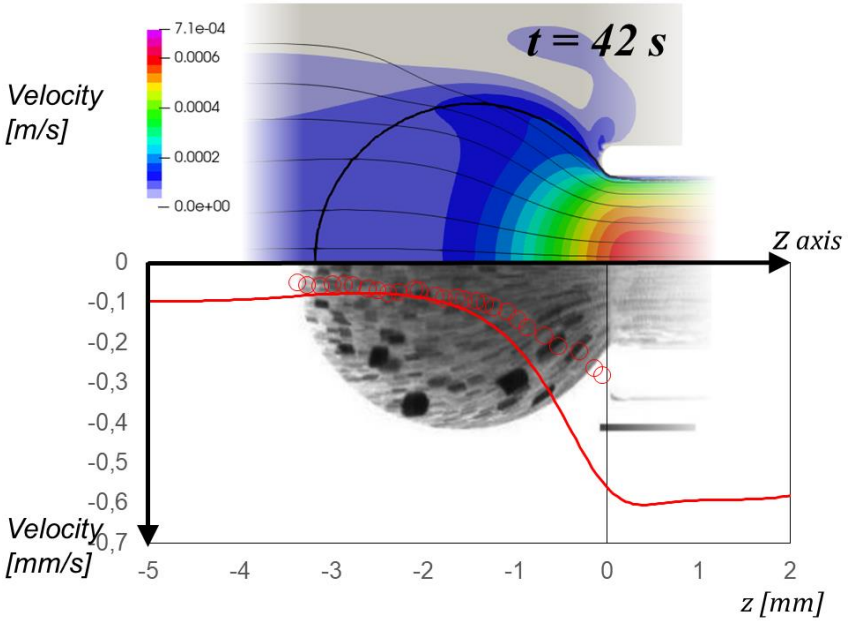

Figure IV-70 *Velocity decay in the proximity of the left extremity of the tube at 42 s for the case with* μ_o *= 5Pa.s*

In the proximity of the tube extremity the velocity is overestimated by the numerical model: experimentally they obtain ≃ 0.3 mm/s while the numerical model gives ≃ 0.6 mm/s. This difference is quite expected accordingly with the discrepancy previously evidenced in the final phase of the case μ_o = 5 Pa.s in **Figure IV-66**(b).

IV.2.2 Modelling of water drainage in a water-wet microfluidic chip

Once the physical relevance of the mathematical model has been highlighted, in this paragraph the model is applied to simulate the water drainage in a water-wet microfluidic rock-type chip (*cf.* experimental results in **paragraph 4.1.2**). The original ambition was to model *in silico* the full experimental procedure drainage → water imbibition → tertiary recovery described in **paragraph 4.1**. However, during the last period of the PhD thesis we faced some technical difficulties – more precisely detailed in the conclusion section – which limited the extensiveness of the numerical part circumscribed in the drainage stage.

IV.2.2.1 Choice of a Representative Volume of the microfluidic chip

Both the microfluidic chips (the rock-type and the uniform one) have an overall size of 10 mm × 20 mm (see **Section III** "Materials and Methods"). The finite element (FE) discretization of the whole chip is computationally too expensive; hence, we decided to model a portion of the chip which is enough large to be representative of the medium and quite small to be not excessively expensive from the computational viewpoint. The choice of the suitable size of this representative volume is not straightforward so we decided to consider two domains: the first one of size 2 mm × 2 mm named here

the “2×2 domain”; the second one of size 5 mm × 5 mm named the “5×5 domain”. This second domain has a surface which is 1/8 of the whole chip.

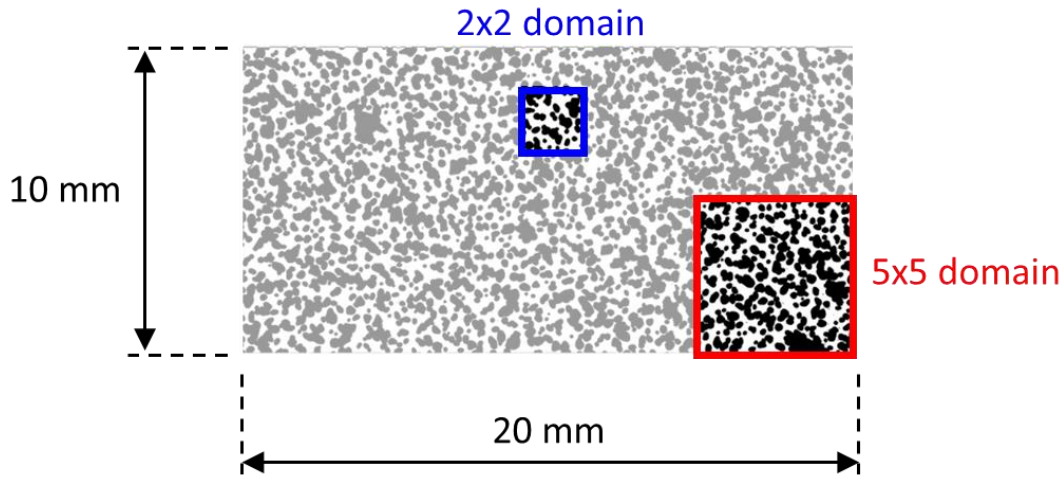

Figure IV-71 *Position for the computational domains used in the numerical simulations*

The *2×2 domain* has been used to perform the preliminary *in silico* analyses to parametrize the numerical model in term of spatial and time discretization. The *2×2 domain* has also been used to analyse how, during the drainage stage, the numerical solution depends on the injection velocity and on the mobility coefficient M_e.

In our water-wet chip, during the drainage stage (*i.e*. the injection of oil which displace water) being the oil 80 times more viscous than water and given the range of the capillary number (*cf.* **paragraph 4.1**) we experimentally obtain an overall piston-like displacement (see **Figure IV-72**). However, if we observe the front at a resolution scale which is an order of magnitude smaller than the centimetre scale of the chip we can observe local fingers having a characteristic size between 0.5 mm and 2 mm (see insert in **Figure IV-72**). This means that our *2×2 domain* having the size of 2 mm is not enough large to be representative of the overall microfluidic chip behaviour and justify the use of the *5×5 domain* which has a more suitable size to consistently compare experimental and numerical results.

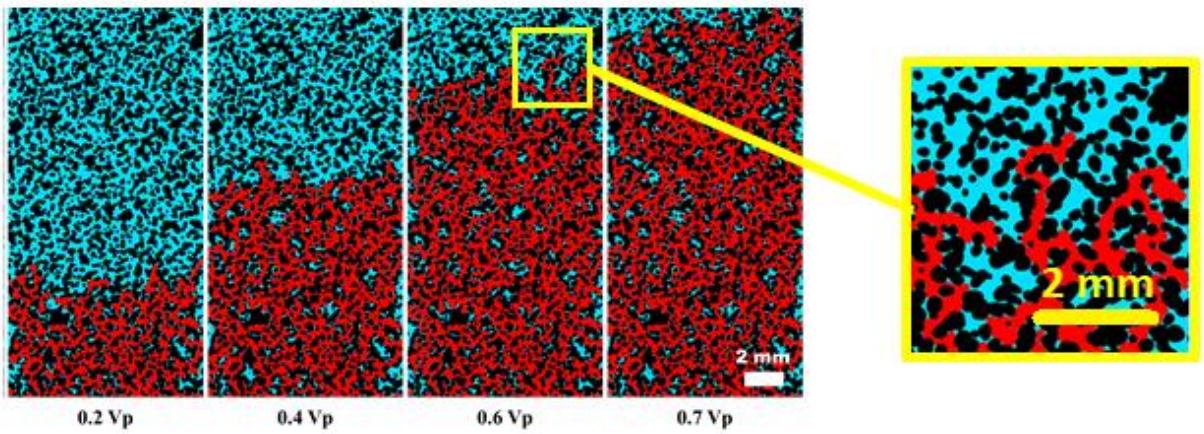

Figure IV-72 Experimental results of the drainage phase (cf paragraph 4.1)

IV.2.2.2 Geometry and boundary and initial conditions

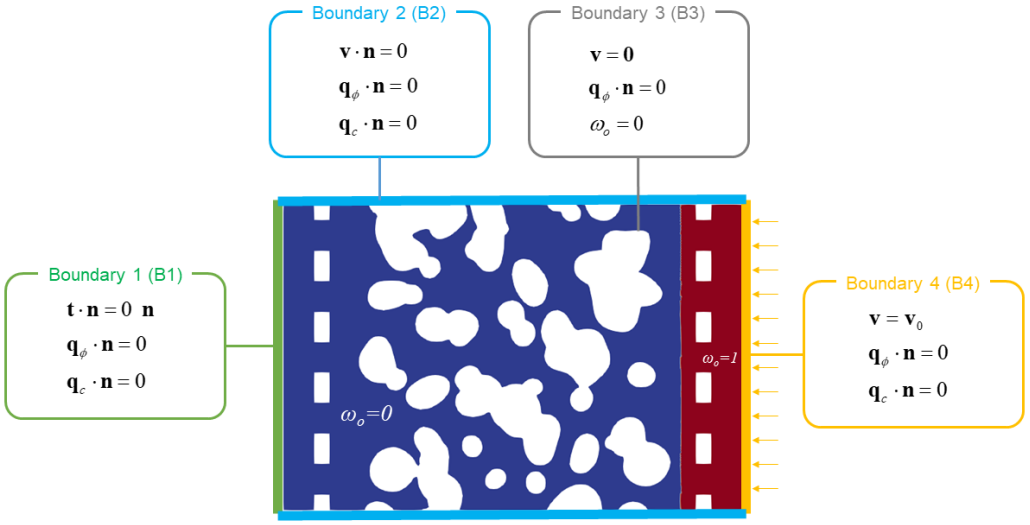

Figure IV-73 Schematization of the boundary conditions for the 2×2 domain

Table IV-9 Parameters of the mathematical model for the oil retraction case

Parameter	Symbol	Value	Unit	Source
Equilibrium value of oil mass fraction	ω^{eq}	1	-	Measured in this work
Interfacial tension between the fluid phases	σ_{oa}	0.056	*N/m*	Measured in this work
Dynamic viscosity of the water-ethanol solution	μa	0.001	*Pa.s*	Measured in this work
Density of the water-ethanol solution	ρa	1000	kg/m^3	Measured in this work
Dynamic viscosity of the silicone oil	μo	0.08	*Pa.s*	Measured in this work
Density of the silicone oil	ρo	1000	kg/m^3	Approximated
Mobility of the *na* interface (reference value)	M_e	5 x 10^{-10}	$m^5\,s^{-1}\,J^{-1}$	Identified

The boundary conditions are depicted in **Figure 4-73** for the *2×2 domain*. The boundary conditions for the *5×5 domain* are exactly the same (the sole geometry of the domain changes).

For the Stokes system we have 4 types of boundary conditions for the 4 bound types B1, B2, B3 and B4:

- on B1 a normal stress equal to 0 Pa is set;
- on B2 we assume that the fluid velocity has no vertical component (vy =0);
- on B3 which corresponds to the surface of inclusions we assume the no-slip condition;
- on B4 we set the injection velocity $\mathbf{v} = \mathbf{v}_0$.

For the Cahn-Hilliard system we have two types of boundary conditions:

- on the boundary B1 U B2 U B4 a natural condition (no normal flow) is assumed for both the chemical potential and the mass fraction of oil;
- on B3 (the surface of inclusions) a non-wetting condition is assumed for the mass fraction of oil while a natural condition (no normal flow) is assumed the chemical potential.

The oil initially saturates the red part in the right extremity of the domain (see **Figure IV-73**).

IV.2.2.3 Spatial and temporal discretization of modelled problem

The governing equation of the model are discretized in space with finite elements (FE) and in time with an implicit finite difference (FD) scheme. A typical mesh size of around 10 μm is adopted in the whole area of the domain. The time discretization is also constant, $\Delta t = 0.002$ s. The parameter ε which controls the interface thickness is 6 μm. As in the previous case the Reynold number is relatively small so the convective part of the time derivative of the velocity vector is neglected. All the material parameters used in the numerical simulations are reported in **Table IV-9** Parameters of the mathematical model for the oil retraction case.

IV.2.2.4 2×2 domain: results and sensitivity analyses

We study here the effect of the magnitude of the injection velocity, $\mathbf{v_0}$, and of the mobility coefficient M_e, on the drainage dynamics. 10 *in silico* experiments are performed with 2 values of injection velocity ($4{\cdot}10^{-4}$ m/s and $1{\cdot}10^{-4}$ m/s) and 5 values for the mobility coefficient (10^{-10} to $5{\cdot}10^{-10}$ $m^5\ s^{-1}\ J^{-1}$). The **Table IV-10** Parameters for the simulated casessummarizes the parameters used in the performed *in silico* experiments.

Table IV-10 *Parameters for the simulated cases*

In silico experiment n.	v_0 [m/s]	M_e [$m^5\ s^{-1}\ J^{-1}$]
1	$4{\cdot}10^{-4}$	$5{\cdot}10^{-10}$
2	$4{\cdot}10^{-4}$	$4{\cdot}10^{-10}$
3	$4{\cdot}10^{-4}$	$3{\cdot}10^{-10}$
4	$4{\cdot}10^{-4}$	$2{\cdot}10^{-10}$
5	$4{\cdot}10^{-4}$	10^{-10}
6	10^{-4}	$5{\cdot}10^{-10}$
7	10^{-4}	$4{\cdot}10^{-10}$
8	10^{-4}	$3{\cdot}10^{-10}$
9	10^{-4}	$2{\cdot}10^{-10}$
10	10^{-4}	10^{-10}

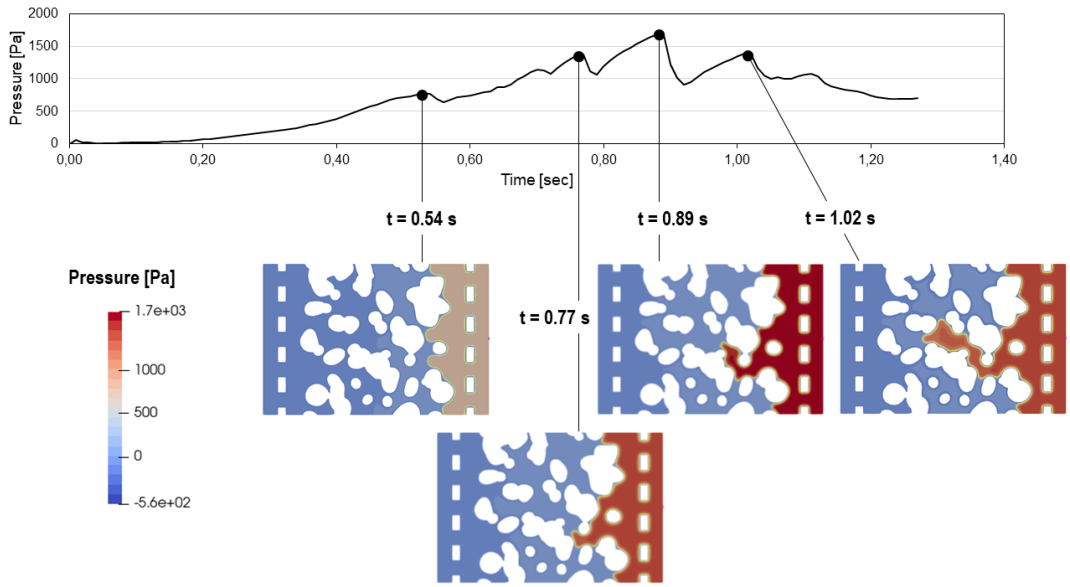

Figure IV-74 *Dynamics of drainage for case 1: advancement of the front and evolution of pressure with time.*

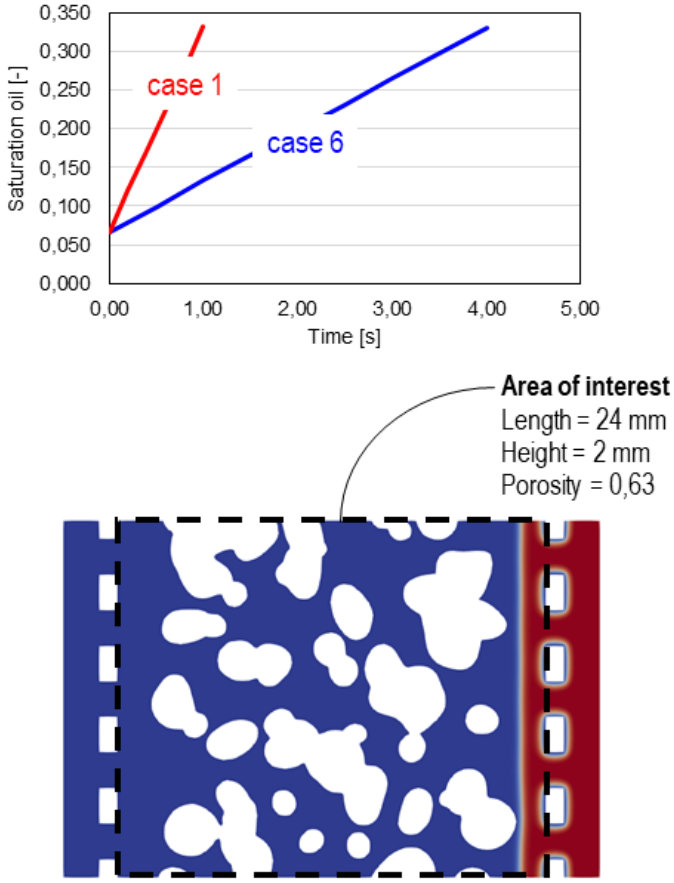

Figure IV-75 *Evolution with time of the saturation degree of the area of interest for case 1 ($v_0 = 4.10^{-4}$ m/s and $M_e = 5{\cdot}10^{-10}$ m^5 s^{-1} J^{-1}) and case 6 ($v_0 = 10^{-4}$ m/s and $M_e = 5.10^{-10}$ m^5 s^{-1} J^{-1}). The image on the bottom refers to the initial condition when So ≈ 0.065.*

We first analyse the behaviour of the case 1 then compare results with other cases to highlight effects of injection velocity and mobility. The evolution of the pressure at the right extremity of the domain for a given injection velocity of $4{\cdot}10^{-4}$ m/s is depicted in the graph in **Figure IV-74Figure IV-75**. The four inserts show the advancement of the front (yellow line) and the pressure distribution at four different time stages. The time stages have been selected to show that the fluctuations in the pressure evolution and the peaks are related to the flow of oil through small channels which induces an increase of the capillary pressure. These fluctuations, which have a consistent physical meaning, emerge also experimentally and have been also evidenced numerically in the work of Yiotis *et al* (2021).

Impact of the injection velocity (case 1 vs case 6). The graph in **Figure IV-75** shows the evolution of the overall saturation of the domain with respect to time for the cases 1 and 6. Being the injection velocity constant the saturation increases linearly as expected. Given the values of the injection velocity we have also verified that the evolution of the saturation in the two cases is the expected one which can be effortlessly calculated analytically once extracted by image analysis the porosity of the area of interest (see **Figure IV-75**). The comparison with the theoretical evolution of the saturation degree is important since allows us to verify that our model correctly preserve mass conservation.

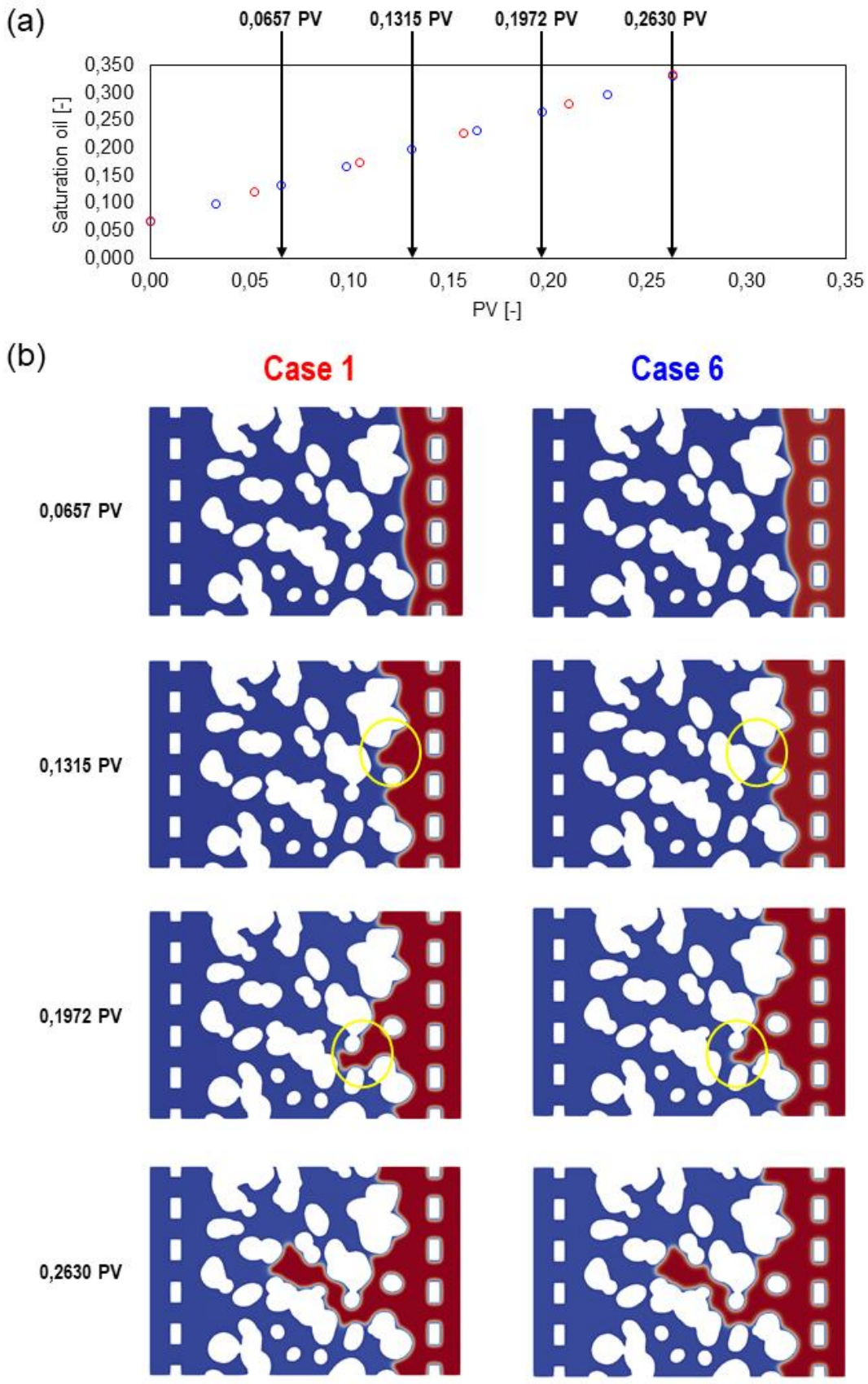

Figure IV-76 *Evolution of the saturation degree of the area of interest with respect to the injected pore volume (PV) for case 1 (v_0 = 4.10^{-4} m/s and M_e = 5·10^{-10} m^5 s^{-1} J^{-1}) and case 6 (v_0 = 10^{-4} m/s and M_e = 5.10^{-10} m^5 s^{-1} J^{-1}) (a); Phases distribution at different stages (b).*

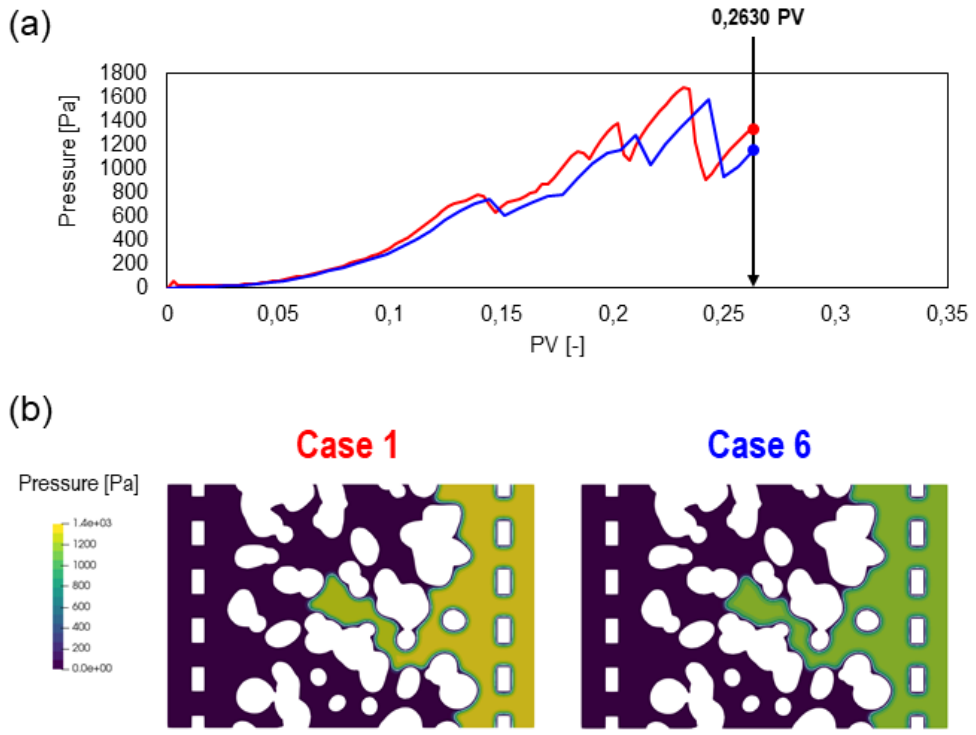

Figure IV-77 *Pressure evolution over the injected pore volume for case 1 (v_0 = 4.10^{-4} m/s and M_e = 5·10^{-10} m^5 s^{-1} J^{-1}) and case 6 (v_0 = 10^{-4} m/s and M_e = 5.10^{-10} m^5 s^{-1} J^{-1}) (a). Pressure distribution in the two cases at 0.2630 PV (b).*

As the injection velocity is different, to suitably compare the results of cases 1 and 6 we express them in **Figure IV-76(a)** as function of the injected pore volume (PV). Obviously the trend is another time linear and this time the results of the two cases are superposed. Then we consider 4 stages (in term of injected pore volume) and we analyse the distribution of phases inside the porous medium in **Figure IV-76(b)**. We do not evidence important differences between the two cases in the configuration of phases; we can only observe that in case 1 (*i.e.* when the velocity is higher) the finger infiltrates the pores slightly faster than in case 6 at the same injected PV.

If we finally analyse the evolution of pressure at the right bound over the injected pore volume in **Figure IV-77(a)** we note that in case 1 (*i.e.* when the velocity is higher) the peaks arrive at a lower injected PV than in case 6. The overall evolution of the pressure (dynamics and magnitude) and the peak values are quite similar (despite in the case 1 the velocity is 4 times higher!) indicating that the pressure rise is essentially governed by capillary forces related to flow within pores.

Impact of the mobility coefficient (case 6 vs case 10).

If we now analyse the effect of the mobility coefficient by comparing the phase distribution at two different stages for case 6 (v_0 = 10^{-4} m/s and M_e = 5·10^{-10} m^5 s^{-1} J^{-1}) and case 10 (v_0 = 10^{-4} m/s and M_e =

10^{-10} m^5 s^{-1} J^{-1}) we observe that in case 10 using a lower mobility coefficient enhances the capacity of the oil to infiltrate the pores at a given injected PV with respect of case 6.

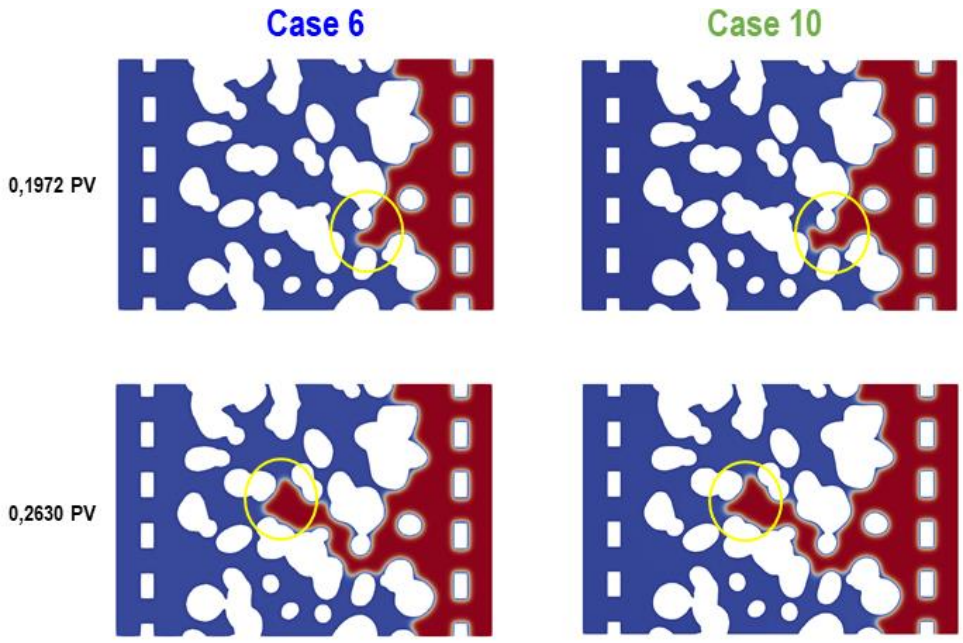

Figure IV-78 *Phases distribution at two different stages for case 6 (v_0 = 10^{-4} m/s and M_e = $5{\cdot}10^{-10}$ m^5 s^{-1} J^{-1}) and case 10 (v_0 = 10^{-4} m/s and M_e = 10^{-10} m^5 s^{-1} J^{-1})*

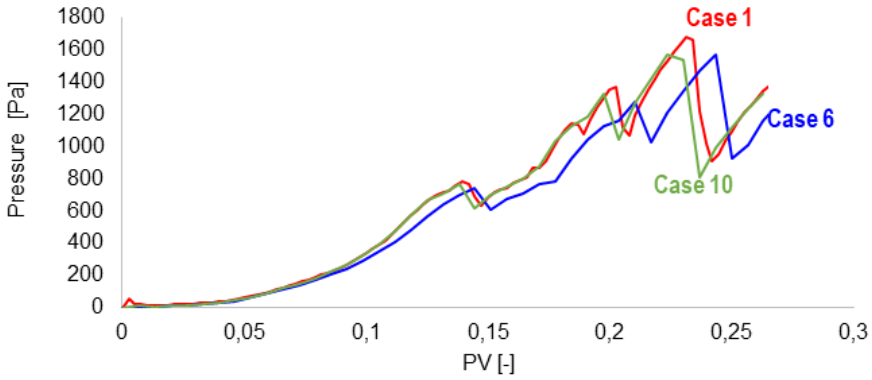

Figure IV-79 *Pressure evolution over the injected pore volume for case 1 (v_0 = 4.10^{-4} m/s and M_e = $5{\cdot}10^{-10}$ m^5 s^{-1} J^{-1}) case 6 (v_0 = 10^{-4} m/s and M_e = 5.10^{-10} m^5 s^{-1} J^{-1}) and case 10 (v_0 = 10^{-4} m/s and M_e = 10^{-10} m^5 s^{-1} J^{-1})*

The mobility coefficient, M_e, governs the diffusive part of the model with the gradient of the chemical potential aging as the driving force pushing the fluid-fluid interface toward the configuration minimizing the free energy of the system. This means that when M_e is lower this diffusive effect decreases so the effect of convective forces (*i.e.* of the velocity) is higher. Due to this reason we can interesting observe that, for the same stage in term of PV, the configuration of phases of case 1 and case 10 is similar. In other words, for the same injected pore volume if we decrease proportionally (or almost proportionally)

both the velocity and the mobility coefficient the results in term of phases configuration does not change. To conclude this analysis, we report in Error! Reference source not found. the pressure evolution over t he injected pore volume for case 1, case 6 and case 10 which confirm the evidenced similarities between cases 1 and 10.

IV.2.2.5 5x5 domain: qualitative comparisons with the experimental results

Based on the results from the 2×2 mm domain study, we fixed the M_e at a reference value of 5 $\times 10^{-10}$ ($m^5\ s^{-1}\ J^{-1}$), and using parameters from lab experiments, we analyse results of *in silico* model within a larger 5×5 domain, investigating the drainage dynamics. **Table IV-11** shows the parameters used in the performed *in silico* experiments with v_0 derived from the experimental injection flow.

Table IV-11 *Parameters for the simulated cases for 5×5 domain*

In silico experiment n.	v_0 [m/s]	M_e [$m^5\ s^{-1}\ J^{-1}$]
11	4.2×10^{-5}	$5\cdot10^{-10}$
12	8.3×10^{-5}	$5\cdot10^{-10}$

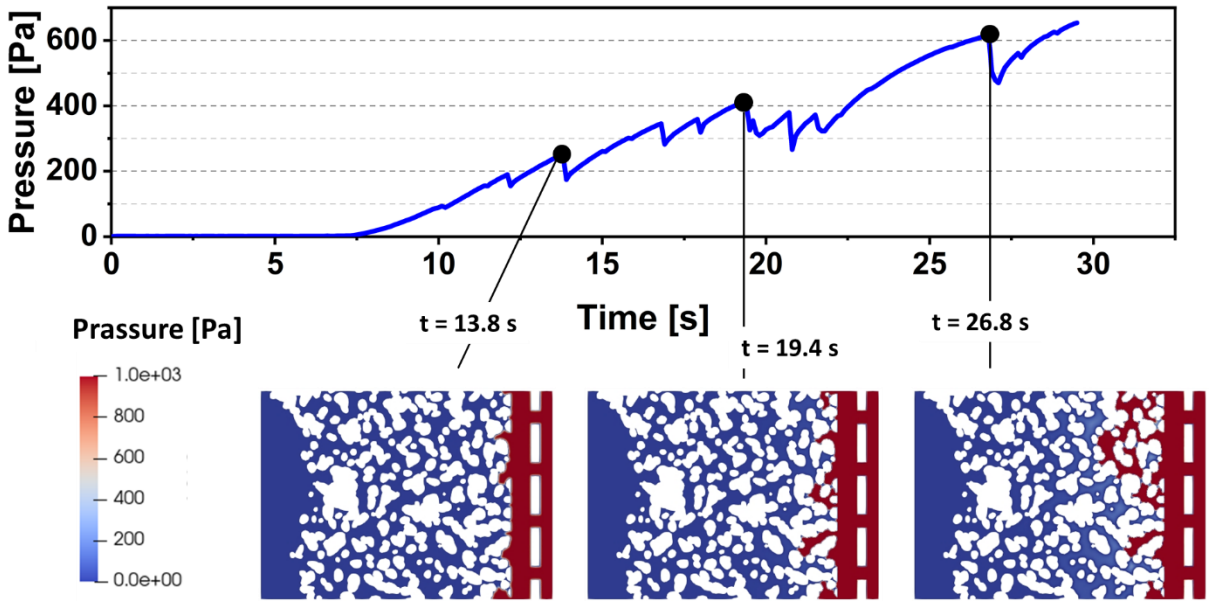

Figure IV-80 *Dynamics of drainage for case 11: advancement of the front and evolution of pressure with time*

We first analyze the behavior in case 11 and then compare the results with the case to highlight the impact of injection velocity. **Figure IV-80** shows the evolution of pressure at the right extremity of the domain when the injection velocity is set at 4.2×10^{-5} m/s. Three inserts display the advancement of the front and the pressure distributions at three different time stages. Similar to the results obtained from the experiments in the 2×2 mm domain, the pressure evolution in the 5×5 mm domain shows the same pattern and trend. Specifically, the peaks in pressure are related to the increase in capillary pressure as oil flows through small pores, followed by a brief drop after breakthrough.

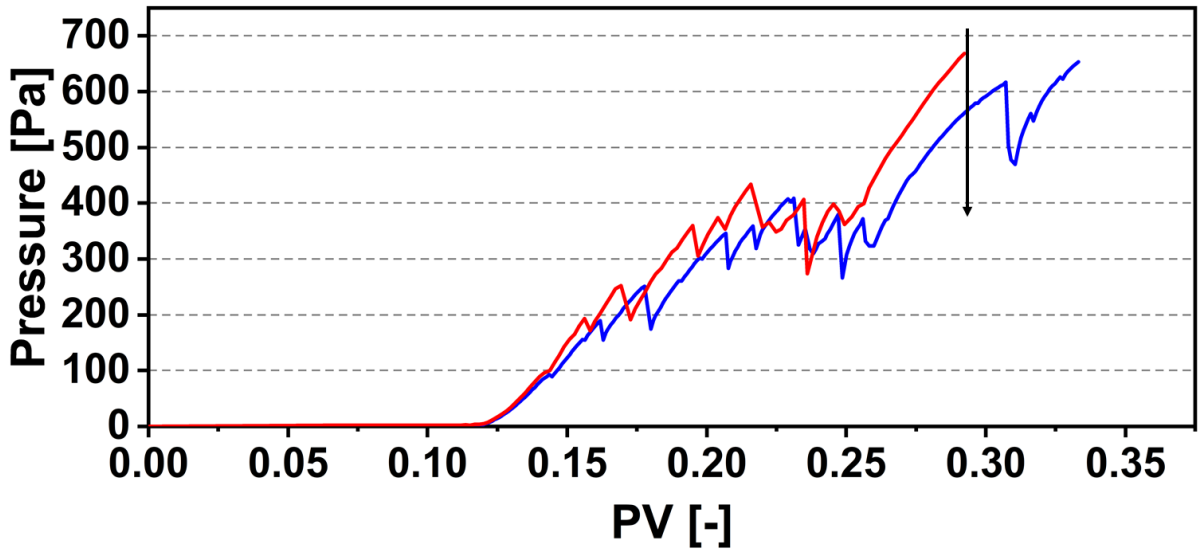

Figure IV-81 *Pressure evolution over the injected pore volume for case 11 (v_0 = 4.2×10^{-5} m/s and M_e = 5·10^{-10} m^5 s^{-1} J^{-1}) and case 12 (v_0 = 8.3×10^{-5} m/s and M_e = 5.10^{-10} m^5 s^{-1} J^{-1})*

Similar to the results for the 2×2 mm domain, the overall changes (dynamics and magnitude) and peaks in pressure under the two different velocities are also very similar, further confirming that the rise in pressure is controlled by capillary forces associated with flow within the pores. The increase in velocity simply accelerates this process. (See **Figure IV-81**)

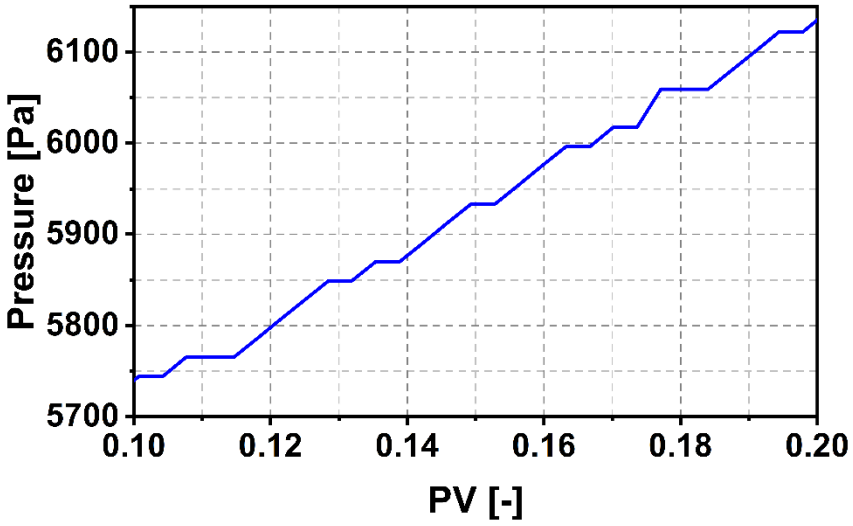

Figure IV-82 *The recorded ΔP versus injected volume when the oil invaded the porous medium saturated with water in lab experiments.*

Indeed, in lab experiments, we also observed fluctuations in pressure. Although our reported pressure versus invading pore volume did not show distinct peaks, it exhibited a stepwise, incremental rising trend, as shown in **Figure IV-82**. Comparing the phenomena observed in lab experiments with those from *in silico* experiments, the instants of pressure rise correspond to the stages when oil flows through

pore throats, followed by a brief plateau period after breakthrough, which corresponds to the rapid saturation of next connected pore bodies by oil.

The differences between the lab experiment results and *in silico* experiment outcomes can be due to difference in the scale of the system. In the lab experiments, we recorded the pressure evolution across the entire chip, which means that due to the influence of pore structure, the pressure drop following breakthrough is balanced out, appearing as a plateau phase. Additionally, the sensitivity of the measuring instruments might also be a significant factor. *In silico* experiments can more precisely record changes in pressure.

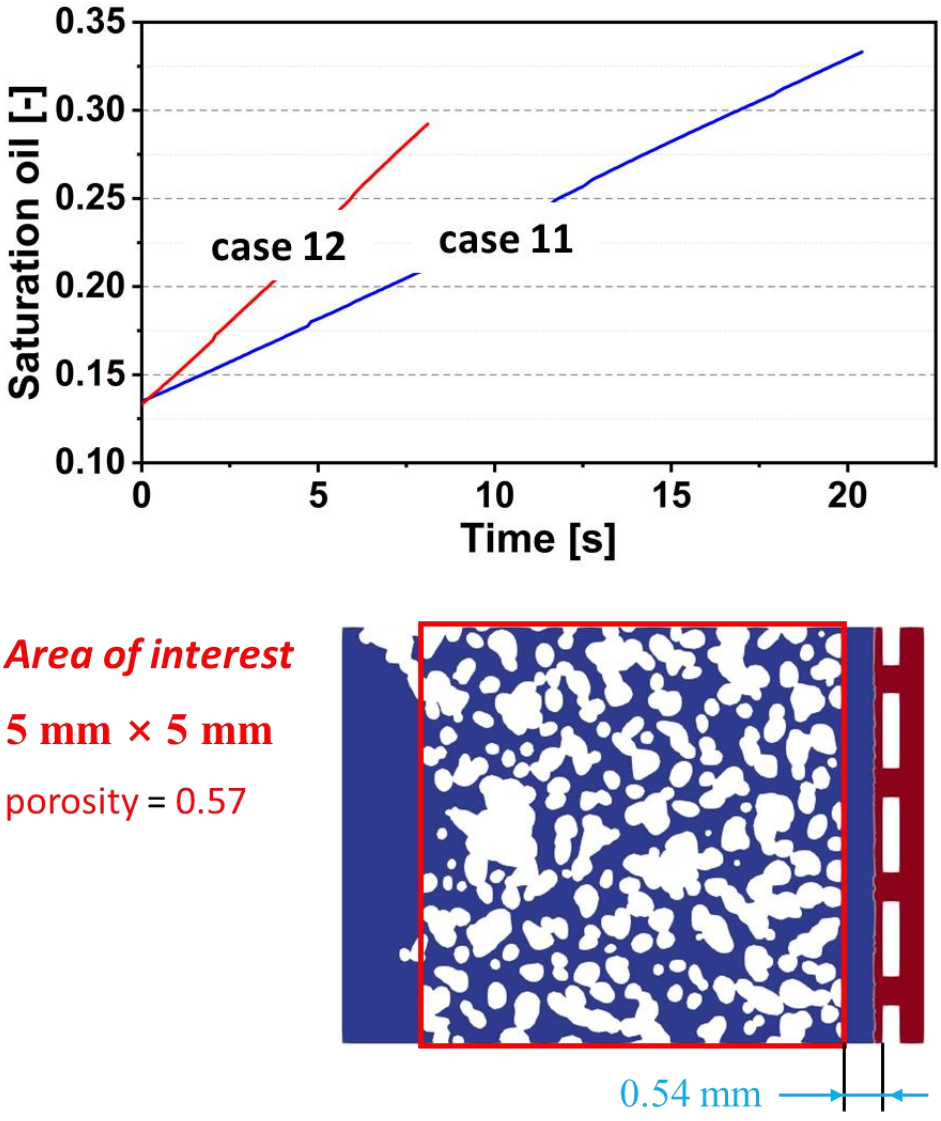

Figure IV-83 *Evolution with time of the saturation degree of the area of interest for case 11 (v_0 = 4.2×10^{-5} m/s and M_e = 5×10^{-10} m^5 s^{-1} J^{-1}) and case 12 (v_0 = 8.3×10^{-5} m/s and M_e = 5×10^{-10} m^5 s^{-1} J^{-1}). The image on the bottom refers to the initial condition of the in silico case.*

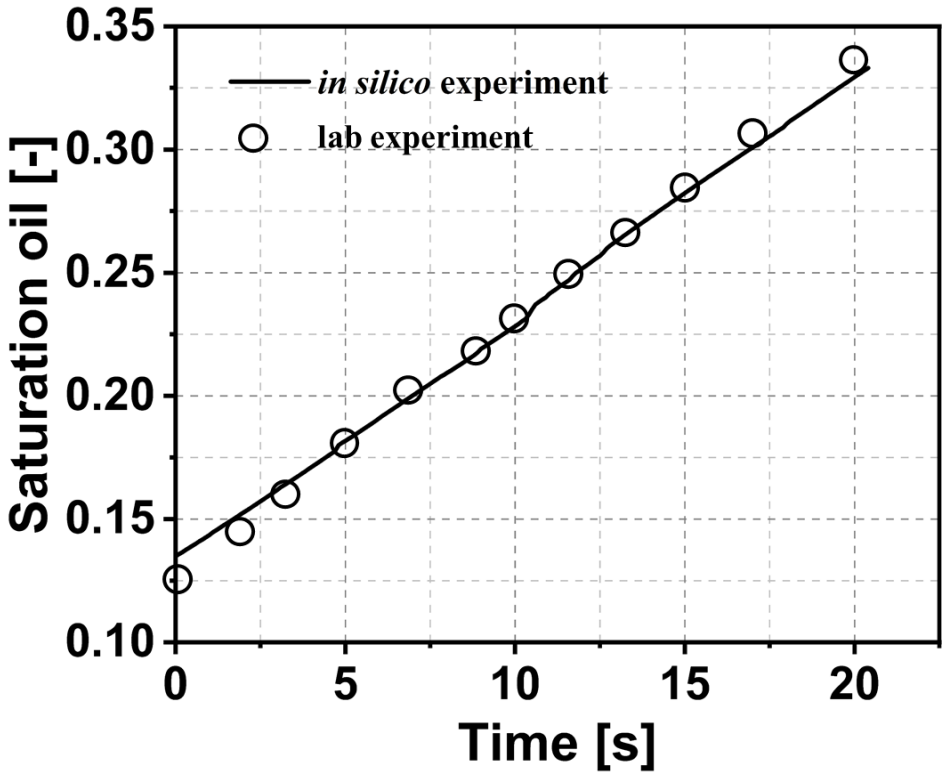

Figure IV-84 The saturation of invaded phase as function of with time in lab experiment and in silico experiment

Figure IV-83 displays the changes in overall saturation over time for cases 11 and 12. Here, we only consider the saturation in the area of interest, excluding the periods during which the fracture width is 0.54 mm. The saturation does increases linearly as expected. We have also compared the lab experiment results under the same conditions with the *in silico* experimental outcomes under case 11, as shown in **Figure IV-84**. The trends the in-saturation changes of them are consistent. So the comparison provides are additional validation, confirming the reliability and practical relevance of our model.

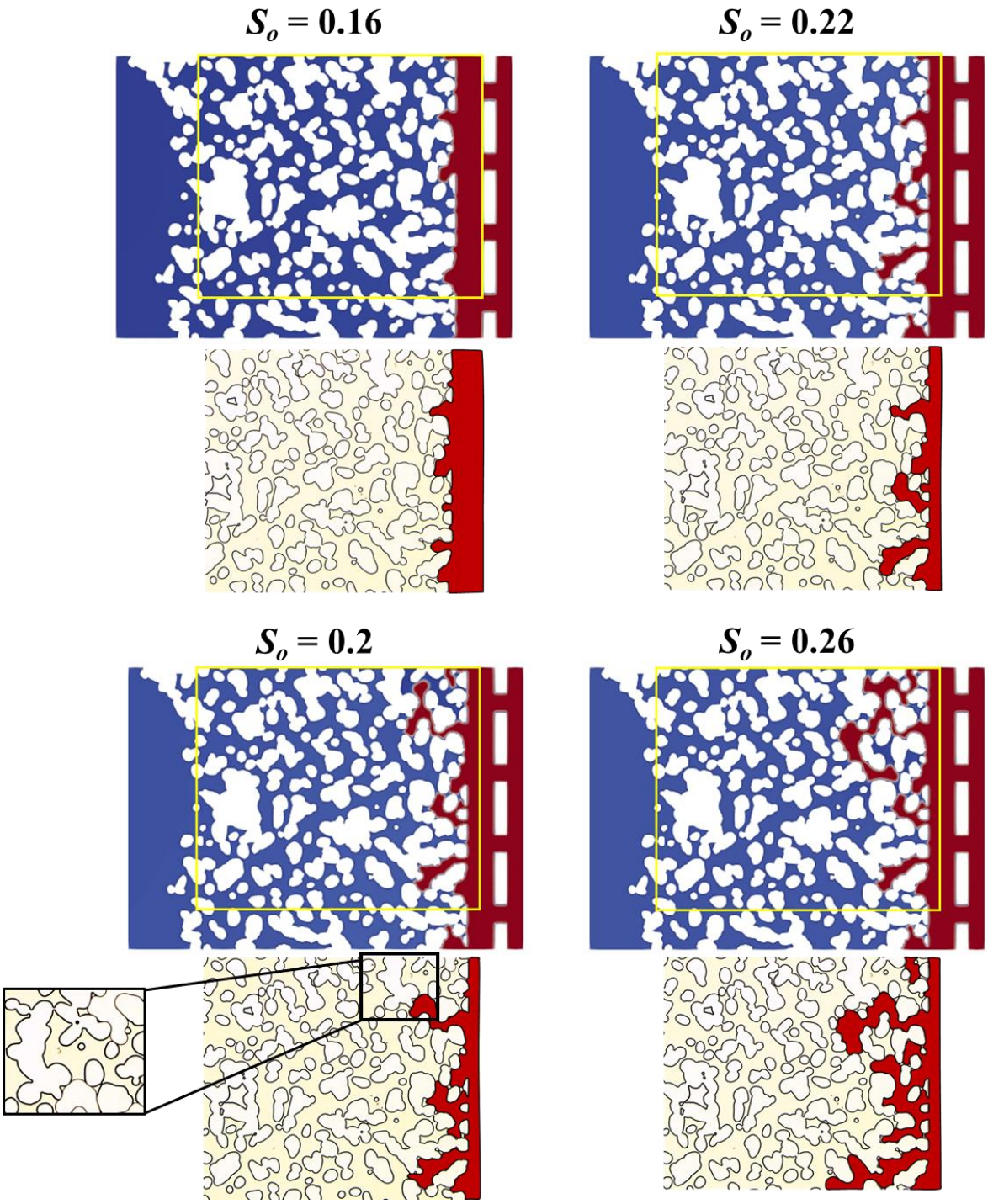

Figure IV-85 *Comparison of the experimentally recorded phase distribution patterns with those of the numerical simulation for case 11. The oil is shown in red.*

To conclude, we also compared the experimental and numerical results for the phase distribution patterns of the fluid-fluid interface at the oil advancement under the same invading phase saturation, with the area within the yellow frame representing the corresponding region recorded in the lab experiments. As shown in **Figure IV-85**, the numerical model initially captured the dynamics of the invading front across the entire range quite well. However, when S_o reached 0.2, we observe some

difference in the fingering patterns (see the black frame area), which can be due again to differences in the geometry of the numerical model which is not representative of the tall chip. Additionally, some subtle differences observed in the *in silico* experiment might be caused by local wettability changes due to impurities on the surface of the micro-model structure.

Interestingly, at S_o = 0.26, lateral or backward movements of advancing fingers were observed in the simulation results, as expected considering the experimental results. As we introduced in the lab experiment section, under these conditions, the flow regime is close to stable displacement, which nevertheless includes capillary fingering at microscopic pore scale. Due to the influence of geometric structures, capillary fingers advancing along the flow direction may be blocked by dead-end pores or very small pore throats, prompting them to seek breakthroughs in other directions, with the direction influenced by the pore structure. We observed similar phenomena in the lab experiments, as shown in **Figure IV-86**: where when the fluid front encountered geometric constraints in the red-framed area and flow was impeded, lateral and even backward breakthroughs occurred in adjacent areas (indicated by red arrows).

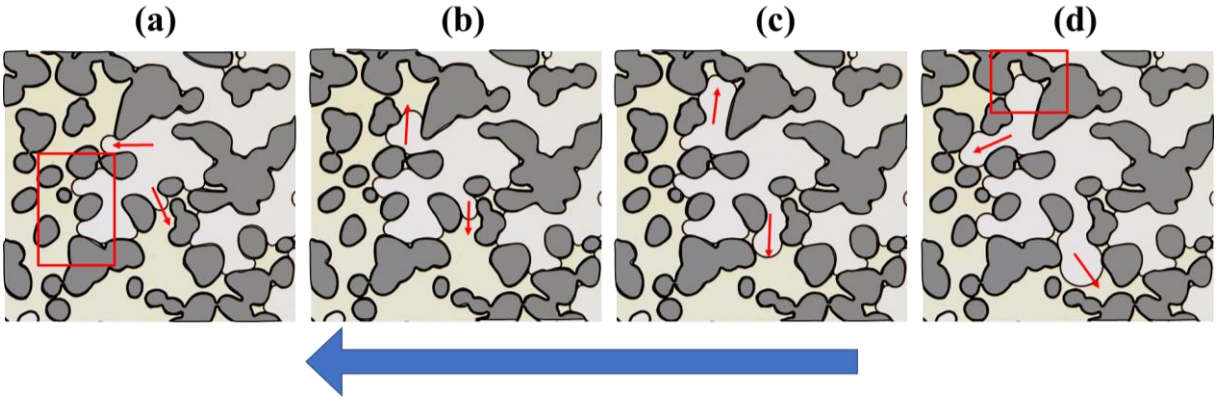

Figure IV-86 *Lateral or backward flow of the fluid -fluid interface at different time stages(a-d). The blue arrow at the bottom indicates the flow direction; the red arrows in the figure represent the oil advancement direction; and the red frames highlight areas where oil is blocked due to small throats or dead-end pores.*

V Conclusions and Perspectives

The aim of this work was to investigate the influence of the viscosity of the injected fluid on EOR at the pore scale after the waterflooding step. This was achieved by developing a four stages experimental protocol using on-chip porous medium models. The experimental study has been supplemented by numerical analyses aiming at facilitating the interpretation of the experiments and at suitably studying the effect of key parameters on the dynamics of fluid-fluid interface advancement.

Concerning the experimental part, investigations were performed using a microfluidic setup that allowed live monitoring of the spatio-temporal changes of saturation and structure of the immiscible fluids in presence. The chips used were water-wet, with either random or regular structures; even we mainly focused on the former. From a quantitative perspective, the experiments were characterized in terms of the capillary number *Ca* and ratio *M* of the viscosity of invading fluid to that of defending fluid. So, depending on the conditions of interest, this gave rise to a capillary fingering displacement regime, a viscous fingering displacement regime or a piston-like displacement regime, and intermediate situations in between as predicted by the conventional logCa/logM diagram.

The main conclusions that can be drawn are as follows:

- **During the drainage period:** The S_{wi} decreased as the applied flow rate increased, with remaining water localized in small pores. The mechanisms at the pore scale were explained and were consistent with the *Ca* and viscosity ratio values.
- **In the waterflooding period:** Oil recovery was observed to stay at modest level and was to some extend sensitive to the water flow rate. The remaining oil saturation taken here as S_{or} was decreased with increasing flow rate. We showed in live how the rupture of oil clusters and oil trapping occur at the pore scale, leaving oil in the form of droplets, blobs, and ganglia that fill pores of particular sizes and structures.
- **After the waterflooding period:** Aqueous Newtonian glycerol/water mixtures were then injected. The viscosity of such mixtures was adjusted beforehand by changing their glycerol content. Consequently, the viscosity ratio *M* of the mixture relative to water varied from 1 to 80. We then demonstrated that oil recovery was enhanced when *M* was increased, with the most significant economic benefit observed in the range of *M* from 1 to 10 with a very significant decrease of S^{or} while for higher M the gain in oil recovery is less pronounced. Anyway, the additional oil recovered was seen to be due to a more effective sweep of larger pores, while the remaining oil was enclosed in smaller and smaller ones. By tracking the number density of droplets, blobs, and ganglia, we showed that the breakage of trapped oil ganglia give rise to smaller ganglia that are left trapped, along with droplets and blobs that were more likely to be recovered. However, at higher *M*, smaller ganglia that are generated after bigger ganglia breaks are also driven away from the chip and the ultimate S^{or} is close to zero. Corollary, it is show that

even that the number density of ganglia changes only smoothly, the decrease in oil saturation that it can from is the most significant. Moreover, the number density of droplets and blobs do significantly decrease. The process of rupture-mobilization of oil clusters was evidenced trough time recording images of fluids displacement at pore scale. In addition, when the number density of each kind of cluster N(s) is plotted against their size (s), it is show to satisfy a power law with an exponent close to 2, as found by others in imbibition experiments.

Finally, to build-up the common CDC (the Capillary Desaturation Curve), we used a new method coming from literature for calculating the Ca, Ca_{new}, that is adapted for 2D microfluidic chips. We show therefore that by plotting S_{or} versus Ca_{new} almost all our experimental outputs do effectively lie on a master curve with a critical capillary number value of approximately 1×10^{-4}, that is consistent with the reported findings in experiments that were restricted to imbibition and drainage only.

Ultimately, of course, all these findings should be applicable to remediation processes where an extra fluid is injected to recover organic liquid pollutants from contaminated subterranean formations and aquifers.

As perspectives and in terms of future directions and to gain deeper insights into the flow of immiscible fluids in saturated porous media, this work could be extended by:

— Using a larger range of viscosity ratios and capillary numbers to scan a broader area of the logCa/logM diagram.

— exploring the expected contribution of elasticity in enhancing sweep efficiency using viscoelastic aqueous fluids, such as polymer solutions, particularly under high flow rate conditions.

— Utilizing chips that are etched with irregular depths to study the effects of varied depth sizes.

— Probing the role of chip's wettability

For the *in silico* modelling part a previous mathematical framework based on Cahn-Hilliard-Navier-Stokes equations (CH-NS) has been readapted to simulate EOR oriented experiments. The di-phasic system has been modelled as a mixture of an oil species and an aqueous species. The CH equations allow to trace the oil-aqueous interface by means of a diffuse interface approach while NS equations allows us to compute the overall dynamics of the two-fluid system. The unknowns of the CH-NS system of equations are the mass fraction of the oil species, the chemical potential, the velocity vector and the pressure of the mixture.

The physical relevance of the mathematical model has been tested on an academic controllable experiment where an oil droplet exits from a glass tube due to its initial instable position. By simulating this experiment:

- We identified a proper order of magnitude for the mobility parameter, M_e, governing the diffusive part of the CH equations;
- We demonstrate that the mathematical model as a comprehensive predictive potential and, once M_e (sole unknown parameter) identified, is able to predict the correct behaviour for two different cases (viscosity of oil equal to 1 Pa.s and 5 Pa.s respectively).

Once the model validated, it is applied to simulate the experiments performed during the thesis. The initial goal was to model the exact experimental procedure consisting of the drainage, imbibition and tertiary recovery stages. However, due to technical difficulties related to convergence issues and to the application of the boundary conditions during imbibition and tertiary recovery stages, the numerical analyses are limited to the drainage stage of the experiment. Furthermore, to have an acceptable computational time we have decided to model only a part of the whole chip geometry; hence, we considered two domains: a "2mm × 2mm" domain where we studied the model sensitivity to the injection velocity and to the mobility parameter, M_e; and a "5mm × 5mm" domain used to be more representative and compare the numerical and experimental solutions during the initial phase of drainage. The results are encouraging since they demonstrate the capability of the mathematical model to suitable represent the physics at play (*e.g.* fingering, lateral or backward front advancement, etc.). However, they have to be considered as preliminary due the improvements needed to overcome the current limitations. More precisely the major needed developments are:

- Accounting for the depth of microfluidic channels in the system of equations which is currently purely 2D in spite of the 2D + depth dimension of the real problem (both CH and NS equations will be impacted by this adjustment);
- Solve the problems encountered for *in silico* imbibition experiments where an unphysical diffusion phenomenon currently limits their reliability. This problem is probably related to the requirement of a revision of boundary conditions after the drainage stage.

We also plan to install *Fenics* within the *Curta* cluster of the regional *Mésocentre* MCIA (https://redmine.mcia.fr/projects/cluster-curta/wiki) to perform the numerical solutions for the whole chip geometry enabling the one-to-one comparisons between experimental and numerical results.

VI Nomenclature

Abbreviations

REV	Representative Elementary Volume
EOR	Enanced oil recovery
OOIP	Original oil in place
w-phase	wetting phase
nw-phase	non-wetting phase
PV	pore volume
CDC	capillary desaturation curve
IFT	interfacial tension
NS	Naiver-Stokes equation
CH	Cahn-Hilliard equation
E_{PW}	pure water experiment
E_{WF}	waterflooding experiment
E_{GM}	glycerol/water mixture flooding experiment

Writing convention	
x	Scalar quantity
$\boldsymbol{x}$	Vector quantity
$\underline{\boldsymbol{x}}$	Tensor Magnitude
x_α	Microscopic quantity
x^α	Macroscopic quantity
Operator	
$\nabla(x)$	Gradient operator
$\boldsymbol{\nabla \cdot x}$	Divergence operator
$:$	Tensor product
$\cdot$	scalar product
$(\,)^T$	top right corner represents the transpose of a matrix
Chapter II	

Symbols	**Description**	**Unit (SI)**
ϕ	porosity	
τ_t	tortuosity factor	
τ	scaling exponent in power law	
ε^{α}	volume fractions of α phase	
θ_s	Static contact angle between w-phase and nw-phase on the solid wall	
ζ	adjustable factor to relate permeability and pore geometry.	
m, λ_d	coefficient related to the distribution of pore sizes	
η	viscosity	Pa·s
ρ	fluid density	(kg/m^3)
λ	mobility	$m^2/(Pa{\cdot}s)$
σ	interfacial tension	mN/m
τ_v	viscous stress	Pa, N/m^2
τ_{IFT}	stress rump across fluid-fluid interface	Pa, N/m^2
$\dot{\gamma}$	shear rate	s^{-1}
μ	chemical potential	J/mol
Φ	bulk energy density	J/m^3
Roman letters	**Description**	**Unit (SI)**
Ca	capillary number	
d_z	etching depth of micromodel	m, μm
$\overline{D}_{throat}$	mean diameter of pore throat	m, μm
f_g	characteristic shape factor of the medium	m^{-1}
$f(w)$	fractional flow	
F_d	Forchheimer drag coefficient	
$\boldsymbol{I}$	2 × 2 identity matrix	
g	acceleration of gravity	m^2/s
G	geomerty of the porous media	
k	permeability	D, m^2
$\overline{\overline{k}}$	intrinsic permeability tensor	D, m^2
k_{rw}	relative permeability of wetting phase	D, m^2
k_{rnw}	relative permeability of non-wetting phase	D, m^2
k^{α}	relative permeability factor	D, m^2
K	intrinsic permeability of the porous medium	D, m^2

$\underline{\boldsymbol{K}}^{\alpha}$	permeability tensor	D, m^2
L	horizontal flow distance	m
M	viscosity ratio	
M_r	mobility ratio	
M_e	mobility coefficient	$m^5\ s^{-1}\ J^{-1}$
n_t	number of capillary tubes	
$N(s)$	number of clusters	
p	pressure	bar, Pa
p_c	capillary pressure	bar, Pa
p^{α}	α-phase pressure	bar, Pa
Δp	pressure drop	bar, Pa
q	volumetric flux density/ Darcy velocity	m/s
R	effective radius of the interface curvature	m, μm
R_d	the radius of curvature in depth	m, μm
Re	Reynolds number	
R_p	radius of tubes	m
R_r	resistance factor in poroue media	
R_{rr}	residual resistance factor in porous media	
s	size of cluster	m^3
S	saturation	
$\bar{S}_{\alpha}$	effective saturation	
S_{sp}	specific surface	m^2
$\underline{\boldsymbol{t}}_{\alpha}$	internal stress tensor in phase α	Pa
v	velocity of the injected fluid	m/s
$\boldsymbol{v}^{\alpha}$	macroscopic fluid velocity	m/s
V	Medium volume	m^3
Chapter III		
Symbols	**Description**	**Unit (SI)**
α	normalization coefficient to recover Young-Laplace law	
ω	mass fraction	
ϕ	chemical potential	J/mol
ε	interface thickness	μm, m
$\boldsymbol{\tau}$	tangent vectors to the boundary	
Ω	geometric domain	

Γ	boundary of domain	
Γ_0	wetting (or non-wetting) portion of the boundary	
Γs	partially wet one besides Γ_0	
Roman letters	**Description**	**Unit (SI)**
b	volumetric force	N/m^3
dN	each injection volume interval	PVm μL
n	outward normal to boundary	
N	total injection volume interval	PV, μL
q	a scalar weight function	
$\mathbf{q}_o$	flux term of advective part	
$\mathbf{q}_\phi$	flux term of diffusive part	
Q	flow rate	μL/min
r_α	chemical reactions term of α phase	
t	stress tensor	N/m^2
$\mathbf{t}_\mu$	stress related to viscous forces	N/m^2
u	diffusion velocity	m/s
v	mixture velocity	m/s
w	a vector weight function	
Chapter IV		
S_{wi}	rreducible water saturation	
S_{or}	residual oil saturation	
$k_{ro}(S_{wi})$	relative permeability of oil at S_{wi}	
$k_{rw}(S_{or})$	relative permeability of water at S_{or}	

VII References

Abdallah, W. et al., 1986. Fundamentals of wettability. *Technology*, Volume 268, pp. 1125-1144.

Abdul Jamil NAZARI, A. F. N. S. H., 2016. Effect of Fractional Flow Curves on the Recovery of Different Types of Oil in Petroleum Reservoirs. *Proceedings of the School of Engineering of Tokai University*, Volume 41, pp. 53-58.

Abidoye, L. K., Khudaida, K. J. & Das, D. B., 2015. Geological carbon sequestration in the context of two-phase flow in porous media: a review. *Critical Reviews in Environmental Science and Technology*, 45(11), pp. 1105-1147.

Abolhasanzadeh, A., Khaz'ali, A. R., Hashemi, R. & Jazini, M., 2020. Experimental study of microbial enhanced oil recovery in oil-wet fractured porous media. *Oil & Gas Science and Technology–Revue d'IFP Energies nouvelles,* Volume 75, p. 73.

Afrapoli, M. S., Alipour, S. & Torsaeter, O., 2012. Analysis of Microscopic Displacement Mechanisms of a MIOR Process in Porous Media with Different Wettability. *Transport in Porous Media* , Volume 93, pp. 705-719.

Agbalaka, C. et al., 2008. The Effect of Wettability on Oil Recovery: A Review. *SPE Asia Pacific Oil and Gas Conference and Exhibition*, pp. SPE-114496-MS.

Ahmadi, M. A., Arabsahebi, Y., Shadizadeh, S. R. & Behbahani, S. S., 2014. Preliminary evaluation of mulberry leaf-derived surfactant on interfacial tension in an oil-aqueous system: EOR application. *Fuel*, Volume 117, pp. 749-755.

Al Hinai, A., Rezaee, R., Esteban, L. & Labani, M., 2014. Comparisons of pore size distribution: a case from the Western Australian gas shale formations. *Journal of Unconventional Oil and Gas Resources*, Volume 8, pp. 1-13.

Alagic, E., Spildo, K., Skauge, A. & Solbakken, J., 2011. Effect of crude oil ageing on low salinity and low salinity surfactant flooding. *Journal of Petroleum Science and Engineering*, 78(2), pp. 220-227.

Al-Bayati, A. et al., 2022. Wettability alteration during low-salinity water flooding. *Energy & Fuels*, 36(2), pp. 871-879.

Alhammadi, A. M. et al., 2017. In situ characterization of mixed-wettability in a reservoir rock at subsurface conditions. *Scientific reports,* 7(1), p. 10753.

Al-Kharusi, A. S. & Blunt, M. J., 2007. Network extraction from sandstone and carbonate pore space images. *Journal of petroleum science and engineering,* 56(4), pp. 219-231.

Allan, J. & Sun, S. Q., 2003. Controls on recovery factor in fractured reservoirs: lessons learned from 100 fractured fields. *In SPE Annual Technical Conference and Exhibition,* pp. pp. SPE-84590.

Allen, S. M. & Cahn, J. W., 1976. Mechanisms of phase transformations within the miscibility gap of Fe-rich Fe-Al alloys. *Acta Metallurgica,* 24(5), pp. 425-437.

Almalik, M. S., Attia, A. M. & Jang, L. K., 1997. Effects of alkaline flooding on the recovery of Safaniya crude oil of Saudi Arabia. *Journal of Petroleum Science and Engineering,* 17(3-4), pp. 367-372.

Almansour, A. O., AlQuraishi, A. A., AlHussinan, S. N. & AlYami, H. Q., 2017. Efficiency of enhanced oil recovery using polymer-augmented low salinity flooding. *Journal of Petroleum Exploration and Production Technology,* Volume 7, pp. 1149-1158.

Alpak, F. O., Riviere, B. & Frank, F., 2016. A phase-field method for the direct simulation of two-phase flows in pore-scale media using a non-equilibrium wetting boundary condition. *Computational Geosciences,* Volume 20, pp. 881-908.

Alzahid, Y. A. et al., 2018. Functionalisation of Polydimethylsiloxane (PDMS)- Microfluidic Devices coated with Rock Minerals. *Scientific Reports,* Volume 8, p. 15518.

Amiri, H. A. & Hamouda, A., 2014. Pore-scale modeling of non-isothermal two phase flow in 2D porous media: Influences of viscosity, capillarity, wettability and heterogeneity. *International Journal of Multiphase Flow,* Volume 61, pp. 14-27.

Amott, E., 1959. Observations relating to the wettability of porous rock. *Transactions of the AIME,* 216(01), pp. 156-162.

Anastasiou, A. et al., 2024. Steady-State Dynamics of Ganglia Populations During Immiscible Two-Phase Flows in Porous Micromodels: Effects of the Capillary Number and Flow Ratio on Effective Rheology and Size Distributions. *Transport in Porous Media,* pp. 1-25.

Anderson, W., 1986. Wettability literature survey-part 2: Wettability measurement. *Journal of petroleum technology,* 38(11), pp. 1246-1262.

Anderson, W., 1987. Wettability Literature Survey-Part 6: The Effects of Wettability on Waterflooding. *Journal of petroleum technology*, 39(12), p. 1605–1622.

Anderson, W. G., 1986. Wettability literature survey-part 1: rock/oil/brine interactions and the effects of core handling on wettability. *Journal of petroleum technology,* 38(10), pp. 1125-1144.

Anderson, W. G., 1987. Wettability Literature Survey Part 5: The Effects of Wettability on Relative Permeability. *Journal of petroleum technology,* 39(11), p. 1453–1468.

Andreini, A., Bianchini, C., Puggelli, S. & Demoulin, F., 2016. Development of a turbulent liquid flux model for Eulerian–Eulerian multiphase flow simulations. *International Journal of Multiphase Flow,* Volume 81, pp. 88-103.

Aniszewski, W., Ménard, T. & Marek, M., 2014. Volume of Fluid (VOF) type advection methods in two-phase flow: A comparative study. *Computers & Fluids,* Volume 97, pp. 52-73.

Anovitz, L. M. & Cole, D. R., 2015. Characterization and analysis of porosity and pore structures. *Reviews in Mineralogy and geochemistry,* 80(1), pp. 61-164.

Arab, D., Bryant, S. L., Torsaeter, O. & Kantzas, A., 2022. Water flooding of sandstone oil reservoirs: Underlying mechanisms in imbibition vs. drainage displacement. *Journal of Petroleum Science and Engineering,* Volume 213, p. 110379.

Arab, D., Kantzas, A. & Bryant, S. L., 2020. Water flooding of oil reservoirs: Effect of oil viscosity and injection velocity on the interplay between capillary and viscous forces. *Journal of Petroleum Science and Engineering,* Volume 186, p. 106691.

Armstrong, R. T. & Berg, S., 2013. Interfacial velocities and capillary pressure gradients during Haines jumps. *Physical Review E,* 88(4), p. 043010.

Ashoori, E. T. L. M. V. D. H. W. R. R., 2010. Fractional-flow theory of foam displacements with oil. *SPE journal,* 15(02), pp. 260-273.

Auradou, H., 2009. Influence of wall roughness on the geometrical, mechanical and transport properties of single fractures. *Journal of Physics D: Applied Physics,* 42(21), p. 214015.

Avendano, J., 2012. *Viscoélasticité et récupération améliorée du pétrole,* s.l.: Université Paris-Est.

Avendano, J. et al., 2013. Entrance and exit effects for a viscoelastic liquid displacing a simple liquid through a contraction. *Journal of Non-Newtonian Fluid Mechanics,* Volume 199, pp. 51-60.

Avendano, J. et al., 2012. Normal Stresses and Interface Displacement: Influence of Viscoelasticity on Enhanced Oil Recovery Efficiency. *Oil & Gas Science and Technology–Revue d'IFP Energies nouvelles,* 67(6), pp. 921-930.

Avraam, D. G. & Payatakes, A. C., 1999. Flow Mechanisms, Relative Permeabilities, and Coupling Effects in Steady-State Two-Phase Flow through Porous Media. The Case of Strong Wettability. *Industrial & engineering chemistry research,* 38(3), pp. 778-786.

Azam, M. R. et al., 2013. Static adsorption of anionic surfactant onto crushed Berea sandstone. *Journal of Petroleum Exploration and Production Technology ,* 3(3), p. 195–201.

Bağcı, Ö., Dukhan, N. & Mustafa, Ö., 2014. Flow Regimes in Packed Beds of Spheres from Pre-Darcy to Turbulent. *Transport in Porous Media,* Volume 104, p. 501–520.

Bashir, A., Haddad, A. S. & Rafati, R., 2022. A review of fluid displacement mechanisms in surfactant-based chemical enhanced oil recovery processes: Analyses of key influencing factors. *Petroleum Science,* 19(3), pp. 1211-1235.

Bear, J. & Buchlin, J. M., 1991. *Modelling and applications of transport phenomena in porous media (Vol. 5).* Buchlin, J. M. ed. Boston: MA: Kluwer Academic Publishers.

Becker, A., Katzen, F., Pühler, A. & Ielpi, L., 1998. Xanthan gum biosynthesis and application: a biochemical/genetic perspective. *Applied Microbiology and Biotechnology,* Volume 50, p. 145–152.

Bera, A., Kumar, T., Ojha, K. & Mandal, A., 2013. Adsorption of surfactants on sand surface in enhanced oil recovery: Isotherms, kinetics and thermodynamic studies. *Applied Surface Science,* Volume 284, pp. 87-99.

Berkowitz, B., 1989. Boundary conditions along permeable fracture walls: Influence on flow and conductivity. *Water Resources Research,* 25(8), pp. 1919-1922.

Beucher, S. & Meyer, F., 2018. *The morphological approach to segmentation: the watershed transformation.In Mathematical morphology in image processing (pp. 433-481).*. s.l.:CRC Press..

Borazjani, S. et al., 2021. Determining water-oil relative permeability and capillary pressure from steady-state coreflood tests. *Journal of Petroleum Science and Engineering,* Volume 205, p. 108810.

Brinkman, H. C., 1949. A calculation of the viscous force exerted by a flowing fluid on a dense swarm of particles. *Flow, Turbulence and Combustion,* 1(1), pp. 27-34.

Brooks, R. H. & Corey, A. T., 1964. Hydraulic properties of porous media. Fort Collins: Hydrology Papers. *Civil Engineering Department, Colorado State University.*

Browne, C. A., Shih, A. & Datta, S. S., 2020. Pore-scale flow characterization of polymer so

Bryan, J. & Kantzas, A., 2007. Enhanced Heavy-Oil Recovery by Alkali-Surfactant Flooding. *SPE Annual Technical Conference and Exhibition,* pp. SPE-110738-MS.

Bryan, J. & Kantzas, A., 2009. Potential for Alkali-Surfactant Flooding in Heavy Oil Reservoirs Through Oil-in-Water Emulsification. *J Can Pet Technol ,* 48(02), p. 37–46.

Buchgraber, M., Clemens, T., Castanier, L. M. & Kovscek, A. R., 2009. The Displacement of Viscous Oil by Associative Polymer Solutions. *SPE Annual Technical Conference and Exhibition,* pp. SPE-122400-MS.

Buijse, M. A., Prelicz, R. M., Barnes, J. R. & Cosmo, C., 2010. Application of Internal Olefin Sulfonates and Other Surfactants to EOR. Part 2: The Design and Execution of an ASP Field Test. *SPE Improved Oil Recovery Symposium,* p. OnePetro.

Cahn, J. W. & Hilliard, J. E., 1958. Free Energy of a Nonuniform System. I. Interfacial Free Energy. *The Journal of chemical physics,* 28(2), p. 258–267.

Canny, M. J., 1977. Flow and transport in plants. *Annual review of fluid mechanics,* 9(1), pp. 275-296.

Carman, P. C., 1937. Fluid flow through a granular be. *Trans. Inst. Chem. Eng. London,* Volume 15, pp. 150-156.

Caudle, B. & Witte, M., 1959. Production Potential Changes During Sweep-Out in a Five-Spot System. *Journal of Petroleum Technology,* 12(12), p. 63–65.

Chang, L. C., Tsai, J. P., Shan, H. Y. & Chen, H. H., 2009. Experimental study on imbibition displacement mechanisms of two-phase fluid using micro model. *Environmental Earth Sciences,* Volume 59, pp. 901-911.

Chatzis, I., Morrow, N. R. & Lim, H. T., 1983. Magnitude and detailed structure of residual oil saturation. *Society of Petroleum Engineers Journal,* 23(02), pp. 311-326.

Chavent, G. J. J., 1986. *Mathematical models and finite elements for reservoir simulation: single phase, multiphase and multicomponent flows through porous media.* s.l.:Elsevier.

Chen Jiang, Z.-Q. Z. X. H. G. L. G.-J. G. T. L., 2017. A quasi-implicit characteristic–based penalty finite-element method for incompressible laminar viscous flows. *International Journal for Numerical Methods in Engineering,* 114(2), pp. 147-171.

Chen, K. et al., 2023. Effects of Capillary and Viscous Forces on Two-Phase Fluid Displacement in the Microfluidic Model. *Energy & Fuels,* 37(22), pp. 17263-17276.

Chen, L. et al., 2022. Pore-scale modeling of complex transport phenomena in porous media. *Progress in Energy and Combustion Science,* Volume 88, p. 100968.

Chen, X. & Yao, G., 2017. An improved model for permeability estimation in low permeable porous media based on fractal geometry and modified Hagen-Poiseuille flow. *Fuel,* Volume 210, pp. 748-757.

Chhabra, R. P., 2010. Non-Newtonian Fluids: An Introduction. *Rheology of Complex Fluids ,* pp. 3-34.

Chierici, G. L., 1984. Novel Relations for Drainage and Imbibition Relative Permeabilities. *Society of Petroleum Engineers Journal,* 24(03), p. 275–276.

Chiu, P.-H. & Lin, Y.-T., 2011. A conservative phase field method for solving incompressible two-phase flows. *Journal of Computational Physics,* 230(1), pp. 185-204.

Clarke, A. et al., 2015. Mechanism of anomalously increased oil displacement with aqueous viscoelastic polymer solutions. *Soft Matter,* 11(18), pp. 3536-3541.

Clarkson, C. R. et al., 2013. Pore structure characterization of North American shale gas reservoirs using USANS/SANS, gas adsorption, and mercury intrusion. *Fuel,* Volume 103, pp. 606-616.

Conn, C. A., Ma, K., Hirasaki, G. J. & Biswal, S. L., 2014. Visualizing oil displacement with foam in a microfluidic device with permeability contrast. *Lab on a Chip,* 14(20), pp. 3968-3977.

Cook, R. L., Jr, H. E. K. & Peiffer, D. G., 1992. High-pressure viscosity of dilute polymer solutions in good solvent. *Macromolecules,* 25(11), pp. 2928-2934.

Corey, A. T., 1994. *Mechanics of immiscible fluids in porous media.* s.l.:Water Resources Publication.

Corredor, L. M. et al., 2019. Heavy oil recovery by surface modified silica nanoparticle/HPAM nanofluids. *Fuel,* Volume 252, pp. 622-634.

Craig, F. C., 1971. *The reservoir engineering aspects of waterflooding.* New York: Society of Petroleum Engineers of AIME.

Dahle, H. K., Espedal, M. S., Ewing, R. E. & Sævereid, O., 1990. Characteristic adaptive subdomain methods for reservoir flow problems. *Numerical Methods for Partial Differential Equations,* 6(4), pp. 279-309.

Darcy, H., 1856. *Les Fontaines Publiques de la Ville de Dijon.* Paris: Victor Dalmond.

Datta, S. S., Ramakrishnan, T. S. & Weitz, D. A., 2014. Mobilization of a trapped non-wetting fluid from a three-dimensional porous medium. *Physics of Fluids,* 26(2).

De Castro, A. R., Oostrom, M. & Shokri, N., 2016. Effects of shear-thinning fluids on residual oil formation in microfluidic pore networks. *Journal of colloid and interface science,* Volume 472, pp. 34-43.

De, G. & Pierre-Gilles, 1985. Wetting: statics and dynamics. *Reviews of modern physics,* 57(3), p. 827.

Dehghan, A. A., Masihi, M. & Ayatollahi, S., 2013. Evaluation of Chemicals Interaction with Heavy Crude Oil through Water/Oil Emulsion and Interfacial Tension Study. *Energy Fuels,* 27(10), p. 5852–5860.

Dehghanpour, H. & Kuru, E., 2009. A New Look at the Viscoelastic Fluid Flow in Porous Media—A Possible Mechanism of Internal Cake Formation and Formation Damage Conrol. *SPE International Symposium on Oilfield Chemistry,* pp. SPE-121640-MS.

Demin, W., Gang, W. & Huifen, X., 2011. Large Scale High Viscous-Elastic Fluid Flooding in the Field Achieves High Recoveries. *SPE Enhanced Oil Recovery Conference,* pp. SPE-144294-MS.

Deng, X. et al., 2021. Relative contribution of wettability Alteration and interfacial tension reduction in EOR: A critical review. *Journal of Molecular Liquids,* Volume 325, p. 115175.

De, S. et al., 2018. Viscoelastic effects on residual oil distribution in flows through pillared microchannels. *Journal of Colloid and Interface Science,* Volume 510, pp. 262-271.

Detwiler, R. L., Rajaram, H. & Glass, R. J., 2009. Interphase mass transfer in variable aperture fractures: Controlling parameters and proposed constitutive relationships. *Water Resources Research,* Volume 45, p. W08436.

Ding, F. & Gao, M., 2021. Pore wettability for enhanced oil recovery, contaminant adsorption and oil/water separation: A review. *Advances in Colloid and Interface Science,* Volume 289, p. 102377.

Ding, H. & Spelt, P. D., 2007. Wetting condition in diffuse interface simulations of contact line motion. *Physical Review E,* 75(4), p. 046708.

Ding, H., Spelt, P. D. & Shu, C., 2007. Diffuse interface model for incompressible two-phase flows with large density ratios. *Journal of Computational Physics,* 226(2), pp. 2078-2095.

Dupuit, J., 1863. *Etudes theoriques et pratiques sur le mouvement des eaux dans les canaux decouverts et a travers les terrains permeables avec des considerations relatives au regime des grandes eaux, au debouche a leur donner et a la marche des alluvions dans les rivieres.* Paris: Dunod.

Dyes, A. B., Caudle, B. H. & Erickson, R. A., 1954. Oil production after breakthrough as influenced by mobility ratio. *Journal of Petroleum Technology*, 6(04), pp. 27-32.

Ehrlich, R., Hasiba, H. & Raimondi, P., 1974. Alkaline Waterflooding for Wettability Alteration-Evaluating a Potential Field Application. *J Pet Technol*, 26(12), p. 1335–1343.

Element, D. J., Goodyear, S. G., Sargent, N. C. & Jayasekera, A. J., 2001. Comparison of polymer and waterflood residual oil saturations. *63rd EAGE Conference & Exhibition*, pp. cp-58.

Eluru, G., Julius, L. A. N. & Gorthi, S. S., 2016. Single-layer microfluidic device to realize hydrodynamic 3D flow focusing. *Lab on a Chip*, 16(21), pp. 4133-4141.

Ewing, R. E., 1991. Simulation of multiphase flows in porous media. *Transport in Porous Media*, Volume 6, p. 479–499.

Farajzadeh, R. B. L. W. L. W. L., 2019. Insights into design of mobility control for chemical enhanced oil recovery. *Energy Reports*, Volume 5, pp. 570-578.

Farhadi, H., Fatemi, M. & Ayatollahi, S., 2021. Experimental investigation on the dominating fluid-fluid and rock-fluid interactions during low salinity water flooding in water-wet and oil-wet calcites. *Journal of Petroleum Science and Engineering*, Volume 204, p. 108697.

Fayers, F. & Muggeridge, A., 1990. Extensions to Dietz theory and behavior of gravity tongues in slightly tilted reservoirs. *SPE Reservoir Engineering*, 5(04), pp. 487-494.

Ferreira, R. B., Falcão, D., Oliveira, V. & Pinto, A., 2015. Numerical simulations of two-phase flow in proton exchange membrane fuel cells using the volume of fluid method – A review. *Journal of Power Sources*, Volume 277, pp. 329-342.

Firozjaii, A. M. & Saghafi, H. R., 2020. Review on chemical enhanced oil recovery using polymer flooding: Fundamentals, experimental and numerical simulation. *Petroleum*, 6(2), pp. 115-122.

Flaaten, A. K. et al., 2008. ASP Chemical Flooding Without the Need for Soft Water. *SPE Annual Technical Conference and Exhibition*, pp. SPE-116754-MS.

Flew, S. & Sellin, R., 1993. Non-Newtonian flow in porous media-a laboratory study of polyacrylamide solutions. *Journal of Non-Newtonian Fluid Mechanics,* Volume 47, pp. 169-210.

Forchheimer, P., 1901. Wasserbewegung durch boden. *Zeitschrift des Vereines Deutscher Ingenieure,* 45(50), pp. 1781-1788.

Forey, N., Atteia, O., Omari, A. & Bertin, H., 2020. Saponin foam for soil remediation: On the use of polymer or solid particles to enhance foam resistance against oil. *Journal of contaminant hydrology,* Volume 228, p. 103560.

Fred I. Stalkup, J., 1983. Status of Miscible Displacement. *J Pet TechnolJ Pet Technol,* 35(04), p. 815–826.

Fulcher, J. R. A., Turgay, E. & Stahl, C., 1985. Effect of Capillary Number and Its Constituents on Two-Phase Relative Permeability Curves. *Journal of Petroleum Technology,* 37(2), p. 249–260.

Furihata, D., 2001. A stable and conservative finite difference scheme for the Cahn-Hilliard equation. *Numerische Mathematik ,* Volume 87, p. 675–699.

Fushui, L., Yang, X. & Yikai, L., 2017. A coupled level-set and volume-of-fluid method for simulating axi-symmetric incompressible two-phase flows. *Applied Mathematics and Computation,* Volume 293, pp. 112-130.

Geet, M. V. & Swennen, R., 2001. Quantitative 3D-fracture analysis by means of microfocus X-Ray Computer Tomography (μCT): An example from coal. *Geophysical Research Letters,* 28(17), pp. 3333-3336.

Georgiadis, A. et al., 2013. Pore-scale micro-computed-tomography imaging: Nonwetting-phase cluster-size distribution during drainage and imbibition. *Physical Review E,* 88(3), p. 033002.

Ghannam, M. & Esmail, M., 1998. Rheological properties of aqueous polyacrylamide solutions. *Journal of Applied Polymer Science,* 69(8), p. 1587–1597.

Gogoi, S. & Gogoi, S. B., 2019. Review on microfluidic studies for EOR application. *Journal of Petroleum Exploration and Production Technology,* Volume 9, pp. 2263-2277.

Gong, F. et al., 2020. Evaluation of geothermal energy extraction in Enhanced Geothermal System (EGS) with multiple fracturing horizontal wells (MFHW). *Renewable Energy,* Volume 151, pp. 1339-1351.

Gray, W. G. C. T. M., 2014. *Introduction to the thermodynamically constrained averaging theory for porous medium systems.* Berlin: Springer.

Gray, W. G. & Miller, C. T., 2005. Thermodynamically constrained averaging theory approach for modeling flow and transport phenomena in porous medium systems: 1. Motivation and overview.. *Advances in Water Resources,* 28(2), pp. 161-180.

Gray, W. G. & Miller, C. T., 2006. Thermodynamically constrained averaging theory approach for modeling flow and transport phenomena in porous medium systems: 3. Single-fluid-phase flow. *Advances in water resources,* 29(11), pp. 1745-1765.

Green, D. W. & Willhite, G. P., 1998. *Enhanced oil recovery.* Richardson: TX: Henry L. Doherty Memorial Fund of AIME, Society of Petroleum Engineers.

Gu, H., Duits, M. H. G. & Mugele, F., 2011. Droplets Formation and Merging in Two-Phase Flow Microfluidics. *International Journal of molecular sciences,* 12(4), pp. 2572-2597.

Guo, H. et al., 2015. Progress of Microbial Enhanced Oil Recovery in China. *SPE Asia Pacific Enhanced Oil Recovery Conference,* pp. SPE-174697-MS.

Guo, H., Song, K. & Hilfer, R., 2020. A critical review of capillary number and its application in enhanced oil recovery. *SPE Improved Oil Recovery Conference,* pp. SPE-200419-MS.

Guo, H., Song, K. & Hilfer, R., 2022. A Brief Review of Capillary Number and its Use in Capillary Desaturation Curves. *Transport in Porous Media ,* 144(1), p. 3–31.

Guo, J. et al., 2006. The effect of alkali on crude oil/water interfacial properties and the stability of crude oil emulsions. *Colloids and Surfaces A: Physicochemical and Engineering Aspects,* 273(1-3), pp. 213-218.

Guo, K., Li, H. & Yu, Z., 2016. In-situ heavy and extra-heavy oil recovery: A review. *Fuel,* Volume 185, pp. 886-902.

H. K. Dahle, M. S. E. R. E. E. O. S., 1990. Characteristic adaptive subdomain methods for reservoir flow problems. *Numerical Methods for Partial Differential Equations,* 6(4), pp. 279-309.

Hadia, N. J., Ashraf, A., Tweheyo, M. T. & Torsæter, O., 2013. Laboratory investigation on effects of initial wettabilities on performance of low salinity waterflooding. *Journal of Petroleum Science and Engineering,* Volume 105, pp. 18-25.

Hamarneh, G. & Li, X., 2009. Watershed segmentation using prior shape and appearance knowledge. *Image and Vision Computing,* 27(1-2), pp. 59-68.

Hascakir, B., 2017. Introduction to Thermal Enhanced Oil Recovery (EOR) special issue. *Journal of Petroleum Science and Engineering,* Volume 154, pp. 438-441.

Heider, Y., 2021. Yousef Heider. *A review on phase-field modeling of hydraulic fracturing,* Volume 253, p. 107881.

Herring, A. L. et al., 2013. Effect of fluid topology on residual nonwetting phase trapping: Implications for geologic CO2 sequestration. *Advances in water resources,* Volume 62, pp. 47-58.

Hirasaki, G. J., Miller, C. A. & Puerto, M., 2011. Recent advances in surfactant EOR. *SPE journal,* 16(04), pp. 889-907.

Hiroyuki, Y. et al., 2005. Measuring hydraulic permeability in a streambed using the packer test. *Hydrological Process,* 19(13), p. 2507–2524.

Homsy, G. M., 1987. Viscous fingering in porous media. *Annual review of fluid mechanics,* 19(1), pp. 271-311.

Horgue, P. et al., 2015. An open-source toolbox for multiphase flow in porous media. *Computer Physics Communications,* Volume 187, pp. 217-226.

Hosseini, B. S., Turek, S., Möller, M. & Palmes, C., 2017. Isogeometric Analysis of the Navier–Stokes–Cahn–Hilliard equations with application to incompressible two-phase flows. *Journal of Computational Physics,* Volume 348, pp. 171-194.

Hou, J. et al., 2005. The role of viscoelasticity of alkali/surfactant/polymer solutions in enhanced oil recovery. *Journal of Petroleum Science and Engineering,* 47(3-4), pp. 219-235.

Howe, A. M. et al., 2015. Visualising surfactant enhanced oil recovery. *Colloids and Surfaces A: Physicochemical and Engineering Aspects,* Volume 480, pp. 449-461.

Hu, G., Kaoping, S. & Hilfer, R., 2022. A Brief Review of Capillary Number and its Use in Capillary Desaturation Curves. *Transport in Porous Media,* 144(1), p. 3–31.

Huh, C. & Pope, G. A., 2008. Residual Oil Saturation from Polymer Floods: Laboratory Measurements and Theoretical Interpretation. *SPE Symposium on Improved Oil Recovery*, pp. SPE-113417-MS.

Hui-Hai Liu, B. L. J. C., 2016. Unconventional Spontaneous Imbibition into Shale Matrix: Theory and a Methodology to Determine Relevant Parameters. *Transport in porous media,* Volume 111, p. 41–57.

Hu, J., Li, A. & Memon, A., 2020. Experimental investigation of polymer enhanced oil recovery under different injection modes. *ACS omega,* 5(48), pp. 31069-31075.

Humphry, K. J. et al., 2014. Impact of wettability on residual oil saturation and capillary desaturation curves. *Petrophysics,* 55(04), pp. 313-318.

Hu, Y., Patmonoaji, A., Zhang, C. & Suekane, T., 2020. Experimental study on the displacement patterns and the phase diagram of immiscible fluid displacement in three-dimensional porous media. *Advances in water resources,* Volume 140, p. 103584.

Hu, Y., Wang, S. & Jamieson, A., 1995. Rheological and rheooptical studies of shear-thickening polyacrylamide solutions. *Macromolecules,* 28(6), p. 1847–1853.

Ibrahim, A. S. E. D. S., 2009. Investigation of the Mobilization of Residual Oil Using Micromodels. *SPE Annual Technical Conference and Exhibition*, pp. SPE-129515-STU.

IEA, 2018. *EOR Production in the New Policies Scenario, 2000–2040 Retrieved from International Energy Agency.* [Online] Available at: https://www.iea.org/data-and-statistics/charts/eor-production-in-the-new-policies-scenario-2000-2040

Iglauer, S. et al., 2010. X-ray tomography measurements of power-law cluster size distributions for the nonwetting phase in sandstones. *Physical Review E,* 82(5), p. 056315.

Iglauer, S., Fernø, M. A., Shearing, P. & Blunt, M. J., 2012. Comparison of residual oil cluster size distribution, morphology and saturation in oil-wet and water-wet sandstone. *Journal of colloid and interface science,* 375(1), pp. 187-192.

Iglauer, S. & Wülling, W., 2016. The scaling exponent of residual nonwetting phase cluster size distributions in porous media. *Geophysical Research Letters,* 43(21), pp. 11-253.

Irmay, S., 1958. On the theoretical derivation of Darcy and Forchheimer formulas. *Eos, Transactions American Geophysical Union,* 39(4), pp. 702-707.

Jackson, A. S., Miller, C. T. & Gray, W. G., 2009. Thermodynamically constrained averaging theory approach for modeling flow and transport phenomena in porous medium systems: 6. Two-fluid-phase flow. *Advances in Water Resources,* 32(6), pp. 779-795.

Jacqmin, D., 1999. Calculation of Two-Phase Navier–Stokes Flows Using Phase-Field Modeling. *Journal of Computational Physics,* 155(1), pp. 96-127.

Jacqmin, D., 2000. Contact-line dynamics of a diffuse fluid interphace. *Journal of Fluid Mechanics,* pp. 57-88.

Jadhunandan, P. P. & Morrow, N. R., 1995. Effect of wettability on waterflood recovery for crude-oil/brine/rock systems. *SPE reservoir engineering,* 10(01), pp. 40-46.

Jahanbakhsh, A. et al., 2020. Review of Microfluidic Devices and Imaging Techniques for Fluid Flow Study in Porous Geomaterials. *Sensors,* 20(14), p. 4030.

Jain, S. S., Mani, A. & Moin, P., 2020. A conservative diffuse-interface method for compressible two-phase flows. *Journal of Computational Physics,* Volume 418, p. 109606.

Jeong, D. & Kim, J., 2017. Conservative Allen–Cahn–Navier–Stokes system for incompressible two-phase fluid flows. *Computers & Fluids,* Volume 156, pp. 239-246.

Jeong, S.-W. & Corapcioglu, M. Y., 2003. A micromodel analysis of factors influencing NAPL removal by surfactant foam flooding. *Journal of Contaminant Hydrology,* 60(1-2), pp. 77-96.

Jr., R. C., King, H. & Peiffer, D., 1992. High-pressure viscosity of dilute polymer solutions in good solvents. *Macromolecules,* 25(11), pp. 2928-2934.

Juárez-Morejón, J. L. et al., 2019. A new approach to polymer flooding: Effects of early polymer injection and wettability on final oil recovery. *SPE Journal*, 24(01), pp. 129-139.

Jung, J. C., Zhang, K., Chon, B. H. & Choi, H. J., 2013. Rheology and polymer flooding characteristics of partially hydrolyzed polyacrylamide for enhanced heavy oil recovery. *Journal of Applied Polymer Science*, 127 (6), pp. 4833-4839.

Kale, S. V., Rai, C. S. & Sondergeld, C. H., 2010. Petrophysical characterization of Barnett shale. *In SPE Unconventional Resources Conference/Gas Technology Symposium,* pp. SPE-131770.

Kalteh, M., Abbassi, A., Saffar-Avval, M. & Harting, J., 2011. Eulerian–Eulerian two-phase numerical simulation of nanofluid laminar forced convection in a microchannel. *International Journal of Heat and Fluid Flow*, 32(1), pp. 107-116.

Kamal, M. S., Hussein, I. A. & Sultan§, A. S., 2017. Review on Surfactant Flooding: Phase Behavior, Retention, IFT, and Field Applications. *Energy Fuels,* 31(8), p. 7701–7720.

Kamal, M. S., Sultan, A. S., Al-Mubaiyedh, U. A. & Hussein, I. A., 2015. Review on Polymer Flooding: Rheology, Adsorption, Stability, and Field Applications of Various Polymer Systems. *Polymer Reviews,* 55(3), pp. 491-530.

Kamal, M. S., Sultan, A. S. & Hussein, I. A., 2015. Screening of amphoteric and anionic surfactants for cEOR applications using a novel approach. *Colloids and Surfaces A: Physicochemical and Engineering Aspects,* Volume 476, pp. 17-23.

Kang, W. L., Zhou, B. B., Issakhov, M. & Gabdullin, M., 2022. Advances in enhanced oil recovery technologies for low permeability reservoirs. *Petroleum Science*, 19(4), pp. 1622-1640.

Kao, C. M. et al., 2004. Evaluation of natural and enhanced PCP biodegradation at a former pesticide manufacturing plant. *Water research,* 38(3), pp. 663-672.

Khaddour, F., Grégoire, D. & Pijaudier-Cabot, G., 2015. Capillary bundle model for the computation of the apparent permeability from pore size distributions. *European Journal of Environmental and Civil Engineering* , 19(2), pp. 168-183.

Khlaifat, A. L., Dakhlallah, D. & Sufyan, F., 2022. A Critical Review of Alkaline Flooding: Mechanism, Hybrid Flooding Methods, Laboratory Work, Pilot Projects, and Field Applications. *Energies,* 15(10), p. 382.

Kizilyaprak, C., Daraspe, J. & Humbel, B. M., 2014. Focused ion beam scanning electron microscopy in biology. *Journal of microscopy*, 254(3), pp. 109-114.

Konstantinos N. Moutsopoulos, I. N. P. V. A. T., 2009. Experimental investigation of inertial flow processes in porous media. *Journal of Hydrology,* 374(3-4), pp. 242-254.

Kornilov, A., Safonov, I. & Yakimchuk, I., 2022. A review of watershed implementations for segmentation of volumetric images. *Journal of Imaging,* 8(5), p. 127.

Kozeny, J., 1927. Ueber kapillare Leitung des Wassers im Boden. *Sitzungsber Akad. Wiss., Wien,* 136(2a), pp. 271-306.

Kuldeep Chaudhary, M. B. C. W. D. P. C. B., 2011. The role of eddies inside pores in the transition from Darcy to Forchheimer flows. *Geophysical Research Letters,* 38(24), p. L24405.

Kumar, N. et al., 2022. Fundamental aspects, mechanisms and emerging possibilities of CO2 miscible flooding in enhanced oil recovery: A review. *Fuel,* Volume 330, p. 125633.

Kundu, P., Kumar, V. & Mishra, I. M., 2016. Experimental and numerical investigation of fluid flow hydrodynamics in porous media: Characterization of pre-Darcy, Darcy and non-Darcy flow regimes. *Powder Technology,* Volume 303, pp. 278-291.

Laben, A. B. et al., 2022. Experimental study on the performance of emulsions produced during ASP flooding. *Journal of Petroleum Exploration and Production Technology,* Volume 12, p. 1797–1809.

Lake, L. W., 1989. *Enhanced oil recovery.* s.l.:N. p..

Lake, L. W., Johns, R., Rossen, B. & Pope, G. A., 2014. *Fundamentals of Enhanced Oil Recovery. 2nd ed.*. Richardson ed. Texas: Texas: Society of Petroleum Engineers.

Larson, R. & Hirasaki, G., 1976. Analysis of the Physical Mechanisms in Surfactant Flooding. . *SPE J,* p. 6003.

Lasseux, D., Ahmadi, A. & Ali Akbar, A. A., 2008. Two-phase inertial flow in homogeneous porous media: A theoretical derivation of a macroscopic model. *Transport in Porous Media,* 75(3), pp. 371-400.

Lasseux, D., Quintard, M. & Whitaker, S., 1996. Determination of Permeability Tensors for Two-Phase Flow in Homogeneous Porous Media. *Transport in Porous Media,* 2(1), pp. 107-137.

Lasseux, D., Valdés-Parada, F. J. & Bellet, F., 2019. Macroscopic model for unsteady flow in porous media. *Journal of Fluid Mechanics,* 862(1), pp. 283-311.

Lawrence, M. & Jiang, Y., 2017. Porosity, pore size distribution, micro-structure. *Bio-aggregates based building materials: state-of-the-art report of the RILEM technical committee,* Volume 236-BBM, pp. 39-71.

Lazar, I., Petrisor, I. G. & Yen, T. F., 2007. Microbial Enhanced Oil Recovery (MEOR). *Petroleum Science and Technology ,* 25(11), pp. 1353-1366.

Le Maout, V. et al., 2020. Role of mechanical cues and hypoxia on the growth of tumor cells in strong and weak confinement: A dual in vitro–in silico approach. *Science advances,* 6(13), p. eaaz7130.

Lei Ding, Q. W. L. Z. D. G., 2020. Application of Fractional Flow Theory for Analytical Modeling of Surfactant Flooding, Polymer Flooding, and Surfactant/Polymer Flooding for Chemical Enhanced Oil Recovery. *Water,* 12(8), p. 2195.

Lei, W. et al., 2020. Enhanced oil recovery mechanism and recovery performance of micro-gel particle suspensions by microfluidic experiments. *Energy Science & Engineering,* 8(4), pp. 986-998.

Lenormand, R., 1986. Pattern growth and fluid displacements through porous media. *Physica A: Statistical Mechanics and its Applications,* 140(1-2), pp. 114-123.

Lenormand, R., Touboul, E. & Zarcone, C., 1988. Numerical models and experiments on immiscible displacements in porous media. *Journal of Fluid Mechanics,* Volume 189, pp. 165 - 187.

Lenormand, R., Zarcone, C. & Sarr, A., 1983. Mechanisms of the displacement of one fluid by another in a network of capillary ducts. *Journal of Fluid Mechanics*, Volume 135, pp. 337-353.

Lewandowska, K., 2007. Comparative studies of rheological properties of polyacrylamide and partially hydrolyzed polyacrylamide solutions. *Journal of Applied Polymer Science*, 103(4), p. 2235–2241.

Lifton, V. A., 2016. Microfluidics: an enabling screening technology for enhanced oil recovery (EOR). *Lab on a Chip*, 16(10), pp. 1777-1796.

Li, G.-Z., Mu, J.-H., Li, Y. & Yuan, S.-L., 2000. An experimental study on alkaline/surfactant/polymer flooding systems using nature mixed carboxylate. *Colloids and Surfaces A: Physicochemical and Engineering Aspects,* 173(1-3), pp. 219-229.

Li, H., Pan, C. & Miller, C. T., 2005. Pore-scale investigation of viscous coupling effects for two-phase flow in porous media. *Physical Review E*, 72(2), p. 026705.

Li, K.-x.et al., 2016. Laboratory Study Displacement Efficiency of Viscoelastic Surfactant Solution in Enhanced Oil Recovery. *Energy Fuels,* 30(6), p. 4467–4474.

Li, K. et al., 2019. Pore-level investigations on the oil displacement mechanisms of a viscoelastic surfactant in porous media. *Journal of Petroleum Science and Engineering,* Volume 173, pp. 748-757.

Li, S. et al., 2022. Prediction of spontaneous imbibition with gravity in porous media micromodels. *Journal of Fluid Mechanics,* Volume A9, p. 952.

Littmann, W. et al., 1992. Late Results of a Polymer Pilot Test: Performance, Simulation Adsorption, and Xanthan Stability in the Reservoir. *SPE/DOE Enhanced Oil Recovery Symposium*, pp. SPE-24120-MS.

Liu, Q., Dong, M., Ma, S. & Tu, Y., 2007. Surfactant enhanced alkaline flooding for Western Canadian heavy oil recovery. *Colloids and Surfaces A: Physicochemical and Engineering Aspects,* 293(1-3), pp. 63-71.

Liu, S. et al., 2008. Favorable Attributes of Alkaline-Surfactant-Polymer Flooding. *SPE Journal*, 13(01), p. 5–16.

Liu, Y. et al., 2023. Motion Characteristics of Gas–Liquid Two-Phase Flow of Microbubbles in a Labyrinth Channel Used for Aerated Drip Irrigation. *Water*, 15(7), p. 1432.

Liu, Z.-x.et al., 2020. Status and progress of worldwide EOR field applications. *Journal of Petroleum Science and Engineering*, Volume 193, p. 107449.

Liu, Z., Yue, X., Hou, J. & Zhang, L., 2002. Comparison of Displacement Oil Mechanism of Polymer, ASP and Foam of ASP in Micro Pores and Dead Ends of Pores. *SPE Asia Pacific Oil and Gas Conference and Exhibition*, pp. SPE-77876-MS.

Li, Z.-S. & Tang, L.-S., 2019. Using Synchrotron-Based X-Ray Microcomputed Tomography to Characterize Water Distribution in Compacted Soils. *Advances in Materials Science and Engineering*, p. 2019.

Logsdon, J. & Kahn, R., 2004. The Arf family tree. *Arf Family GTPases*, pp. 1-21.

Lomeland, F. & Ebeltof, A., 2008. A New Versatile Capillary Pressure Correlation. *Paper SCA 2008-08 presented at the International Symposium of the Society of Core Analysts held in Abu Dhabi*, Volume 29.

Lomeland, F., Ebeltoft, E. & Thomas, W. H., 2005. A new versatile relative permeability correlation. *In International symposium of the society of core analysts*, Volume 112.

Lostaglio, M., 2019. An introductory review of the resource theory approach to thermodynamics. *Reports on Progress in Physics*, 82(11), p. 114001.

Lund, T., Lecourtier, J. & Müller, G., 1990. Properties of xanthan solutions after long-term heat treatment at 90°C. *Polymer Degradation and Stability*, 27(2), pp. 211-225.

Luquot, L., Rodriguez, O. & Gouze, P., 2014. Experimental Characterization of Porosity Structure and Transport Property Changes in Limestone Undergoing Different Dissolution Regimes. *Transport in Porous Media*, Volume 101, p. 507–532.

M. Ferer, C. J. G. S. B. J. C. G. A. D. H. S., 2004. Crossover from capillary fingering to viscous fingering for immiscible unstable flow: Experiment and modeling. *Physical Review E,* 70(1), p. 016303.

M. Rücker, S. B. R. T. A. A. G. H. O. A. S. R. N. N. B. A. M. L. L. M. W. F. K. F. E. M. K., 2015. From connected pathway flow to ganglion dynamics. *Geophysical Research Letters,* 42(10), pp. 3888-3894.

M.J. Simpson, T. C., 2003. Comparison of finite difference and finite element solutions to the variably saturated flow equation. *Journal of Hydrology*, 270(1-2), pp. 49-64.

Maaref, S., Rokhforouz, M.-R. & Ayatollahi, S., 2017. Numerical investigation of two phase flow in micromodel porous media: Effects of wettability, heterogeneity, and viscosity. *The Canadian Journal of Chemical Engineering*, 95(6), pp. 1213-1223.

Ma, B.-d.et al., 2015. Influence of polymer on dynamic interfacial tensions of EOR surfactant solutions. *Journal of Applied Polymer Science*, 131(15).

Malkus, D. S., Pritchard, W. G. & Yao, M., 1992. The hole-pressure effect and viscometry. *Rheologica Acta* , Volume 31, p. 521–534.

Ma, N. et al., 2022. Laboratory Study on the Oil Displacement Process in Low-Permeability Cores with Different Injection Fluids. *ACS Omega*, 7(9), p. 8013–8022.

Manrique, E. J., Muci, V. E. & Gurfinkel, M. E., 2007. EOR Field Experiences in Carbonate Reservoirs in the United States. *SPE Res Eval & Eng*, 10(06), p. 667–686.

Manshad, A. K. et al., 2017. Wettability alteration and interfacial tension (IFT) reduction in enhanced oil recovery (EOR) process by ionic liquid flooding. *Journal of Molecular Liquids*, Volume 248, pp. 153-162.

Masalmeh, S. K., 2003. The effect of wettability heterogeneity on capillary pressure and relative permeability. *Journal of Petroleum Science and Engineering,* 39(3-4), pp. 399-408.

Mason, G., Fischer, H., Morrow, N. R. & Ruth, D. W., 2010. Correlation for the effect of fluid viscosities on counter-current spontaneous imbibition. *Journal of petroleum science and engineering,* 72(1-2), pp. 195-205.

Mayer, A. S. & Miller, C. T., 1993. An experimental investigation of pore-scale distributions of nonaqueous phase liquids at residual saturation. *Transport in porous media,* Volume 10, pp. 57-80.

Mckee, F., 2013. *Etude de la mise à l'échelle des écoulements diphasiques en milieux hétérogènes par une approche d'optimisation,* Nantes: s.n.: s.n.

McMillan, M. D., Rahnema, H., Romiluy, J. & Kitty, F. J., 2016. Effect of exposure time and crude oil composition on low-salinity water flooding. *Fuel,* Volume 185, pp. 263-272.

Mejia, L. et al., 2020. Coreflood on a chip: Core-scale micromodels for subsurface applications. *Fuel,* Volume 281, p. 118716.

Meybodi, H. E., Kharrat, R. & Araghi, M. N., 2011. Experimental studying of pore morphology and wettability effects on microscopic and macroscopic displacement efficiency of polymer flooding. *Journal of Petroleum Science and Engineering,* 78(2), pp. 347-363.

Miller, C. T. & Gray, W. G., 2005. Thermodynamically constrained averaging theory approach for modeling flow and transport phenomena in porous medium systems: 2. Foundation. *Advances in Water Resources,* 28(2), pp. 181-202.

Mitchell, J., Lyons, K., Howe, A. M. & Clarke, A., 2016. Viscoelastic polymer flows and elastic turbulence in three-dimensional porous structures. *Soft Matter,* 12(2), pp. 460-468.

Mogensen, K. & Masalmeh, S., 2020. A review of EOR techniques for carbonate reservoirs in challenging geological settings. *Journal of Petroleum Science and Engineering,* Volume 195, p. 107889.

Mokheimer, E. M. A. et al., 2019. A Comprehensive Review of Thermal Enhanced Oil Recovery: Techniques Evaluation. *J. Energy Resour. Technol. Mar,* 141(3), p. 030801.

Moortgat, J., Li, Z. & Firoozabadi, A., 2011. Three-Phase Compositional Modeling of CO2 Injection by Higher-Order Finite Element Methods with CPA Equation of State. *SPE Reservoir Simulation Symposium,* pp. SPE-141907-MS.

Morrow, N. R., 1979. Interplay of capillary, viscous and buoyancy forces in the mobilization of residual oil. *Journal of Canadian Petroleum Technology,* 18(03).

Muggeridge, A. et al., 2014. Recovery rates, enhanced oil recovery and technological limits. *Philosophical Transactions of the Royal Society A: Mathematical, Physical and Engineering Sciences*, 372(2006), p. 20120320.

Muskat, M., 1938. The flow of homogeneous fluids through porous media. *Soil Science*, 46(2), p. 169.

Nasr, S., Soudi, M. R. & Haghighi, M., 2007. Xanthan Production by a Native Strain of X. campestris and Evaluation of Application in EOR. *Pakistan Journal of Biological Sciences*, 10(17), pp. 3010-3013.

Nath, P., Arun, R. K. & Chanda, N., 2014. A paper based microfluidic device for the detection of arsenic using a gold nanosensor. *Rsc Advances*, 4(103), pp. 59558-59561.

Ng, K. M. & Payatakes, A. C., 1980. Stochastic simulation of the mobilization, breakup and stranding of oil ganglia in water-wet granular porous media during immiscible displacement. *AIChE J*, 26(3), pp. 419-429.

Nie, C. et al., 2021. Stability Dynamic Characteristic of Oil-in-Water Emulsion from Alkali–Surfactant–Polymer Flooding. *ACS Omega*, 6(29), p. 19058–19066.

Nikolaos, K. K., Hassan, M., Holger, S. & Vahid, N., 2019. Nonmonotonic Effects of Salinity on Wettability Alteration and Two-Phase Flow Dynamics in PDMS Micromodels. *Water Resources Research*, 55(11), pp. 9826-9837.

Nilsson, M. A. et al., 2013. Effect of fluid rheology on enhanced oil recovery in a microfluidic sandstone device. *Journal of Non-Newtonian Fluid Mechanics*, Volume 202, pp. 112-119.

Nimmo, J. R., 2004. Porosity and pore size distribution. *Encyclopedia of Soils in the Environment*, 3(1), pp. 295-303.

Nobakht, M., Moghadam, S. & Gu, Y., 2007. Effects of viscous and capillary forces on CO2 enhanced oil recovery under reservoir conditions. *Energy & Fuels*, 21(6), pp. 3469-3476.

Nooruddin, H. A. M. E. H., 2011. Modified Kozeny–Carmen correlation for enhanced hydraulic flow unit characterization. *Journal of Petroleum Science and Engineering*, 80(1), pp. 107-11.

Olajire, A. A., 2014. Review of ASP EOR (alkaline surfactant polymer enhanced oil recovery) technology in the petroleum industry: Prospects and challenges. *Energy,* Volume 77, pp. 963-982.

Oss, C. J. v., 2007. Development and applications of the interfacial tension between water and organic or biological surfaces. *Colloids and Surfaces B: Biointerfaces,* 54(1), pp. 2-9.

P. G. Ranjith, W. D., 2007. Nonlinear single-phase flow in real rock joints. *Water Resources Research,* 43(9), p. W09502.

Pal, N., Saxena, N. & Mandal, A., 2018. Characterization of alkali-surfactant-polymer slugs using synthesized gemini surfactant for potential application in enhanced oil recovery. *Journal of Petroleum Science and Engineering,* Volume 168, pp. 283-300.

Pancharoen, M., Thiele, M. R. & Kovscek, A. R., 2010. Inaccessible Pore Volume of Associative Polymer Floods. *SPE Improved Oil Recovery Symposium,* pp. SPE-129910-MS.

Pankajakshan, R., Mitchell, B. J. & Taylor, L. K., 2011. Simulation of unsteady two-phase flows using a parallel Eulerian–Lagrangian approach. *Computers & Fluids,* 41(1), pp. 20-26.

Pasquier, S., Quintard, M. & Davit, Y., 2017. Modeling two-phase flow of immiscible fluids in porous media: Buckley-Leverett theory with explicit coupling terms. *Physical Reviw Fluids,* 2(10), pp. 104101/1-104101/19.

Patel, J. et al., 2015. Recent developments in microbial enhanced oil recovery. *Renewable and Sustainable Energy Reviews,* Volume 52, pp. 1539-1558.

Paterson, L., 1984. Diffusion-Limited Aggregation and Two-Fluid Displacements in Porous Media. *Physical review letters,* 52(18), p. 1621.

Philip Binning, M. A. C., 1999. Practical implementation of the fractional flow approach to multi-phase flow simulation. *Advances in Water Resources,* 22(5), pp. 461-478.

Pini, R. & Benson, S. M., 2013. Simultaneous determination of capillary pressure and relative permeability curves from core-flooding experiments with various fluid pairs. *Water resources research,* 49(6), pp. 3516-3530.

Piroird, K., Clanet, C. & Quéré, D., 2011. Capillary extraction. *Langmuir,* 27(15), pp. 9396-9402.

Pivello, M. et al., 2014. A fully adaptive front tracking method for the simulation of two phase flows. *International Journal of Multiphase Flow,* Volume 58, pp. 72-82.

Pope, G. A., 1980. The Application of Fractional Flow Theory to Enhanced Oil Recovery. *SPE J.,* 20(03), p. 191–205.

Prem, B. et al., 2016. Influence of wettability and permeability heterogeneity on miscible CO2 flooding efficiency. *Fuel,* Volume 166, pp. 219-226.

Pu, W. et al., 2018. A comprehensive review of polysaccharide biopolymers for enhanced oil recovery (EOR) from flask to field. *Journal of Industrial and Engineering Chemistry,* Volume 61, pp. 1-11.

Qi, P., Ehrenfried, D. H., Koh, H. & Balhoff, M. T., 2017. Reduction of Residual Oil Saturation in Sandstone Cores by Use of Viscoelastic Polymers. *SPE Journal,* 22(02), p. 447–458.

Quan, S., Lou, J. & Schmidt, D. P., 2009. Modeling merging and breakup in the moving mesh interface tracking method for multiphase flow simulations. *Journal of Computational Physics,* 228(7), pp. 2660-2675.

Rabbani, H. S. et al., 2018. Suppressing viscous fingering in structured porous media. *Proceedings of the National Academy of Sciences,* 115(19), pp. 4833-4838.

Rabinovich, A., Anto-Darkwah, E. & Mishra, A. M., 2019. Determining Characteristic Relative Permeability From Coreflooding Experiments: A Simplified Model Approach. *Water Resources Research,* 55(11), pp. 8666-8690.

Raeini, A. Q., Blunt, M. J. & Bijeljic, B., 2012. Modelling two-phase flow in porous media at the pore scale using the volume-of-fluid method. *Journal of Computational Physics,* 231(17), pp. 5653-5668.

Raffa, P., A, A., Broekhuis & Picchioni, F., 2016. Polymeric surfactants for enhanced oil recovery: A review. *Journal of Petroleum Science and Engineering,* Volume 145, pp. 723-733.

Rai, K., McComb, T., Rodriguez, E. & Withers, R., 2012. Development of a Tool to Predict Technical Success of Polymer Flooding Applications. *SPE Improved Oil Recovery Symposium,* pp. SPE-153878-MS.

Ramstad, T. & Hansen, A., 2016. Cluster evolution in steady-state two-phase flow in porous media. *Physical review E,* 73(2), p. 026306.

Raney, K., Ayirala, S., Chin, R. & Verbeek, P., 2012. Surface and Subsurface Requirements for Successful Implementation of Offshore Chemical Enhanced Oil Recovery. *SPE Prod & Oper,* 27(03), p. 294–305.

Reddi, L. N., Menon, S. & Pant, A., 1998. Pore-scale investigations on vibratory mobilization of LNAPL ganglia. *Journal of hazardous materials,* 62(3), pp. 211-230.

Reed, R. L., Healy, R. N. & Shah, D. O., 1977. Some physicochemical aspects of microemulsion flooding: a review. *Improved oil recovery by surfactant and polymer flooding,* pp. 383-437.

Ren, F. et al., 2017. Two-phase flow pipe network method for simulation of CO2 sequestration in fractured saline aquifers. *International Journal of Rock Mechanics and Mining Sciences,* Volume 98, pp. 39-53.

Rezaei, A. et al., 2016. Using surface modified clay nanoparticles to improve rheological behavior of Hydrolized Polyacrylamid (HPAM) solution for enhanced oil recovery with polymer flooding. *Journal of Molecular Liquids,* Volume 222, pp. 1148-1156.

Rimsha, A., Vahid, N., Hamidreza, E. & Pedro, J. M.-F., 2020. Impact of pore morphology on two-phase flow dynamics under wettability alteration. *Fuel,* Volume 268, p. 117315.

Rock, A. et al., 2020. On the Role of Polymer Viscoelasticity in Enhanced Oil Recovery: Extensive Laboratory Data and Review. *Polymers,* 12(10), p. Polymers.

Roland Lenormand, E. T. C. Z., 1988. Numerical models and experiments on immiscible displacements in porous media. *Journal of Fluid Mechanics,* Volume 189, pp. 165 - 187.

Roof, J. G., 1970. Snap-off of oil droplets in water-wet pores. *Society of Petroleum Engineers Journal,* 10(01), pp. 85-90.

Rouquerol, J. et al., 1994. Recommendations for the characterization of porous solids. *Pure and Applied Chemistry,* 66(8), pp. 1739-1758.

Russell, J. B. & Strobel, H., 1989. Effect of ionophores on ruminal fermentation. *Applied and environmental microbiology,* 55(1), pp. 1-6.

Ryan, T. J., 1980. Microcirculation in psoriasis: blood vessels, lymphatics and tissue fluid. *Pharmacology & therapeutics,* 10(1), pp. 27-64.

Ryazanov, A. V., Sorbie, K. S. & Van Dijke, M. I. J., 2014. Structure of residual oil as a function of wettability using pore-network modelling. *Advances in Water Resources,* Volume 63, pp. 11-21.

Saadat, M. et al., 2020. Development of a microfluidic method to study enhanced oil recovery by low salinity water flooding. *Acs Omega,* 5(28), pp. 17521-17530.

Sabhapondit, A., Borthakur, A. & Haque, I., 2003. Water soluble acrylamidomethyl propane sulfonate (AMPS) copolymer as an enhanced oil recovery chemica. *Energy Fuels,* 17(3), p. 683–688.

Saffman, P. G. & Taylor, G. I., 1958. The penetration of a fluid into a porous medium or Hele-Shaw cell containing a more viscous liquid. *Proceedings of the Royal Society of London. Series A. Mathematical and Physical Sciences,* 245(1242), pp. 312-329.

Sahar, B., Rabbani, H. S. & Shokri, N., 2021. Physics-driven investigation of wettability effects on two-phase flow in natural porous media: recent advances, new insights, and future perspectives. *Transport in Porous Media,* Volume 140, pp. 85-106.

Saha, R., Uppaluri, R. V. & Tiwari, P., 2019. Impact of natural surfactant (reetha), polymer (xanthan gum), and silica nanoparticles to enhance heavy crude oil recovery. *Energy & Fuels,* 33(5), pp. 4225-4236.

Salehi, M., Johnson, S. J. & Liang, J.-T., 2008. Mechanistic Study of Wettability Alteration Using Surfactants with Applications in Naturally Fractured Reservoirs. *Langmuir,* 24(24), p. 14099–14107.

Samanta, A., Bera, A., Ojha, K. & Mandal, A., 2012. Comparative studies on enhanced oil recovery by alkali–surfactant and polymer flooding. *Journal of Petroleum Exploration and Production Technology* , 2(2), pp. 67-74.

Samanta, A., Ojha, K. & Mandal, A., 2011. Interactions between Acidic Crude Oil and Alkali and Their Effects on Enhanced Oil Recovery. *Energy Fuels*, 25(4), p. 1642–1649.

Santis, A. D., Colombo, M., Hanson, B. & Fairweather, M., 2021. A generalized multiphase modelling approach for multiscale flows. *Journal of Computational Physics,* Volume 436, p. 110321.

Santvoort, J. v. & Golombok, M., 2016. Sweep enhancers for oil recovery. *Journal of Petroleum Exploration and Production Technology,* Volume 6, p. 473–480.

Santvoort, J. v. & Golombok, M., 2018. Improved recovery from fractured oil reservoirs. *Journal of Petroleum Science and Engineering,* Volume 167, pp. 28-36.

Saravanan, A. et al., 2020. A review on systematic approach for microbial enhanced oil recovery technologies: Opportunities and challenges. *Journal of Cleaner Production,* Volume 258, p. 120777.

Schechter, D., Zhou, D. & Orr Jr, F., 1994. Low IFT drainage and imbibition. *Journal of Petroleum science and Engineering,* 11(4), pp. 283-300.

Schroth, M. H. et al., 1998. Multifluid flow in bedded porous media: laboratory experiments and numerical simulations. *Advances in Water Resources*, 22(2), pp. 169-183.

Schulte, T. H., Bardell, R. L. & Weigl, B. H., 2002. Microfluidic technologies in clinical diagnostics. *Clinica Chimica Acta*, 321(1-2), pp. 1-10.

Scott, G., Collins, H. & Flock, D., 1965. Improving Waterflood Recovery of Viscous Crude Oils by Chemical Control. *J Can Pet Technol,* 4(04), p. 243–251.

Sedaghat, M. H., Ghazanfari, M. H., Parvazdavani, M. & Morshedi, S., 2013. Experimental Investigation of Microscopic/Macroscopic Efficiency of Polymer Flooding in Fractured Heavy Oil Five-Spot Systems. *J. Energy Resour. Technol.*, 135(3), p. 032901.

Sen, R., 2008. Biotechnology in petroleum recovery: The microbial EOR. *Progress in Energy and Combustion Science,* 34(6), pp. 714-724.

Senyou An, H. E. O. E. G.-B. V. N., 2020. Transition From Viscous Fingering to Capillary Fingering: Application of GPU-Based Fully Implicit Dynamic Pore Network Modeling. *Water Resources Research*, 56(12), p. e2020WR028149.

Seright, R. S., Fan, T., Wavrik, K. & Balaban, R. d. C., 2011. New Insights Into Polymer Rheology in Porous Media. *SPE J.,* 16(01), p. 35–42.

Seright, R. S., Seheult, M. & Talashek, T., 2009. Injectivity Characteristics of EOR Polymers. *SPE Res Eval & Eng*, 12(05), p. 783–792.

Shahab, M., Jain, S. S. & Dodd, M., 2017. Interface-capturing methods for two-phase flows: An overview and recent developments. *Center for Turbulence Research Annual Research Briefs,* 2017(13), pp. 117-135.

Shang, X., Bai, Y., Sun, J. & Dong, C., 2019. Performance and displacement mechanism of a surfactant/compound alkaline flooding system for enhanced oil recovery. *Colloids and Surfaces A: Physicochemical and Engineering Aspects,* Volume 580, p. 123679.

SHARMA, A., 2015. Level set method for computational multi-fluid dynamics: A review on developments, applications and analysis. *Sadhana,* Volume 40, p. pages627–652.

Sharma, P., Kostarelos, K. & Salman, M., 2021. Optimization of closed-cycle oil recovery: a non-thermal process for bitumen and extra heavy oil recovery. *RSC advances*, 11(43), pp. 26554-26562.

She, H. et al., 2019. Recent Advance of Microbial Enhanced Oil Recovery (MEOR) in China. *Geofluids and Energy for the XXI Century,* Volume 2019, pp. 1-16.

Sheng, J. J., 2010. *Modern chemical enhanced oil recovery: theory and practice.* s.l.:.Gulf Professional Publishing.

Sheng, J. J., 2013. A Comprehensive Review of Alkaline-Surfactant-Polymer (ASP) Flooding. *SPE Western Regional & AAPG Pacific Section Meeting 2013 Joint Technical*, pp. SPE-165358-MS.

Sheng, J. J., Leonhardt, B. & Azri, N., 2015. Status of Polymer-Flooding Technology. *J Can Pet Technol,* 54(02), p. 116–126.

Shiran, B. S. & Skauge, A., 2013. Enhanced Oil Recovery (EOR) by Combined Low Salinity Water/Polymer Flooding. *Energy Fuels,* 27(3), p. 1223–1235.

Shojaei, M.-J., Ghazanfari, M. H. & Masihi, M., 2015. Relative permeability and capillary pressure curves for low salinity water flooding in sandstone rocks. *Journal of Natural Gas Science and Engineering,* Volume 25, pp. 30-38.

Shui, L., Eijkel, J. C. & Van den Berg, A., 2007. Multiphase flow in microfluidic systems–Control and applications of droplets and interfaces. *Advances in colloid and interface science,* 133(1), pp. 35-49.

Shutang, G., Huabin, L. & Hongfu, L., 1995. Laboratory Investigation of Combination of Alkali/Surfactant/Polymer Technology for Daqing EOR. *SPE Res Eng ,* 10(03), p. 194–197.

Singh, K. et al., 2017. Dynamics of snap-off and pore-filling events during two-phase fluid flow in permeable media. *Scientific reports,* 7(1), p. 5192.

Skauge, A. et al., 2018. Polymer Flow in Porous Media: Relevance to Enhanced Oil Recovery. *Colloids and Interfaces,* 2(3), p. 27.

Slompo, P. H. S., Pinto, M. A. V. & Oliveira, M. L., 2023. Comparison between Van Genuchten and Brooks-Corey Parameterizations in the Solution of Multiphase Problems in Rigid One-Dimensional Porous Media. *Journal of Computational and Theoretical Transport,* 52(6), pp. 429-451.

Sochi, T., 2010. Non-Newtonian flow in porous media. *Polymer,* 51(22), pp. 5007-5023.

Sochi, T. & Blunt, M. J., 2008. Pore-scale network modeling of Ellis and Herschel–Bulkley fluids. *Journal of Petroleum Science and Engineering,* 60(2), pp. 105-124.

Sorbie, K. S., 2013. *Polymer-improved oil recovery.* s.l.:Springer Science & Business Media.

Spildo, K., Johannessen, A. M. & Skauge, A., 2012. Low Salinity Waterflood at Reduced Capillarity. *SPE Improved Oil Recovery Symposium,* pp. SPE-154236-MS.

Stegemeier, G. L., 1974. Relationship of Trapped Oil Saturation to Petrophysical Properties of Porous Media. *SPE Improved Oil Recovery Symposium,* pp. SPE-4754-MS.

Stegemeier, G. L., 1976. Mechanisms of entrapment and mobilization of oil in porous media. *AICRE Mtng,* Volume 81st, pp. 55-91.

Subbaiah, R., 2013. A review of models for predicting soil water dynamics during trickle irrigation. *Irrigation Science,* 31(3), pp. 225-258.

Sukpisan, J., Kanatharana, J., Sirivat, A. & Wang, S. Q., 1998. The specific viscosity of partially hydrolyzed polyacrylamide solutions: Effects of degree of hydrolysis, molecular weight, solvent quality and temperature. *Journal of Polymer Science Part B: Polymer Physics,* 36(5), pp. 743-753.

Sun, D. M., Zang, Y. G. & Semprich, S., 2015. Effects of airflow induced by rainfall infiltration on unsaturated soil slope stability. *Transport in Porous Media,* Volume 107, pp. 821-841.

Sun, X. et al., 2022. Study on Micro Production Mechanism of Corner Residual Oil after Polymer Flooding. *Polymers,* 14(5), p. 878.

Tadros, T. F., 2006. *Applied surfactants: principles and applications.* s.l.:John Wiley & Sons.

Takeshi, T., Fei, J. & Kenneth, T. C., 2016. Characterization of immiscible fluid displacement processes with various capillary numbers and viscosity ratios in 3D natural sandstone. *Advances in Water Resources,* Volume 95, pp. 3-15.

Talon, L., Bouguemari, R., Yiotis, A. & Salin, D., 2023. Fragmentation and coalescence dynamics of non-wetting blobs during immiscible two-phase flows in porous media. *Physical Review Fluids,* 8(9), p. 093602.

Tang, J., Smit, M., Vincent-Bonnieu, S. & Rossen, W. R., 2019. New capillary number definition for micromodels: The impact of pore microstructure. *Water Resources Research,* 55(2), pp. 1167-1178.

Tavakkoli, O. et al., 2022. SDS–Aluminum Oxide Nanofluid for Enhanced Oil Recovery: IFT, Adsorption, and Oil Displacement Efficiency. *ACS Omega,* 7(16), p. 14022–14030.

Tavakkoli, O. et al., 2022. Effect of nanoparticles on the performance of polymer/surfactant flooding for enhanced oil recovery: A review. *Fuel,* Volume 312, p. 122867.

Terry, R. E., 2001. Enhanced oil recovery. *Encyclopedia of physical science and technology,* 18(1), pp. 503-518.

Tripathi, S. et al., 2016. Microdevice for plasma separation from whole human blood using bio-physical and geometrical effects. *Scientific reports,* 6(1), p. 26749.

Urbissinova, T. S., Trivedi, J. & Kuru, E., 2010. Effect of Elasticity During Viscoelastic Polymer Flooding: A Possible Mechanism of Increasing the Sweep Efficiency. *J Can Pet Technol,* 49(12), p. 49–56.

Van Genuchten, M. T., 1980. A closed-form equation for predicting the hydraulic conductivity of unsaturated soils. *Soil science society of America journal,* 44(5), pp. 892-898.

van Steijn, V., Kleijn, C. R. & Kreutzer, M. T., 2009. Flows around confined bubbles and their importance in triggering pinch-off. *Physical review letters,* 103(21), p. 214501.

Vasudevan, M., Shen, A., Khomami, B. & Sureshkumar, R., 2008. Self-similar shear thickening behavior in CTAB/NaSal surfactant solutions. *J. Rheol.,* 52(2), p. 527–550.

Waheed, S. et al., 2016. 3D printed microfluidic devices: enablers and barriers. *Lab Chip,* Volume 16, pp. 1993-2013.

Wang, D. et al., 2001. Viscous-Elastic Fluids Can Mobilize Oil Remaining after Water-Flood by Force Parallel to the Oil-Water Interface. *SPE Asia Pacific Improved Oil Recovery Conference,* pp. SPE-72123-MS.

Wang, D. et al., 2000. Viscous-Elastic Polymer Can Increase Microscale Displacement Efficiency in Cores. *SPE Annual Technical Conference and Exhibition,* pp. SPE-63227-MS.

Wang, D., Li, Q., Gong, X. & Wang, Y., 2000. The Engineering and Technical Aspects of Polymer Flooding in Daqing Oil Field. *International Oil and Gas Conference and Exhibition in China,* pp. SPE-64722-MS.

Wang, D. et al., 2007. The Influence of Viscoelasticity on Displacement Efficiency—From Micro- to Macroscale. *SPE Annual Technical Conference and Exhibition,* pp. SPE-109016-MS.

Wang, D., Xia, H., Liu, Z. & Yang, Q., 2001. Study of the Mechanism of Polymer Solution With Visco-Elastic Behavior Increasing Microscopic Oil Displacement Efficiency and the Forming of Steady "Oil Thread" Flow Channels. *SPE Asia Pacific Oil and Gas Conference and Exhibition*, pp. SPE-68723-MS.

Wang, D., Xia, H., Yang, S. & Wang, G., 2010. The Influence of Visco-Elasticity on Micro Forces and Displacement Efficiency in Pores, Cores and in the Field. *SPE EOR Conference at Oil & Gas West Asia*, pp. SPE-127453-MS.

Wangen, M., 1993. Vertical migration of hydrocarbons modelled with fractional flow theory. *Geophysical Journal International,* 115(1), pp. 109-131.

Wang, L. et al., 2017. Advances in improved/enhanced oil recovery technologies for tight and shale reservoirs. *Fuel,* Volume 210, pp. 425-445.

Wang, Y. et al., 2013. Experimental study of crossover from capillary to viscous fingering for supercritical CO2–water displacement in a homogeneous pore network. *Environmental science & technology*, 47(1), pp. 212-218.

Wegner, J., Hincapie, R. E., Födisch, H. & Ganzer, L., 2015. Novel Visualisation of Chemical EOR Flooding Using a Lab-on-a-Chip Setup Supported by an Extensive Rheological Characterisation. *SPE Asia Pacific Enhanced Oil Recovery Conference,* pp. SPE-174648-MS.

Wei, B., Romero-Zerón, L. & Rodrigue, D., 2014. Mechanical Properties and Flow Behavior of Polymers for Enhanced Oil Recovery. *Journal of Macromolecular Science, Part B,* 53(4), pp. 625-644.

Wei, B., Romero-Zerón, L. & Rodrigue, D., 2014. Oil displacement mechanisms of viscoelastic polymers in enhanced oil recovery (EOR): a review. *Journal of Petroleum Exploration and Production Technology,* Volume 4, p. 113–121.

Weitz, D. A., Stokes, J. P., Ball, R. C. & Kushnick, A. P., 1987. Dynamic capillary pressure in porous media: Origin of the viscous-fingering length scale. *Physical review letters,* 59(26), p. 2967.

Wenxiang, W. & Demin, W., 2007. Effect of the Visco-elasticity of Displacing Fluids on the Relationship of Capillary Number and Displacement Efficiency in Weak Oil-Wet Cores. *Asia Pacific Oil and Gas Conference and Exhibition*, pp. SPE-109228-MS.

Wever, D., Picchioni, F. & Broekhuis, A., 2011. Polymers for enhanced oil recovery: A paradigm for structure–property relationship in aqueous solution. *Progress in Polymer Science,* 36(11), pp. 1558-1628.

Whitaker, S., 1986. Flow in Porous Media I: A Theoretical Derivation of Darcy's Law. *Transport in Prous Media,* 3(1), pp. 3-25.

Whitaker, S., 1986. Flow in Porous Media II: The Governing Equations for Immiscible, Two-Phase flow. *Transport in Porous Media,* Volume 1, pp. 105-125.

Whitaker, S., 1996. The Forchheimer equation: a theoretical development. *Transport in Porous media,* 25(1), pp. 27-61.

Wilkinson, D. & Willemsen, J. F., 1983. Invasion percolation: a new form of percolation theory. *Journal of physics A: Mathematical and general,* 16(14), p. 3365.

Wörner, M., 2012. Numerical modeling of multiphase flows in microfluidics and micro process engineering: a review of methods and applications. *Microfluidics and Nanofluidics,* 12(6), p. 841–886.

Wu, Y. et al., 2012. Development of New Polymers with Better Performance under Conditions of High Temperature and High Salinity. *SPE EOR Conference at Oil and Gas West Asia*, pp. SPE-155653-MS.

Wyatt, K., Pitts, M. J. & Surkalo, H., 2002. Mature Waterfloods Renew Oil Production by Alkaline-Surfactant-Polymer Flooding. *SPE Eastern Regional Meeting. SPE*, pp. SPE-78711-MS.

Xia, H. F. et al., 2008. Mechanism of the Effect of Micro-Forces on Residual Oil in Chemical Flooding. *SPE Symposium on Improved Oil Recovery*, pp. SPE-114335-MS.

Xianglei Zheng, N. M. T. S. Y. J. J., 2017. Effect of capillary and viscous force on CO2 saturation and invasion pattern in the microfluidic chip. *JGR Solid Earth,* 122(3), pp. 1634-1647.

Xia, Q., Kim, J. & Li, Y., 2022. Modeling and simulation of multi-component immiscible flows based on a modified Cahn–Hilliard equation. *European Journal of Mechanics - B/Fluids*, Volume 95, pp. 194-204.

Xie, D., Hou, J., Doda, A. & Trivedi, J., 2016. Application of Organic Alkali for Heavy-Oil Enhanced Oil Recovery (EOR), in Comparison with Inorganic Alkali. *Energy Fuels*, 30(6), p. 4583–4595.

Xu, D. et al., 2019. Mechanisms of imbibition enhanced oil recovery in low permeability reservoirs: Effect of IFT reduction and wettability alteration. *Fuel*, Volume 244, pp. 110-119.

Xu, W. et al., 2014. Effect of pore geometry and interfacial tension on water-oil displacement efficiency in oil-wet microfluidic porous media analogs. *Physics of Fluids,* 26(9), p. 093102.

Y., H. & Jenning, J., 1975. A Study of Caustic Solution-Crude Oil Interfacial Tensions. *SPE Journal*, 15(03), p. 197–202.

Yang, Y. et al., 2019. Microscopic determination of remaining oil distribution in sandstones with different permeability scales using computed tomography scanning. *Journal of Energy Resources Technology*, 141(9), p. 092903.

Yang, Z. et al., 2016. Fluid trapping during capillary displacement in fractures. *Advances in Water Resources*, Volume 95, p. 264–275.

Yan, Y., Li, X. & Ito, K., 2020. Numerical investigation of indoor particulate contaminant transport using the Eulerian-Eulerian and Eulerian-Lagrangian two-phase flow models. *Experimental and Computational Multiphase Flow*, Volume 2, p. 31–40.

Yeganeh, M. et al., 2016. Capillary desaturation curve fundamentals. *SPE Improved Oil Recovery Conference*, pp. SPE-179574-MS.

Yi-Feng Chen, S. F. D.-S. W. R. H., 2017. Visualizing and quantifying the crossover from capillary fingering to viscous fingering in a rough fracture. *Water Resources Research*, 53(9), pp. 7756-7772.

Ying, W. et al., 2013. Experimental Study of Crossover from Capillary to Viscous Fingering for Supercritical CO2–Water Displacement in a Homogeneous Pore Network. *Environ. Sci. Technol.*, 47(1), p. 212–218.

Yin, H. J. et al., 2012. Flow Characteristics of Viscoelastic Polymer Solution in Micro-Pores. *SPE EOR Conference at Oil and Gas West Asia*, pp. SPE-154640-MS.

Yiotis, A., Karadimitriou, N. K., Zarikos, I. & Steeb, H., 2021. Pore-scale effects during the transition from capillary-to viscosity-dominated flow dynamics within microfluidic porous-like domains. *Scientific Reports,* 11(1), p. 3891.

Young, L. C., 1984. A study of spatial approximations for simulating fluid displacements in petroleum reservoirs. *Computer Methods in Applied Mechanics and Engineering*, 47(1-2), pp. 3-46.

Yue, P., Dooley, J. & Feng, J. J., 2008. A general criterion for viscoelastic secondary flow in pipes of noncircular cross section. *Journal of Rheology*, 52(1), p. 315–332.

Yu, F. et al., 2019. New insights into flow physics in the EOR process based on 2.5 D reservoir micromodels. *Journal of Petroleum Science and Engineering*, p. 181.

Yun, W. et al., 2020. Toward reservoir-on-a-chip: Rapid performance evaluation of enhanced oil recovery surfactants for carbonate reservoirs using a calcite-coated micromodel. *Scientific reports*, 10(1), p. 782.

Zahid, S., Khan, H. A. & Zahoor, M. K., 2007. A Review on Microbial Enhanced Oil Recovery With Special Reference to Marginal/Uneconomical Reserves. *Production and Operations Symposium*, pp. SPE-107052-MS.

Zaitoun, A. & Kohler, N., 1988. Two-Phase Flow Through Porous Media: Effect of an Adsorbed Polymer Layer. *SPE Annual Technical Conference and Exhibition*, pp. SPE-18085-MS.

Zarikos, I., Terzis, A., Hassanizadeh, S. M. & Weigand, B., 2018. Velocity distributions in trapped and mobilized non-wetting phase ganglia in porous media. *Scientific reports*, 8(1), p. 13228.

Zhang, C. et al., 2011. Influence of viscous and capillary forces on immiscible fluid displacement: Pore-scale experimental study in a water-wet micromodel demonstrating viscous and capillary fingering. *Energy & Fuels*, 25(8), pp. 3493-3505.

Zhang, Y., Xie, X. & Morrow, N. R., 2007. Waterflood Performance by Injection of Brine With Different Salinity for Reservoir Cores. *SPE Annual Technical Conference and Exhibition,* pp. SPE-109849-MS.

Zhao, B. & Mohanty, K. K., 2019. Effect of wettability on immiscible viscous fingering in porous media. *Journal of Petroleum Science and Engineering,* Volume 174, pp. 738-746.

Zhao, J., Yao, G. & Wen, D., 2019. Pore-scale simulation of water/oil displacement in a water-wet channel. *Frontiers of Chemical Science and Engineering,* Volume 13, pp. 803-814.

Zhaoqin Huang, X. Y. J. Y., 2014. A Two-Phase Flow Simulation of Discrete-Fractured Media using Mimetic Finite Difference Method. *Communications in Computational Physics,* 16(3), pp. 799-816.

Zhong, L., Mayer, A. & Glass, R. J., 2001. Visualization of surfactant-enhanced nonaqueous phase liquid mobilization and solubilization in a two-dimensional micromodel. *Water Resources Research,* 37(3), pp. 523-537.

Zhu, S. et al., 2020. Research on optimal timing range for early polymer injection in sandstone reservoir. *Energy Reports,* Volume 6, pp. 3357-3364.

Zivar, D., Pourafshary, P. & Moradpour, N., 2021. Capillary desaturation curve: does low salinity surfactant flooding significantly reduce the residual oil saturation?. *Journal of Petroleum Exploration and Production,* Volume 11, pp. 783-794.